NASA CONTRACTOR REPORT

NASA CR

NASA CR-486

SPECTRA AND SPACE-TIME CORRELATIONS
OF THE FLUCTUATING PRESSURES
AT A WALL BENEATH A SUPERSONIC
TURBULENT BOUNDARY LAYER PERTURBED
BY STEPS AND SHOCK WAVES

by W. V. Speaker and C. M. Ailman

NASA CR-486

SPECTRA AND SPACE-TIME CORRELATIONS OF THE FLUCTUATING

PRESSURES AT A WALL BENEATH A SUPERSONIC TURBULENT

BOUNDARY LAYER PERTURBED BY STEPS AND SHOCK WAVES

By W. V. Speaker and C. M. Ailman

ACKNOWLEDGMENT

CONTENTS

FIGURES

SPECTRA AND SPACE-TIME CORRELATIONS OF THE FLUCTUATING PRESSURES AT A WALL BENEATH A SUPERSONIC TURBULENT BOUNDARY LAYER PERTURBED BY STEPS AND SHOCK WAVES

By W. V. Speaker
C. M. Ailman
Missile and Space Systems Division
Douglas Aircraft Company, Inc.

SUMMARY

Pressure fluctuations induced at a wall by a turbulent boundary layer were obtained in uniform flow at subsonic speeds and in both uniform and perturbed flow at supersonic speeds. The flow perturbations resulted from use of forward- and aft-facing steps and shock waves. The data are presented in terms of spatial distribution of overall levels, energy distribution in the frequency domain, and broad-band correlation in space and time. Included in the analysis are discussions on the following:

(1) Mach number dependence of the overall levels in uniform flow

(2) Methods of nondimensionalizing the power spectra to compress the data

(3) Comparison of results from several experimenters

(4) Typical power spectra for specific regions of perturbed flow

(5) Convection velocities in uniform and perturbed flows

(6) Space-time correlations of the fluctuating pressures

(7) Feasibility of separating the cross-correlation function into a product of functions dependent on only one variable

(8) Mathematical descriptions of the cross-correlation functions.

Section 1

INTRODUCTION

The advent of the supersonic flight era has precipitated studies to further increase our knowledge of in-flight environments at higher Mach numbers. In addition, specific mission requirements have caused flight vehicles to be designed with profiles conducive to considerable perturbation of the normally well-behaved turbulent boundary layer. Because of this trend, in 1963 a preliminary research study (ref. 1) was performed on the sidewall of a blowdown wind tunnel at the Douglas Aircraft Company's Aerophysics Laboratory. This earlier study examined the static and fluctuating pressures at a wall beneath a turbulent boundary layer for a range of Mach numbers from 0.4 to 3.5, and at Mach number 3.5 for several configurations which perturbed the flow. Because of certain limitations in data measurements and analysis, the experimental approach was expanded to include (1) larger frequency range, (2) definition of spatial distributions in greater detail, (3) space-time correlations of the fluctuating pressures in addition to description of the energy distribution in the spatial and frequency domains, and (4) preliminary structural response studies of idealized structure. This report documents the result of the first three of these program extensions, as applied to a new series of tests performed in January 1965. The fourth item, based on tests performed in May 1965, is discussed under separate cover (ref.2). The test results detailed in this report include both subsonic and supersonic unperturbed turbulent boundary-layer data which may be used to compare this work with the work of other experimenters. In addition, an aft-facing step, an impinging shock wave, and step-spoilers--in some instances equivalent to forward-facing steps--are included. The boundary layer was at all times fully developed, turbulent, and two-dimensional during passage over the instrumented insert in an essentially rigid wall of the wind tunnel. Where possible, the results are generalized to typical parameters, but the actual data are comparable to an approximate geometrical scale factor of one-fifth.

Section 2

NOMENCLATURE

2.1 Symbols

b	constant used in section 5.4, $\sec^{-1}$
c	velocity of sound, fps
c_f	skin-friction coefficient, dimensionless
d	transducer diameter, in.
f	frequency, cps
$F(\omega)$	power spectral density, $(\text{psi})^2/\text{rad}/\text{sec}$
FPL	fluctuating pressure level, dB re 0.0002 dyn/cm^2
h	step height, in.
H	form parameter = δ^*/θ, dimensionless
i	$\sqrt{-1}$
K, L	constants used in section 5.4, dimensionless
M	Mach number, dimensionless
P	static pressure, psia
p	fluctuating pressure, psi
$\sqrt{\bar{p}^2}$	root mean squared (rms) fluctuating pressure, psi
$<p^2>$	time average of the fluctuating pressure squared
q	dynamic pressure, psi
Re	Reynolds number based on a characteristic parameter
	R_δ = Re using boundary-layer thickness
	R_{δ^*} = Re using boundary-layer displacement thickness
	R_θ = Re using boundary-layer momentum thickness
	R_x = Re using longitudinal length
T	time in sec, or temperature in deg (Rankine)
u	local velocity in the boundary layer, fps
U	stream velocity, fps
U_c	convection velocity of the pressure signature, fps
V_s, V_m	integral area scales, defined in section 5.6

x	distance in the direction of the flow, in.
Δx	incremental distance in the x-direction
y	distance perpendicular to the wall, in.
z	distance in the plane of the wall, perpendicular to the tunnel centerline, in.
β	angle between the direction of flow and an arbitrary direction in the plane of the wall, deg
δ	boundary-layer thickness, in.
δ^*	boundary-layer displacement thickness, in.
θ	boundary-layer momentum thickness, in.
λ_x, λ_z	integral length scales in the x-and z-directions, in.
ξ	separation distance between measuring stations, in.
μ	absolute viscosity, lb-sec/ft^2
ρ	density, lb-sec^2/ft^4
τ	time delay, sec
τ_c	time delay between cross-correlation maxima, sec
τ_w	wall shearing stress, psi
ω	angular frequency, rad/sec

Subscripts

e	condition at the edge of the boundary layer
i	incompressible
LE	leading edge of step
s	start of static pressure rise for impinging shock wave
TE	trailing edge of step
t	stagnation conditions
w	conditions at the wall
∞	free-stream conditions
x	in direction of the flow
z	in plane of wall, perpendicular to tunnel centerline

6

2.2 Description of Broad-Band Space-Time Correlations

Before presenting the space-time correlation results for each of the types of flow, nomenclature is briefly discussed below. These preliminary remarks are true for all subsequent discussions unless stated otherwise

The space-time cross-correlation function, calculated from measured data at two different transducer locations for a period of time 2T, can be expressed mathematically as the integral

$$\psi_{12}(\vec{\xi}, \tau) = \lim_{T \to \infty} \frac{1}{2T} \int_{-T}^{T} p_1(\vec{x}_1, t) p_2(\vec{x}_1 + \vec{\xi}, t + \tau) dt \tag{1}$$

where $\psi_{12}(\vec{\xi}, \tau)$ is the space-time correlation function, dependent only on the separation distance, $\vec{\xi}$, between the two locations in space, and the time difference, τ, between the signal records of each of the measurements (under the usual assumptions of homogeneity, stationarity, and ergodicity)

$p_1(\vec{x}_1, t)$ is the pressure signature at location 1 (described in the spatial domain by the vector $\vec{x}_1$) at the time, t

$p_2(\vec{x}_1 + \vec{\xi}, t + \tau)$ is the pressure signature at location 2 delayed by a time difference, τ, from the signature at location 1

$\vec{x}$ is the position vector that has components in the x-direction (the direction of the flow in the plane of the measuring surface) and in the z-direction (perpendicular to the direction of the flow and in the plane of the measuring surface).

Measurements were made in the xz-plane for each of the types of flow examined. Measurements were taken on a line at 0°, 30°, 60°, and 90° to the flow direction. This coverage supplied ample information for contour mapping of the correlation functions when time translation of the data was included (see below).

Throughout this report, the broad-band space-time cross-correlation functions are normalized as follows:

$$R(\vec{\xi}\cos\beta, \vec{\xi}\sin\beta, \tau) = \frac{\psi_{12}(\vec{\xi}, \tau)}{\sqrt{\psi_{11}(0,0)\psi_{22}(0,0)}} = \frac{\psi_{12}(\vec{\xi}, \tau)}{\sqrt{<p_1^2><p_2^2>}} \tag{2}$$

where $<>$ designates a time average. The mean squared values are uncorrected for system response or pressure cancellation effects, but the

limitation in frequency of these broad-band calculations (160 to 16 000 cps) reduced those errors to a negligible quantity.

For simplicity in notation, the following conventions will be adopted: $R(\xi_x, 0, \tau)$ will mean the space-time cross-correlation in the x-direction calculated from two signals from two positions in space separated by a distance, $\vec{\xi}$, in the x-direction. Likewise, $R(0, \xi_z, \tau)$ will be the space-time correlation in the z-direction. For positions in the plane, $R(\xi\cos\beta, \xi\sin\beta, \tau)$ will signify the space-time correlation of two pressure signatures measured at two spatial locations with a separation distance, $\vec{\xi}$, in inches, an x-component of $\vec{\xi}$ equal to $\vec{\xi}\cos\beta$, a z-component of $\vec{\xi}$ equal to $\vec{\xi}\sin\beta$, where β is the angle in degrees between the separation vector $\vec{\xi}$ and the direction of the flow, and τ is the time increment of delay in seconds.

The particular values of the space-time correlation functions at $\tau = 0$, commonly called the correlation coefficient (involving only spatial character- istics) will be designated $C(\xi_x, 0, 0)$, $C(0, \xi_z, 0)$, or $C(\xi\cos\beta, \xi\sin\beta, 0)$ for the x-direction, z-direction, and intermediate directions, respectively. These functions can be found in either of two ways: (1) the data from several transducer locations can be examined at an instant of time in the frame of reference of the fixed boundary, or (2) alternatively, the correlation coefficient in a frame of reference moving with the boundary layer can be measured at a single location in the fixed boundary over a period of time. These two procedures permit definition of the correlation coefficient in the fixed frame at an instant of time, $\tau = 0$, or taking data at time, $\tau \neq 0$, to deduce the correlation coefficient measured by an observer moving with the boundary layer. In the latter case, the translation in space is achieved by using the position of the maximum (of the space-time correlation in the frame of reference fixed with respect to the rigid boundary) to define the convection velocity and then finding the new ξ_x by subtracting the appropriate $U_c\tau$ $(\xi_x - U_c\tau)$. The time dependence of the magnitude, again found by watching the decay of the maximum in time, is used to extrapolate the magnitude in time. This deduction of the correlation coefficient for the moving frame results in a curve identical to that found by measuring the instantaneous coefficient in the fixed frame but augments the number of data points, lending credence to the resultant curve.

Admittedly, using the second procedure introduces an assumption not previously substantiated: i.e., the entire correlation coefficient, calculated for the frame of reference moving with the turbulent boundary layer, changes in exactly the same prescribed way with time (time is invariant in both frames of reference). In the supersonic flow data, this assumption is good and can be verified because the time difference between the zeros of the space-time correlation function remains a constant for any spatial location. For subsonic flow, the argument is not as well substantiated. This technique, then, was used for supersonic flow in the unperturbed case, and in the direction of the flow only for supersonic perturbed flow (thus avoiding the complications of possible lateral convection velocities).

Section 3

APPARATUS, TESTING PROCEDURES, AND DATA HANDLING TECHNIQUES

3.1 Wind Tunnel

All measurements during the test were taken on the sidewall of the Trisonic One-Foot Wind Tunnel at the Douglas Aerophysics Laboratory. The tunnel is a blowdown-to-atmosphere facility with a Mach number range from 0.2 to 3.5, generated by fixed-contour nozzle blocks. Modifications to the facility to eliminate background noise associated with choked-valve flow are described and illustrated in ref. 1. Further details concerning the wind tunnel may be found in ref. 3.

3.2 Model Description

Test models included two interchangeable 14.5-in. diam. inserts and various flow disturbances, such as shock-wave generators, aft-facing steps, and step-spoilers. The two inserts are described in more detail in sub-sections 3.4 and 3.5.

The flow disturbances were constructed so that they spanned the tunnel from floor to ceiling with approximately 1/8-in. clearance and presented essentially a two-dimensional flow field near the centerline of the sidewall. The shock-wave generator is shown in fig. 1 and is described in ref. 1. The shock angle for these tests was set at 7.5°.

The aft-facing steps were fabricated from 3/4-in. laminates of plywood covered with masonite. The laminates covered the tunnel sidewall from the stilling chamber to the upstream edge of the insert and were contoured to their respective Mach number shapes (fig. 2). From the upstream edge to the center of the insert, a 3/4-in.-thick piece of aluminum was used to complete the aft-facing step. The aluminum plate was interchangeable with all the contoured laminates and was pinned to the sidewall to minimize longitudinal flow deviations. The aluminum plate had 26 static-pressure orifices located at 1/4-in. intervals longitudinally on the top surface and two orifices on the face of the step. There were also provisions for two transducers on the top surface and one on the step face.

The step-spoilers were similar to the two-dimensional roughness elements of ref. 1. They varied in height from 1/4 in. to 1-1/2 in. and were about 1.3 in. wide (to fit between two fluctuating pressure locations). Fig. 3 shows the 3/4-in. step-spoiler with the sidewall insert rotated 180° (for space-time correlation measurements). Each step-spoiler had four static-pressure orifices and provisions for three fluctuating pressure transducers on the top surface.
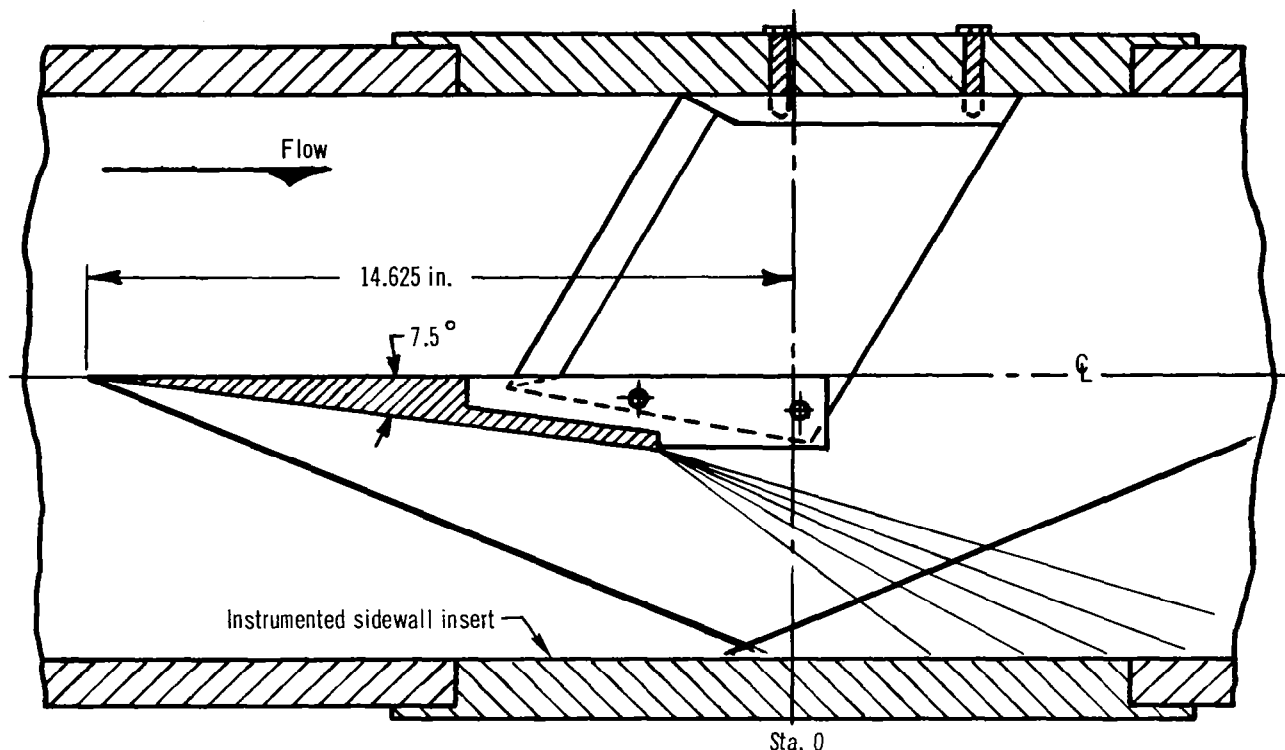
Figure 1. Shock-Wave Generator

Besides the flow disturbances noted above, devices to thicken the bound-ary layer were provided for subsonic Mach numbers and for M = 2.5 and 3.5. A preliminary investigation was conducted early in the test program to deter-mine the size, length, and location of sandpaper-type roughness that would produce about a 100% increase in boundary-layer thickness at M = 3.5. A typical configuration tested is shown in fig. 4, where the length of the final configuration chosen is indicated. The grit size was no. 4, which averaged about 1/4 in. high. A similar pattern was used at M = 2.5. For subsonic testing, grit size no. 4 was also used, but the grit was placed on the sidewall only for the first 2 ft. downstream of the stilling chamber.

3.3 Boundary-Layer Profiles

Boundary-layer velocity profiles were obtained using the three-probe total-pressure rake illustrated in ref. 1. The rake position was continuously varied, and its position was measured by a shaft-position encoder that pro-vided an overall accuracy of ±0.003 in. The total pressures were reduced to local Mach numbers and velocities by standard equations, assuming no variation existed in static pressure or stagnation temperature across the boundary layer. The local velocity within the boundary layer was plotted on logarithmic paper as a function of distance from the sidewall (fig. 5). If it is assumed that the velocity profile follows the 1/n power law in the outer part of the boundary layer, then a straight line can be drawn through the

Flow

Tunnel sidewall

Fluctuating pressure insert

Fluctuating pressure measurement location

Gap faired with clay

Static pressure orifices

Plywood laminate

7 in. × 3/4 in. Aluminum
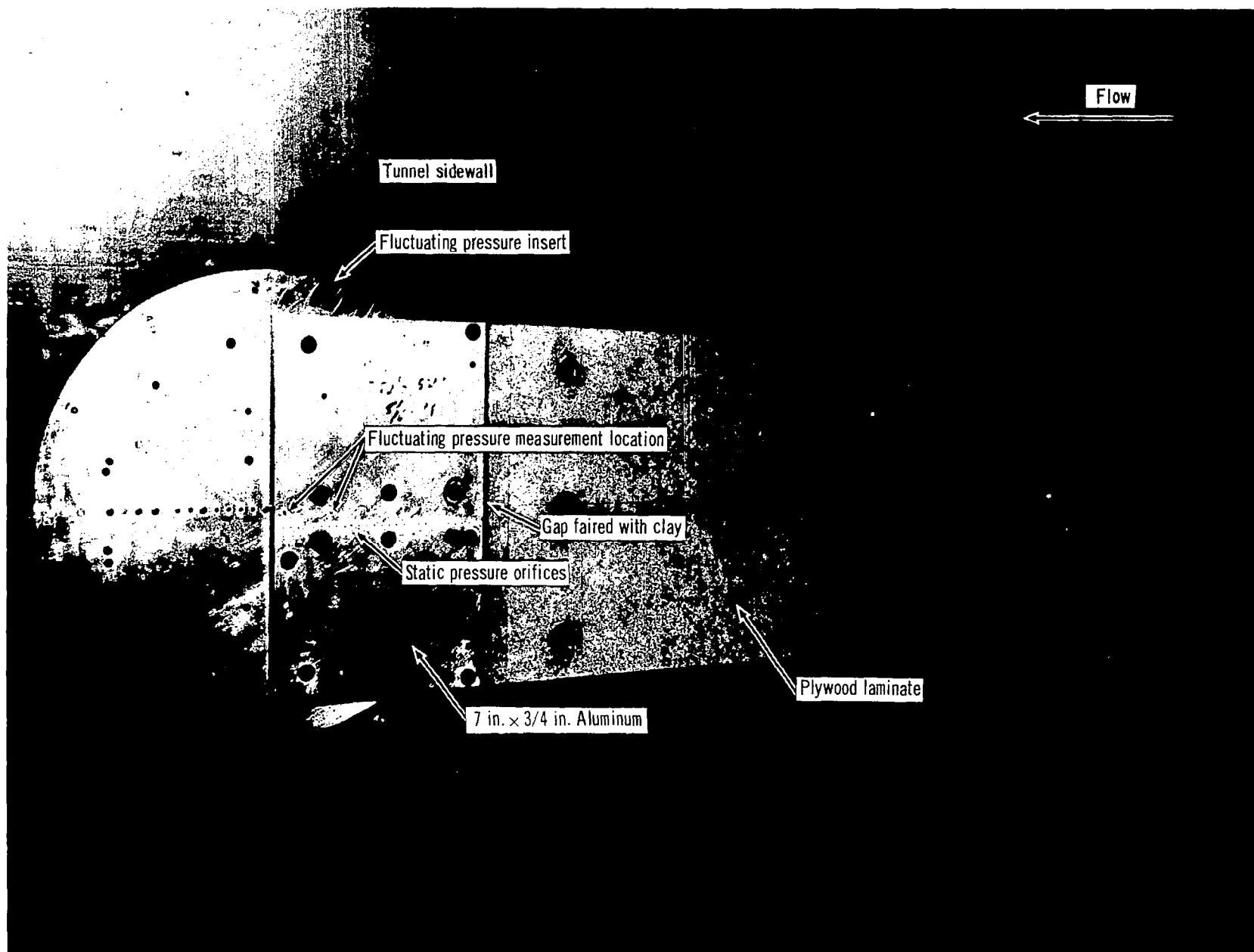
Figure 2. Aft-Facing Step as Used for Testing at M = 3.45

11
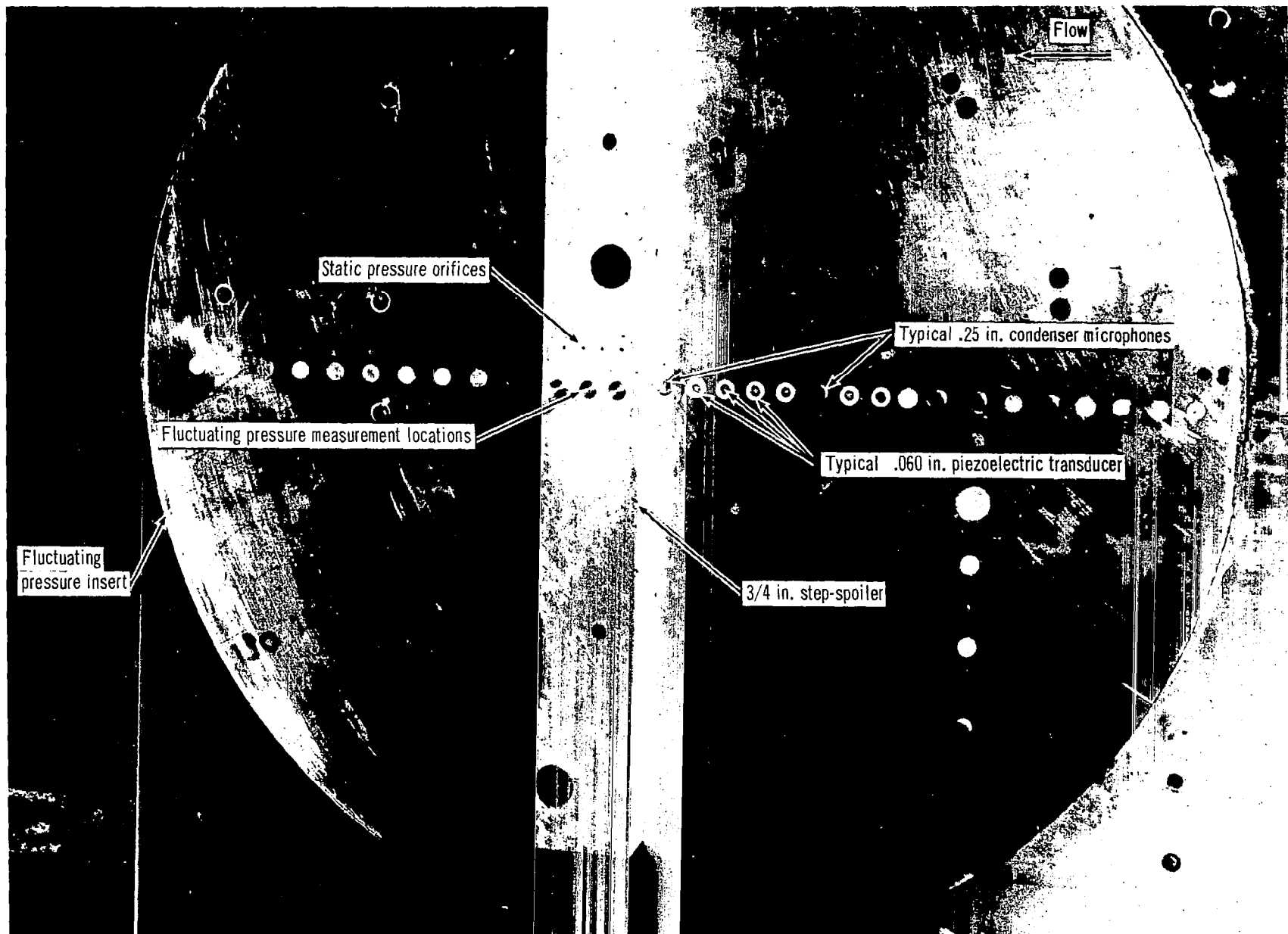
Figure 3. Fluctuating Pressure Insert with 3/4-in. Step-Spoiler Installed
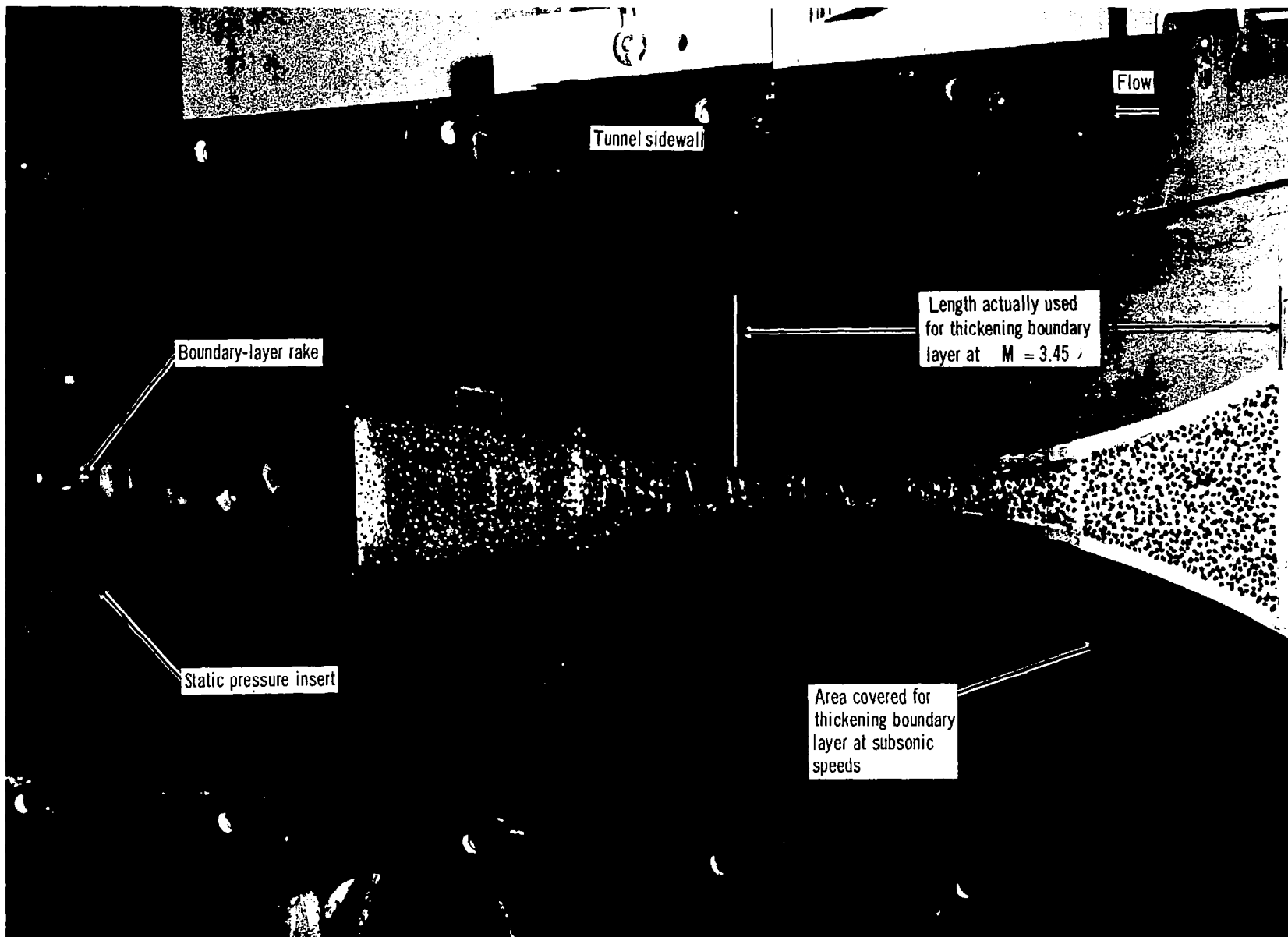
Figure 4. Boundary-Layer Thickening Device
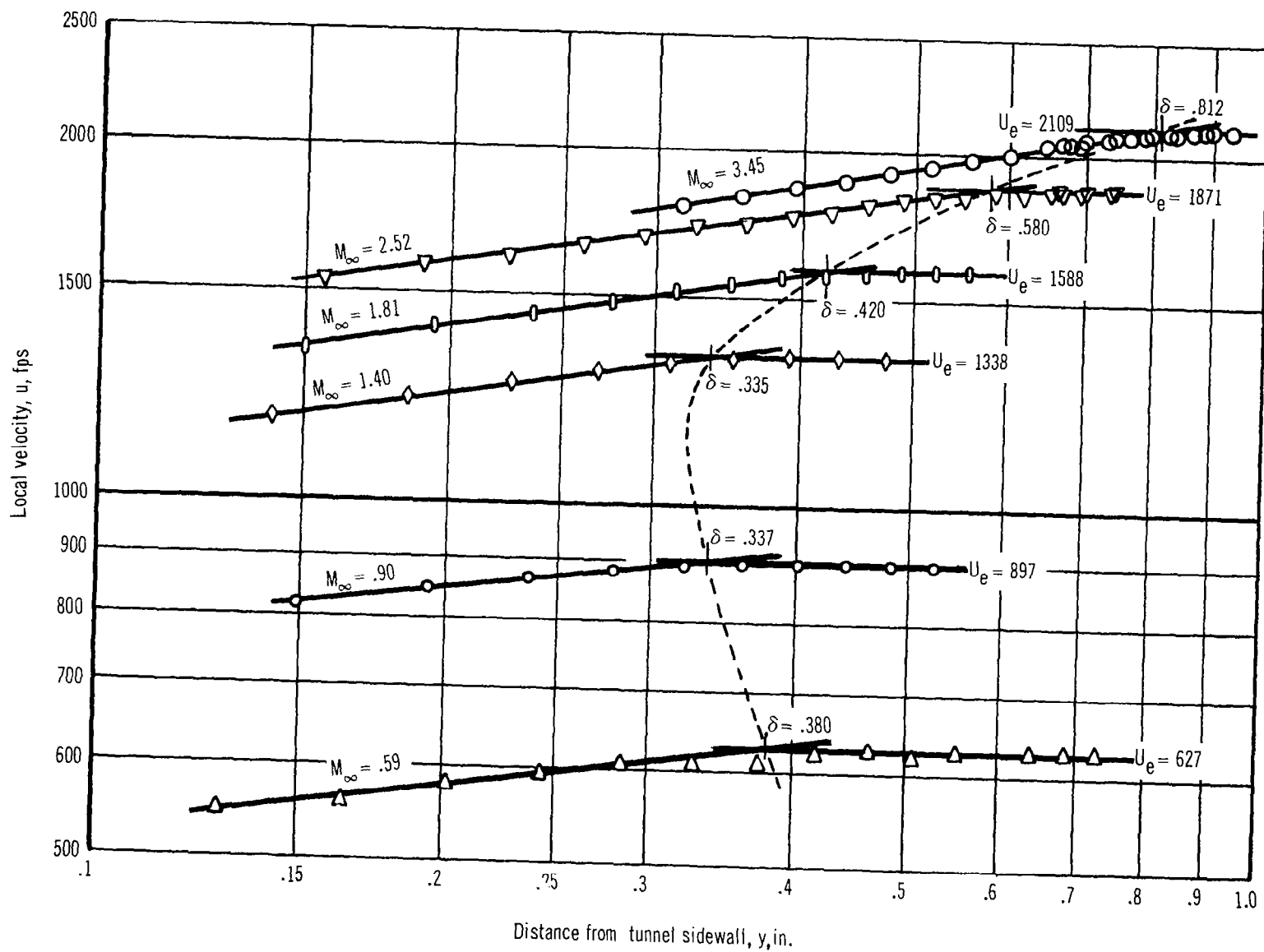
Figure 5. Determination of Boundary Layer Thicknesses

data. The distance from the wall at which this line intersects a line of constant velocity at the edge of the boundary layer is defined as δ.

The profiles were nondimensionalized using δ and U_e and produced profiles such as shown in fig. 6. Fig. 7 shows the nondimensional profiles as a function of displacement thickness $δ^*$. By use of equations and methods described in appendix A, values of other boundary-layer parameters were obtained. These are listed in table I, and some are shown in fig. 8 as functions of Mach number.

TABLE I

BOUNDARY-LAYER PROPERTIES IN THE TRISONIC
ONE-FOOT WIND TUNNEL

(Data apply to tunnel station 0 (insert centerline))

Mach No.	U_∞ (fps)	q_∞ (psi)	δ (in.)	$δ^*$ (in.)	Θ (in.)	H	Re/in x 10^6	c_f	τ_w (psi)
0.42	463	2.35	0.493	0.0661	0.0505	1.31	0.32	0.00240	0.00565
0.42(a)	448	2.26	0.573	0.0915	0.0723	1.26	0.32	0.00227	0.00513
0.59	634	3.92	0.380	0.0560	0.0373	1.50	0.42	0.00231	0.00906
0.59(a)	634	3.91	1.200	0.0985	0.0752	1.31	0.42	0.00207	0.00810
0.90	906	6.66	0.337	0.0514	0.0322	1.59	0.52	0.00218	0.0145
1.40	1340	9.74	0.335	0.0661	0.0302	2.19	0.60	0.00189	0.0184
1.41(b)	1328	9.74	0.330	0.0655	0.0300	2.18	0.62	0.00189	0.0184
1.81	1583	10.54	0.420	0.1010	0.0359	2.82	0.64	0.00163	0.0172
2.50(c)	1878	25.56	0.534	0.1484	0.0346	4.29	1.71	0.00110	0.0281
2.52	1872	11.42	0.580	0.1722	0.0394	4.37	0.78	0.00123	0.0141
2.55(a)	1860	11.13	0.642	0.1828	0.0437	4.18	0.78	0.00119	0.0133
3.39(a)	2080	12.74	1.415	0.5660	0.0905	6.25	1.13	0.00076	0.00975
3.45	2110	12.08	0.812	0.3304	0.0493	6.70	1.08	0.00085	0.0102
3.48(b)	2140	11.75	0.805	0.3240	0.0490	6.62	1.05	0.00085	0.00997

(a) Thickened boundary layer.
(b) Aft-facing step--data apply to station x_w = -0.5 in.
(c) High Reynolds number.

Legend:

Symbol	Mach no.	δ (in.)	U_e (fps)	R_δ
⊡	.42	.493	465	158 000
■	.42 Thickened	.573	448	183 000
△	.59	.380	627	160 000
▲	.59 Thickened	1.200	632	504 000
○	3.45	.812	2109	878 000
●	3.39 Thickened	1.415	2079	1 600 000
----	$u/U_e = (y/\delta)^{1/7}$			
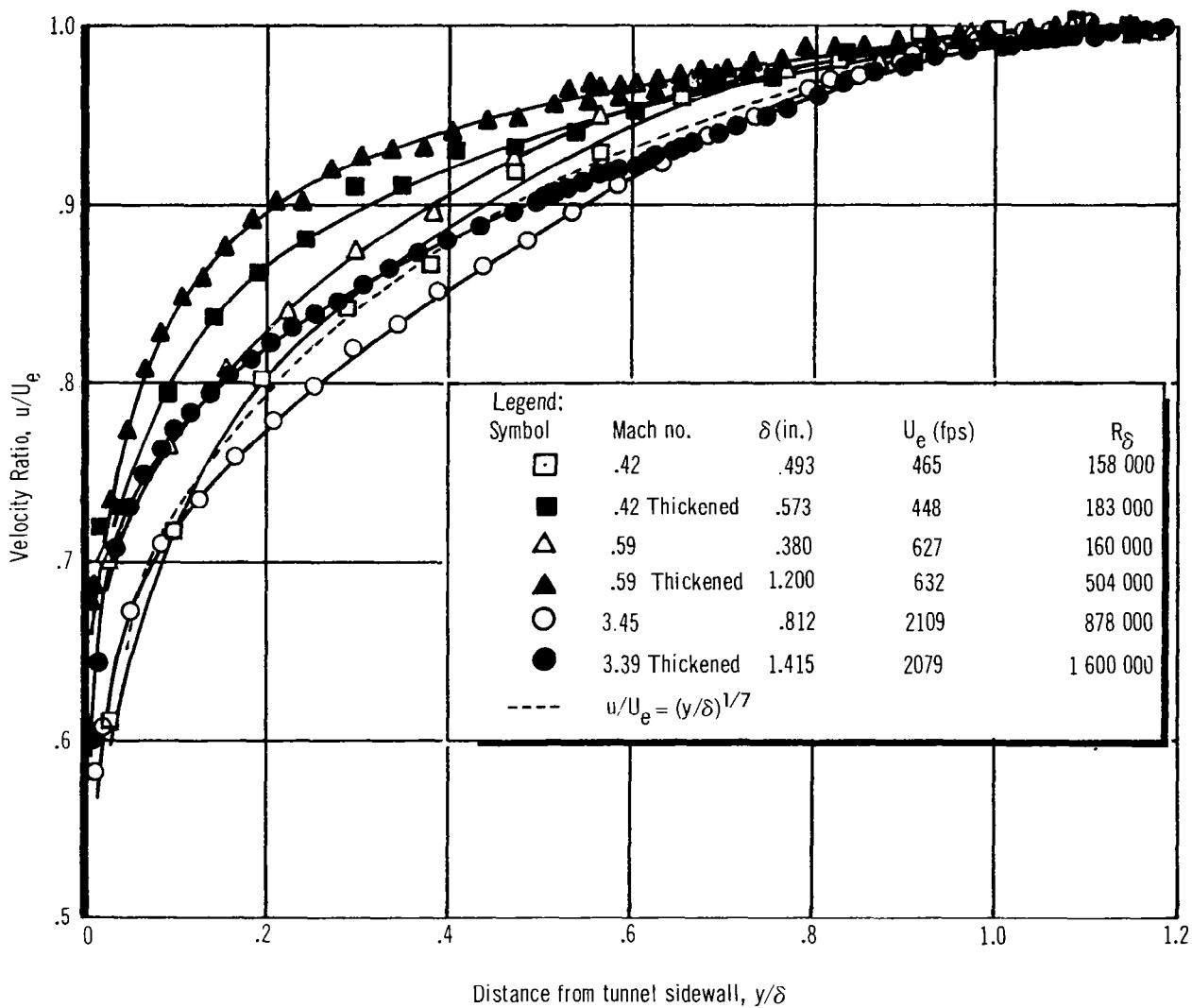
Figure 6. Nondimensionalized Velocity Profiles for Normal and Artificially Thickened Turbulent Boundary Layers (Profiles Measured at the Center of the Tunnel Sidewall Insert)

16

Velocity ratio, u/U_e

Symbol	Mach no.	δ^* (in.)	U_e (fps)	R_{δ^*}
□	.42	.0661	465	21 200
△	.59	.0560	627	23 500
○	.90	.0514	897	26 700
◇	1.40	.0661	1338	39 700
0	1.81	.1010	1588	64 600
▽	2.50	.1484	1878	264 000
▽	2.52	.1722	1871	142 000
○	3.45	.3304	2109	357 000

Distance from tunnel sidewall, y/δ^*
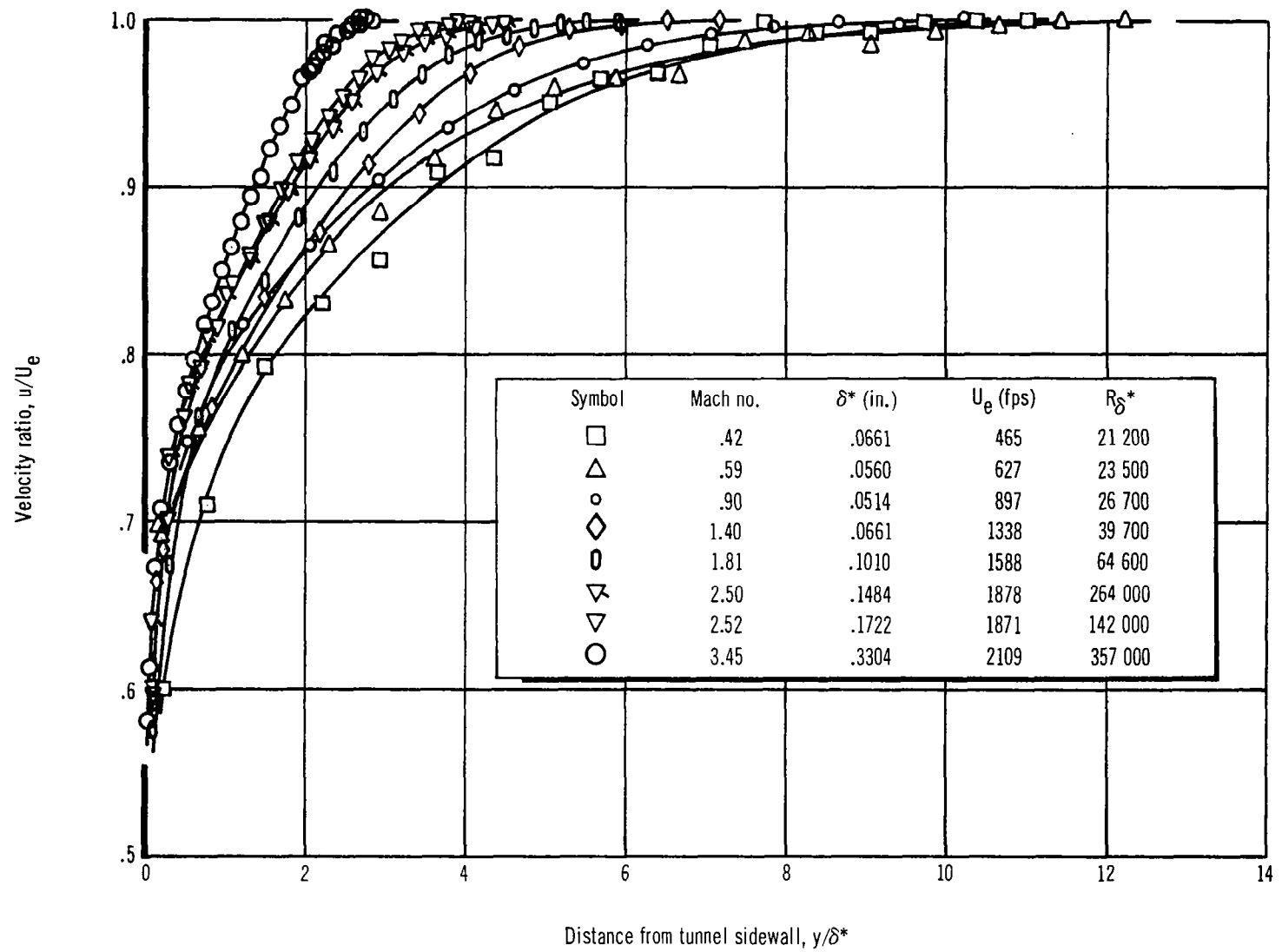
Figure 7. Nondimensionalized Boundary Layer Velocity Profiles at the Center of the Tunnel Sidewall Insert
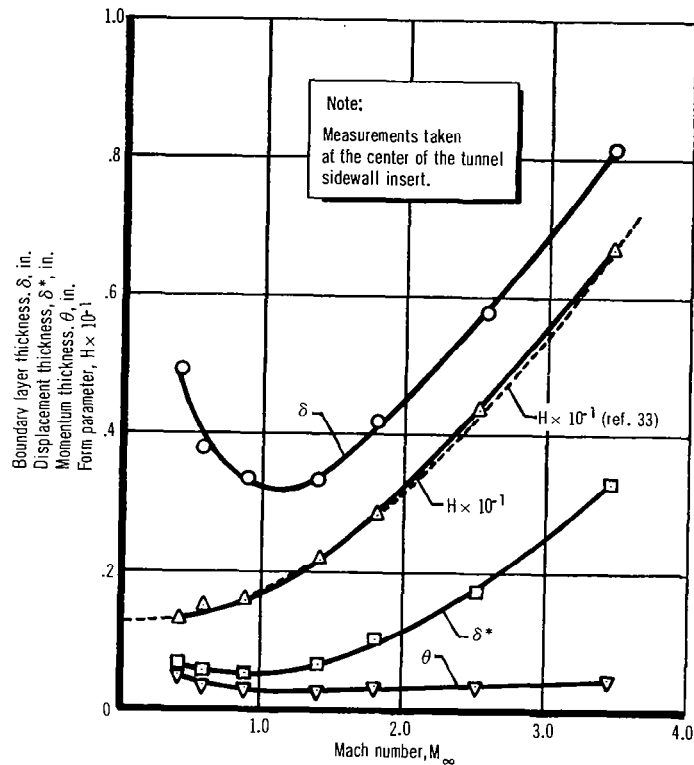
Figure 8. Boundary Layer Parameters as Functions of Mach Number

3.4 Static Pressure Distributions

Static-pressure measurements were made on, and ahead of, a 14.5-in. diam. insert in the sidewall of the test section. Static-pressure orifices in the insert were located 1/4-in. apart in two longitudinal rows adjacent to the sidewall centerline. The orifices in the two rows were staggered so that (assuming two-dimensional flow) the effective orifice spacing was 1/8 in. In addition, five orifices were spaced at 1/2-in. intervals between 1-1/4 and 3-1/4 in. upstream of the insert. The pressures were sensed using Statham 15-psi differential transducers in a Datex Pressure Scanner that was capable of sensing 160 pressures in 8 sec. The static pressure data were reduced to pressure ratio form, P/P_∞, where P_∞ is calculated from the calibrated Mach number and total pressure. Uniform flow static pressure distributions for each Mach number tested are shown in fig. 9 (A through G). An indication of the change in pressure ratio in terms of Mach number change is indicated on each plot. A comparison of the pressure distributions over aft-facing steps at M = 1.41 and 3.48 is shown in fig. 10.
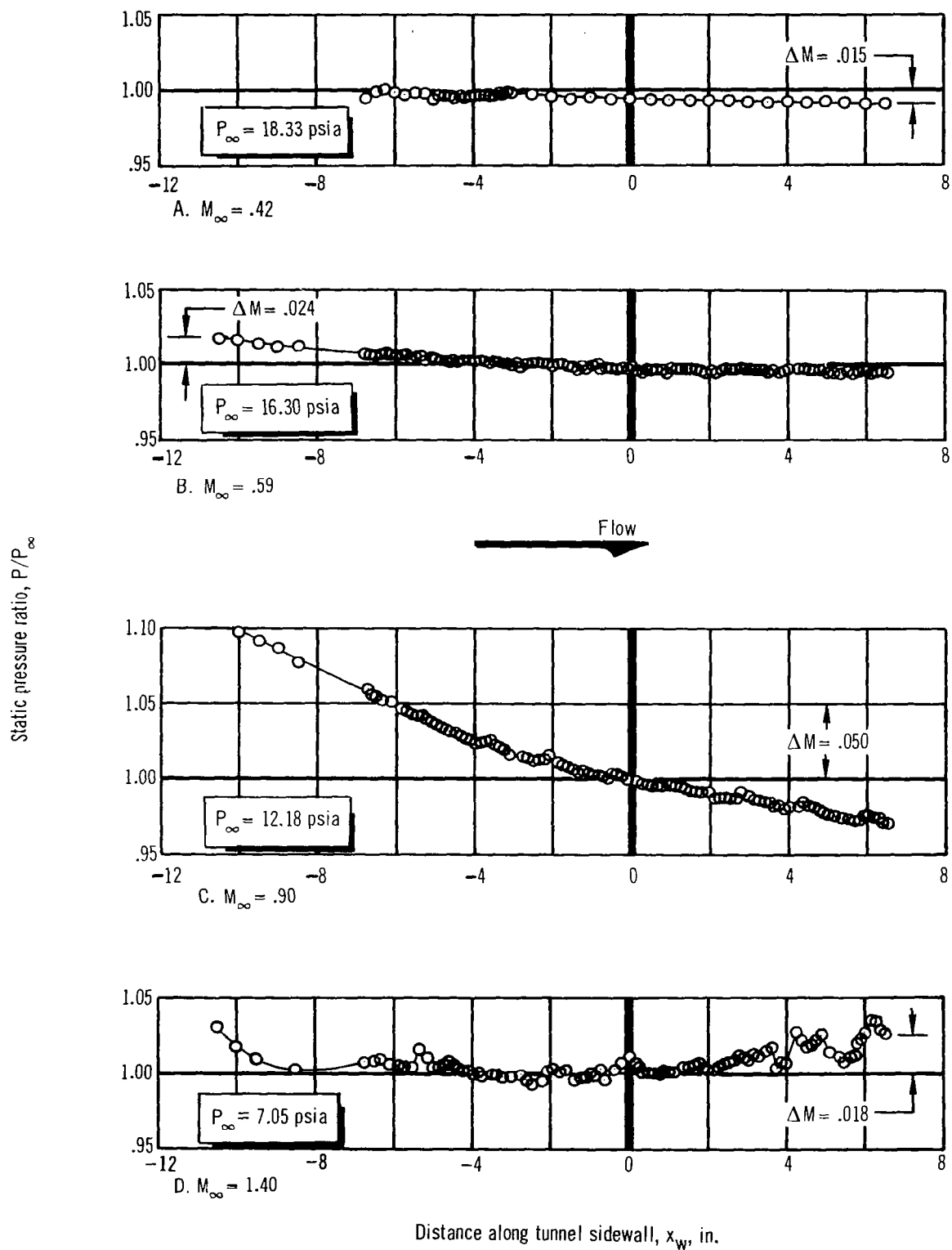
Figure 9. Static Pressure Distribution Along the Tunnel Sidewall in Unperturbed Flow
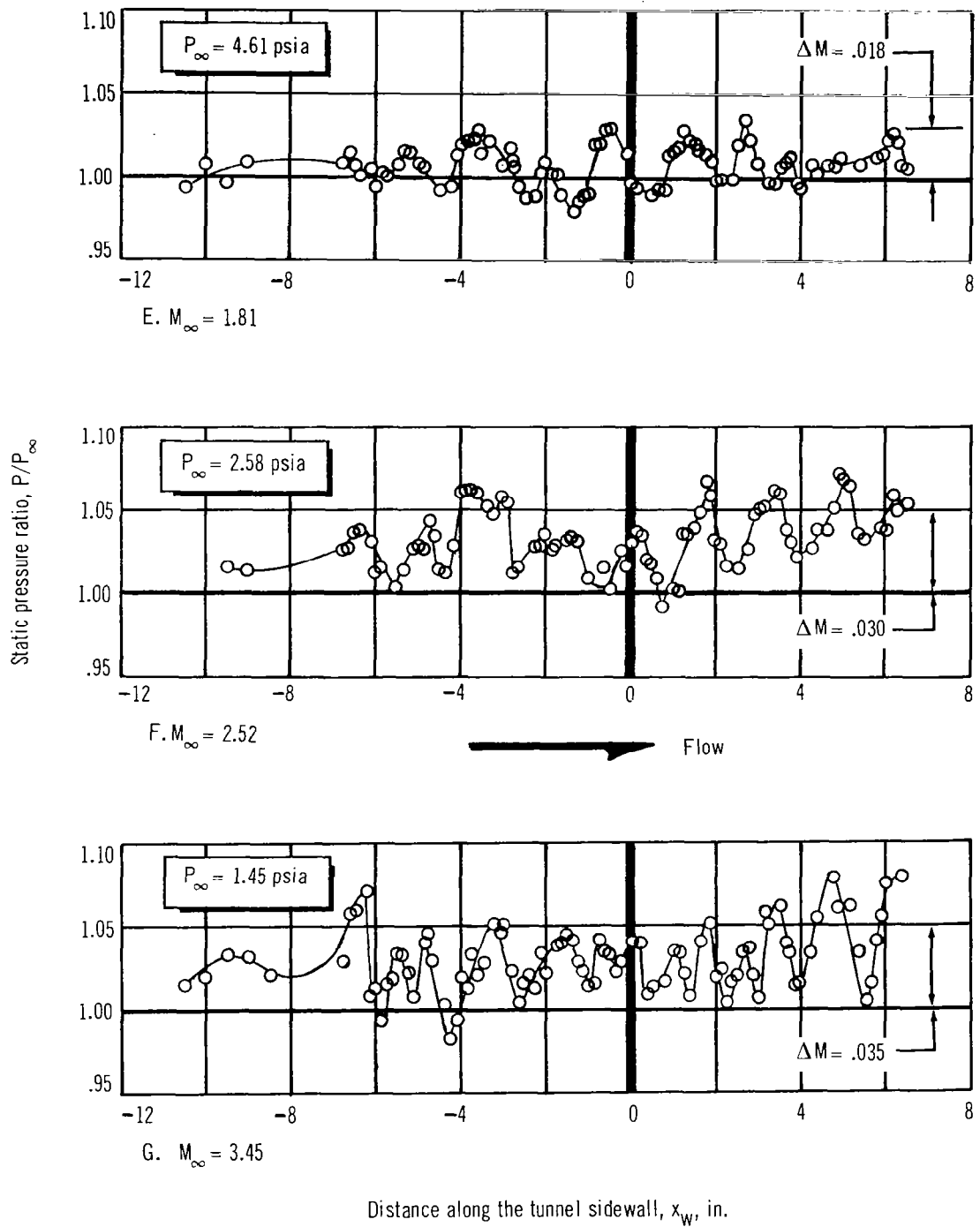
Figure 9. (Concluded).
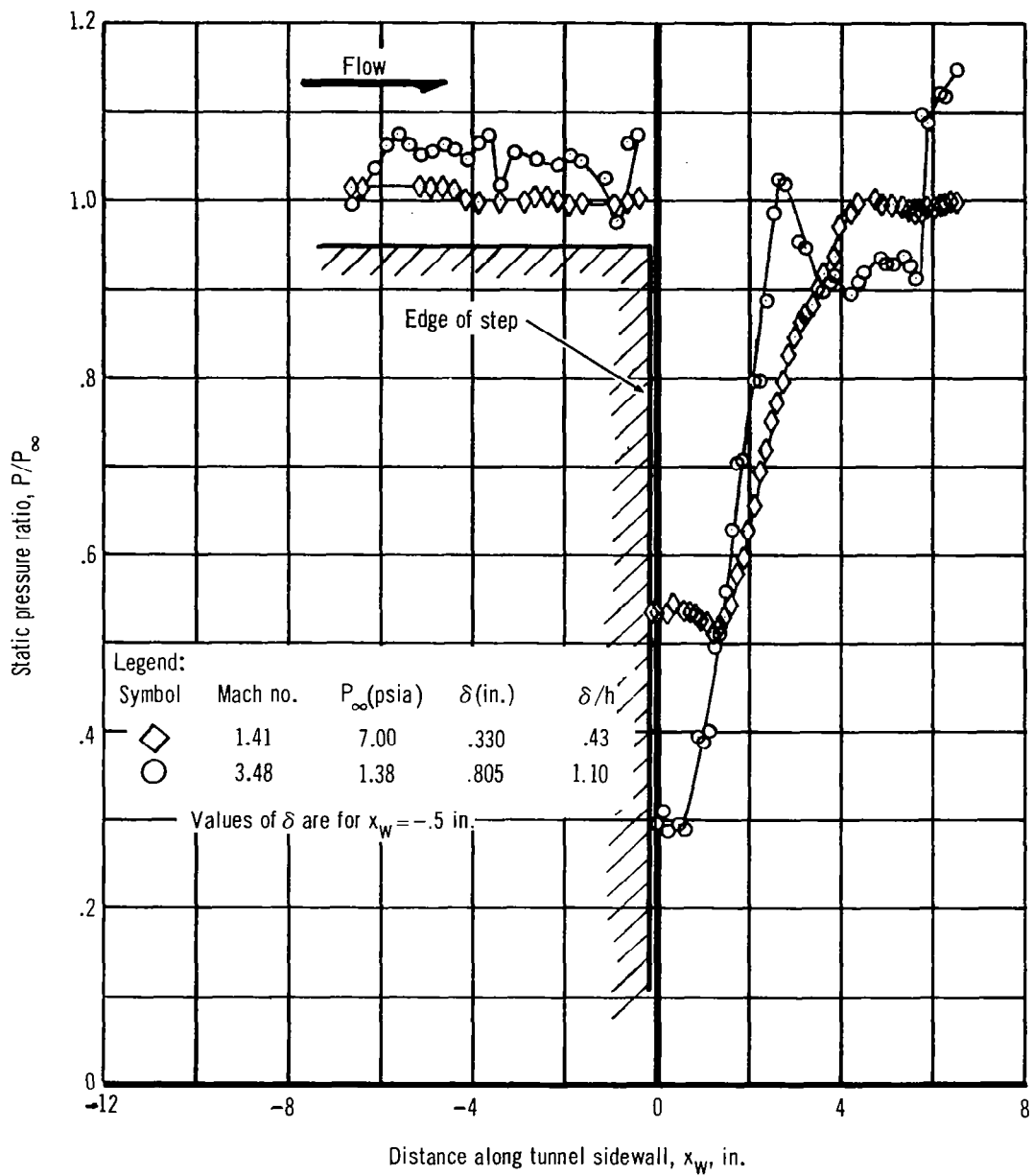
Figure 10. Static Pressure Distributions in the Vicinity of a 3/4-in. Aft-Facing Step at M_∞ = 1.41 and 3.48

3.5 Fluctuating Pressure Measurements

To obtain fluctuating pressure data in a frequency range of 1 to 150 000 cps, a versatile system was required. Such a system was assembled and is diagrammed in fig. 11. Transducers were mounted in the sidewall insert in any 11 of 36 possible locations (see fig. 12) for each run. Five were 0.25-in. Brüel and Kjaer (B&K) condenser microphones (Model 4136) with an effective sensing diameter of 0.133 in., and six were Atlantic Research Corp. LD 107-M1 piezoelectric transducers with a sensing element diameter of 0.060 in. Possible locations of the microphones and transducers are shown in fig. 12. The outputs of three of the B&K microphones were recorded on 1 to 20 000-cps FM channels. The output of one B&K microphone was recorded simultaneously on both 20 000-cps FM and 100 to 150 000-cps direct mode (AM). One B&K microphone, six ARC transducers, and one Model 2215 Endevco accelerometer (monitoring the vibratory response of the insert) were recorded on 100 to 150 000-cps AM channels. The 14th channel was used for voice cuing and timing information. Fig. 11 shows the various types of support electronics, as well as the type of sound-wave calibrator used at the beginning of each day of testing to calibrate and qualify the system. Special calibration procedures were used on various parts of the system and these are detailed in appendix B. Table II tabulates typical corrections to the power spectra applied to account for equipment characteristics such as system rolloff, transducer response, and transducer size effects (see appendix C).

3.6 Test Procedures

The supersonic test section was used exclusively for all measurements taken during the tests, because measurements with the porous-wall transonic test section would have been of questionable validity. Static pressure distributions, boundary-layer profiles, and fluctuating pressure measurements were obtained for uniform flow conditions at M = 0.42, 0.59, 0.90, 1.40, 1.81, 2.52, and 3.45. Boundary-layer profiles and fluctuating pressure measurements were obtained for an artificially thickened boundary layer at M = 0.42, 0.59, 2.55, and 3.39. Static and fluctuating pressure data were taken in the vicinity of an aft-facing step at M = 1.41 and 3.48[*] and also at M = 3.45 for a 7.5° incident shock wave, and four step-spoilers. At M = 2.50, boundary-layer profiles and fluctuating pressures were also obtained at a Reynolds number 2.2 times higher than normal.

For runs in which static pressures and/or boundary-layer profiles were measured, the tunnel was operated at constant stagnation pressure; i.e., with a choked control valve. The normal variation in stagnation pressure was less than ±0.4% during a run, and repeatability of a given stagnation pressure for a series of the runs was within 0.4%. The stagnation temperature drop during these runs ranged between 2° and 6° and the resulting Reynolds number increase varied from 0.2% to 0.8%.

---

[*]The choice of Mach numbers for the forward- and aft-facing steps was predicated on the advice of Mr. Charles Coe of NASA-Ames Research Center. Mr. Coe has been conducting extensive wind tunnel tests on three-dimensional axisymmetric models with various steps and ramps over a wide range of Mach numbers.
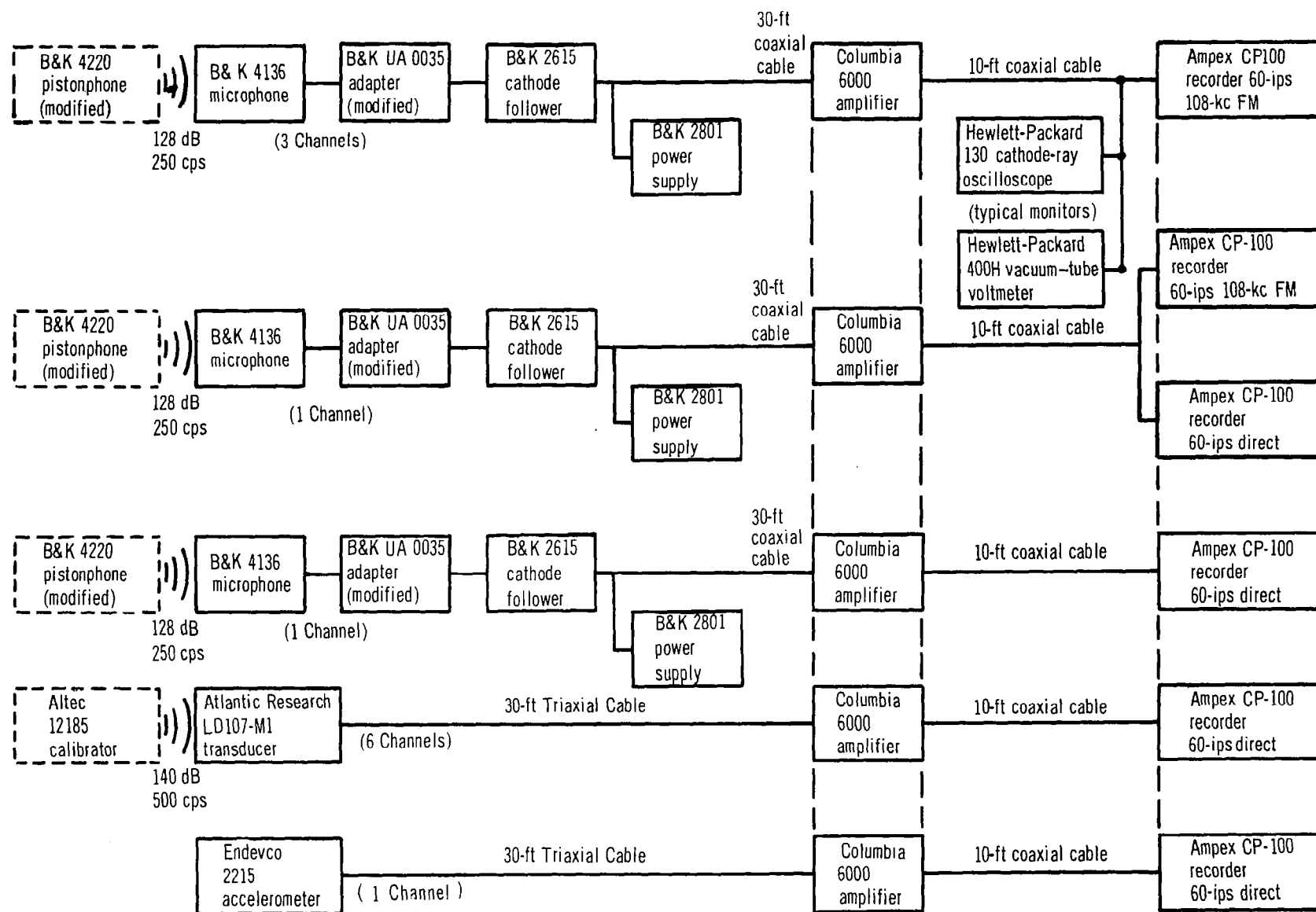
Figure 11. Schematic Diagram for the Acoustical Data-Acquisition System
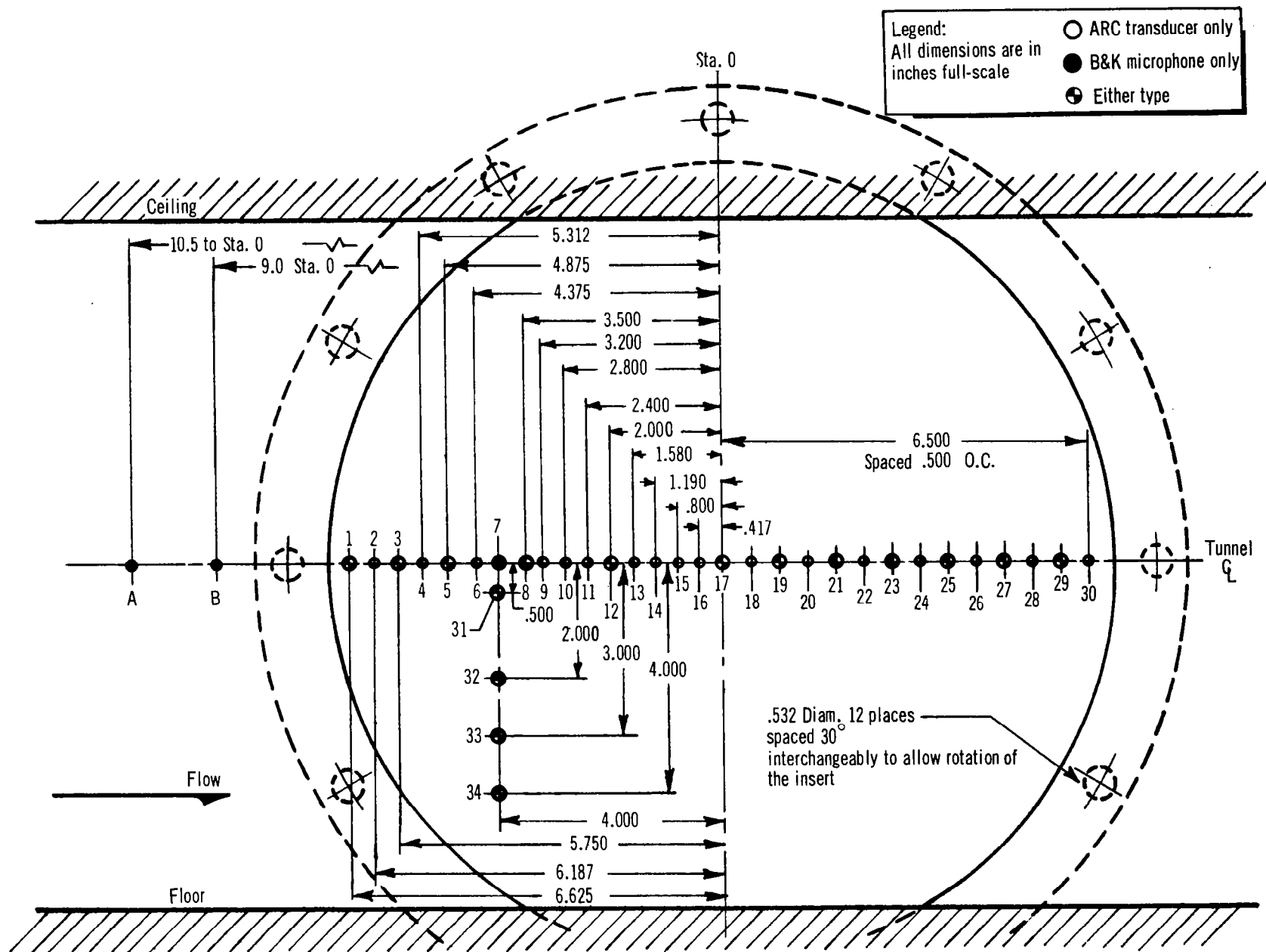
Figure 12. Acoustically Instrumented Sidewall Insert

TABLE II

TYPICAL CORRECTIONS TO THE POWER SPECTRA [a]

Run 60 (M_∞ = 3.45, Unperturbed Flow)

1/3-Octave band center frequency, cps	Transducer sensitivity correction, dB		Electrical system correction, dB		Static pressure correction, dB		Finite size correction, dB (appendix C)	
	Track 7	Track 13	Track 7	Track 13	Track 7	Track 13	Track 7	Track 13
315	0	0	+3.5	+2.5	0	0	0	0
400	0	0	+1.0	+1.0	0	0	0	0
500	0	0	0	0	0	0	0	0
630	0	0	-1.0	-1.0	0	0	0	0
800	0	0	-1.5	-2.0	0	0	0	0
1000	0	0	-2.0	-2.5	0	0	0	0
1250	0	0	-2.5	-2.5	0	0	0	0
1600	0	0	-2.5	-2.5	0	0	0	0
2000	0	0	-2.0	-2.5	0	0	0	0
2500	+0.5	+0.5	-1.5	-2.5	0	0	0	0
3150	+0.5	+1.0	-1.5	-2.5	0	0	+0.5	0
4000	0	+0.5	-1.5	-2.5	0	0	+0.5	0
5000	0	-1.0	-1.5	-2.5	0	0	+0.5	0
6300	0	-1.5	-1.5	-2.5	0	0	+0.5	0
8000	+0.5	-1.5	-2.0	-2.5	0	0	+0.5	+0.5
10 000	+0.5	-1.0	-2.0	-3.0	0	0	+0.5	+0.5
12 500	0	-0.5	-2.5	-3.0	0	0	+1.0	+0.5
16 000	+0.5	0	-3.0	-3.0	0	0	+1.0	+0.5
20 000	+1.0	0	-3.5	-3.5	0	0	+1.5	+0.5
25 000	+1.5	+0.5	-4.0	-3.5	-1.0	0	+2.0	+1.0
31 500	+1.5	+1.0	-4.0	-4.0	-5.0	0	+2.5	+1.0
40 000	+1.5	+1.0	-4.0	-4.0	-16.0	0	+3.0	+1.5
50 000	+1.5	+1.0	-4.0	-4.5	-35.0	0	+3.5	+1.5
63 000	+1.0	0	-3.5	-4.5	-2.0	0	+4.5	+2.0
80 000	+3.5	-2.5	-3.0	-4.5	+6.0	0	+5.5	+2.0
100 000	+10.5	-4.5	-2.5	-4.5	+12.0	0	+7.0	+2.5
125 000	—	-6.5	-2.0	-4.5	—	0	+8.0	+3.0

[a] Track 7 is a B&K microphone on direct record.
Track 13 is an ARC transducer on direct record.

The majority of the fluctuating pressure measurements were made by partially bypassing the main control valve such that the flow was not choked. The tunnel stagnation pressure therefore essentially equalled the reservoir pressure and dropped continuously during a run. Using a storage volume of 34 500 ft^3, the falloff in stagnation pressure and temperature was minimized. Table III indicates the variation of the average pressures, temperatures, and Reynolds numbers at each of the Mach numbers for which fluctuating pressures were measured. The average run duration was 10 sec.

TABLE III

VARIATION OF PARAMETERS FOR FLUCTUATING PRESSURE RUNS

Mach no.	Average stagnation pressure (psia)	Pressure variation during run (%)	Average temperature and variation during run (^{O}R--%)	Average unit Reynolds no.	Reynolds no. variation during run (%)
0.42	21	±8.5	525 ± 0.4	0.32	±6
0.59	21	±9.5	525 ± 0.5	0.42	±9
0.90	21	±11	525 ± 0.6	0.52	±19
1.40	22.5	±10	525 ± 0.8	0.61	±9
1.81	25.5	±9	525 ± 0.8	0.64	±6
2.50	98	±5	525 ± 0.9	1.74	±3.5
2.52	46	±4	525 ± 0.8	0.78	±3
3.45	104	±2	525 ± 1.0	1.11	±0.5

The fluctuating pressure levels were essentially constant during the duration of the run at M = 2.5 and 3.5, but dropped as much as 3 to 5 dB at the other Mach numbers. Levels indicated in this report correspond to the average Reynolds numbers listed above. It may be seen by comparing table III to table I that the average Reynolds numbers for the fluctuating pressure tests are nearly the same as for the boundary-layer profile and static pressure tests. For this reason, deviations in data caused by Reynolds number variation are assumed to be of second-order effect.

3.7 Fluctuating Pressure Data Reduction

Reduction of the test data tapes was divided into three main parts:

(1) Data evaluation, and acquisition of approximate composite values for the root mean squared (rms) pressure corresponding to the rms voltage recorded on the magnetic tape

(2) Power spectra of the fluctuating pressures for an extended frequency range (to approximately 112 000 cps)

(3) Calculation of space-time cross-correlations and cross-power spectra

The instrumentation, computer programs, and mathematics necessarily utilized in each of the above are detailed in the following subsections.

3.7.1 Data Evaluation. -- To evaluate data quality, time histories of the rms composite signal for every data track for each run were obtained. The equipment utilized was typically a Sanborn averaging meter (not a true rms device) and an associated graphic recorder. The upper usable limit of this equipment is approximately 30 000 cps above which serious roll-off is introduced. Since the data were uncorrected for all the usual system errors, it was felt that the limitations of the Sanborn equipment were tolerable for the purpose: namely, to prove stationarity, repeatability, and to a limited degree, data acceptability. From this cursory survey of the data, several factors (e.g. dropouts, data instability at some time during a run, an erratic data track, etc.) become apparent, which aided in the choice of data to be analyzed thoroughly by the techniques described below.

3.7.2 Power Spectra.--It was the intent of part of the study to extend the frequency range of the measurements and examine the distribution of energy in space and frequency domains. To permit this, electronics were utilized that allowed data acquisition to 150 000 cps when properly corrected for system influences (see section 3.5). The digital data reduction of such a frequency range presented a distinct challenge. First, the memory core of the computer had to be utilized efficiently in accumulating enough information to carry a power spectral density to a high frequency. Next, the analog-to-digital converter had to be modified such that all the normally shared six digitizing channels were combined into a single channel. The additional requirement of at least two-and-one-half samples per cycle to adequately define a frequency set the upper limit at 14 000 cps for the sampling rate

available (35 000 bits per second). Tape speed reduction to one-eighth the recorded speed (as large a reduction as practical with the Mincom tape recorders before signal degradation occurred) would then permit frequencies up to 112 000 cps to be examined. A sharp filter cutoff above 14 000 cps reduced fold-back to a minimum.

A further limitation was inherent in the existing system because of the finite sampling time required by the converter. To sample a bit, 28 μ sec would normally be required. However, in this time interval, a 112 000-cps frequency would progress through four-tenths of a cycle (the digitizer recognizes 112 000 cps as 14 000 cps at the reduced speeds). To reduce the potential error from this effect, a sample and hold amplifier was inserted between the playback electronics and the digitizer. The result was a system capable of performing data reduction on frequencies up to 112 000 cps with a minimum amount of error (the amount of cyclic change during the digitizing process was reduced from 40% of a complete cycle to 5%). Fig. 13 is a block diagram of the system just described.

With the digitizing process completed, a computer program calculated the auto-correlation of the data and its Fourier transform (the mathematics for which are given in section 3.7.3). The program was modified somewhat for this extended frequency study. Instead of a fixed, incremental band of frequencies, the bandwidth increased with increasing frequency, reducing the total computer time markedly. The power spectra were averaged over each band, divided by the bandwidth, and plotted at the geometrical center of the frequency band. A total of 44 bands were calculated for the frequency range of 46 to 140 000 cps. The presence of some 60-cycle noise in the AM reproduce system necessitated the exclusion of data below 300 cps in further discussions.

3.7.3 <u>Broad-Band Space-Time Correlations</u>.--To obtain data suitable for cross-correlating, six channels of information on the magnetic tapes were transformed to the FM mode (to avoid the introduction of 60-cycle noise) and were digitized simultaneously. Figs. 14 and 15 indicate the block diagrams of such a system. This system permitted cross-correlation between channels connected to the same stack of record gaps (to avoid discrepancies in time) for the same interval of time 2T. The technique of cross-correlating data is simply an averaging process over the interval of time 2T. After digitizing, a computer program operates on the data to calculate correlation functions. Such a process is described mathematically in series form (the form used by the computer) as,

$$\psi(\xi, \tau) = \lim_{N \to \infty} \frac{1}{N} \sum_{n=1}^{N} p_1(\vec{x}, t_n) p_2(\vec{x} + \vec{\xi}, t_n + \tau) \tag{3}$$

where $\vec{x}$ and $\vec{\xi}$ are two-dimensional vectors in the plane of the rigid wall. The assumptions of homogeneity, ergodicity, and stationarity permit an arbitrary
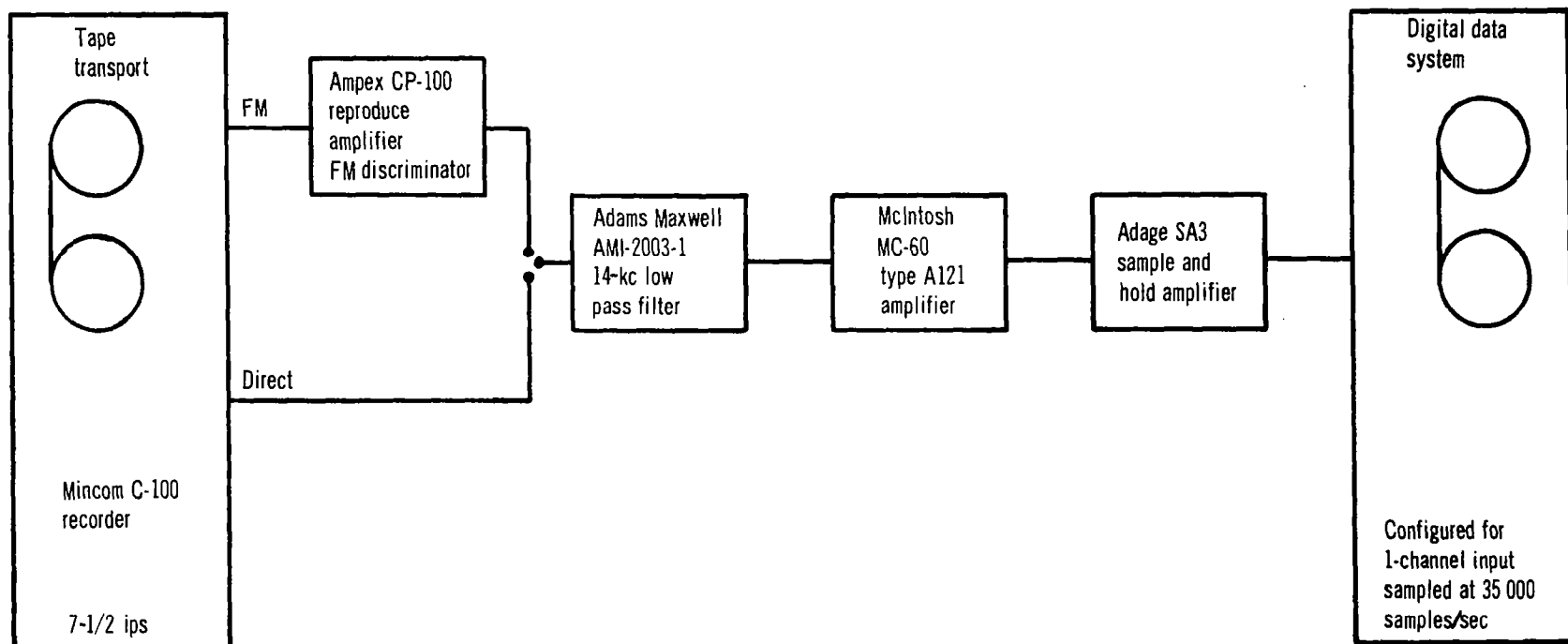
Figure 13. High-Frequency Data-Processing System
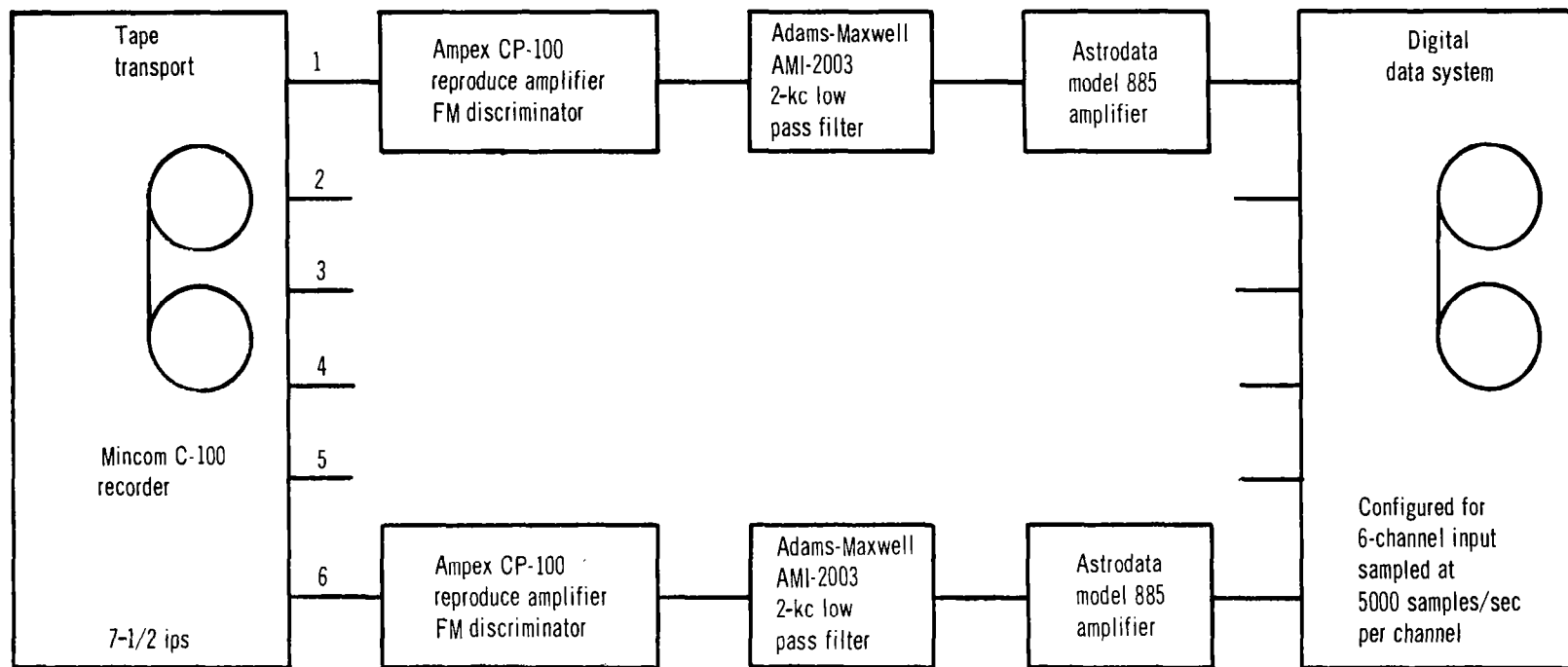
Figure 14. FM Data-Processing System
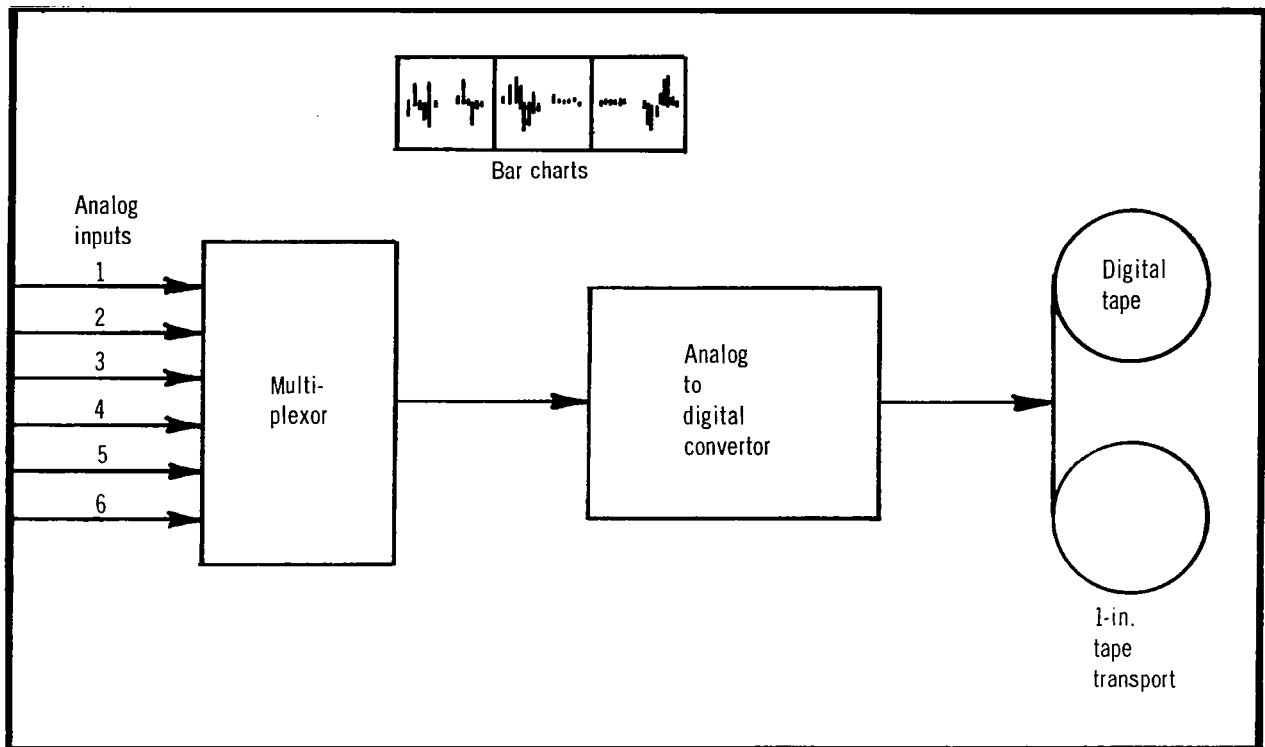
Figure 15. Digital Data System

choice of time interval and examination of a single pair of channel to describe the cross-correlation between two spatial points in time. The resultant correlation function only depends on spatial separations, ξ , and the time difference, τ . Normalization of the results was performed in all cases; for auto-correlations, the mean squared pressure, $R(0,0)$, was the normalizing factor, while for cross-correlations, the square root of the product of the mean squared pressures $[R_1(0,0)R_2(0,0)]^{1/2}$ was used. The frequency range of the data used was 160 to 16 000 cps. A sharp filter was employed to avoid fold-back of higher frequencies. A smooth distribution function for amplitudes was required; grossly irregular data samples were not included. An additional requirement on the data utilized in calculations of cross-correlations was that the composite rms signal levels be comparable. Thus, if one channel in a sequence was lower or higher than the others, it was automatically disqualified from further use in correlation calculations because the reasons for such discrepancies had not been established.

The cross-power spectral density was found by taking the Fourier transform of the cross-correlation function. The equations relating the cross-correlation, R_{12}, the cross-power spectra, ϕ_{12}, and their inverses are as follows:

$$\phi_{12}(\vec{\xi}, \omega) = \frac{1}{2\pi} \int_{-\infty}^{\infty} d\tau \, R_{12}(\vec{\xi}, \tau) \, e^{-i\omega\tau} \tag{4}$$

$$R_{12}(\vec{\xi}, \tau) = \int_{-\infty}^{\infty} d\omega \, \phi_{12}(\xi, \omega) \, e^{i\omega\tau}. \tag{5}$$

The relative phase versus frequency was measured between each pair of channels used for cross-correlation measurements. This phase measurement included the electronics from data acquisition through data reduction. The phase was permitted to vary a finite amount before disqualification of the data (the computer program did not lend itself to correction for a phase difference between channels that varied with frequency). See appendix B for the accepted limits.

Section 4

RESULTS

Most of the results of this experimental investigation concerned measurements in a supersonic boundary layer. However, to present a continuous picture of the fluctuating forces that a vehicle might encounter in flight, measurements were also taken at subsonic Mach numbers. Fluctuating pressure levels (FPL's) are presented for unperturbed flow at M = 0.42, 0.59, and 0.90; space-time correlations are included for M = 0.59.

For supersonic speeds, pressure fluctuation levels are given for the unperturbed boundary layer at M = 1.40, 1.81, 2.52, and 3.45 and space-time correlations at M = 3.45. FPL's and space-time correlations are given for an aft-facing step at both M = 1.41 and 3.48. FPL's are presented for a 1/4-in. step-spoiler at M = 3.45, a 3/8-in. step-spoiler at M = 1.40 and 3.45, and a 1-1/2-in. step-spoiler at M = 3.45. Both FPL's and space-time correlations are given for a 3/4-in. step-spoiler and a 7.5° shock wave at M = 3.45.

4.1 Boundary Layer Characteristics

It is generally desirable to non-dimensionalize the fluctuating pressure data with respect to some characteristic parameter in the boundary layer. Since these parameters vary along the tunnel sidewall, these variations must be defined with distance. It is, of course, impractical to make measurements at every station where fluctuating pressure data are recorded. An alternative means is to record data at one or two stations and to calculate the variation between and beyond. The procedures used to calculate the boundary-layer characteristics are described in appendix A, which includes illustrations of the variations with distance of δ, δ^*, θ, and c_f.

When the boundary layer is perturbed by steps or shock waves, the data are referred to the pertinent parameters for the unperturbed flow.

4.2 Subsonic Unperturbed Flow

In the original investigation (ref. 1), the spectra of the unperturbed boundary-layer pressure fluctuations were basically flat throughout the measured frequency range (32 to 88 000 cps). The intent of the present investigation was to define the roll-off point of the spectrum by using piezoelectric transducers to check the validity of the data at high frequencies

from the condenser microphones used previously, and to extend the measurements to even higher frequencies. Also planned was a second method that would increase the nondimensional frequency range ($\omega\delta^*/U_\infty$) by artificially thickening the boundary layer, thus increasing δ^*. The artificial-thickening device was more productive at M = 0.59, yielding a 76% increase in δ^*, than at M = 0.42, which only yielded a 38% increase.

Spectra for the three subsonic Mach numbers, 0.42, 0.59, and 0.90 plus spectra for the thickened boundary layers at M = 0.42 and 0.59 were obtained. The power spectral density in (psi)^2/rad/sec was normalized with respect to dynamic pressure squared, displacement thickness, and free-stream velocity and was plotted as a function of reduced frequency or Strouhal number, $\omega\delta^*/U_\infty$, as is normally done in the literature. A variation with distance can be detected, although it will be more readily apparent in the overall rms FPL's when normalized with respect to dynamic pressure, or wall shearing stress, and plotted as a function of distance along the tunnel sidewall. **

At M = 0.42, there are no significant differences in the spectra of the unthickened and thickened boundary layers except at the furthest upstream station, x_w = -10.5 in. (fig. 16 and 17). In the unthickened boundary layer, the spectrum level at x_w = -10.5 in. is of the same order as at the downstream stations resulting in an overall value that is higher than would be expected (fig. 18). For the thickened boundary layer, the fluctuating pressure spectrum at x_w = -10.5 in. falls off at much lower Strouhal numbers than for the rest of the data. It is apparent that the boundary layer in the thickened case has not fully developed at x_w = -10.5 in., but within a few inches downstream, the spectral shapes appear similar to that data for the unthickened boundary layer.

At M = 0.59, the spectral levels are slightly higher for the unthickened case than for the thickened cases (see figs. 19 and 20). However, the curves roll off somewhat sooner. The net result is that the overall levels (fig. 21) are basically the same for the two cases. It may be seen that the overall levels between x_w = 0 and +4 in. exhibit more scatter than the rest of the data. Changes up to ±2 dB are required to bring the rms levels into line in this region. Although 2 dB is an appreciable error, the introduction of such an error is possible as discussed in section 3.6 since these data were taken during different runs from the upstream data and may have been digitized at different times.

**It should be noted that the fluctuating pressure spectra and overall levels presented in this report have been corrected for finite size effects (appendix C).
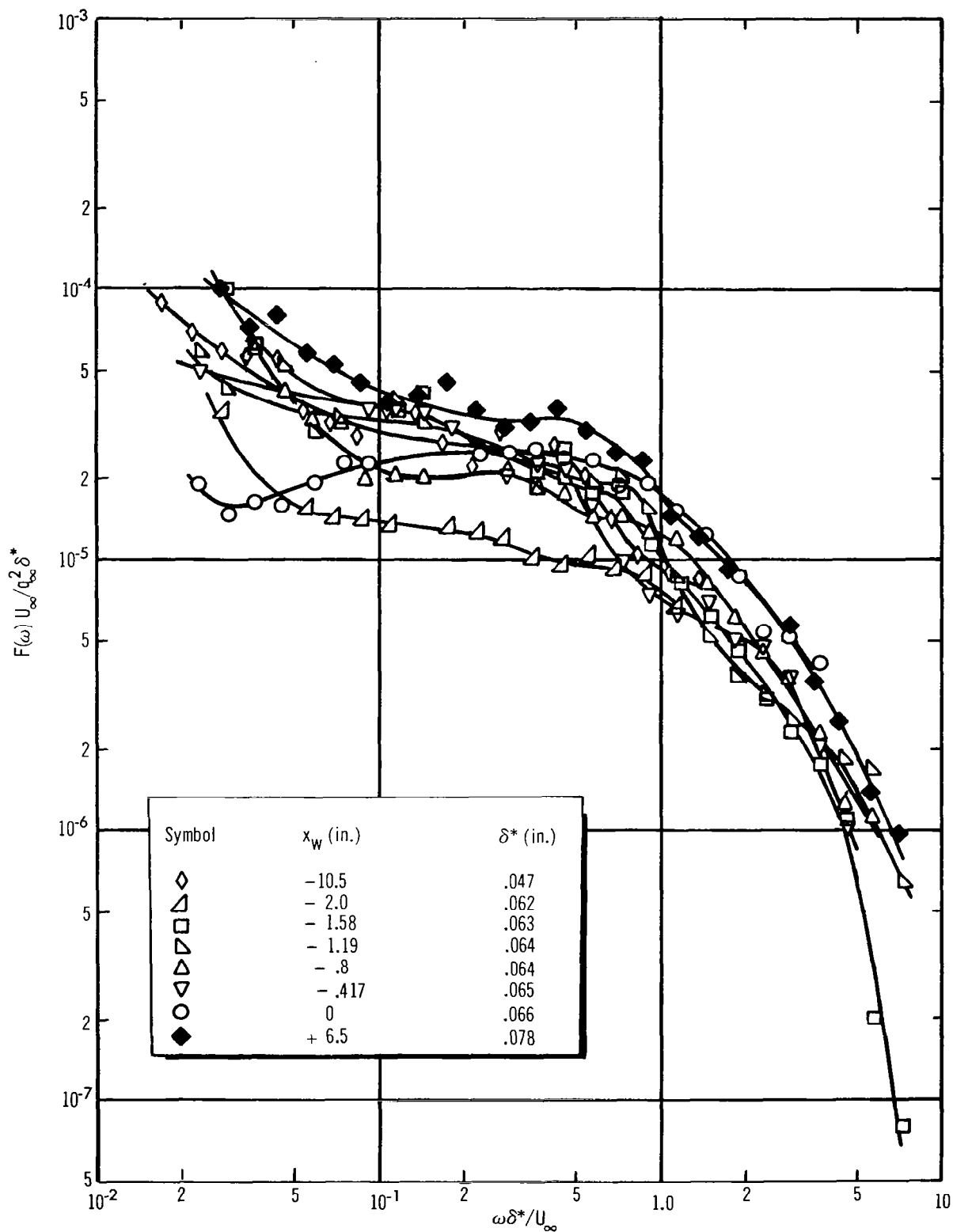
Figure 16. Nondimensional Power Spectra of the Wall Pressure Fluctuations, $M_\infty = .42$ (Unthickened Boundary Layer)

Symbol	x_w (in.)	δ^* (in.)
◇	−10.5	.047
◁	− 2.0	.062
□	− 1.58	.063
▷	− 1.19	.064
△	− .8	.064
▽	− .417	.065
○	0	.066
◆	+ 6.5	.078

Figure 17. Nondimensional Power Spectra of the Wall Pressure Fluctuations, $M_\infty = .42$
(Thickened Boundary Layer)

The plot shows $F(\omega) U_\infty / q_\infty^2 \delta^*$ on the vertical axis versus $\omega\delta^*/U_\infty$ on the horizontal axis.

Symbol	x_w (in.)	δ^* (in.)
◇	−10.5	.074
○	−4.875	.084
◁	−2.0	.088
□	−1.58	.089
△	− .8	.090
▽	−.417	.091
○	0	.092
◆	+6.5	.102

36

Flow

at $x_w = 0$ $R_\theta = 16\ 150$; $R_x = 10.9 \times 10^6$ (unthickened)
$R_\theta = 23\ 100$; $R_x = 17.0 \times 10^6$ (thickened)

○ Unthickened boundary layer
△ Thickened boundary layer
Filled symbols — condenser microphone (FM)
Tagged symbols — condenser microphone (AM)

Distance along tunnel sidewall, x_w, in.

Figure 18. Variation of the rms Pressure Fluctuations Along the Tunnel Sidewall, $M_\infty = .42$

Figure 19. Nondimensional Power Spectra of the Wall Pressure Fluctuations, $M_\infty = .59$ (Unthickened Boundary Layer)
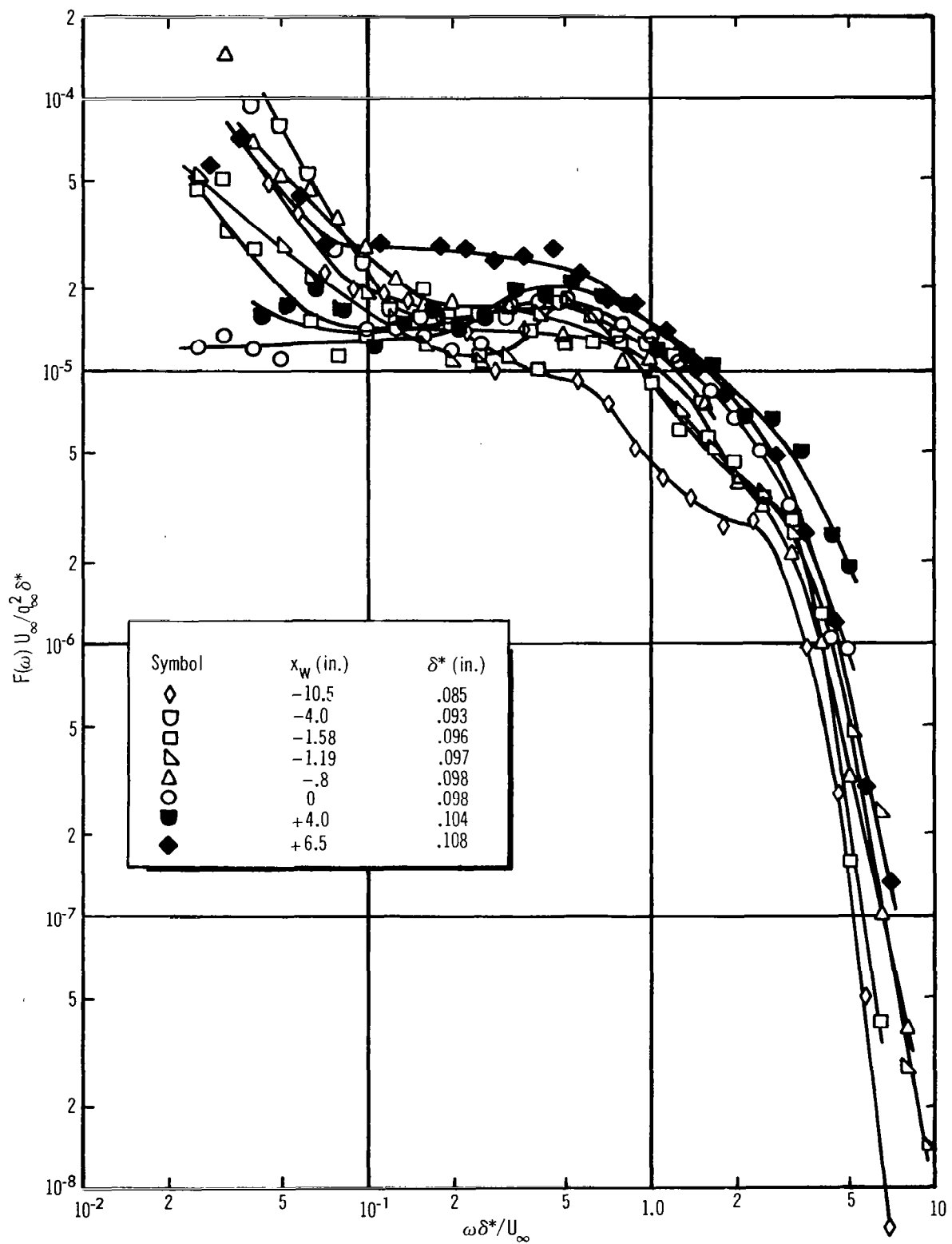
Figure 20. Nondimensional Power Spectra of the Wall Pressure Fluctuations, $M_\infty = .59$ (Thickened Boundary Layer)
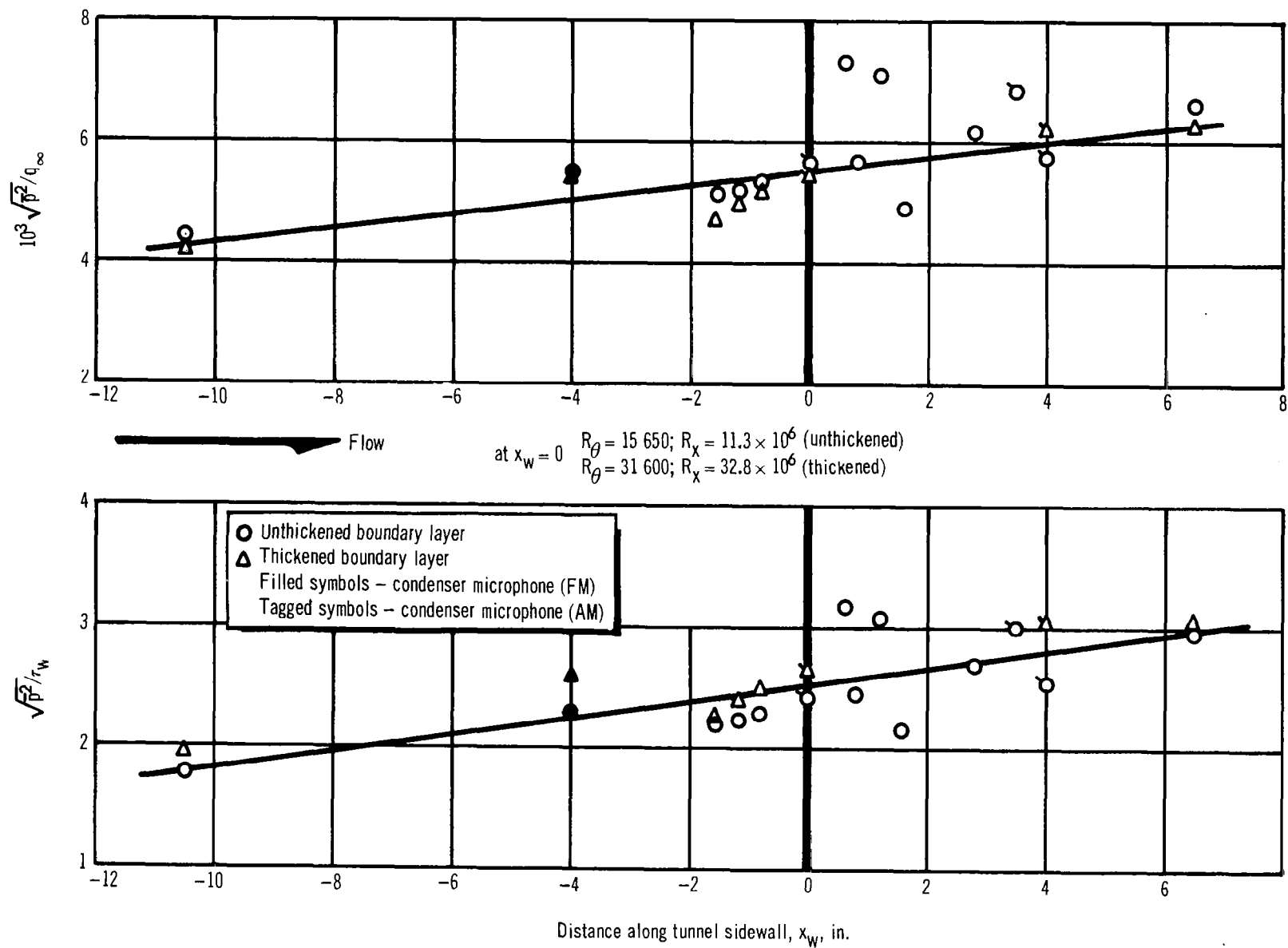
Figure 21. Variation of the rms Pressure Fluctuations Along the Tunnel Sidewall, $M_\infty = .59$

At M = 0.90, (figs. 22 and 23), the spectrum at station x_w = -10.5 in. shows the same trends as for M = 0.42. In addition, the data show the same phenomenon reported previously (ref. 1) in that spectra at some stations are relatively flat and others exhibit markedly elevated levels in the low frequencies. The overall level at x_w = +6.5 in. (fig. 23) is noticeably higher than at other stations and this may be caused by the proximity of the transducer to the normal shock in the diffuser. In fact, a sharp peak in the spectrum was noted between 13 000 and 15 000 cps (Strouhal number = 0.45) at all stations downstream of x_w = -1.2 in. The peak was ignored in the calculation of overall levels since it was considered to be a phenomenon peculiar to this specific wind tunnel. An interesting exercise would be to perform a narrow band cross-correlation of the data in a frequency range that included this peak to determine if evidence of a disturbance propagating upstream exists. Broad-band cross-correlations, similar to those performed on the M 0.59 data discussed below, are not sufficiently detailed for identification of such a propagating signal.

Since this study emphasized supersonic flow, measurement locations were not suitably placed for complete definition of the pressures associated with subsonic flow. In addition, signal-to-noise ratios were lower, restricting accuracy in the normalized cross-correlation function to ±0.05. Hence, the correlation calculations presented for this type of flow are only approximate. They do indicate trends, however, that are comparable to results noted in more detailed studies by other investigators (e.g., ref. 4 and 5). These calculations represent space-time correlations of pressures measured at a rigid wall resulting from an unperturbed subsonic boundary layer. Fig. 24 is a plot of the data points defining the correlation coefficient (τ = 0) in the x-direction (the direction of the flow). The abscissa is non-dimensionalized to the displacement thickness δ^*, as is customarily done in the literature. For comparison, the measured values for the same function from ref. 4 at similar Mach numbers are also presented in fig. 24. It should be noted that additional data points to those actually calculated for τ = 0 are obtainable from values of $\tau \neq 0$ when the time-decay function is utilized. Thus, some of the data points represent ($\xi_x - U_c \tau$) values multiplied by a suitable time decay function—taken to be the exponential decay function found by Bull in ref. 4—exp. ($-0.04\ U_\infty \tau / \delta^*$). For details of this technique, see section 2.2.

Fig. 25 shows the correlation coefficient in the plane of the measurements for M = 0.59. The turbulent boundary layer was undisturbed and slowly growing (δ^* varied 3% in the region of the measurement). The equal correlation contour lines shown in fig. 25 are only approximate, since instrumentation could not be placed close enough to the reference point to properly define the high values of normalized correlation (0.5 to 1.0). Also, the lateral (z-direction) correlation coefficient was poorly defined. Hence, fig. 25 presents data trends found at this subsonic Mach number. For comparison, results of two other experimenters are shown in figs. 26 and 27 (ref. 4 and 5).

Figure 22. Nondimensional Power Spectra of the Wall Pressure Fluctuations, $M_\infty = .90$

42

at $x_w = 0$ $R_\theta = 16\ 750$; $R_x = 12 \times 10^6$

Filled symbols — condenser microphone (FM)
Tagged symbols — condenser microphone (AM)

Distance along tunnel sidewall, x_w, in.
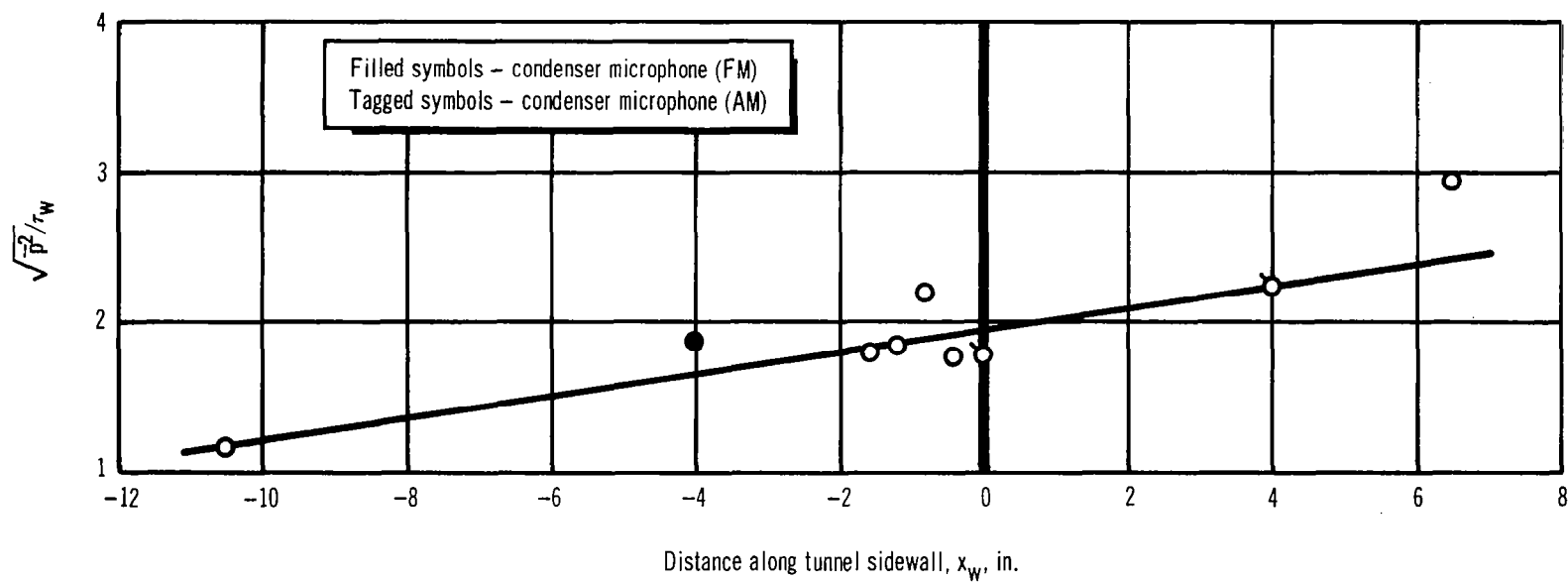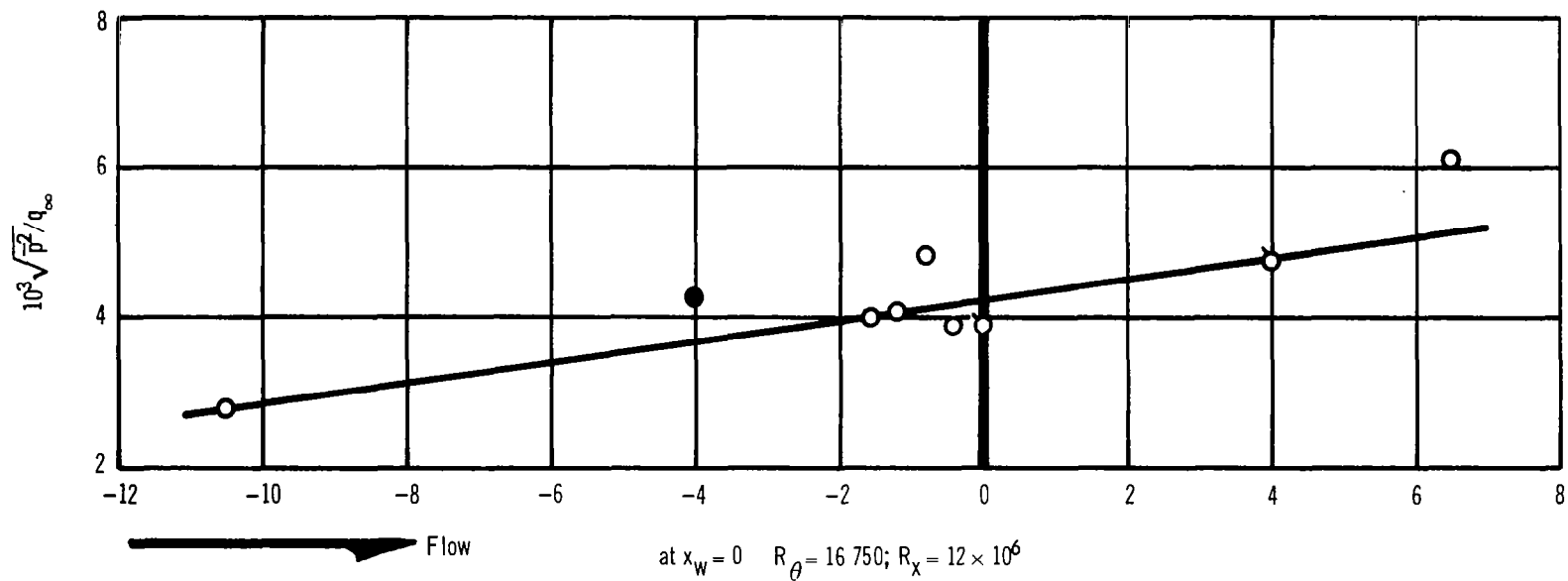
Figure 23. Variation of the rms Pressure Fluctuations Along the Tunnel Sidewall, $M_\infty = .90$
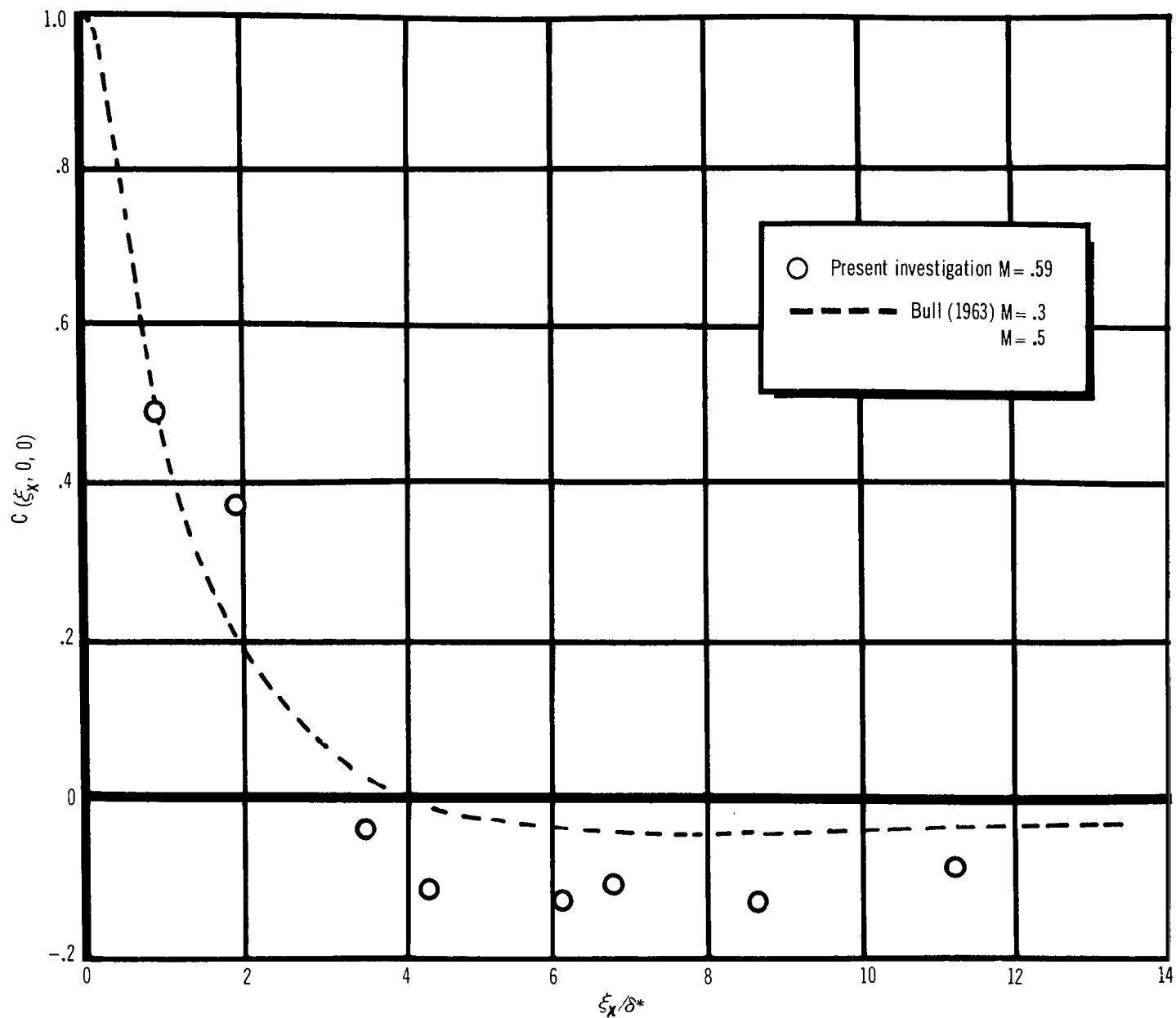
Figure 24. Comparison of Longitudinal Correlation Coefficients for Subsonic Unperturbed Flow
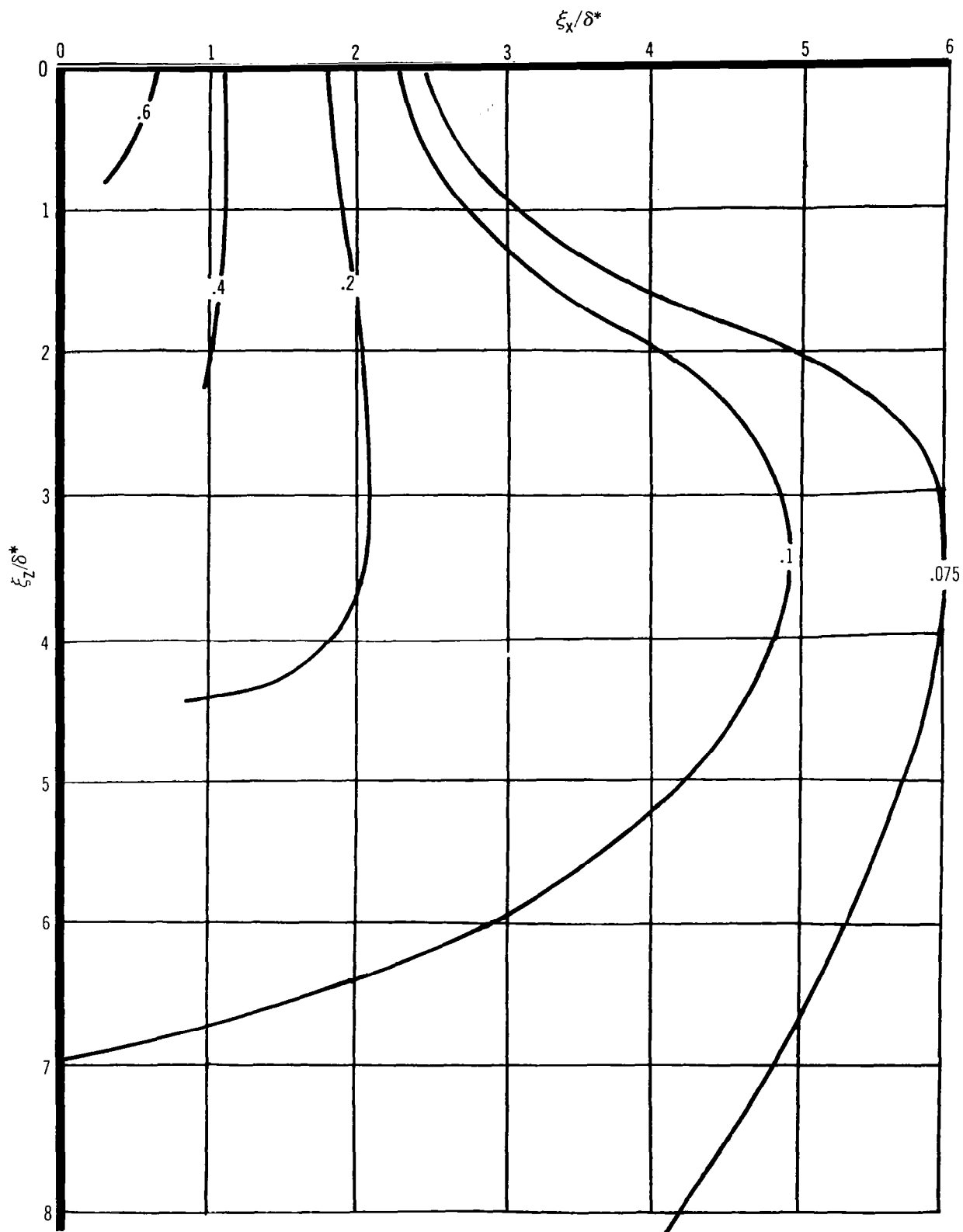
Figure 25. Approximate Contours of Equal Correlation Coefficient in Unperturbed Flow, Present Investigation, M = .59
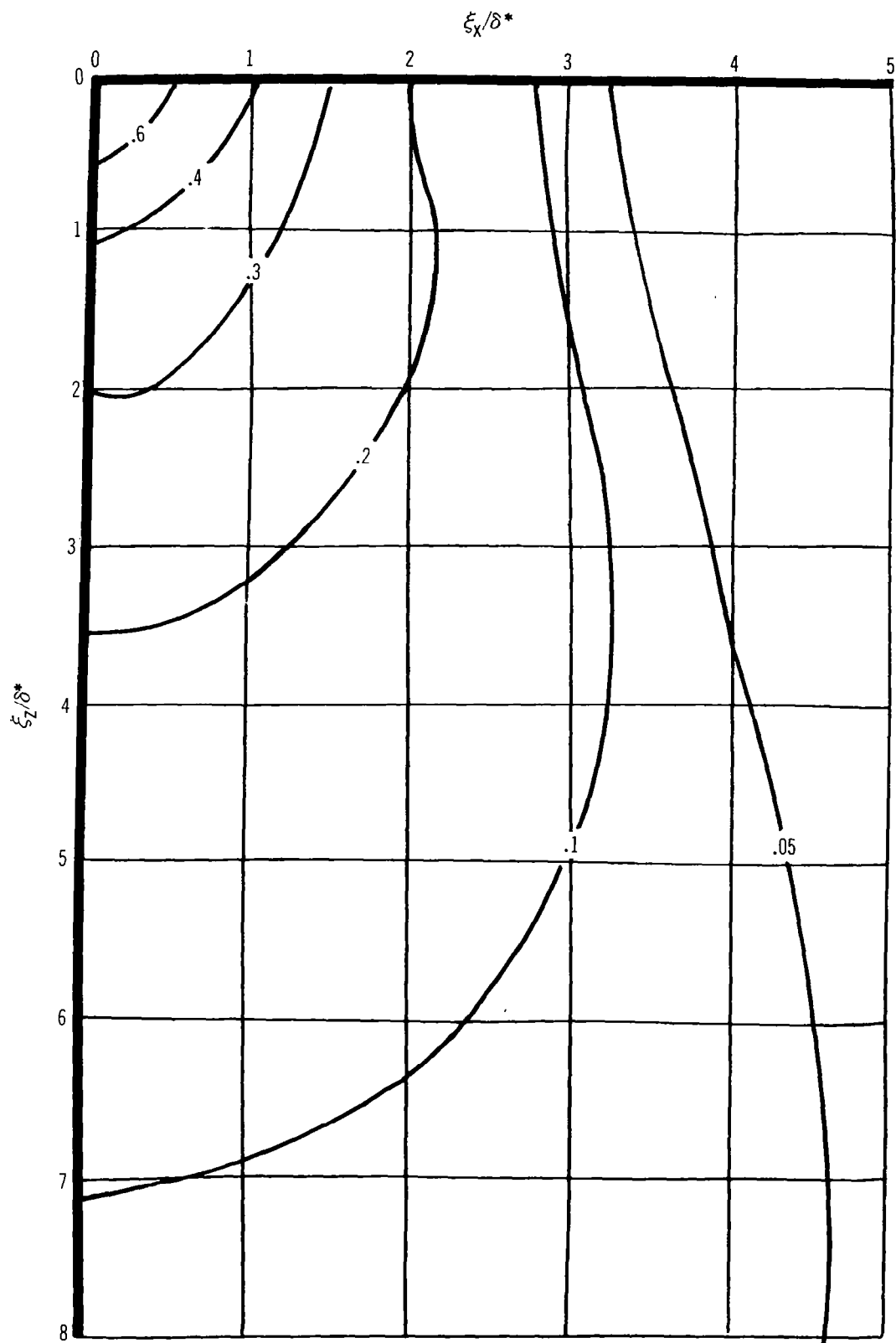
Figure 26. Approximate Contours of Equal Correlation Coefficient in Unperturbed Flow, Bull, et al. (1963), M = .3 or .5
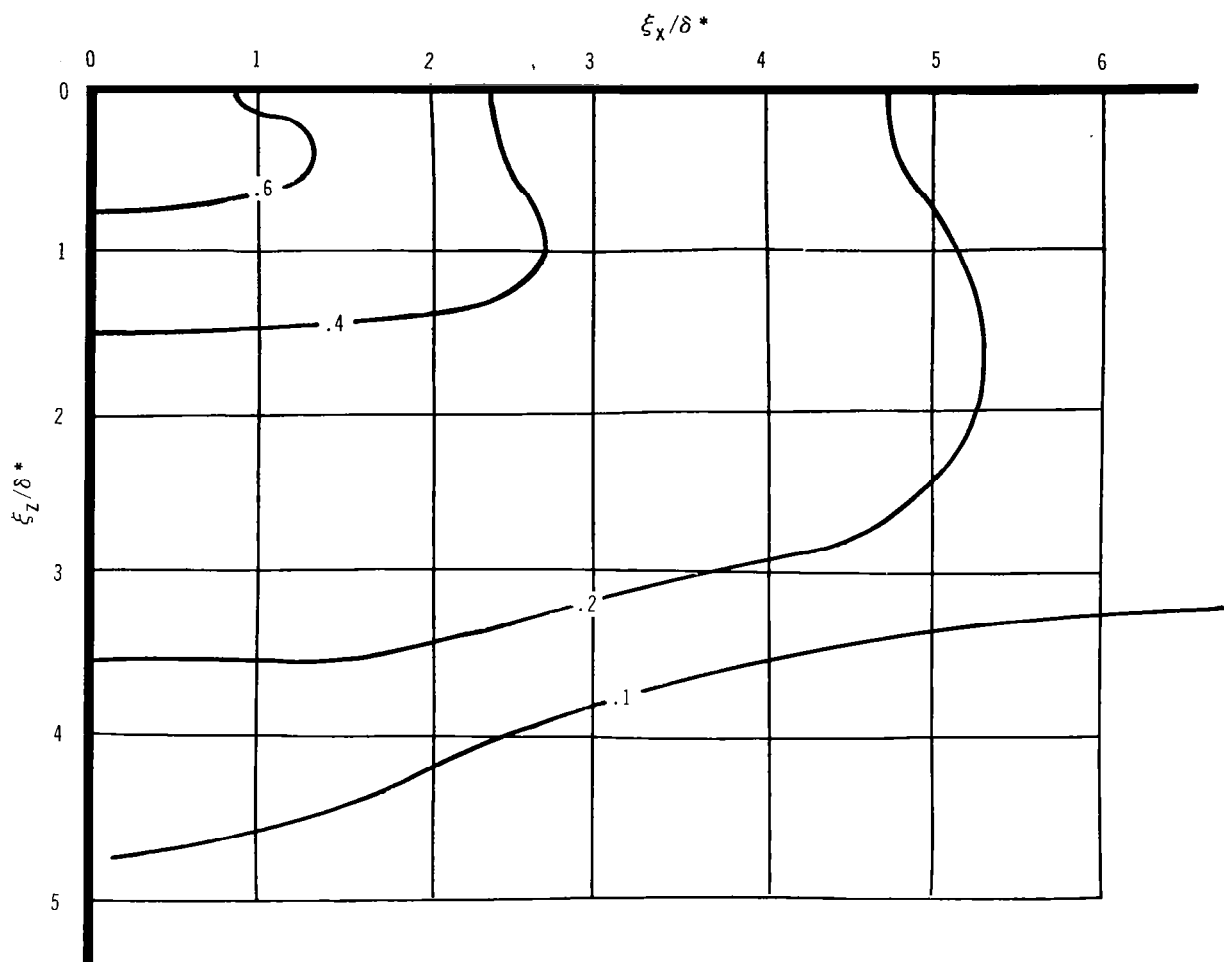
Figure 27. Approximate Contours of Equal Correlation Coefficient in Unperturbed Flow.
Maestrello Data (1964), M = .52

Using the space-time correlation data to extract information concerning the velocity of convection for the pressure signature, the data points are plotted on fig. 28. For comparison, the curve found in ref. 4 is also plotted showing considerable agreement between the two.

Calculation of an integral length scale in the direction of the flow defined as:

$$\lambda_x = \int_{-\infty}^{\infty} \left| C\left(\xi_x, 0, 0\right) \right| d\xi_x \qquad (6)$$

gave $\lambda_x/\delta = 0.7$ for this study. By comparison, Bull calculated $\lambda_x/\delta = 0.4$ for a two-dimensional boundary layer at $M = 0.5$. The difference stems from the larger negative lobe calculated for this study.
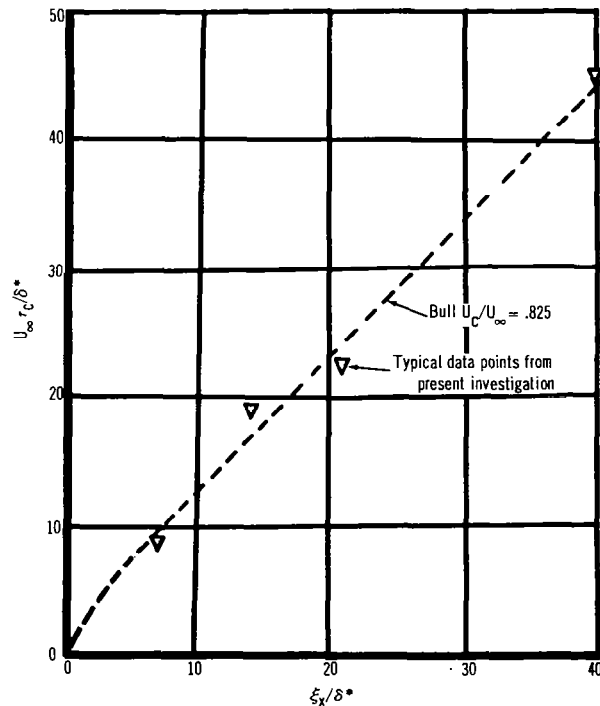
Figure 28. Convection Velocity for Subsonic (M ≈ .3 to .6) Pressure Fluctuations

4.3 Supersonic Unperturbed Flow

The first noticeable difference between the subsonic and supersonic power spectra is the much greater scatter of the data in the range of 0.01 < Strouhal number $(\omega \delta^*/U_\infty)$ < 1.0 for the supersonic data. At all Mach numbers below 3.45, the variations in level at the low frequencies can be as much as 10 to 15 dB between adjacent measuring stations. Most investigators have reported similar problems at low frequencies. However, the data coalesce nicely at the higher frequencies, except for the furthest stations upstream.

The different spectral shapes at M = 1.40 (fig. 29) are similar to those obtained in ref. 1 at this Mach number. In the present investigation, more scatter appears to occur at the lowest frequencies. Looking at the static pressure distribution at M = 1.40 (fig. 9D), it appears that a weak shock is impinging at about x_W = -0.6 in. This would explain the high levels in the low-frequency region at x_W = -0.417 in. since the characteristics of the spectrum shape near a shock wave are high levels at low frequencies (also see section 4.6). It is also probable that the boundary layer at x_W = -6.625 in. is not yet well developed, resulting in a spectrum shape similar to the thickened boundary-layer shape at that upstream station at M = 0.42. (See discussion of M 0.42 data in section 4.2.) If the point at x_W = -0.417 in. is disregarded on fig. 30, the overall levels are reasonably consistent and show only slight variation with distance along the wall.

At M = 1.81 (fig. 31 and 32), the scatter in data can be reduced somewhat by disregarding the data at x_W = -1.19 in. and -0.8 in. by an argument similar to that above. The extreme downstream point on fig. 32 is also high as may be seen from its spectral shape in fig. 31. The reason for this is not known at this time.

Figs. 33, 34, and 35 present data for two different Reynolds numbers at M = 2.52. The spectra show two distinct levels in the low-frequency regions. For reasons discussed below, it is concluded that the lower levels are suspect. At x_W = +2.5 in., the transducer is located at the termination of a favorable pressure gradient region. Data from a 5° expansion (not presented in this report) indicate that the spectrum levels are lower in an expansion region than in unperturbed flow. At x_W = 0 and +3.0 in., the measurements were sensed by condenser microphones recorded in direct mode (AM). For reasons not entirely resolved, data from the condenser microphones became increasingly unreliable as the Mach number increased (and the static pressure decreased). At subsonic Mach numbers where the static pressures were near atmospheric and there were no microphone resonances, both the AM- and FM-recorded data were reasonably consistent. The FM data were
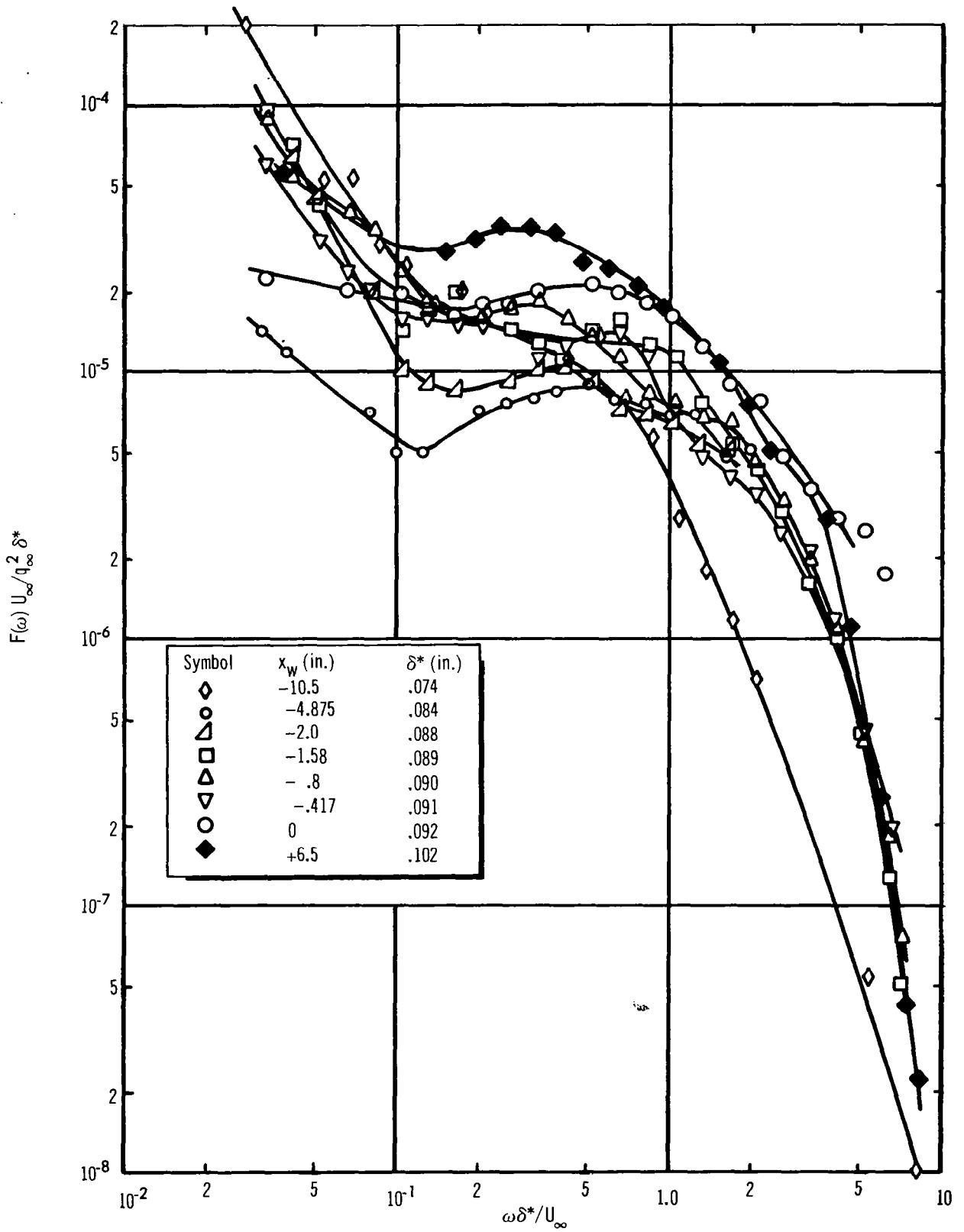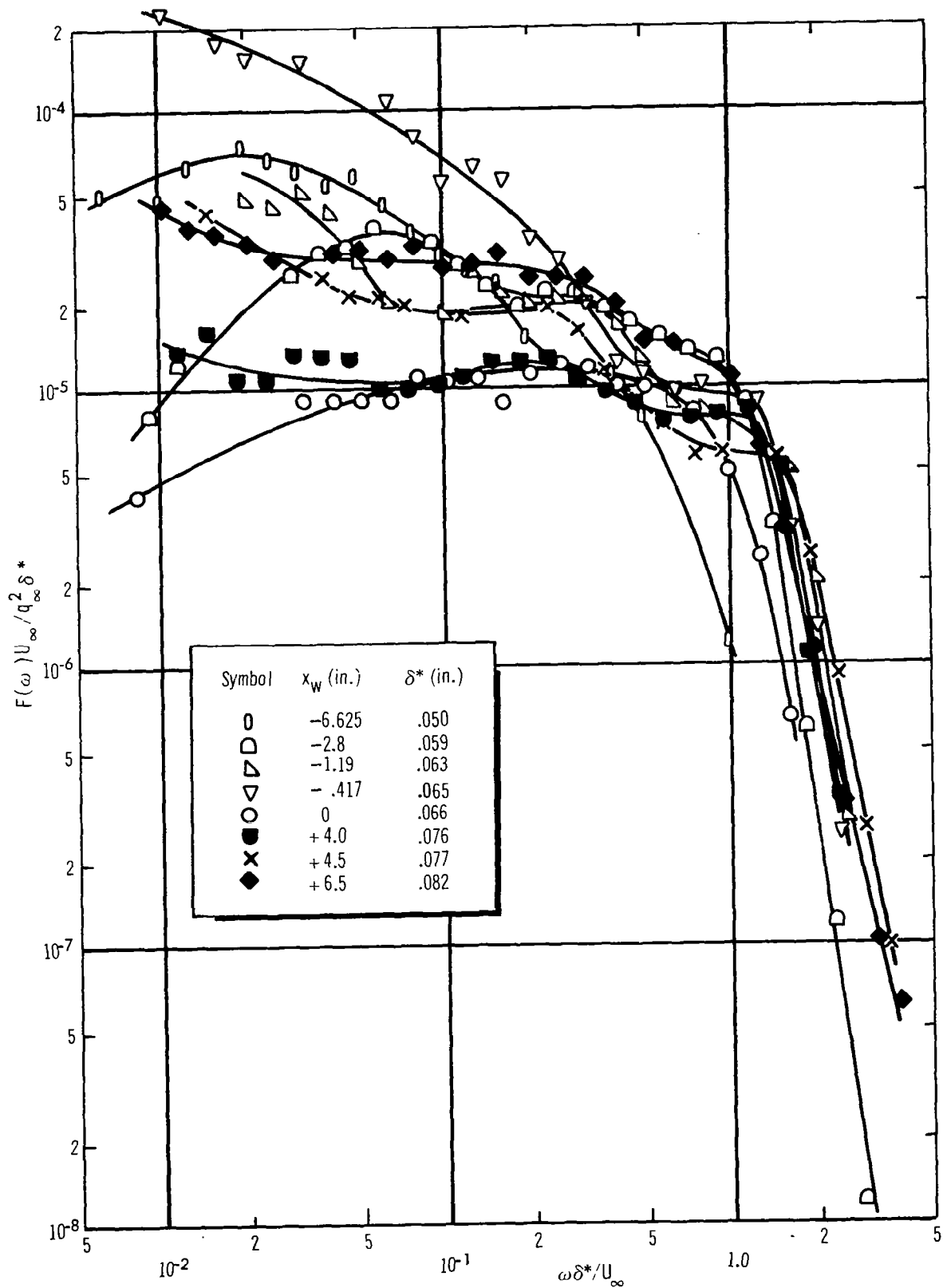
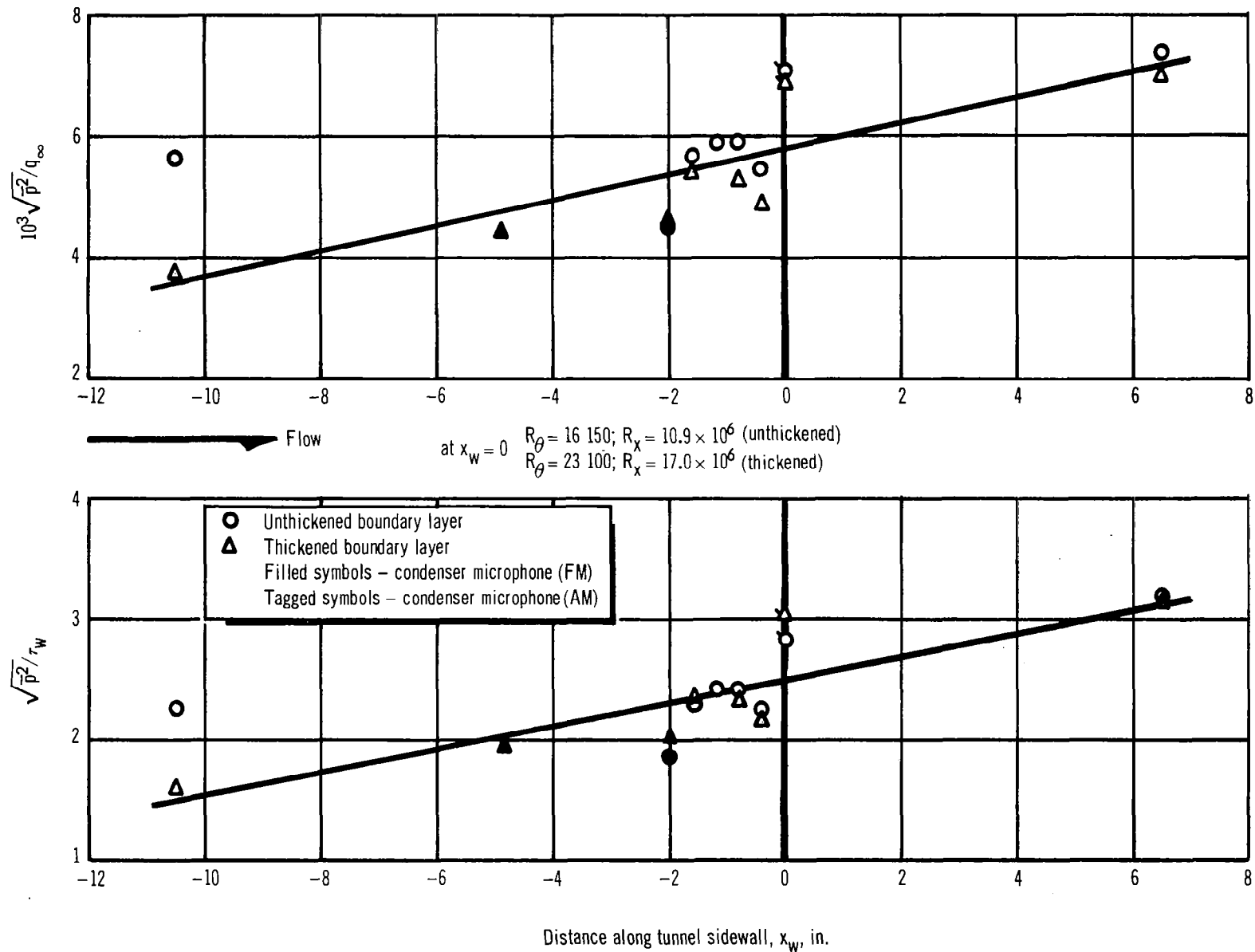Figure 29. Nondimensional Power Spectra of the Wall Pressure Fluctuations, $M_\infty = 1.40$

50
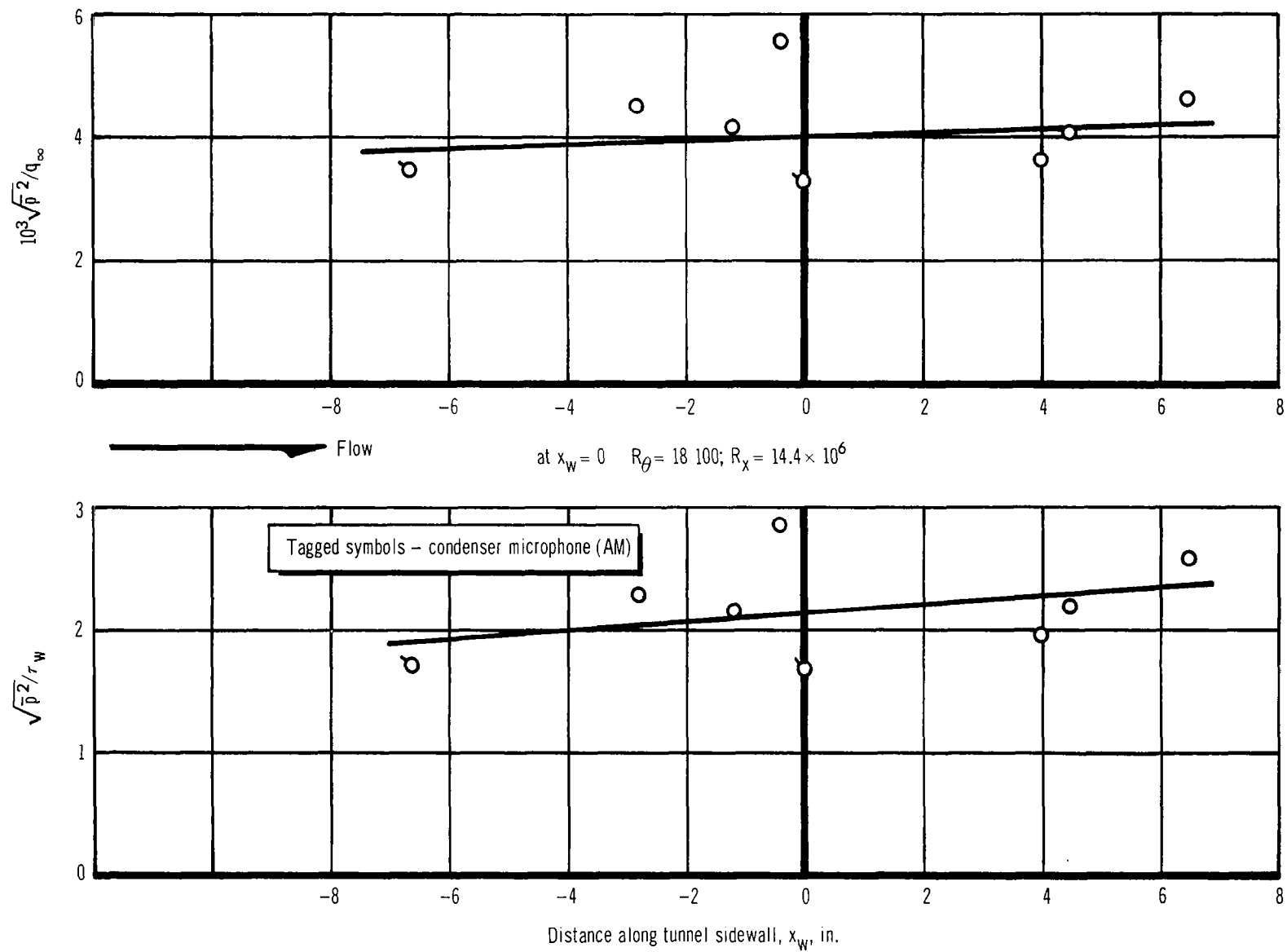
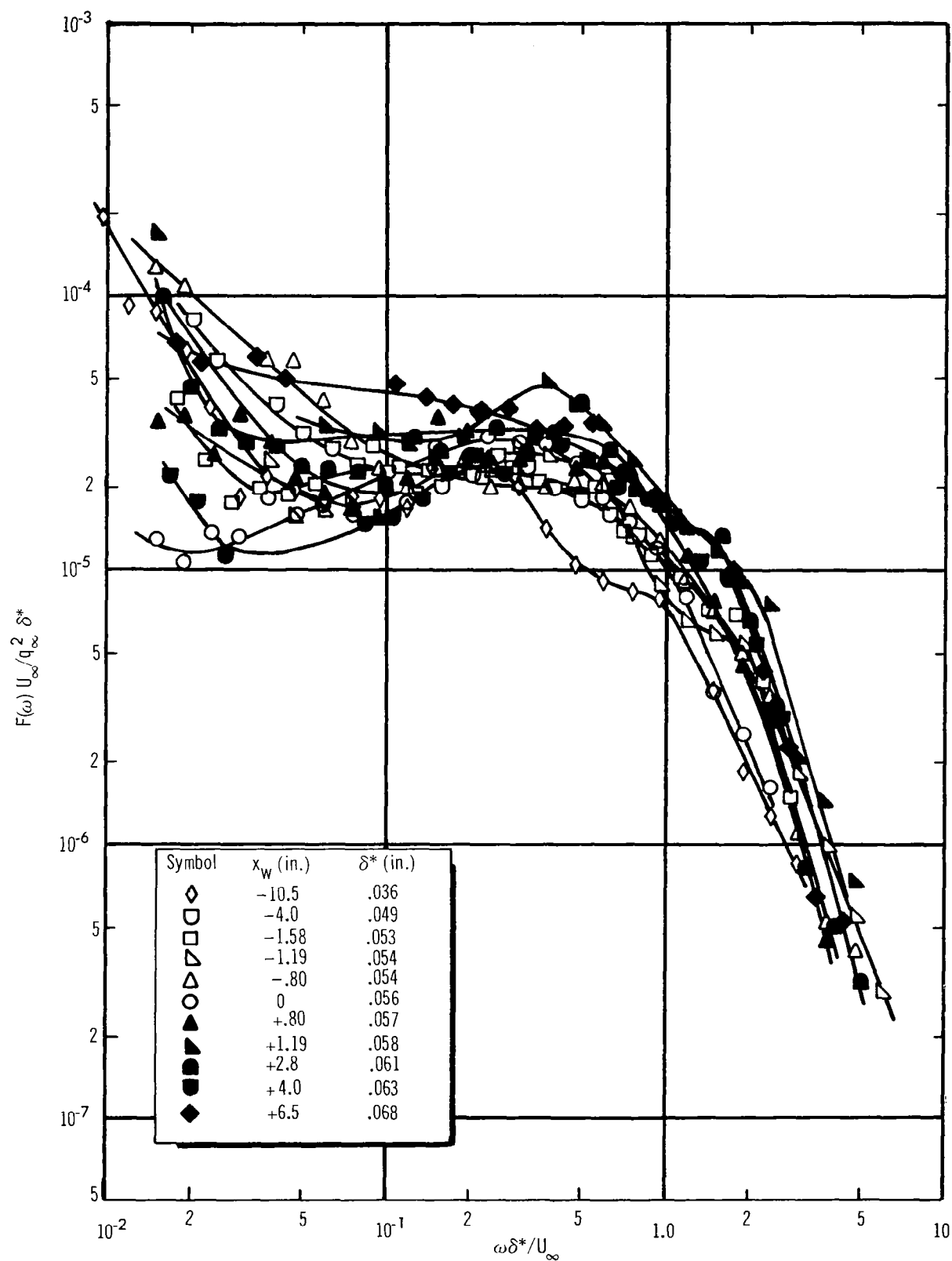Figure 30. Variation of the rms Pressure Fluctuations Along the Tunnel Sidewall, $M_\infty = 1.40$
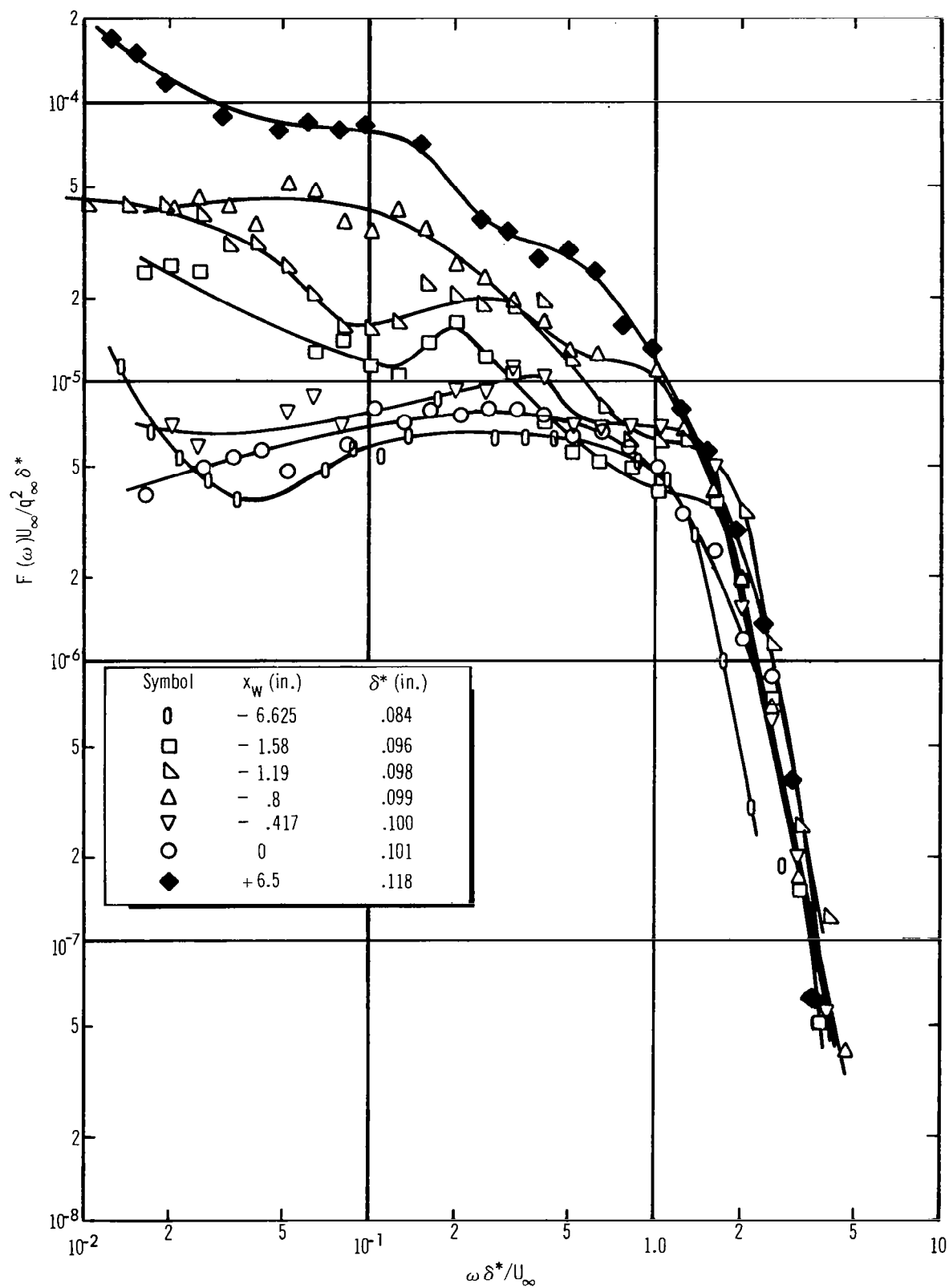
Figure 31. Nondimensional Power Spectra of the Wall Pressure Fluctuations, $M_\infty = 1.81$

The plot axes are labeled:

- Vertical axis: $F(\omega)U_\infty/q_\infty^2 \delta^*$
- Horizontal axis: $\omega \delta^*/U_\infty$

Symbol	x_w (in.)	δ^* (in.)
◐	− 6.625	.084
□	− 1.58	.096
◁	− 1.19	.098
△	− .8	.099
▽	− .417	.100
○	0	.101
◆	+ 6.5	.118
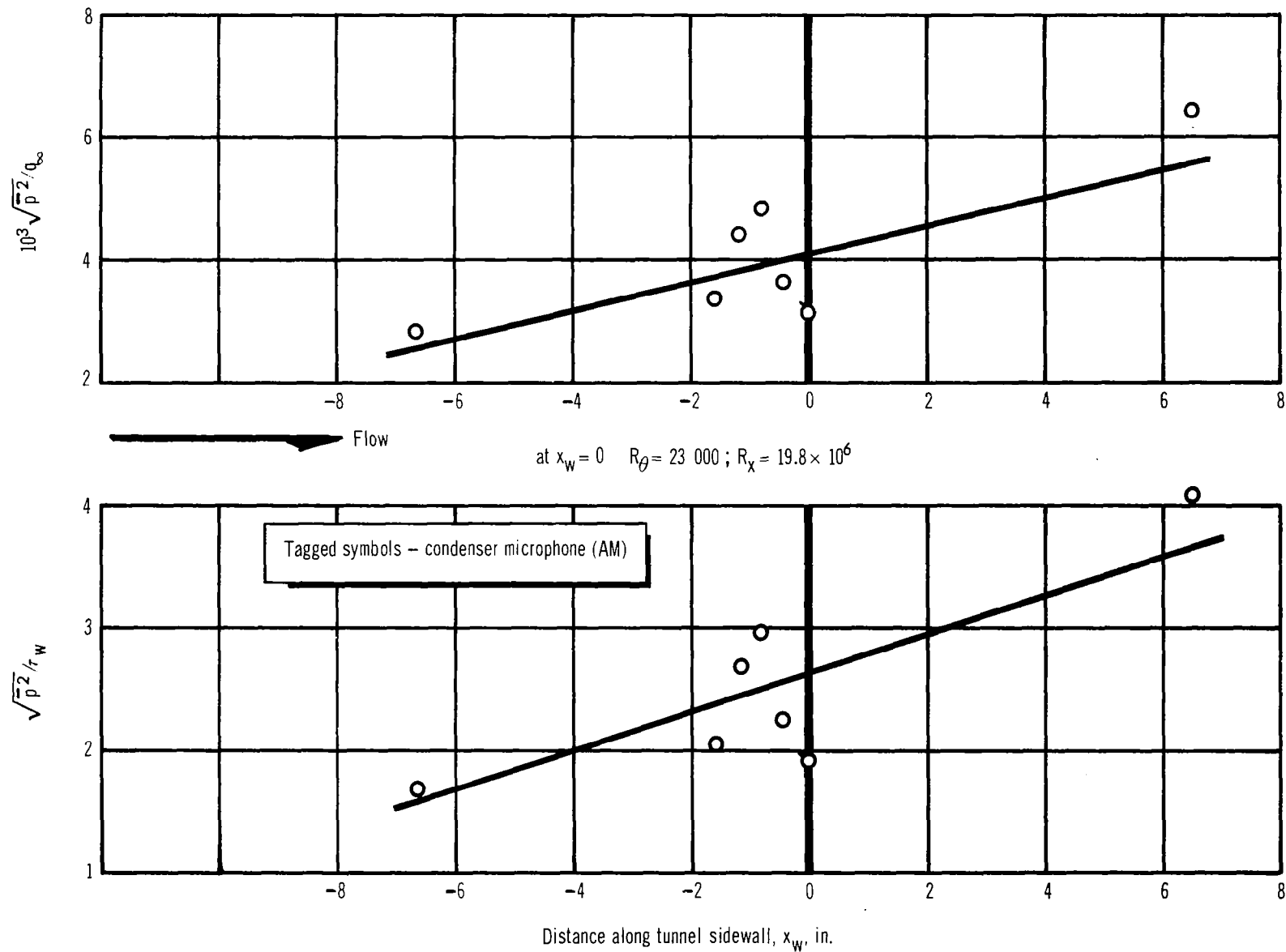
Figure 32. Variation of the rms Pressure Fluctuations Along the Tunnel Sidewall, $M_\infty = 1.81$

at $x_w = 0$ $R_\theta = 23\ 000$; $R_x = 19.8 \times 10^6$

Tagged symbols — condenser microphone (AM)

Distance along tunnel sidewall, x_w, in.
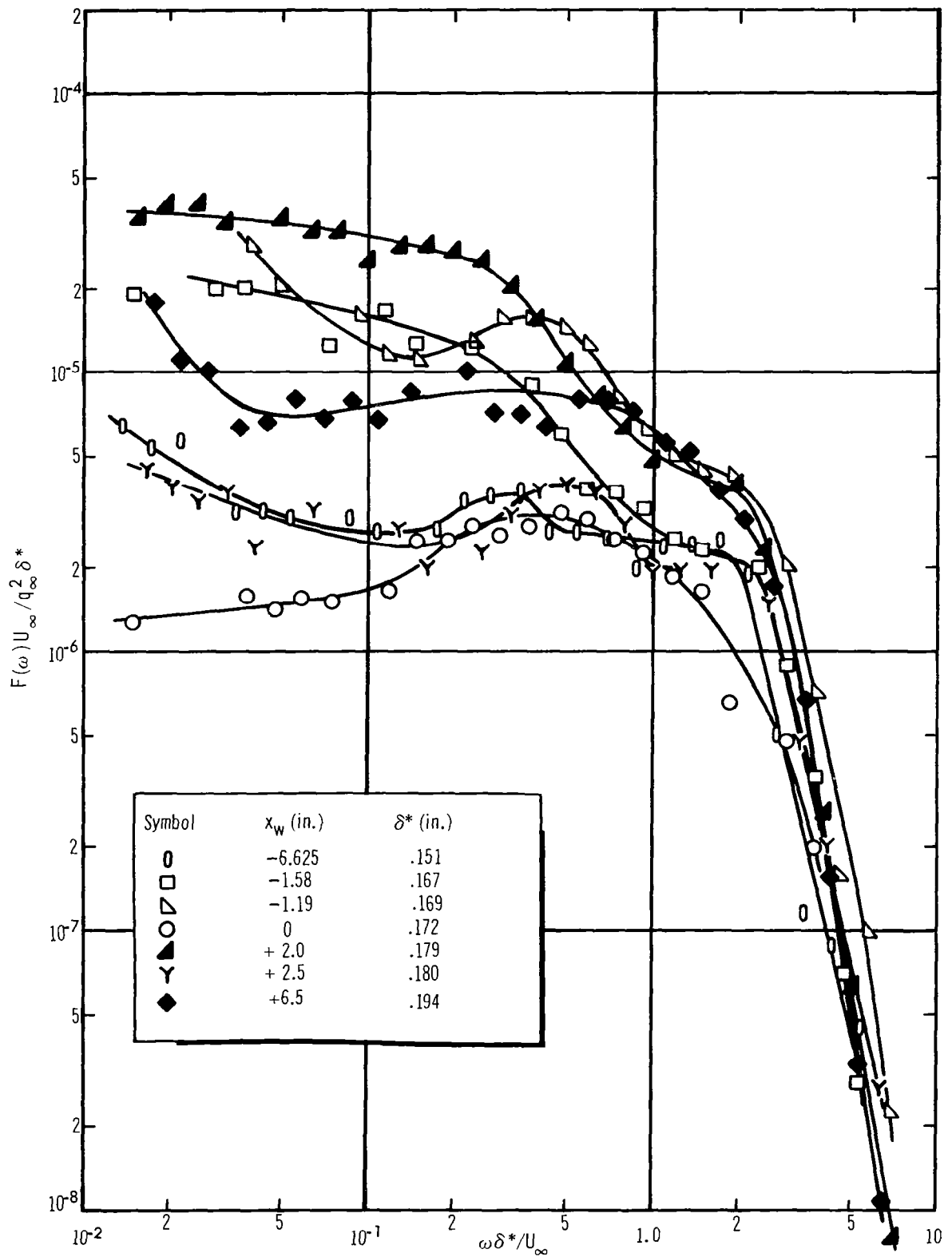
Figure 33. Nondimensional Power Spectra of the Wall Pressure Fluctuations, $M_\infty = 2.52$ (Re/In. = .78 × 10^{6})
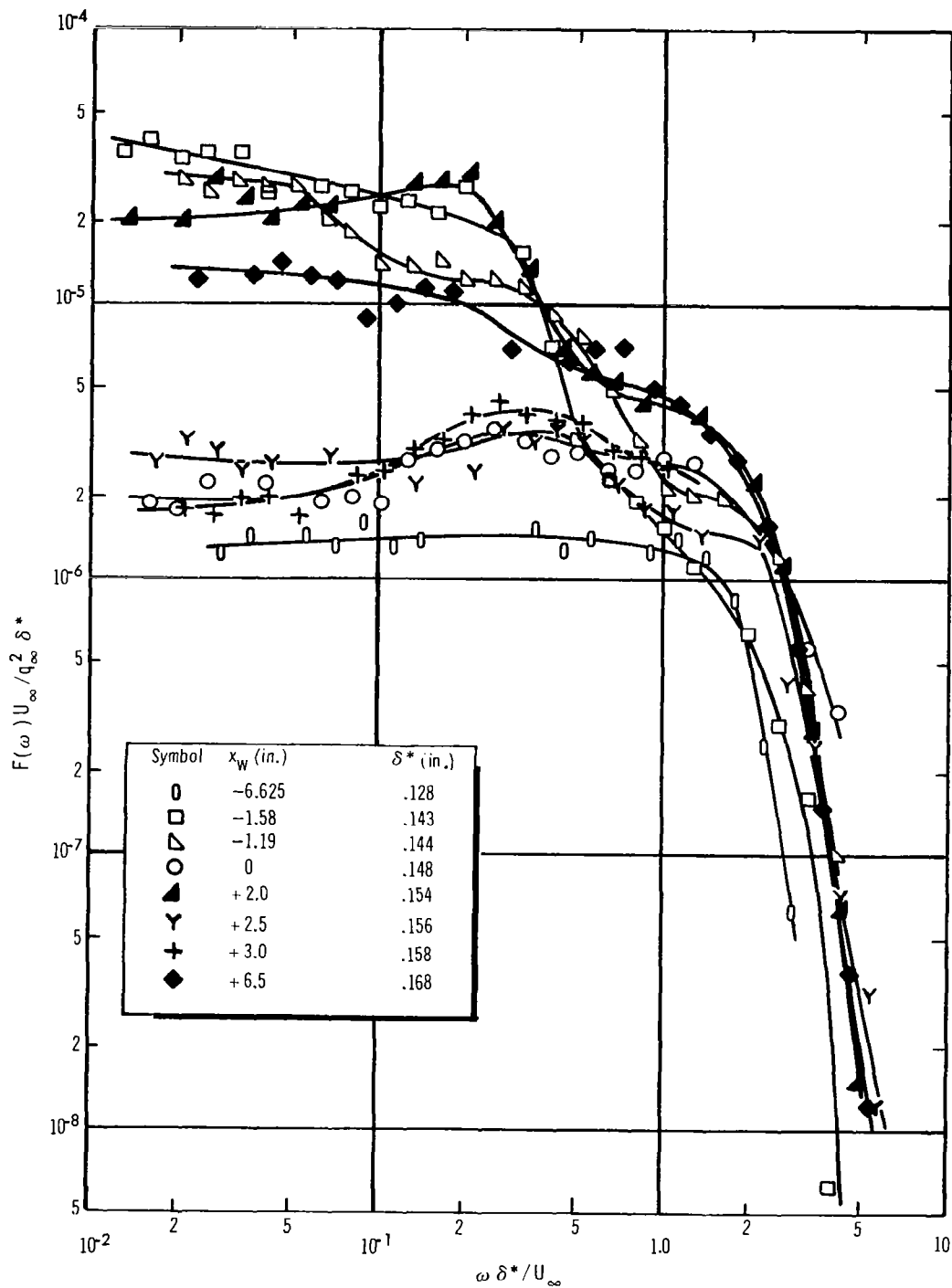
Figure 34. Nondimensional Power Spectra of the Wall Pressure Fluctuations, $M_\infty = 2.50$ (Re/In. $= 1.74 \times 10^6$)
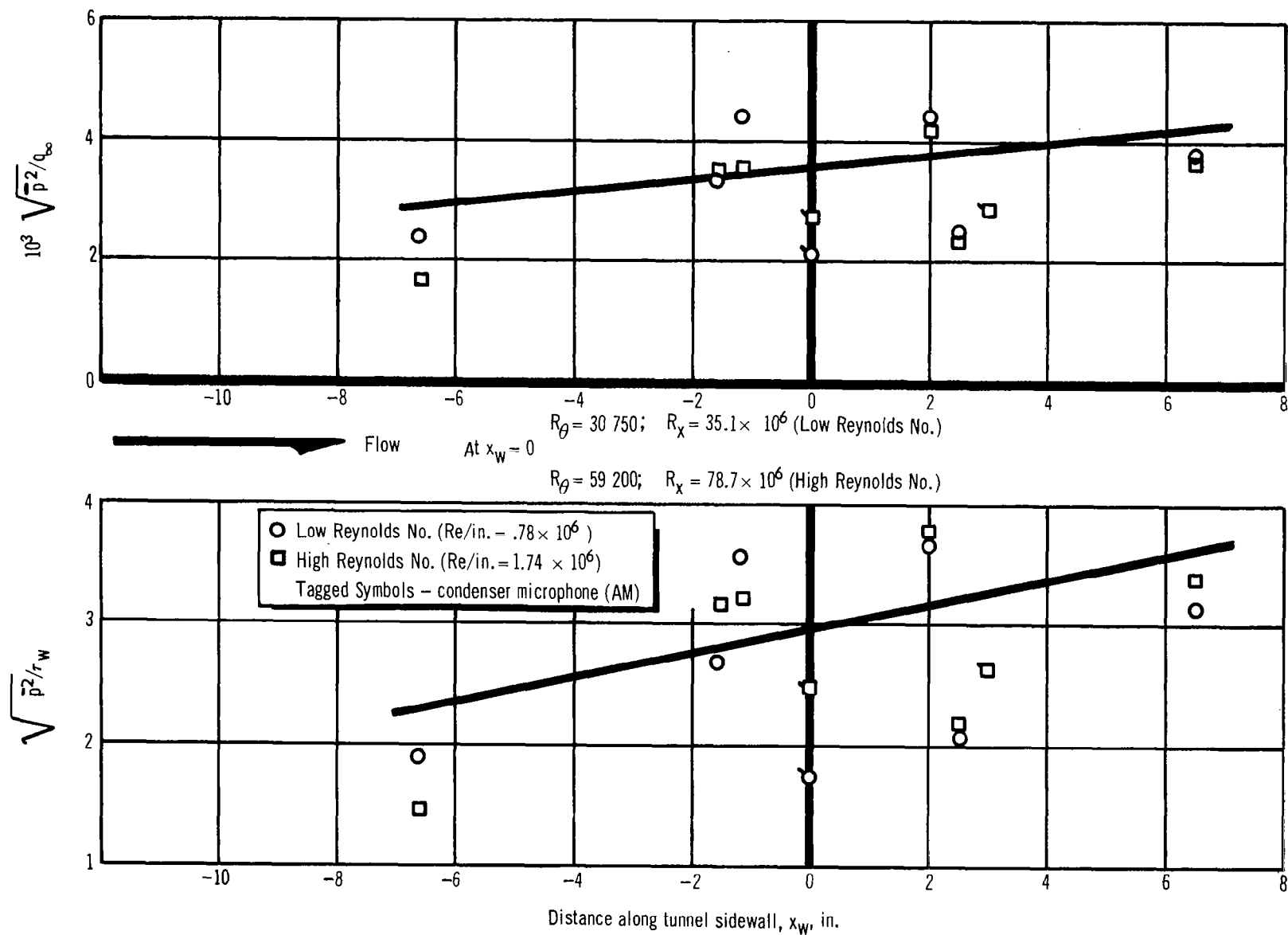
Figure 35. Variation of the rms Pressure Fluctuations Along the Tunnel Sidewall, $M_\infty = 2.52$

only plotted if the curves showed enough roll-off to allow extrapolation to high frequencies and thus calculation of the overall levels. As the Mach number increased and static pressure decreased, the microphones began to show a resonance peak at progressively lower frequencies and it became more difficult to correct for this resonance as its magnitude increased. In addition, at supersonic Mach numbers, the FM (condenser microphone) data unaccountedly fell 5 to 10 dB below the levels from the piezoelectric transducers (always AM-recorded). Even the AM-recorded condenser microphone data showed slightly lower spectral levels than the piezoelectric transducers. Consequently, the condenser microphone data above Strouhal number = 2.0 at M = 2.52 and 3.45 are considered to be only approximate. With the foregoing as evidence, the curve was drawn through the higher levels in fig. 35.

The effect of increasing the Reynolds number at M = 2.5 is not immediately apparent, since the rms value may increase or decrease at any given station. Clearly, a more comprehensive and systematic approach is needed to verify any variation of $\sqrt{\overline{p^2}}/q_\infty$ or $\sqrt{\overline{p^2}}/\tau_w$ with Reynolds number.

Data were also taken at M = 2.52 for a thickened boundary layer. Apparently, a very unstable condition existed at the downstream end of the thickening device because each time the configuration was run, the downstream edge of the metal backing strip pulled loose from the wall and blew down the tunnel. Examination of the data showed a great deal of scatter in the power-spectral densities, in the rms levels, and in the boundary-layer profiles. For this reason, the data were considered invalid.

Because of its obvious application to the supersonic transport in cruising flight, M = 3.45 received the most attention during the test program. Fig. 36 presents power spectra for the unthickened boundary layer and fig. 37 gives the overall rms values with respect to q_∞ and τ_w. Data from several runs on the unthickened boundary layer are given in the figures. Although not all of the data from the more than 25 stations are presented, a sufficient amount is shown to indicate trends. Most of the data fall within a small band of scatter. The transducer at x_w = -6.625 in. lies within a fairly steep adverse pressure gradient, again probably caused by a weak shock impinging, and the high rms levels may be caused in part by this fact. An enigma is seen in the data downstream of x_w = +1.6 in., where a decrease in overall levels appears. The reason for this decrease has not yet been determined.

Thickening the boundary layer at M = 3.45 resulted in a general level increase averaging about 5 dB. An exception to the 5 dB increase occurred in the region between x_w = -1.58 and 0 in., where a large perturbation in the flow caused very high rms levels. The effect can be seen in fig. 37 at x_w = -1.58, -1.19, and -0.8 in.

Fig. 38 shows the calculated space-time correlations of the fluctuating pressures in the x-direction for the uniform unthickened boundary layer at M = 3.45. This $R(\xi_x, 0, \tau)$ function provides considerable information.
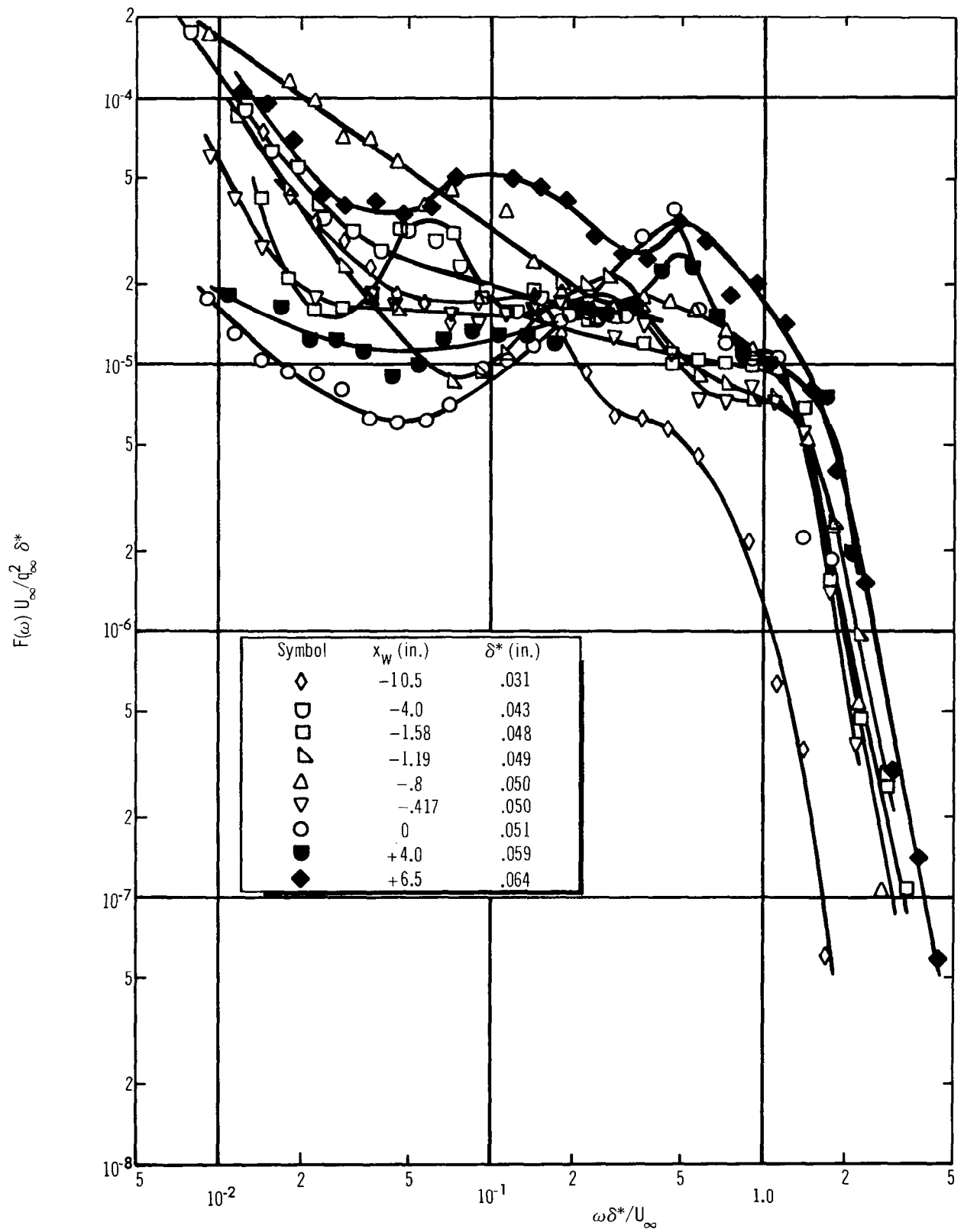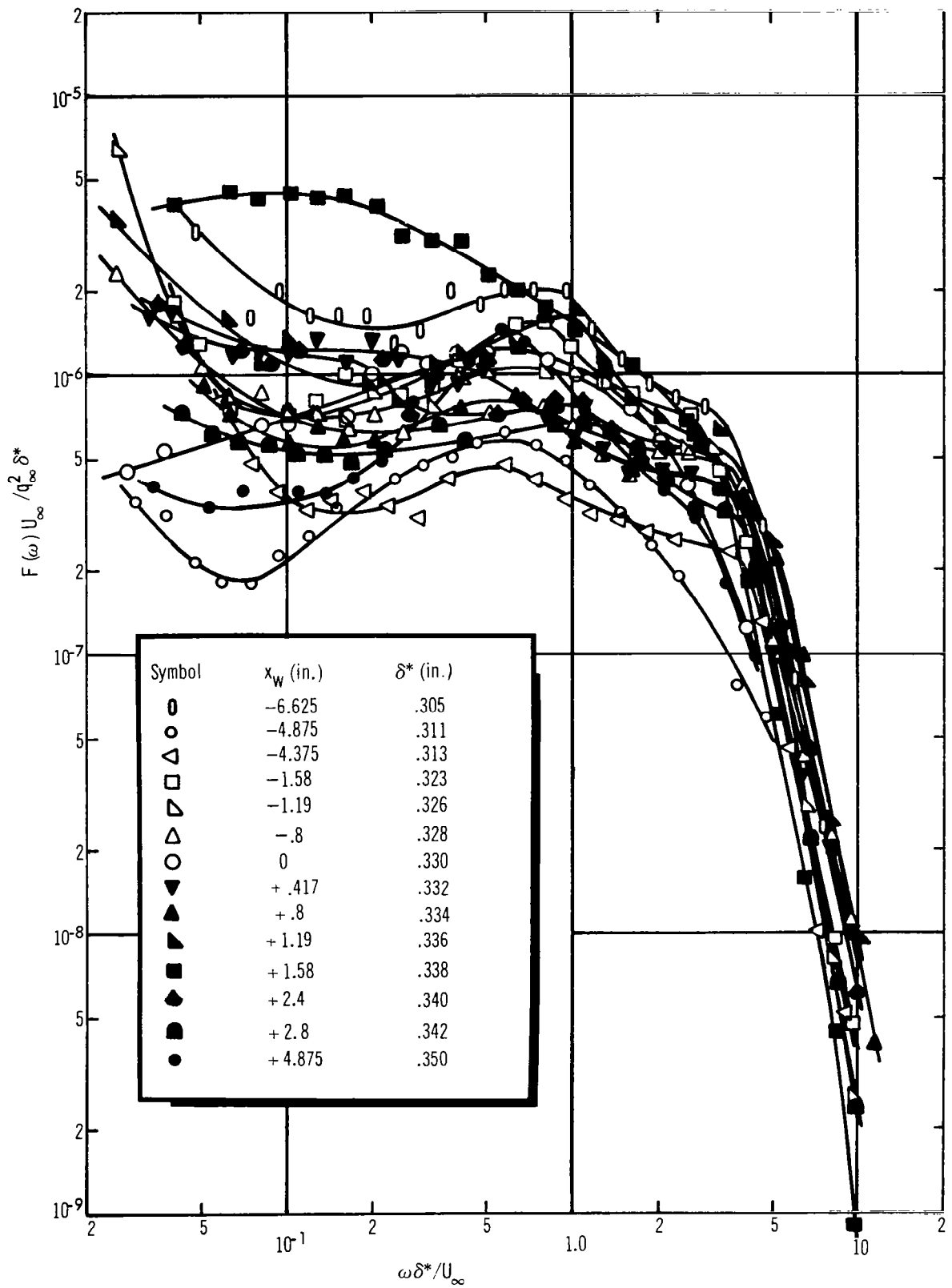
Figure 36. Nondimensional Power Spectra of the Wall Pressure Fluctuations, $M_\infty = 3.45$
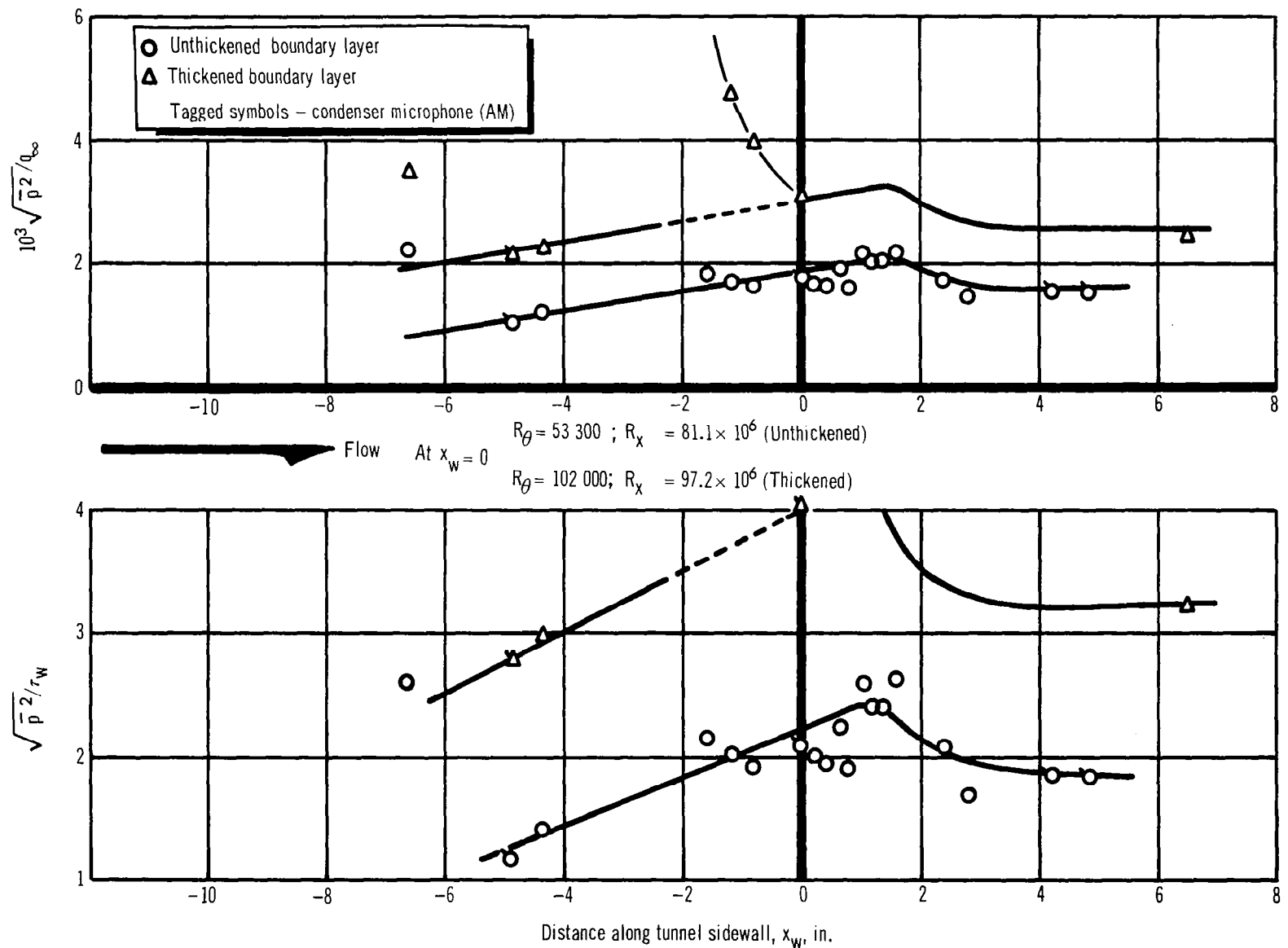
Figure 37. Variation of the rms Pressure Fluctuations Along the Tunnel Sidewall, $M_\infty = 3.45$

The figure contains the following legend and labels:

- O Unthickened boundary layer
- △ Thickened boundary layer

Tagged symbols — condenser microphone (AM)

Flow   At $x_w = 0$

$R_\theta = 53\,300$; $R_x = 81.1 \times 10^6$ (Unthickened)

$R_\theta = 102\,000$; $R_x = 97.2 \times 10^6$ (Thickened)

Top plot vertical axis: $10^3 \sqrt{\bar{p}^2}/q_\infty$

Bottom plot vertical axis: $\sqrt{\bar{p}^2}/\tau_w$

Bottom plot horizontal axis: Distance along tunnel sidewall, x_w, in.

	ξ_X (in.)	ξ_X/δ^*
●	.417	1.26
□	.80	2.42
▲	1.19	3.6
◇	1.58	4.78
◖	2.0	6.05
◗	2.4	7.27
▷	3.5	10.6

Figure 38. Space-Time Cross-Correlations of the Fluctuating Pressure in Unperturbed Flow at M = 3.45

First, the time dependence of the spatial correlation in the moving frame of reference (riding with the boundary layer) is determined by the time decay of the maxima of each space-time correlation trace on fig. 38. Fig. 39 shows these maximum points plotted separately, with an approximate best fit curve through them. A mathematical description for this curve was determined:

$$R_{max} (\tau) = R(0,0,0) \cdot \frac{1}{1 + 1.27 \times 10^4 \tau} = \frac{1}{1 + 1.27 \times 10^4 \tau} \qquad (7)$$

where τ is in seconds and $R(0,0,0)$ is the normalized autocorrelation for zero separation and zero time delay, identically equal to one. Since time is the same in both the moving frame and the fixed frame of reference (fixed with respect to the measurement locations), this same relationship holds in either frame of reference.

Second, the $R(\xi_x, 0, \tau)$ function provides information about the convection velocity of the pressure signature as it moves across different measurement
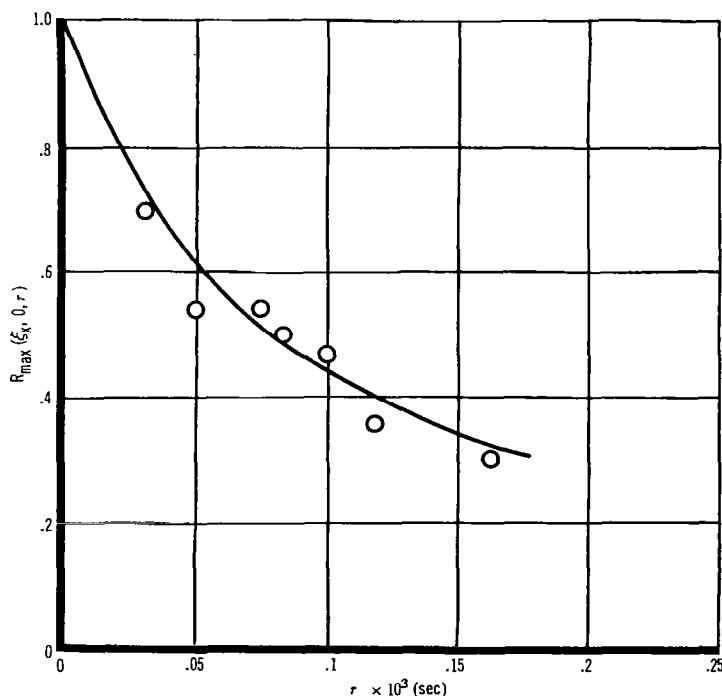
Figure 39. Time Dependence of the Space-Time Cross-Correlation Maximum in Unperturbed Flow at M = 3.45

61

locations. It is of interest to plot the convection velocity versus the separation distance between transducer locations. This kind of plot, shown in fig. 40, indicates the wide variation possible as the pressure signature moves downstream. The marked change is undoubtedly caused by higher velocity components being predominantly influential at larger spatial separations. These higher-velocity components are found well out in the turbulent boundary layer (away from the rigid boundary) in the constant stress portion of the boundary layer. Examination of the coherency of various frequency ranges for the cross-spectra indicates that the frequencies of maximum coherency (or correlation) decrease as the separation distance increases. The result is an association of low-frequency components (large eddies) with the high-velocity region (constant stress region) of the turbulent boundary layer. Since narrow-band correlation calculations have not yet been performed on this data, detailed information as to the structure of the pressure signature cannot be readily extracted here. Kistler and Chen (ref. 6) calculated a value for U_c/U_∞ of approximately 0.6 for M = 3.5 by use of small values of ξ_x/δ^*. As can be seen from fig. 40, if only the small values of ξ_x/δ^* are utilized, a misleadingly low value of U_c/U_∞ will result. An analogous situation exists for subsonic unperturbed flow and is shown for comparison on fig. 40.
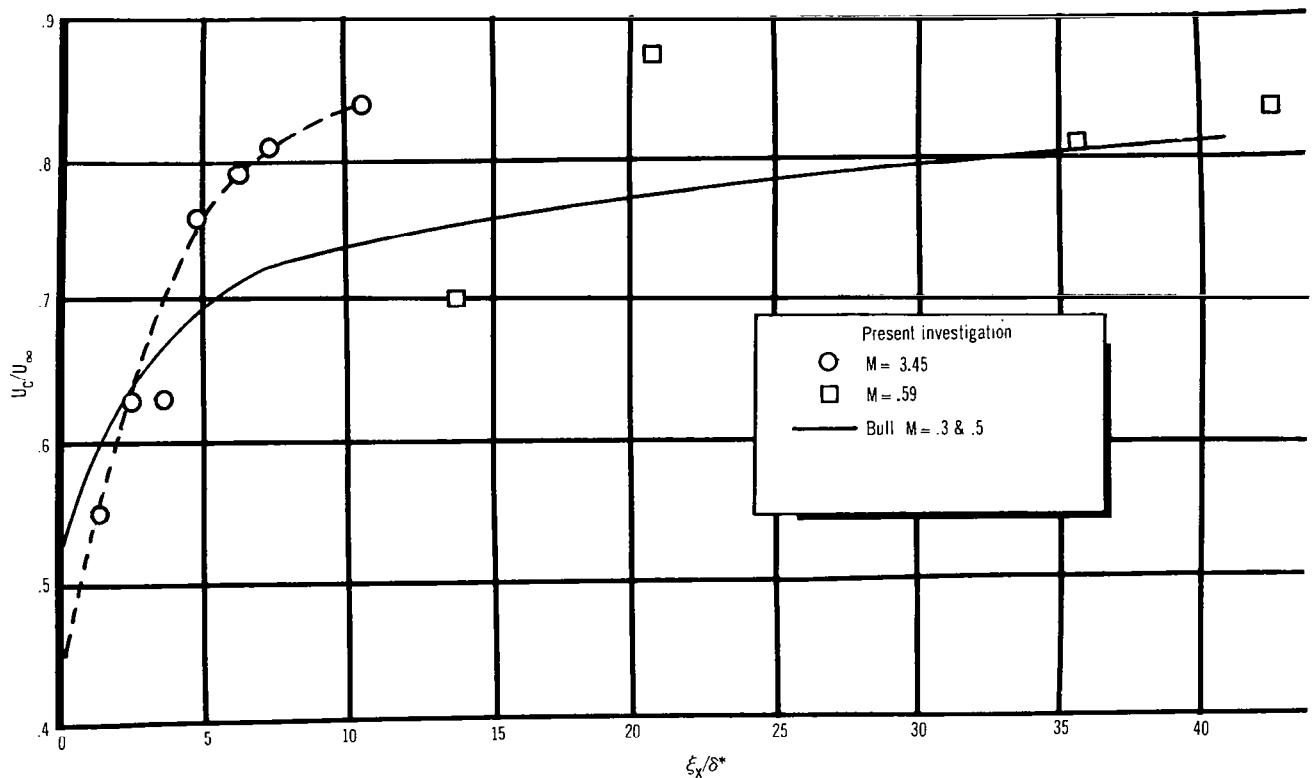
Figure 40. Variation of Convection Velocity with Transducer Separation

Fig. 41 presents the convection velocity data in a manner that compresses the data to a straight line of constant slope (removing the dependence on spatial separation).

Using the values extracted from figs. 39 and 40 for U_c, τ, and the time dependent decay, values for C (ξ_x, 0, 0) can be obtained by extrapolating data measured at different locations at times other than $\tau = 0$, (see section 2.2 for further details of this technique). The assumption used is that the spatial and temporal parts of the correlation function are separable. The data shown in fig. 38 support such an assumption by inspection.

For further confirmation, the positive and first negative humps to the curves are describable mathematically in a limited range of variables as

$$R\left(\xi_x, 0, \tau\right) = 0.4e^{-0.75\xi_x} \sin\left[\frac{\pi\{\tau - (0.044\xi_x - 0.017)\}}{0.55}\right] - 0.054\xi_x + 0.5$$

$$(8)$$

which indicates the temporal part is separable. A great deal more will be said about separability of functions of each variable in section 5.6. Suffice it to say that since the time and space parts are separable, an adequate number of data points are obtainable to form the curves as shown on figs. 42 and 43, which show the correlation coefficients in the x- and z-directions and fig. 44, which shows equal correlation coefficient contours in the plane for the unperturbed supersonic boundary layer (with an accuracy of ± 0.05). In these figures, the spatial dimensions have been divided by the displacement thickness. For subsequent work in perturbed flows, a better nondimensionalizing factor is momentum thickness, θ. Defined as the loss in momentum across the turbulent boundary layer even if the boundary layer is separated from the rigid wall, θ is the parameter least likely to change markedly from unperturbed to perturbed or even in separated flow conditions.

From fig. 42, the integral length scales can be graphically evaluated. These lengths were calculated as follows:

$$\lambda_x = 0.91 \text{ in.}$$

and

$$\lambda_z = 0.896 \text{ in. (if the long tail is included)}$$

These values are relatively high and result in a high value for the λ_z/λ_x ratio ($\simeq 1.0$). Comparison with the results of ref. 6 is highly unsatisfactory, since a value of λ_x/δ of approximately 0.09 was reported for M = 3.5, while for this study, $\lambda_x/\delta = 1.12$. However, in ref. 6, λ_x is defined as $\lambda_x = \int_{-\infty}^{\infty} C(\xi_x, 0, 0)d\xi_x$, which is considerably different from the usual interpretation in which the absolute value of C is used within the integral.
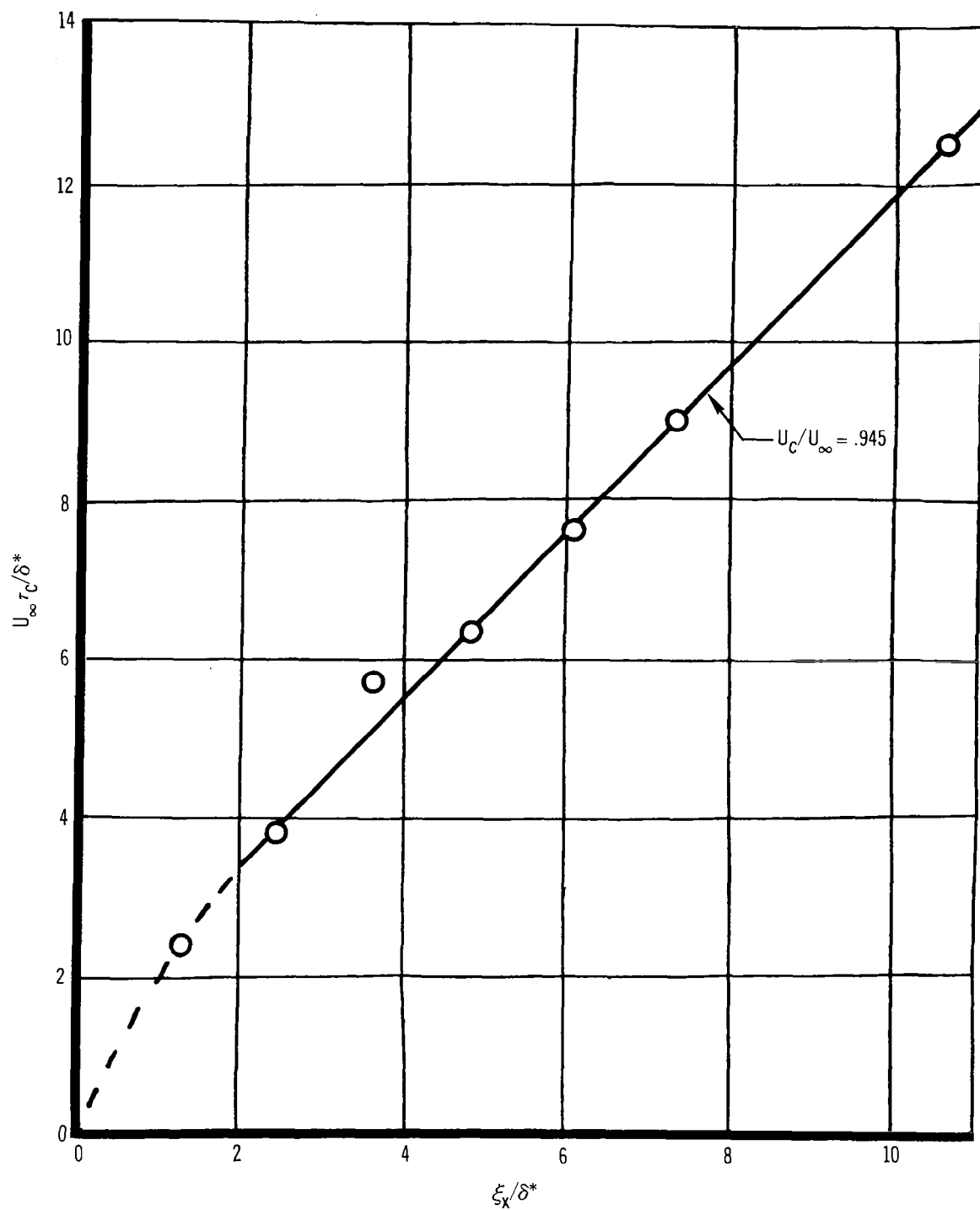
Figure 41. Nondimensionalized Convection Time Versus Nondimensionalized Spatial Separation for Unperturbed Flow at M = 3.45
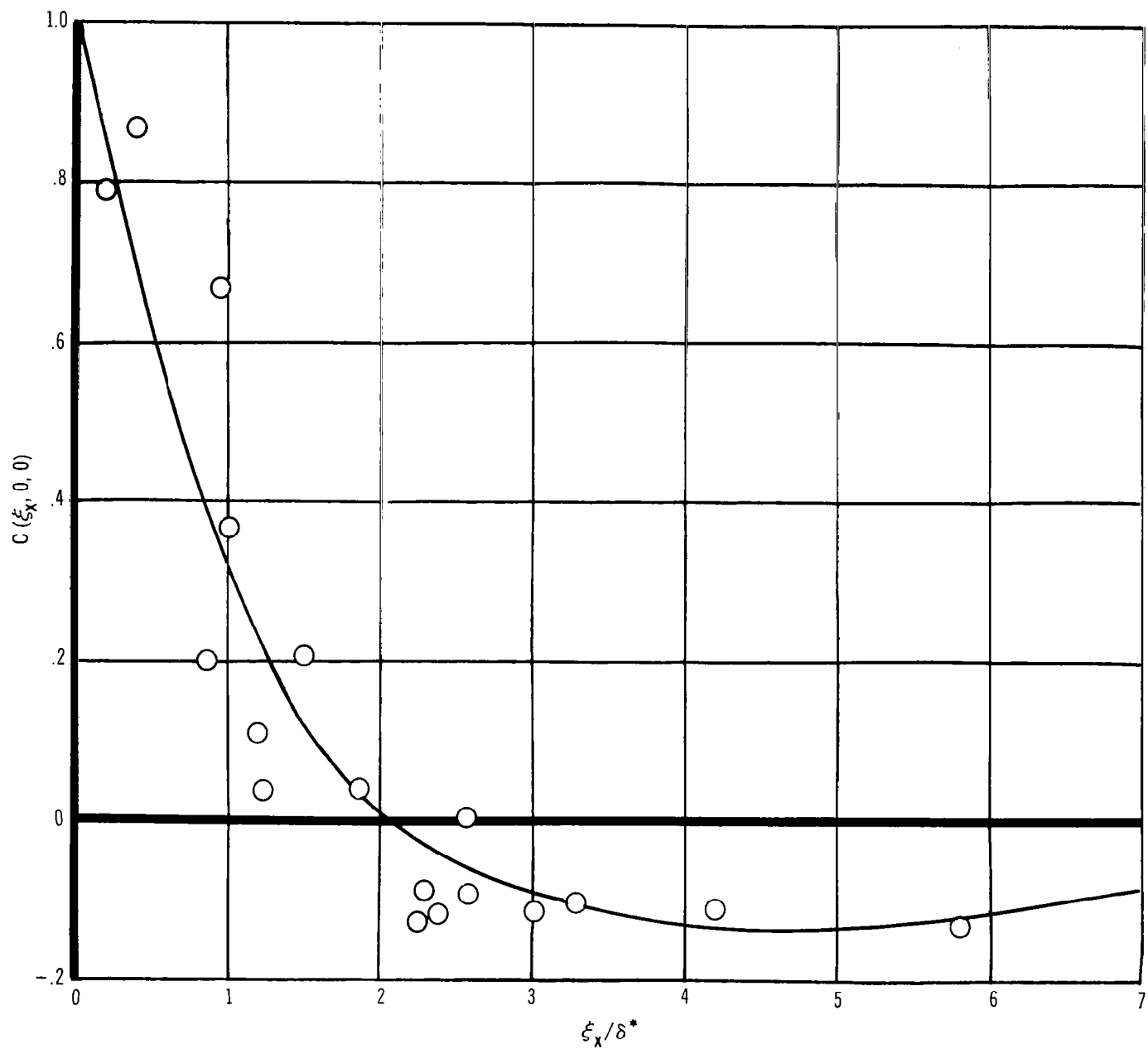
Figure 42. Longitudinal Correlation Coefficient for Unperturbed Flow at M = 3.45
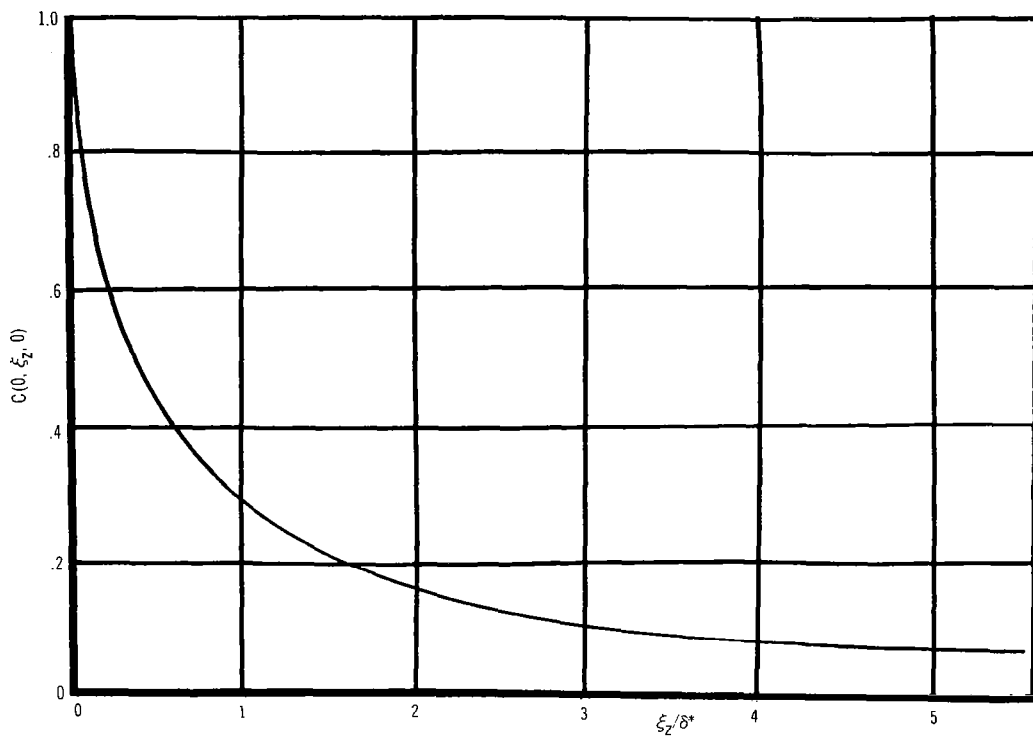
Figure 43. Correlation Coefficient in a Direction Perpendicular to the Unperturbed Flow, M = 3.45
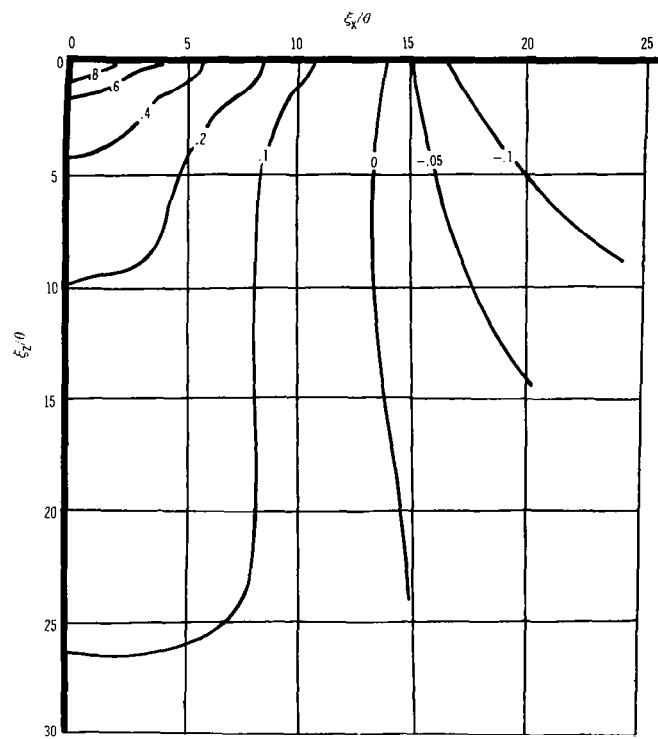
Figure 44. Approximate Contours of Equal Correlation Coefficient in Unperturbed Flow, M = 3.45

If λ_x for this study is defined as above (from Kistler and Chen), a value of $\lambda_x/\delta = 0.129$ results (the much smaller value resulting from the long negative tail of the longitudinal correlation coefficient). It is noted here that smaller integral length scales are more comparable to those found for perturbed flow conditions (see discussions).

4.4 Aft-Facing Steps in Supersonic Flow

In this study, an aft-facing step was tested at M = 1.41 and 3.48. The step-height (nominally 3/4 in.) was a constant for the two Mach numbers. Table IV provides a list of the pertinent boundary layer parameters ratioed to step-height at each Mach number. These parameters were measured on the step at $x_w = -0.5$ in., which is 0.38 in. upstream of the step face.

TABLE IV

STEP-HEIGHT TO BOUNDARY-LAYER THICKNESS RATIOS

Mach No.	h (in.)	δ/h	δ^*/h	Θ/h
1.41	0.737	0.43	0.088	0.040
3.48	0.737	1.10	0.448	0.066

Fig. 45 illustrates the variation in static and fluctuating pressures with increasing distance (expressed in step-heights) downstream of the step at M = 1.41. The fluctuating pressure remains constant for only 1/2 to 3/4 of a step-height downstream of the step face. The levels begin to rise through the base region, which extends about two step-heights, and continues to rise to $\Delta x_{TE}/h = 4.5$ to 5. This corresponds approximately to the reattachment point. From this point, the fluctuating pressure levels decrease although they do not return to clear tunnel levels within the nine step-heights that were the limits in this investigation.

Fig. 46 shows the same variations for M = 3.48. The fluctuating pressure levels in the base region begin to rise almost immediately and reach a peak about three step-heights downstream of the step face, which is once again in the region of flow reattachment for this Mach number (ref. 7). The levels decrease beyond this point reaching a nearly constant level, after about five step-heights, of some 2.5 times the clear tunnel level.

Power spectra for the two Mach numbers are shown in figs. 47 and 48. The data are normalized with respect to momentum thickness (measured on top of the step) rather than displacement thickness because momentum thickness shows the least change across the expansion fan at the edge of the step of any of the boundary layer parameters. Spectra for only a few stations are
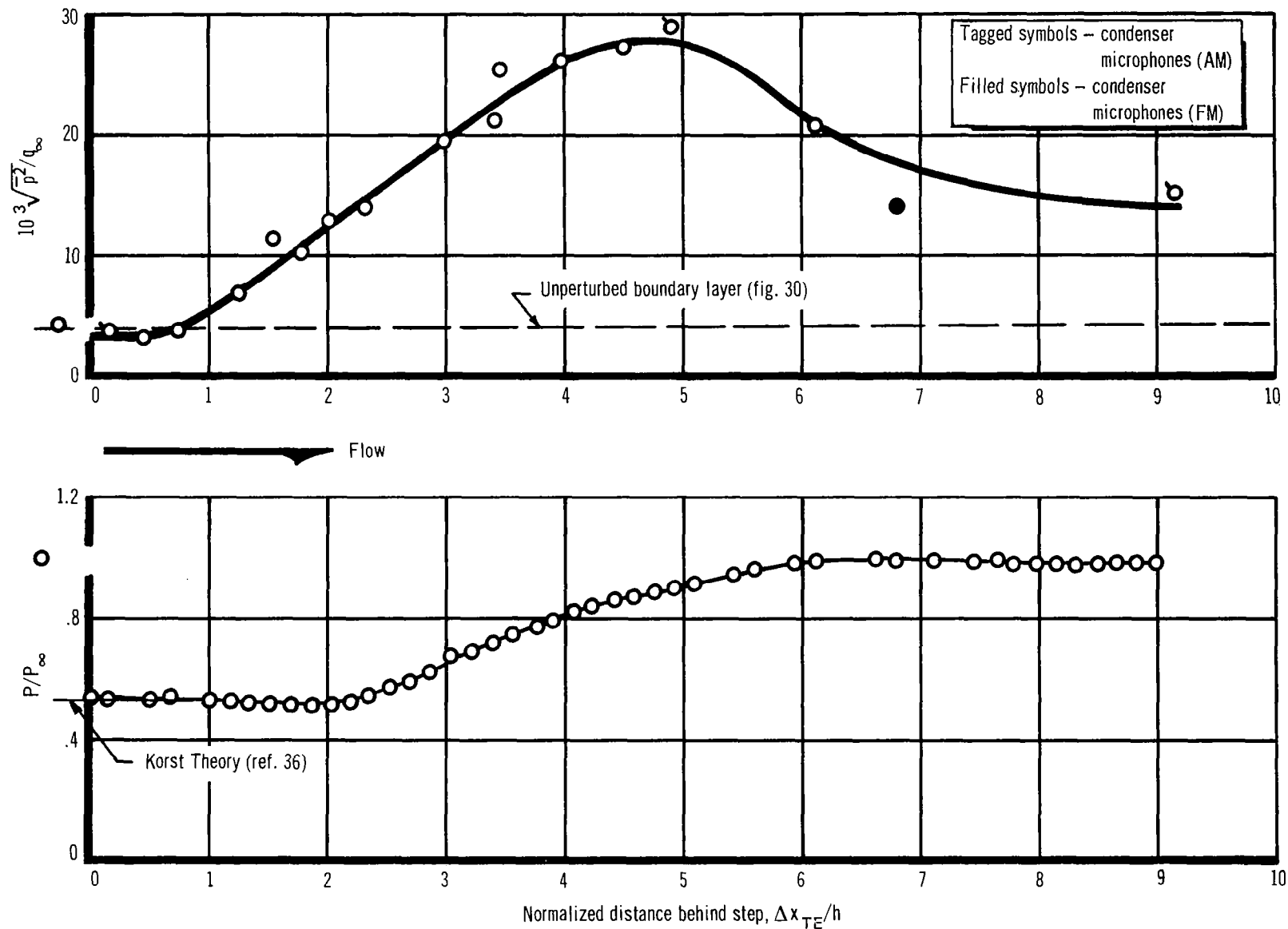
Figure 45. Static and Fluctuating Pressure Distributions Behind an Aft-Facing Step, $M_\infty = 1.41$, $\theta/h \approx .040$
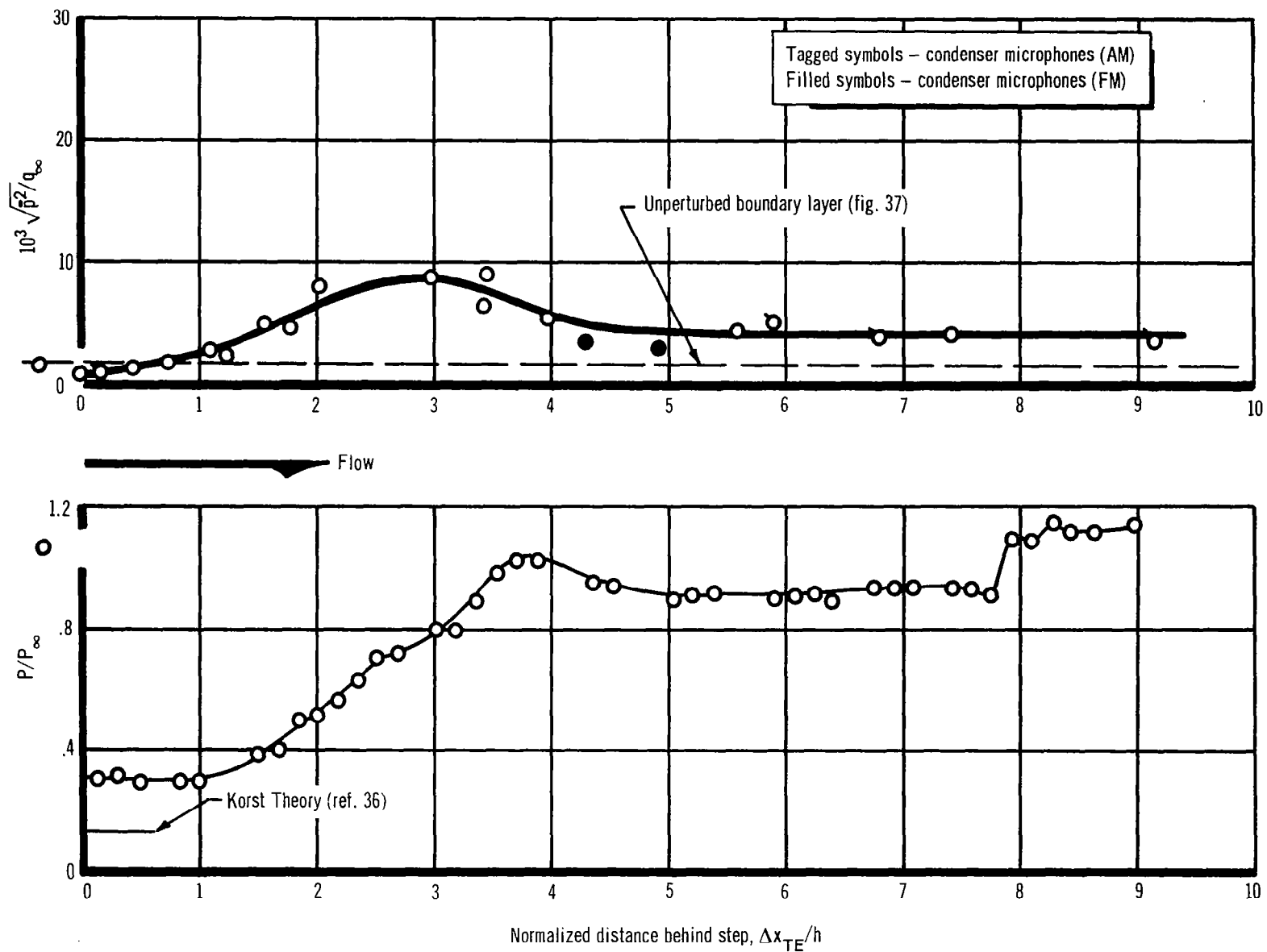
Figure 46. Static and Fluctuating Pressure Distribution Behind an Aft-Facing Step, $M_\infty = 3.48$, $\theta/h = .066$
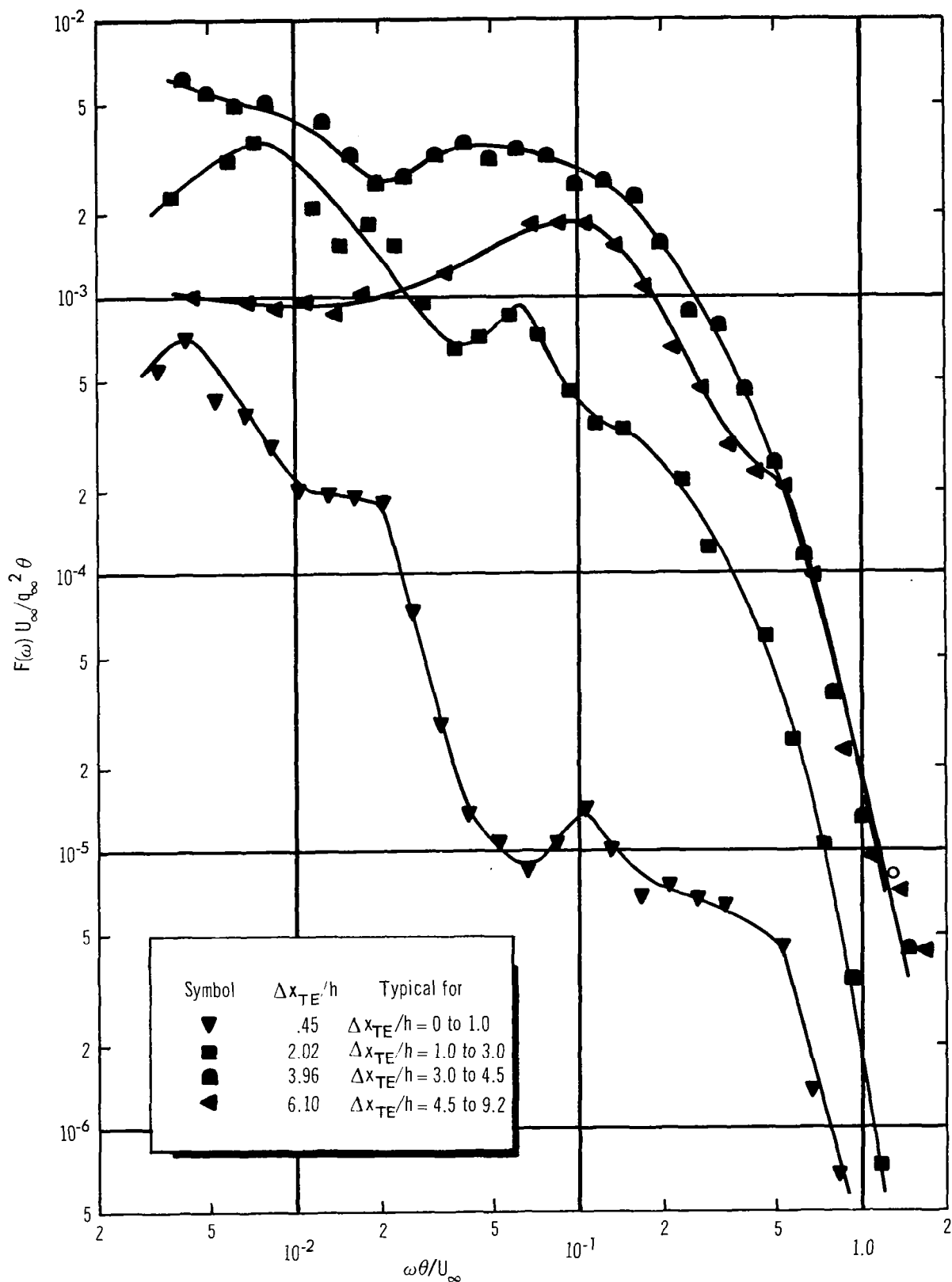
Figure 47. Typical Power Spectra in the Vicinity of an Aft-Facing Step, $M_\infty = 1.41$, $\theta/h = .040$
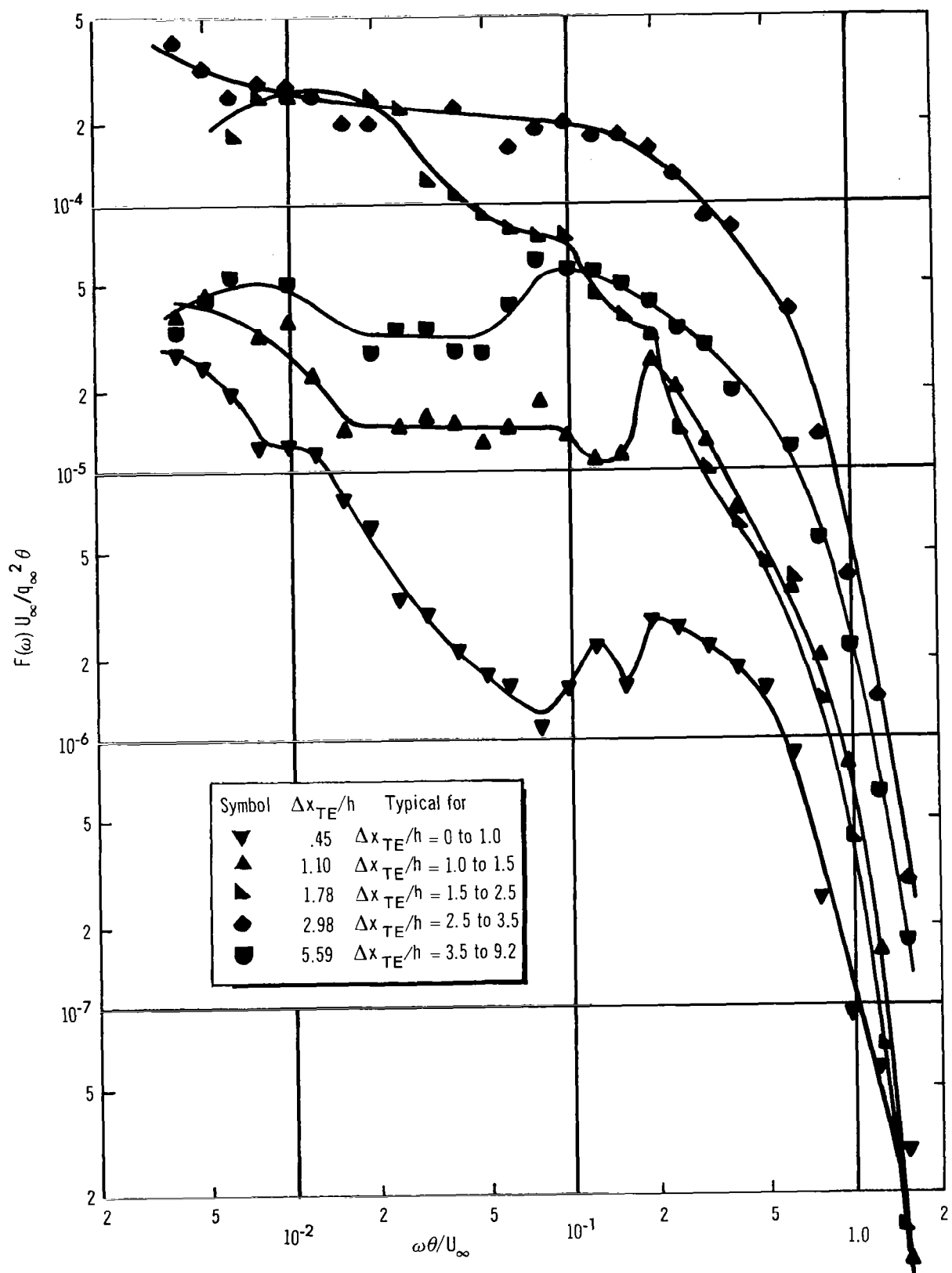
Figure 48. Typical Power Spectra in the Vicinity of an Aft-Facing Step, $M_\infty = 3.48$, $\theta/h = .066$

shown in these figures since, except for level, they typify regions of flow behind the step.[*] At M = 1.41, the rapidly falling spectrum near the bottom of fig. 47 is typical of $0 < \Delta x_{TE}/h < 1.0$. The next highest spectrum, for $1.0 < \Delta x_{TE}/h < 3.0$, shows that energy is gained at all frequencies, but more in the range of $0.04 < \omega\theta/U_\infty < 0.4$. Between $3.0 < \Delta x_{TE}/h < 4.5$, little energy is gained in the lower frequencies, but the main contribution to the overall level comes from $0.02 < \omega\theta/U_\infty < 0.2$. Beyond reattachment (downstream of $\Delta x_{TE}/h = 4.5$) there is a decrease in energy in the lower frequencies and the curves actually show a hump at Strouhal number $\omega\theta/U_\infty = 0.1$.

The trends at M = 3.48 are similar but less pronounced, possibly due to Mach number effects (or possibly to a smaller ratio of step-height to boundary-layer thickness). The lowest curve in fig. 48 does not fall off as rapidly as at M = 1.41, and it is characterized by a double hump in the spectrum between $0.1 < \omega\theta/U_\infty < 0.2$. (The double hump was not seen at M = 1.41.) This spectrum is typical of the entire base region at M = 3.45 ($0 < \Delta x_{TE}/h < 1.0$). Between $1.0 < \Delta x_{TE}/h < 1.5$, the double hump gives way to a single sharp peak at $\omega\theta/U_\infty = 0.2$ and considerable energy is gained in the range $0.02 < \omega\theta/U_\infty < 0.5$. In the region of reattachment ($2.5 < \Delta x_{TE}/h < 3.5$), the spectrum is nearly flat to $\omega\theta/U_\infty = 0.2$. Beyond reattachment ($3.5 < \Delta x_{TE}/h \leq 9.2$), the spectral shapes are similar to those at M = 1.41, exhibiting a hump at $\omega\theta/U_\infty = 0.1$.

Although there are some dissimilarities in the spectral data between the two Mach numbers, the trends can be generalized as follows:

(1) A rapidly falling spectrum in the base region with an overall level comparable to clear tunnel levels

(2) A large amplitude gain in the middle frequency range just downstream of the base region

(3) An additional gain in amplitude in the low and middle frequencies up to the reattachment point

(4) A decrease in the energy at low frequencies beyond reattachment, resulting in a typically humped spectrum

---

[*] In section 3.7.2, it was noted that 44 frequency bands were calculated for the frequency range 46 to 140 000 cps. In addition, some data were available from the space-time correlation work that had 400 bands in the frequency range $160 < f < 16\,000$ cps. These data were used to fair the power-spectra curves for 3/4-in. forward- and aft-facing steps and the 7.5° shock wave.

Space-time cross-correlations were calculated for the aft-facing step for both of the Mach numbers discussed in the spectral results. At M = 1.41, the composite FPL's maximized 8.5 dB above the levels of M = 3.48. The FPL's and static pressure distributions, plotted versus spatial distance from the step face in the direction of the flow, showed a shortening of the separated flow region with increasing Mach number for the different θ/h ratios used. The spatial correlation coefficients found within the separated regions of flow seem to bear out this trend, since the correlation coefficient is compressed in space for the higher Mach number. Figs. 49 and 50 show the approximate contours of equal correlation coefficients for M = 1.41 and M = 3.48 within the separated regions of flow, and near to the step face.

Time decay functions of the maxima were found to fit the following expressions

for M = 1.41 $\qquad R_{max}(\tau) = R(0, 0, 0) \cdot \dfrac{1}{1 + 1.1 \times 10^5 \tau}$ $\qquad\qquad$ (9)

for M = 3.48 $\qquad R_{max}(\tau) = R(0, 0, 0) \cdot \dfrac{1}{1 + 6.3 \times 10^4 \tau}$. $\qquad\qquad$ (10)

Since the composite levels vary with distance behind the step face, an attempt was made to differentiate between regions of the flow as to their space-time correlation characteristics. It was found that the temporal portion remained essentially the same throughout the flow. However, various differences were apparent in the spatial part. For example, fig. 51 shows the x-direction correlation coefficient for two regions of the flow at M = 3.48. The two curves differ considerably. The same sort of variation was observed at M = 1.41, except that the two types of curves were reversed for comparable locations in the flow. The pronounced low-frequency cross-spectral content was not so apparent immediately behind the step face at M = 3.48, which would tend to produce a smaller area over which the pressures were correlated. However, the reappearance of a narrow-band or predominantly low-frequency type of correlation coefficient further downstream seems inexplicable. The spectral differences presented earlier indicate this same variation. Narrow-band correlation data might be helpful in resolving this anomaly. Fig. 52 is given to show how the contours of equal correlation coefficient would look in the region of reattachment if the lateral direction coefficient is assumed invariant in space.

A general schematic of the spatial correlation characteristics of the fluctuating pressures behind the aft-facing steps dealt with in this study can be extracted from the measured data. Such a conceptual schematic is presented below where the maximum FPL's occurred approximately 0.14 h/θ behind the step face for both Mach numbers.
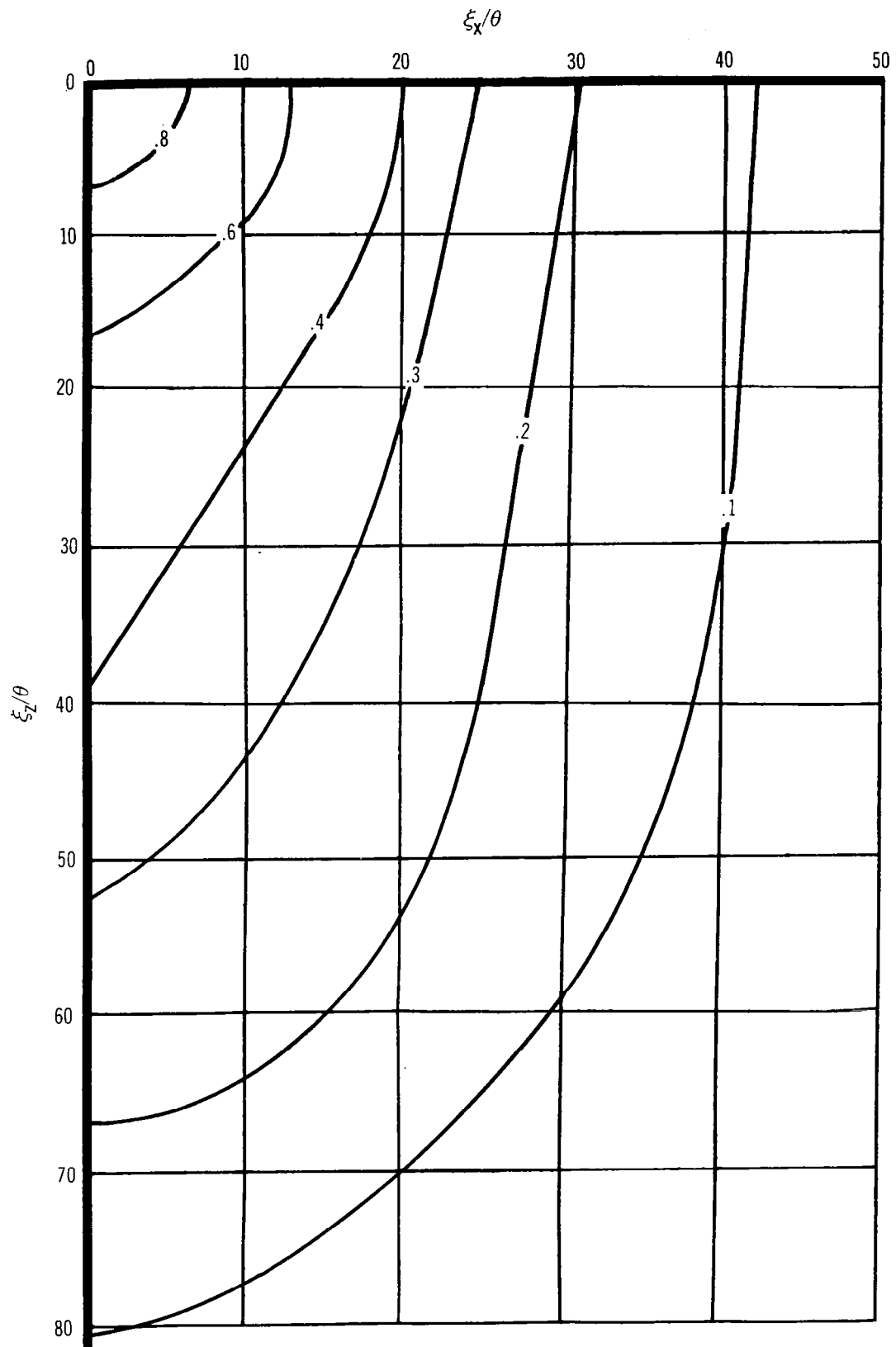
Figure 49. Approximate Contours of Equal Correlation Coefficient for an Aft-Facing Step, Near Step Face, M = 1.41, θ/h = .040
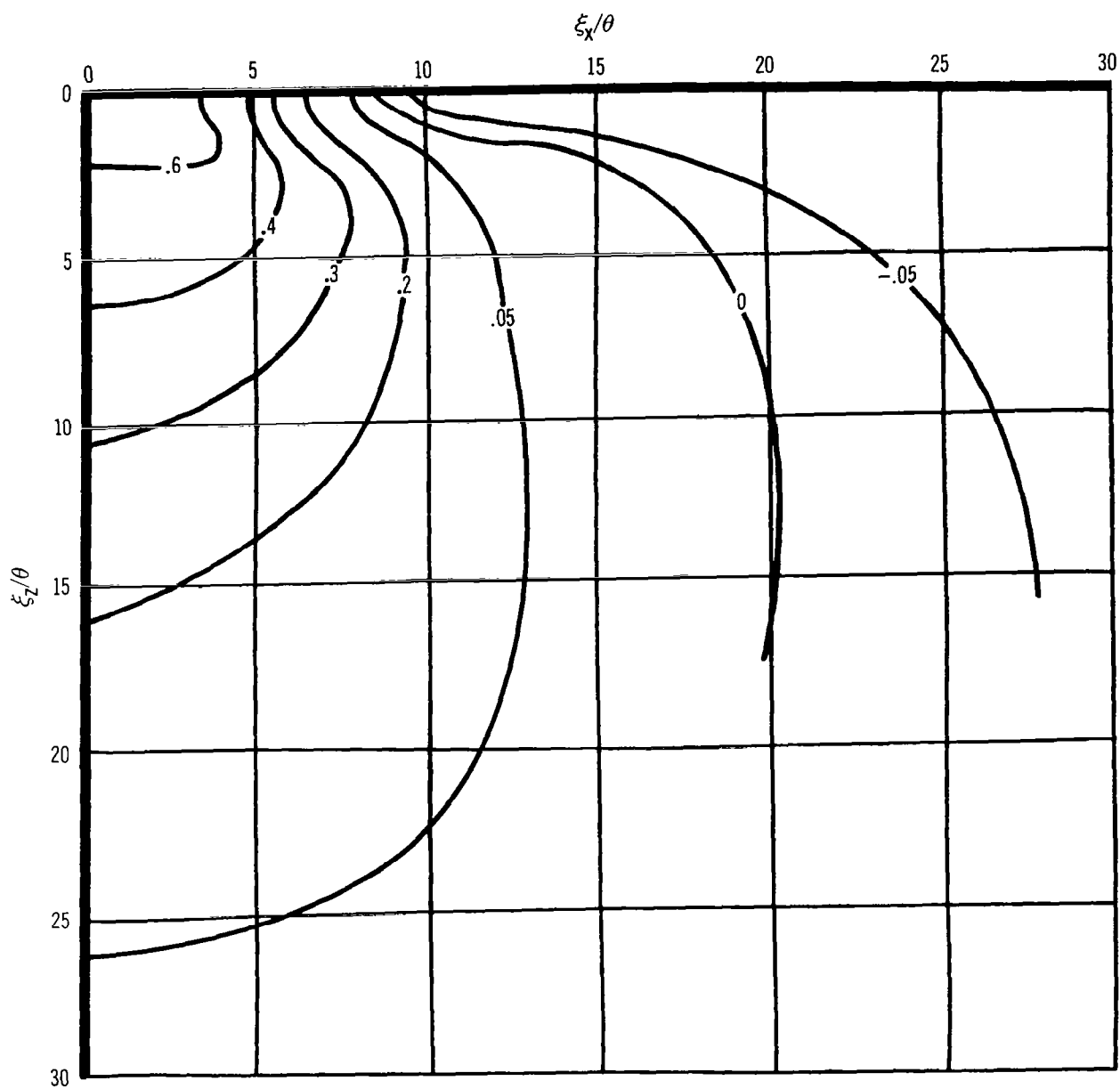
Figure 50. Approximate Contours of Equal Correlation Coefficient for an Aft-Facing Step, Near Step Face, M = 3.48, θ/h = .066
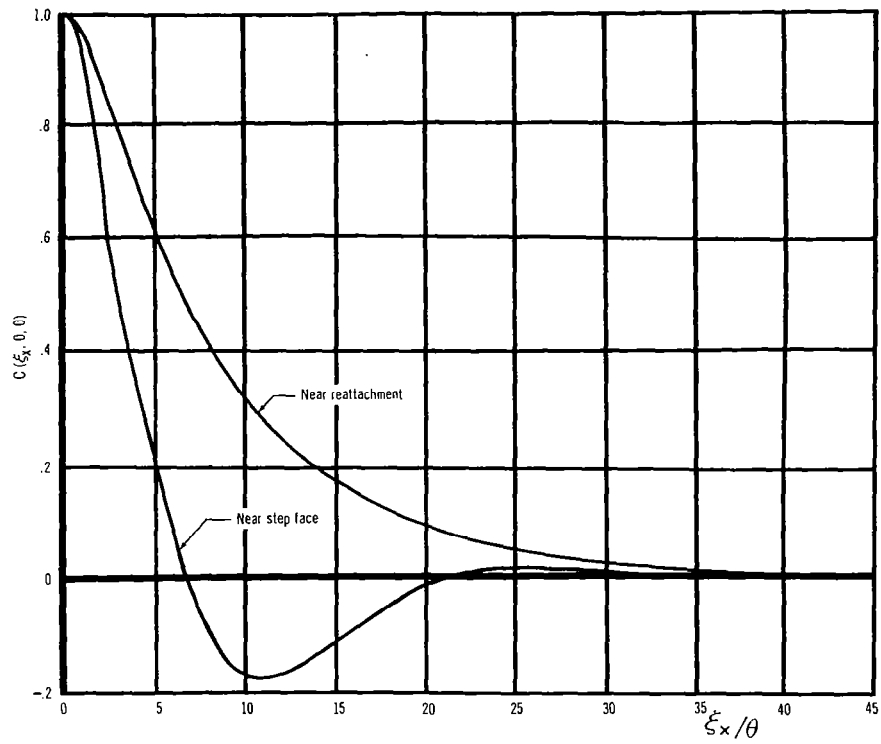
Figure 51. Longitudinal Correlation Coefficients Behind an Aft-Facing Step, M = 3.48, θ/h = .066
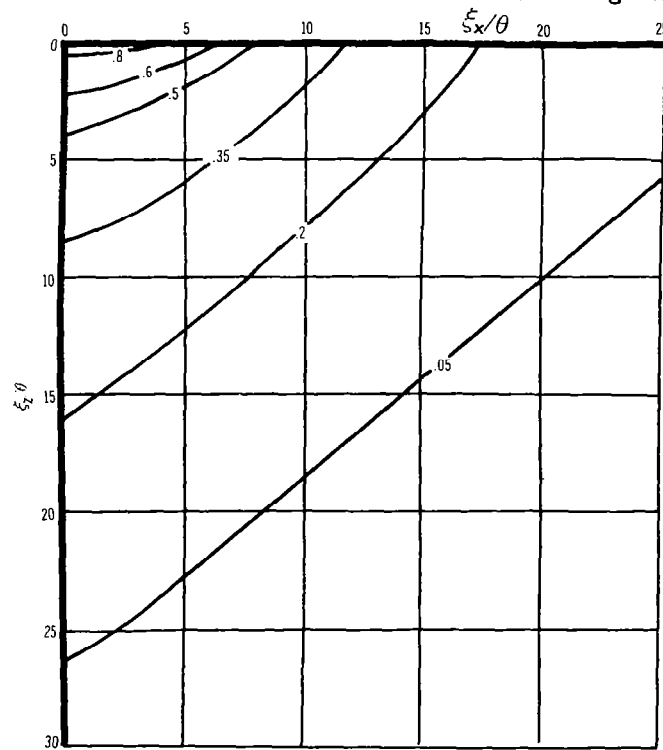
Figure 52. Approximate Contours of Equal Correlation Coefficient for an Aft Facing Step, Near Reattachment, M = 3.48, θ/h = .066
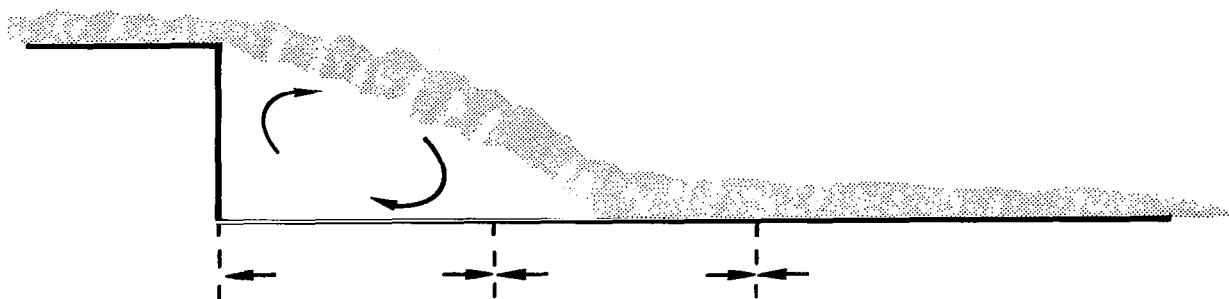
(1) Two step-heights	(1) 0.5 to 1.0 step-heights	(1) Rapidly loses spatial correlation with the high level FPL's and indicates a phase reversal of the pressure signature
(2) Good spatial correlation	(2) Increasingly poor spatial correlation	
(3) Increasing FPL's	(3) High FPL's	(2) Decreasing FPL's

At each Mach number, high convection velocities, comparable in magnitude to free-stream velocities, were noted in a direction perpendicular to the flow. The direction was from the ceiling towards the centerline, but insufficient data exist to determine whether its direction was continuous along the whole step or whether a true mirror image of the quadrant can be assumed. This prompted an investigation to find the origin of this velocity. As noted in the following discussion, only the pressure signature from the turbulent boundary layer was found to be an acceptable source. (Fig. 53 shows the data for M = 3.48 from which these lateral convection velocities were calculated.) Vibration levels of the structure were so low as to preclude any influence on the results. The trace velocity of a sound wave traveling at some angle other than along the line of measurement can have a magnitude from $c \leq U \leq \infty$, where c is the velocity of sound at the temperature and density of the measurement. It was suggested, therefore, that perhaps a sound-generating mechanism was producing a wave that traveled in a preferential direction to trace a velocity on the $\beta = 90^{\circ}$ line, equal to the velocity calculated from the correlation results. Assuming this to be the case, preferential directions of 43° and 73° were calculated for M = 1.41 and M = 3.48, respectively. These are nearly the angles of the bulges in the equal correlation coefficient contours on figs. 49 and 50. Three considerations seem to disprove the proposition that the lateral convection velocity is caused by an acoustic wave. First, there does not seem to be a physical phenomenon associated with the flow that is capable of producing such a high energy acoustic wave. Second, the cross-spectra (and coherency function) do not indicate a band of frequencies that are consistently correlated in the two-dimensional space. This negates the possibility of the problem being caused by resonances of the enclosed volume. (The forward-facing step, which also has an enclosed volume, did not demonstrate lateral velocities.) Third, if such a wave were being produced, the correlation coefficient contours should exhibit "bulges" in a direction perpendicular to the direction of propagation (preferred direction) of the waves. This is not supported by the M 3.48 case.

For these reasons, it would appear that the calculated high convection velocities, in a direction perpendicular to the main boundary-layer flow, and
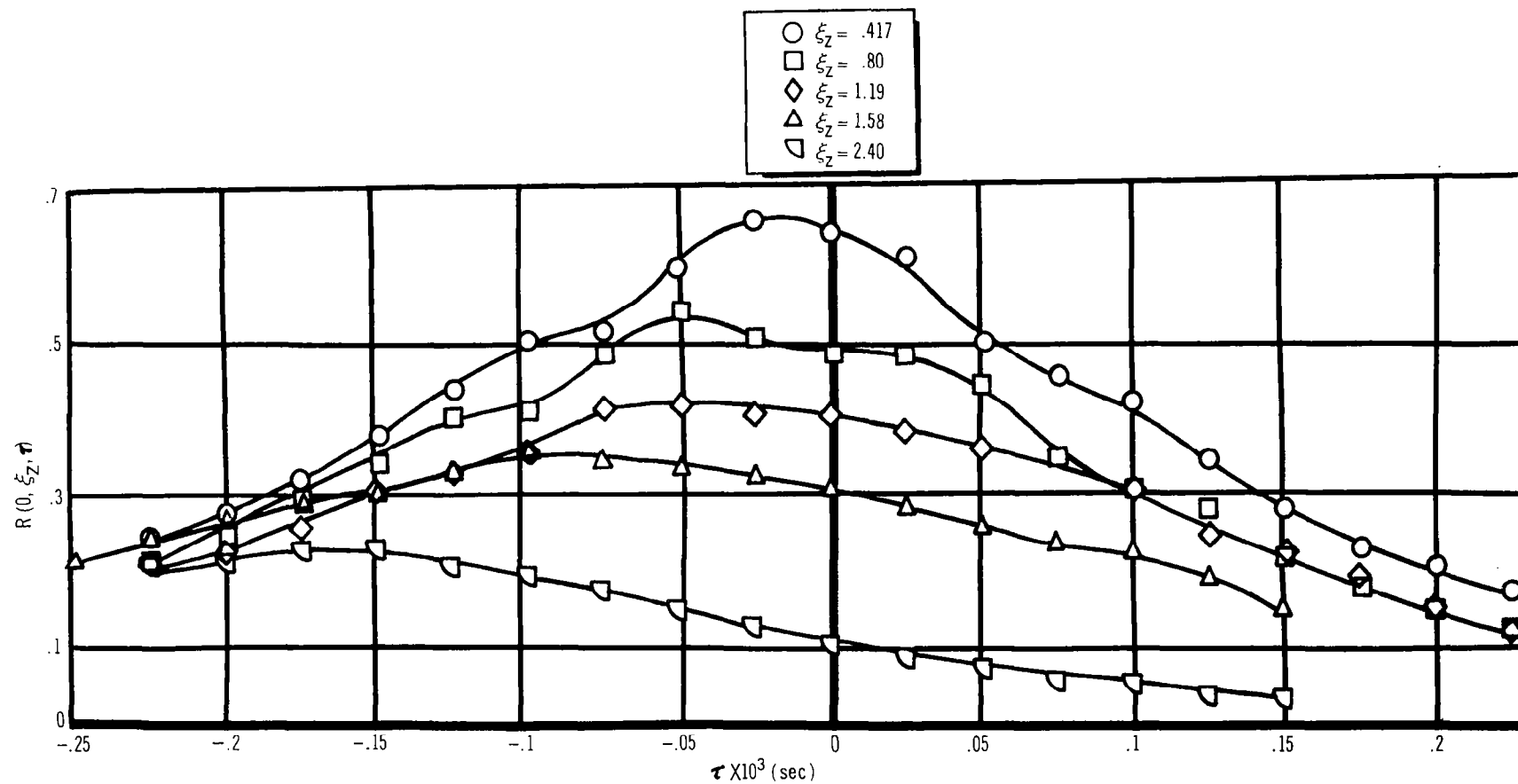
Figure 53. Space-Time Cross-Correlations in the Lateral Direction for an Aft-Facing Step,
Near Step Face, $M_\infty = 1.41$

in the separated region behind an aft-facing step, are caused by some phenomenon associated with turbulence in the flow. Roshko and Thomke (ref. 7) present an oil-flow photograph of the region behind an aft-facing step on an axisymmetric model showing evidence of circulating flow in a series of "cells" around the circumference of the model. This flow is assumed to be of low velocity compared to that of the main stream. Investigation is certainly needed of possible correlation of the cellular flow structure shown in ref. 7 with the high lateral convection velocities (calculated from the pressure signature) discussed here. In particular, it should be determined whether the presence of the tunnel floor and ceiling induces a more pronounced circulation of the trapped air on the sidewall.

Uniformity between the two different Mach number runs was observed for the convection velocity in the direction of the flow. Each exhibited the following trends. The correlated pressure signature possessed predominantly high velocity components (essentially equal to free stream) near the step face, but the main contributing components had lower velocities as the distance from the step face was increased, until much lower velocities ($U_c/U_\infty \approx 0.6$) were indicated for the pressure signature in the disturbed region of reattachment. This would suggest that the high velocity components contribute to the pressure signature near the step face, but are lost rapidly in the phenomenon of reattachment with only the low velocity components remaining recognizable downstream. The direction of the convection velocity indicates that the pressure signature originates in the separated turbulent boundary layer and operates on the trapped air to produce the pressures at the wall. The reverse flow at the wall might contribute a small amount to the apparent decrease in U_c, but for obvious reasons, this effect must be small.

4.5 Step-Spoilers in Supersonic Flow

Step-spoilers that range in nominal height from 1/4 to 1-1/2 in. were tested during the investigation. The widths of the steps were constant (1.3 in.) for all cases to simplify the instrumentation and test setup. In retrospect, it appears that it would have been desirable to have maintained a constant height-to-width ratio. In general, the discussion that follows will be pertinent to forward-facing steps although some comments will be made on the measurements behind the step-spoilers.

Only one step configuration was tested at M = 1.40. The data for the 3/8-in. step are shown in fig. 54. The overall levels of $\sqrt{\bar{p}^2}/q_\infty$ reach a maximum of 28×10^{-3} immediately ahead of the step that is almost equal to the maximum level downstream of the step. Faired curves of data from the 3/4-in. aft-facing step are also shown in fig. 54. Agreement for both static and fluctuating pressures is good.

Fig. 55 shows the static and fluctuating pressure data for a 1.4-in. step-spoiler at M = 3.45. It will be noted that a large increase in fluctuating pressure level occurred just upstream of the static pressure increase. *

---

* Since the static and fluctuating pressure measurements were taken at two different times on different sidewall inserts, the possibility exists of a small discrepancy in alignment. This could account for the apparent fluctuating pressure level increase upstream of any detectable static pressure increase.

Figure 54. Static and Fluctuating Pressure Distributions for a 3/8-in. Step-Spoiler, $M_\infty = 1.40$, $\theta/h = .078$

Figure 55. Static and Fluctuating Pressure Distributions for a 1/4-in. Step-Spoiler, $M_\infty = 3.45$, $\theta/h = .195$

A maximum of $\sqrt{\overline{p^2}}/q_\infty = 17.5 \times 10^{-3}$ was recorded well ahead of the step ($\Delta x_{LE} = 0.8h$), which was only slightly higher than the levels on top of the step, 0.8h downstream of the step face. Behind the step, agreement with the data from the 3/4-in. aft-facing step was fairly good.

Data for a 3/8-in. step-spoiler at M = 3.45 are presented in fig. 56. The rms levels are generally higher at all locations before the step except at $\Delta x_{LE}/h = 0.6$. The level on top of the step is about 18×10^{-3} at $\Delta x_{LE} = -0.5h$. Downstream of the step, agreement with data from a 3/4-in. aft-facing step is poor.

Fig. 57 shows the static and fluctuating pressure distributions for a 3/4-in. step-spoiler at M = 3.45. Since space-time correlations were to be performed over the plane of the sidewall, a great deal more data were available. It may be seen from the data that three peaks are present in the fluctuating pressure distribution. The first (and lowest) peak coincides with the beginning of the steepest pressure rise. A dip in the overall level occurs when the static pressures level off (beyond separation) followed by a broad peak that has a level about 25% higher than the first. About two step-heights from the step face, another dip in level takes place, followed by the final maximum at the step face. This level is about $\sqrt{\overline{p^2}}/q_\infty = 31.5 \times 10^{-3}$. On top of the step immediately downstream of the step face, the level falls below 20×10^{-3}, nearly the same as for the two smaller steps. Downstream of the step, the static pressure data indicate that an unusual condition exists, much as for the 3/8-in. step. It has been postulated that interference waves between the shock wave emanating from the separation region upstream of the step and the expansion fan at the leading edge of the step may have been propagated into the base region. Since this is a special case that can only exist for a limited range of step height-to-width ratios, the data downstream of the 3/8-in. and 3/4-in. steps will not be considered further. It is obvious, however, that this condition is present in many practical three-dimensional configurations of interest to the vehicle designer.

The largest step-spoiler tested was nominally 1-1/2 in. high. Data from this configuration are given in fig. 58. Insufficient data were taken to allow accurate fairing of a curve, but it can be seen that the trends are similar to fig. 57, i. e., higher values at $\Delta x_{LE}/h = 3.5$ than at $\Delta x_{LE}/h = 6.0$, and still higher values at the step face. The rms level on top of the step again drops to a value of $\sqrt{\overline{p^2}}/q_\infty$ near 20×10^{-3}. This configuration, which is about twice the boundary-layer thickness, produces the highest overall levels, as expected. It is apparent that testing of even larger steps is needed to confirm the continued increase in level with step height.

Downstream of the 1-1/2 in. step-spoiler, the static pressures show that a base condition once again exists, although in a foreshortened region. The fluctuating pressures show an immediate level increase, probably because the flow has had little chance to stabilize while passing over the spoiler.
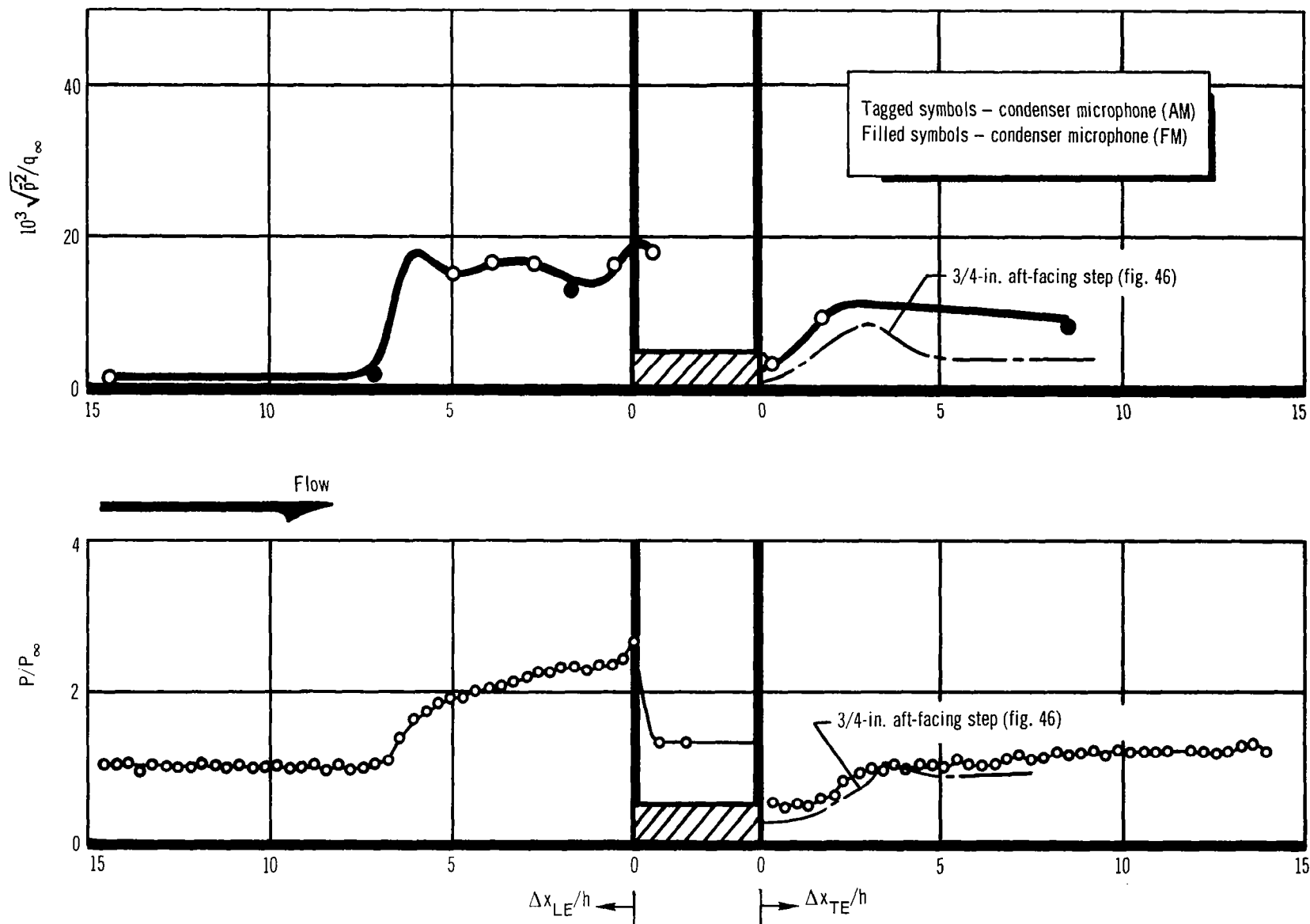
Figure 56. Static and Fluctuating Pressure Distributions for a 3/8-in. Step-Spoiler, $M_\infty = 3.45$, $\theta/h = .132$
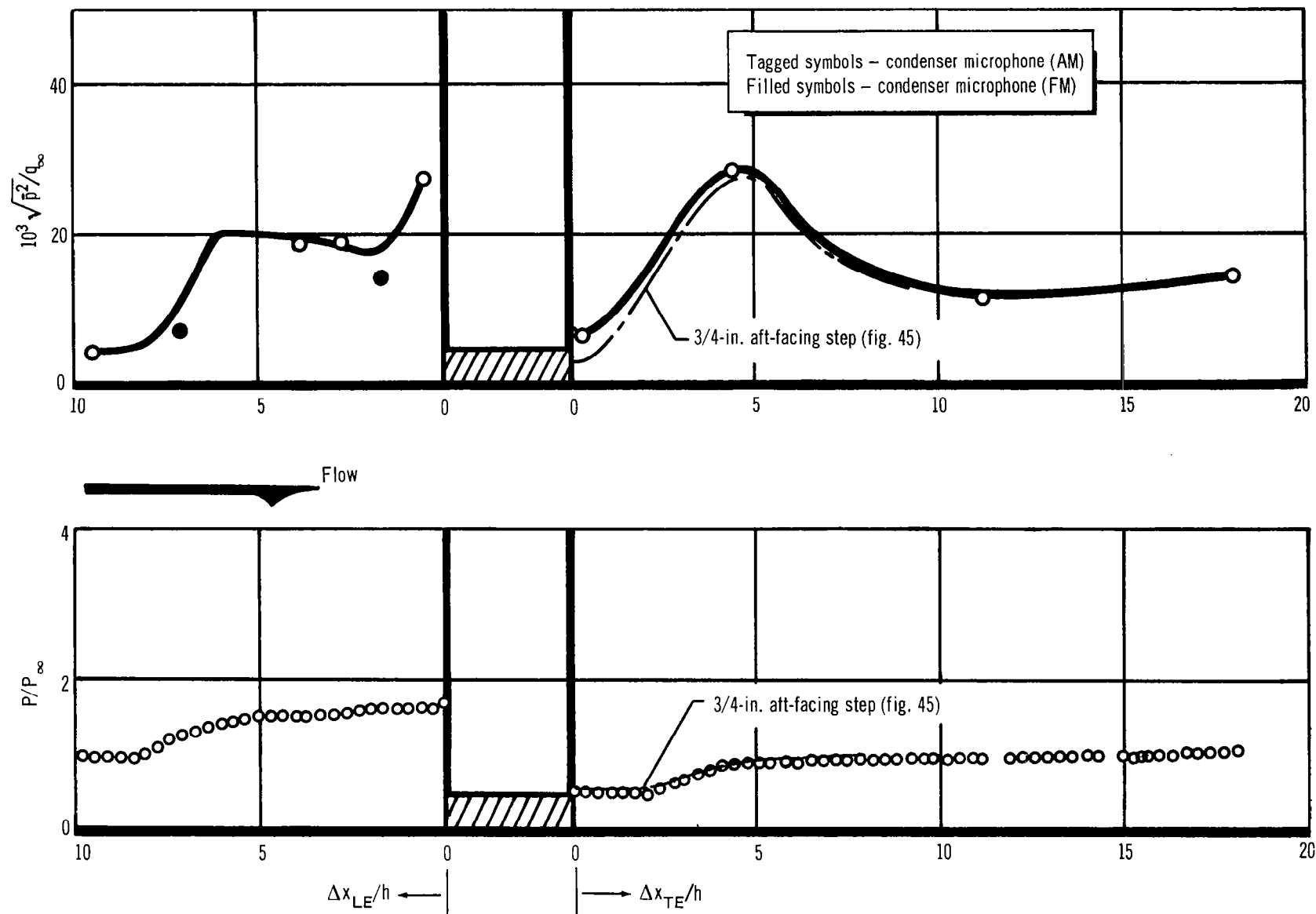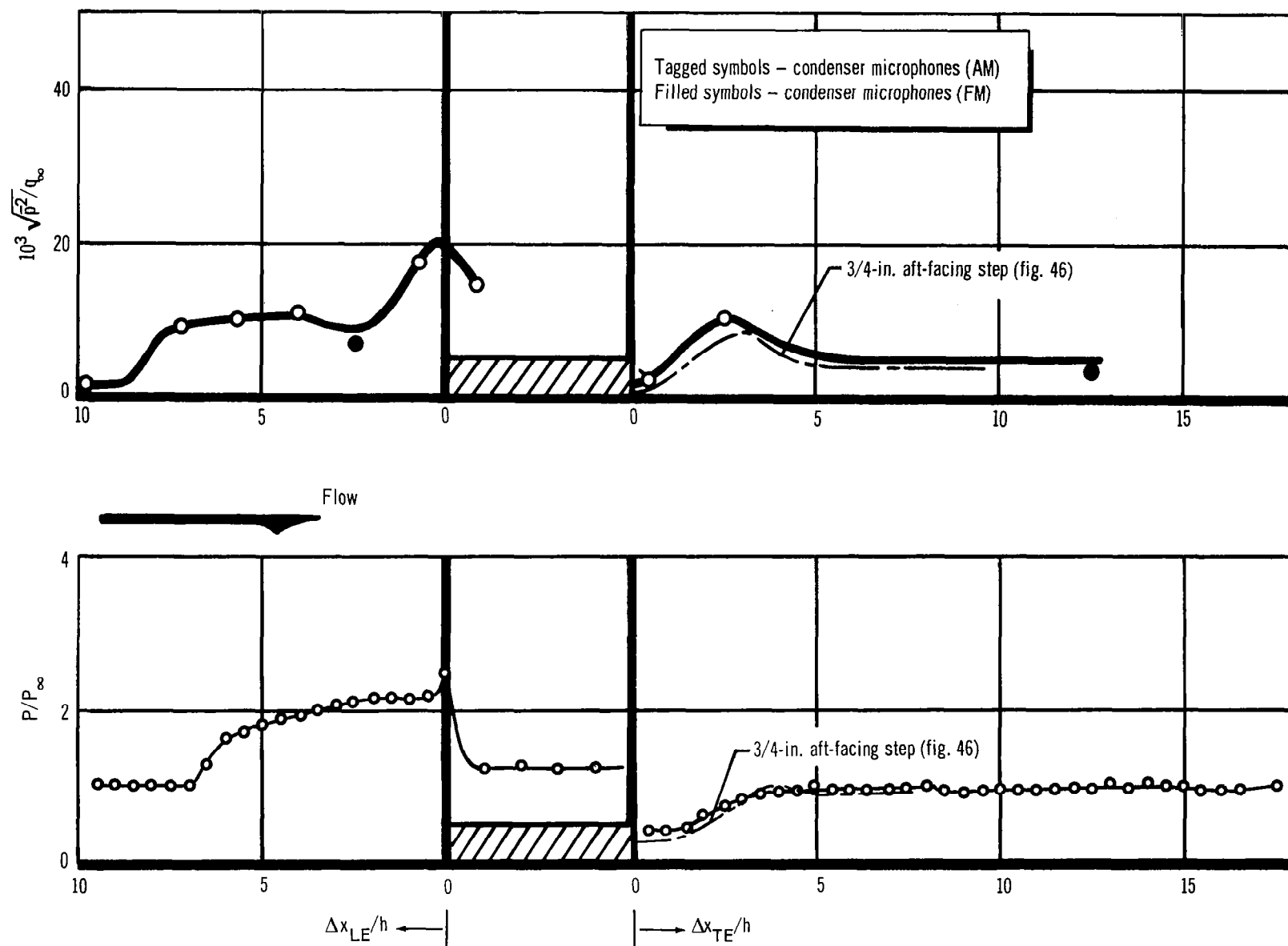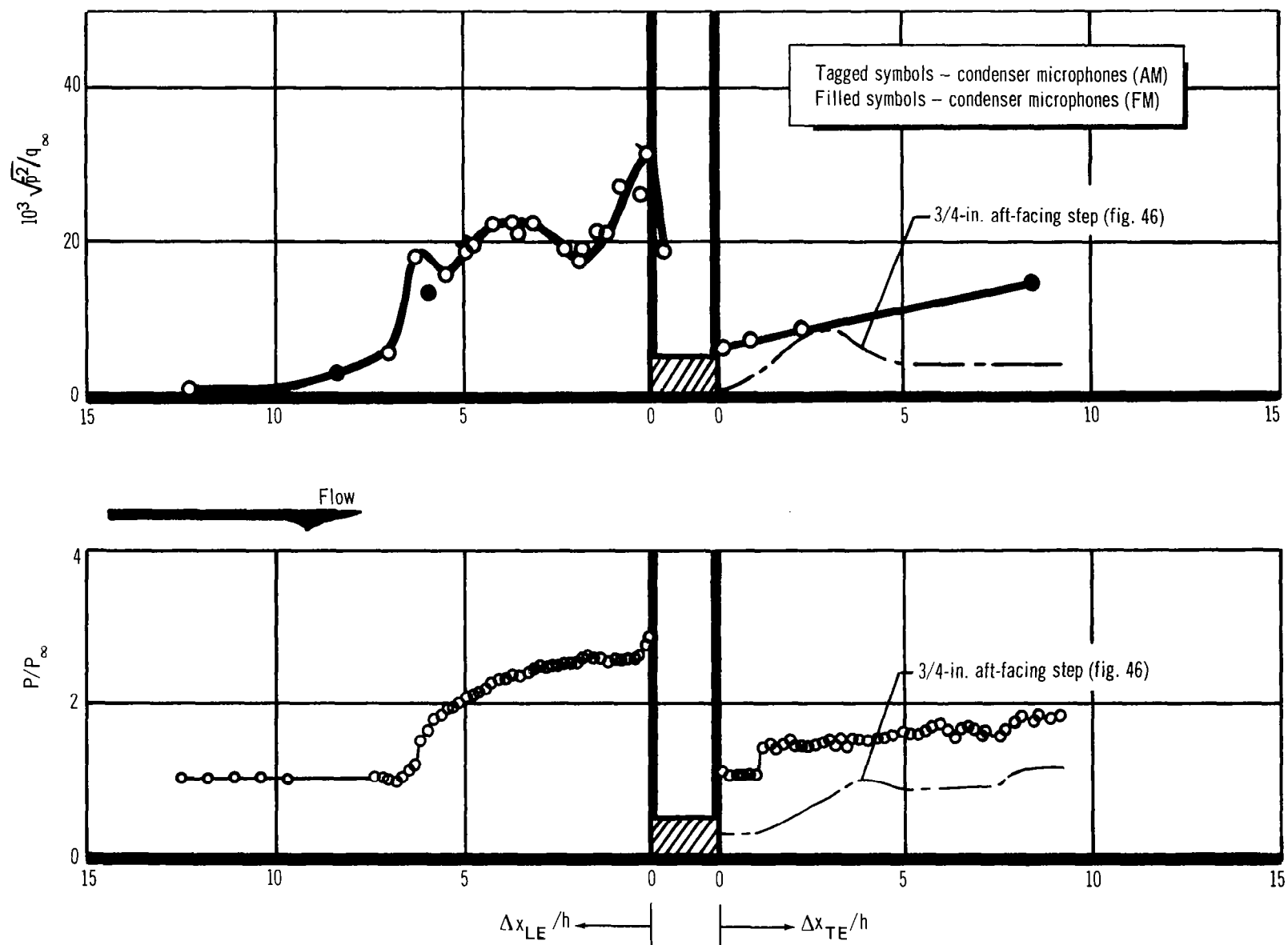
Figure 57. Static and Fluctuating Pressure Distributions for a 3/4-in. Step-Spoiler, $M_\infty = 3.45$, $\theta/h = .067$
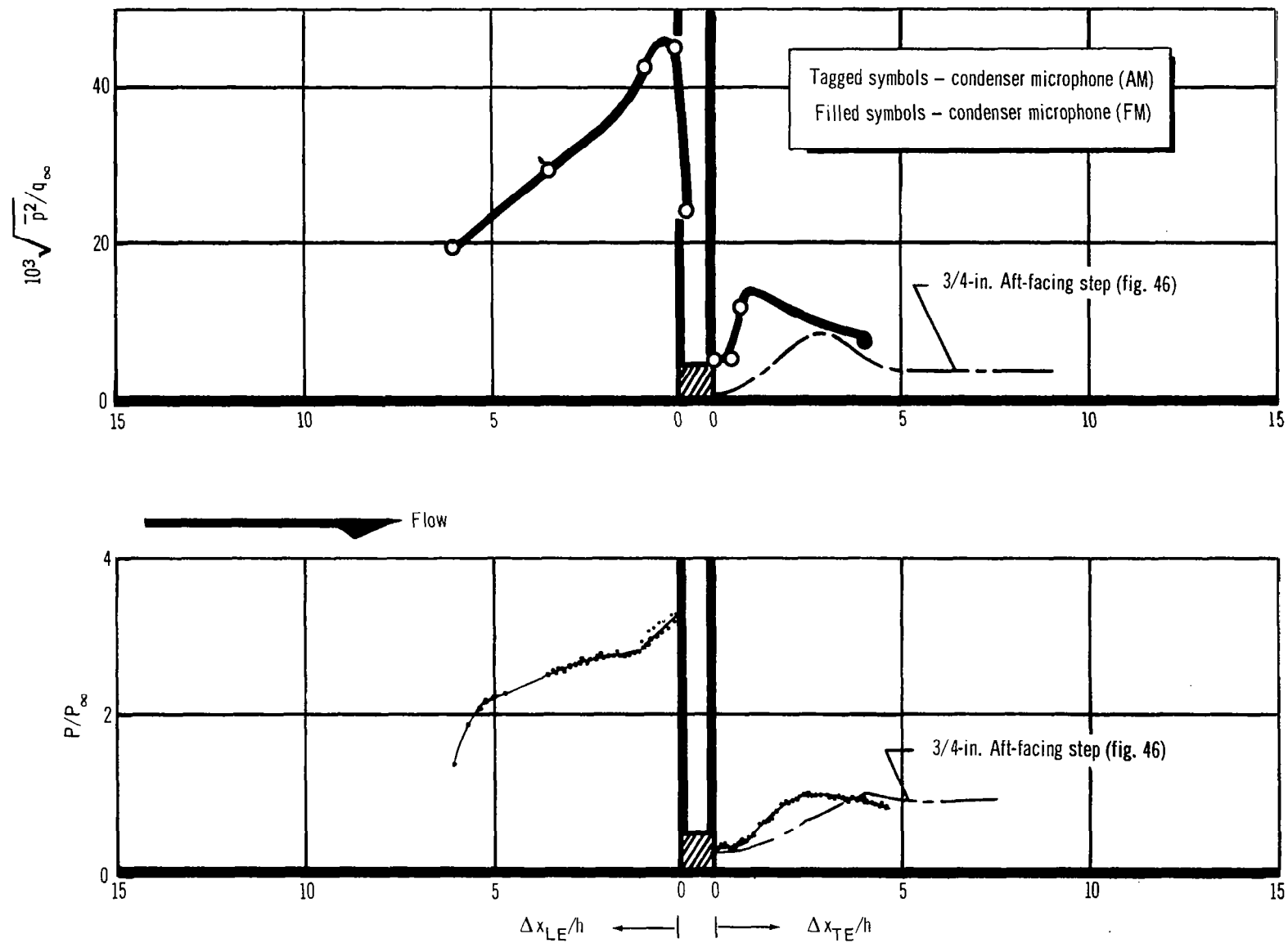
Figure 58. Static and Fluctuating Pressure Distributions for a 1-1/2-In. Step-Spoiler, $M_\infty = 3.45$, $\theta/h = .032$

Forward-facing step data at the two Mach numbers may be compared by looking at the same step-heights or by comparing similar boundary-layer thickness-to-step-height ratios. In the former case, the overall levels ahead of the step are nearly the same when values of $\sqrt{\bar{p}^2}/q_\infty$ are compared. For the same step-height, the ratio $(\sqrt{\bar{p}^2}/q_\infty)_{perturbed}$ to $(\sqrt{\bar{p}^2}/q_\infty)_{unperturbed}$ is about 9.0 at M = 3.45 and 4.5 at M = 1.40. If data at similar boundary-layer thickness ratios ($\theta/h \simeq 0.07$) are compared, the overall levels at M = 3.45 are found to be slightly higher than at M = 1.40 and the ratios of perturbed to unperturbed $\sqrt{\bar{p}^2}/q_\infty$ are now about 12.5 at M = 3.45 and 4.5 at M = 1.40.

Spectral shapes for the various step-heights at M = 3.45 are similar in the four regions ahead of the step; therefore, comments on the spectra for the 3/4-in. step (fig. 59) generally apply to all the steps tested. In the range $7.1 < \Delta x_{LE}/h < 6.1$ (the effects extend slightly upstream of 7.1h for the smaller steps), the lowest spectra on fig. 59 apply. The slope is slightly less for the smaller steps, but all show the concentration of energy to be at frequencies below $\omega\theta/U_\infty = 0.01$, with a peak sometimes discernible near 0.005. This agrees with Kistler's observations (ref. 8) that the majority of the energy is contained in the region below 1000 cps ($\omega\theta/U_\infty = 0.012$). The present data did not indicate the "on-off" behavior, and a very sharp low-frequency peak, that Kistler mentioned. Therefore, the data were not filtered below 1000 cps.

As the distance before the step decreased to about 6h, addition of spectral energy in the high frequencies resulted in a peak in the overall level (fig. 57). Between $4.5 > \Delta x_{LE}/h > 3.0$, the spectrum (fig. 59) began to flatten between $\omega\theta/U_\infty = 0.03$ and 0.3. (A secondary double peak was noted around $\omega\theta/U_\infty = 0.2$. The spectra for the smaller steps showed only a single peak.) From $3.0 > \Delta x_{LE}/h > 2.0$ a double-humped spectrum became observable. This became more pronounced in the region from $\Delta x_{LE}/h = 2$ to 0 (uppermost curve on fig. 59). (Note: the magnitude of this double hump increases with increasing step-height.) In the region just upstream of the step, the levels increased fairly uniformly at all frequencies. On top of the step, the spectrum shape was similar to the shape in the low frequencies, but the high-frequency hump had virtually disappeared and the spectrum rolled off sharply.

Spectral shapes for the 3/8-in. step-spoiler at M = 1.40 (not shown) were generally similar to those at M = 3.45. Specific exceptions did exist, but a sufficient amount of data was not taken in order to detail the effects of Mach number.

Some generalizations can be made for forward-facing steps on the basis of the data presented in this section:

(1) The fluctuating pressure levels increase markedly at the beginning of the static pressure rise, at about seven step-heights upstream of the step. The energy at this point is concentrated at the low frequencies.
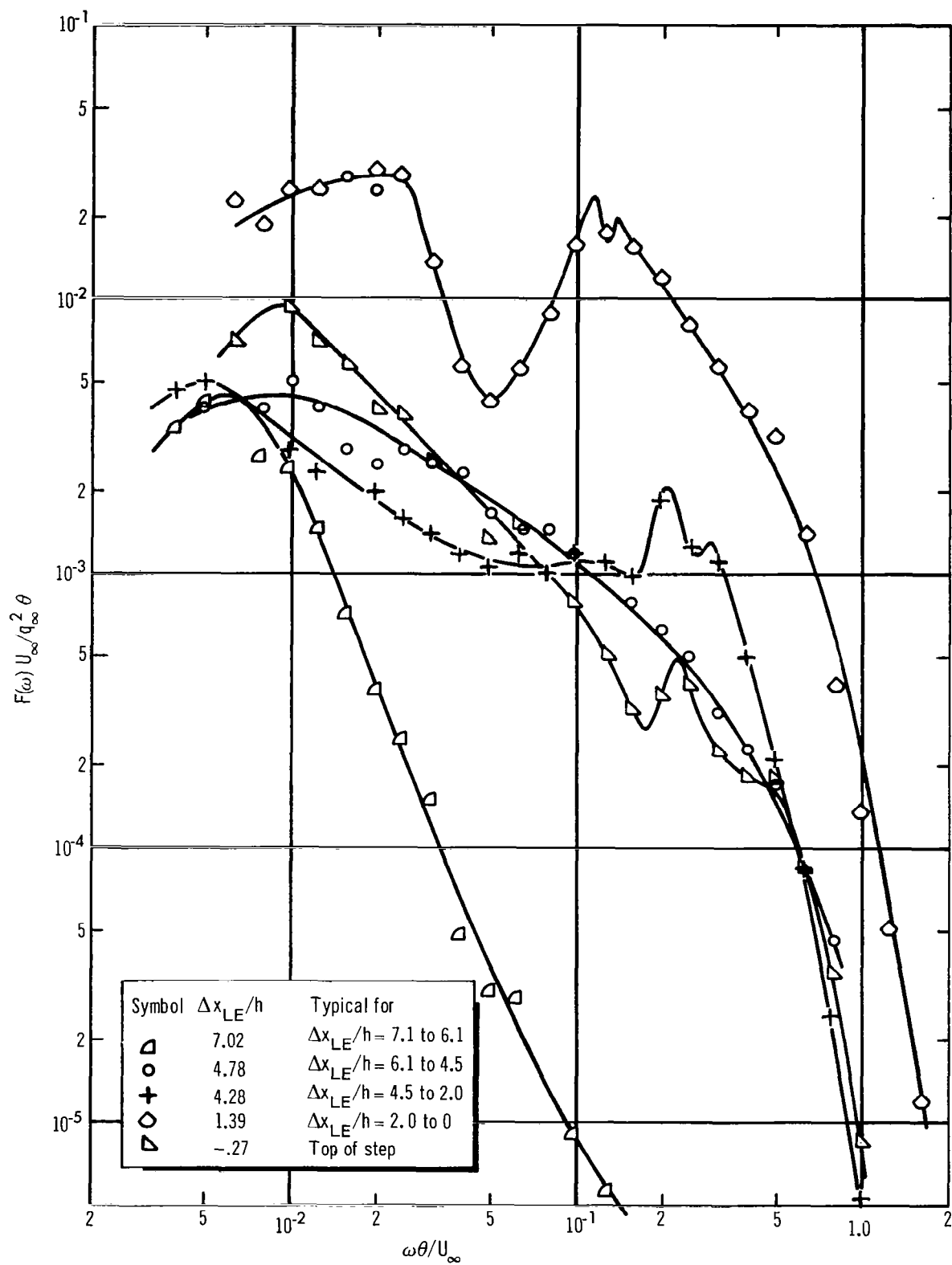
Figure 59. Typical Power Spectra in the Vicinity of a 3/4-in. Forward-Facing Step,
$M_\infty = 3.45$, $\theta/h = .067$

(2) The overall FPL's decrease downstream of separation, then increase again in the region of decreasing static pressure gradient. The spectrum gains more and more energy at the higher frequencies as distance to the step face decreases.

(3) Directly in front of the step, the overall level increases in the region of the steep static pressure gradient. For large steps, the spectra exhibit a pronounced double hump.

(4) FPL's on top of the step (behind the expansion) are lower than those upstream of the step, but are much higher than clear-tunnel levels.

Examination of the data from the 3/4-in. step-spoiler at M = 3.45 permits study of the space-time cross-correlations for a forward-facing step ($\delta/h = 1.1$). As noted in previous studies (refs. 8 and 9), the region of separated flow caused by a forward-facing step is marked by a multihumped spatial distribution of maximum pressures in the direction of the flow (see also fig. 57). The first peak is caused by the separation phenomenon itself, and the other peaks in overall FPL's occur in the region of separation ahead of the step face. The space-time correlation calculations performed here indicated that the pressure signature of the first hump (one suggestive of the predominantly low-frequency content spectra) is rapidly lost--in about three step-heights--and that a new pressure signature, associated with the separated flow, is then in effect until the step face is reached. This second pressure signature does not change its spatial characteristics (correlation coefficient) appreciably throughout the region. Fig. 60 indicates the variation in correlation coefficient associated with the different spatial maxima of FPL's. Fig. 61 shows the minimal variation in correlation coefficient within the region of flow near the step face and associated with the second pressure signature. The placement of transducers for this study did not permit a complete mapping of the correlation coefficient associated with the separation phenomenon (several step-heights away from the step face) as the $\beta > 0°$ field was only comprehensively covered near the step face. Due to the high FPL's associated with the separation phenomenon, it would appear worthwhile to survey this region in a later study.

The present study's coverage must necessarily concentrate on the high FPL's near the step face. Fig. 62 presents the contours of equal correlation coefficient for the pressures found near the step face. The maximum of this spatial distribution was found to decay in time as

$$R_{max} (\xi_x, 0, \tau) \approx R(0, 0, 0) \cdot \frac{1}{1 + 3 \times 10^4 \tau} . \qquad (11)$$

(The above values are shown as approximately equal because a minor variation existed within the separated flow region, and the coefficient of τ in the above expression was not exactly definable for all of the space-time curves.)
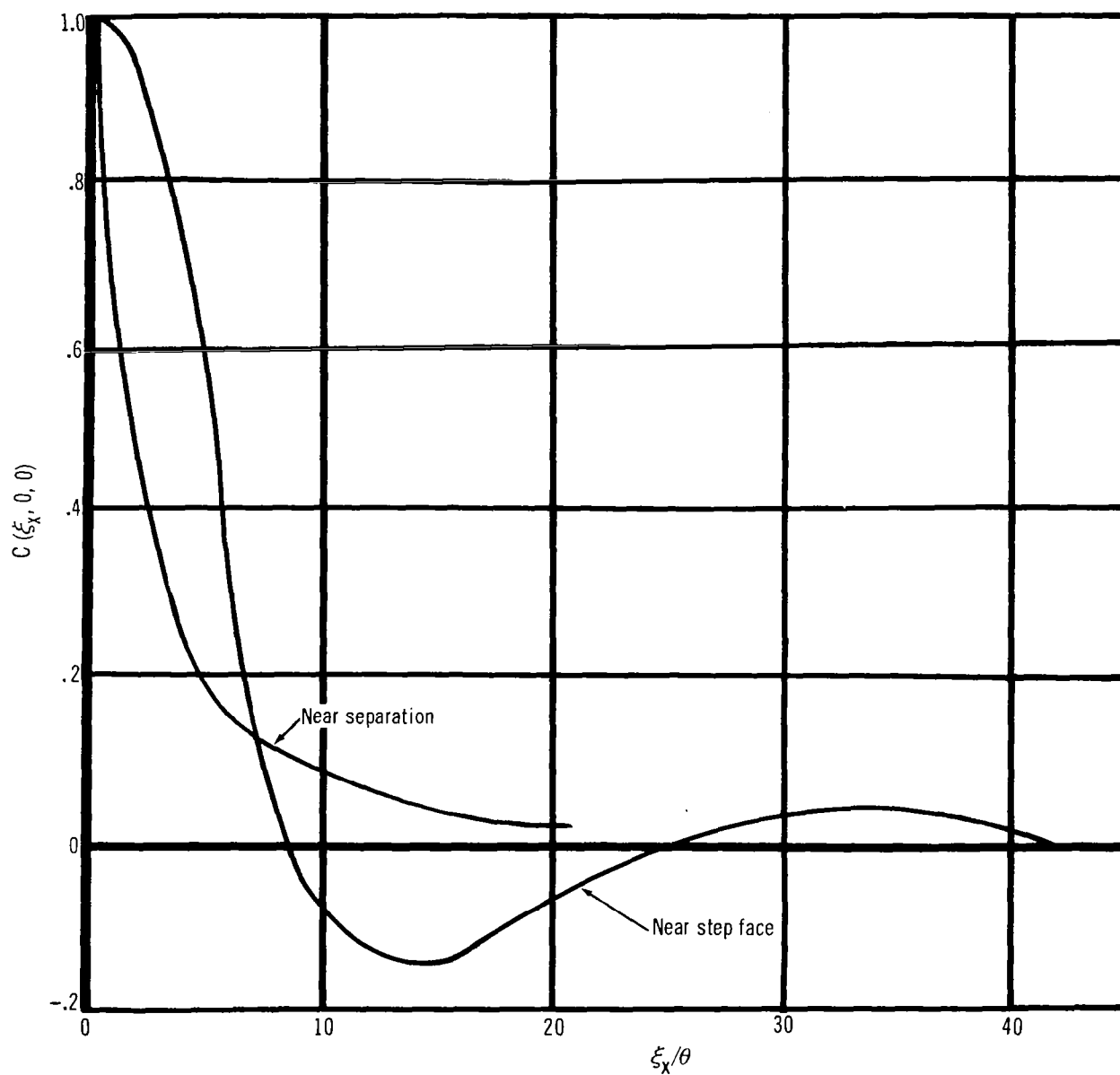
Figure 60. Longitudinal Correlation Coefficients in Front of a Forward-Facing Step, M = 3.45, $\theta/h = .067$
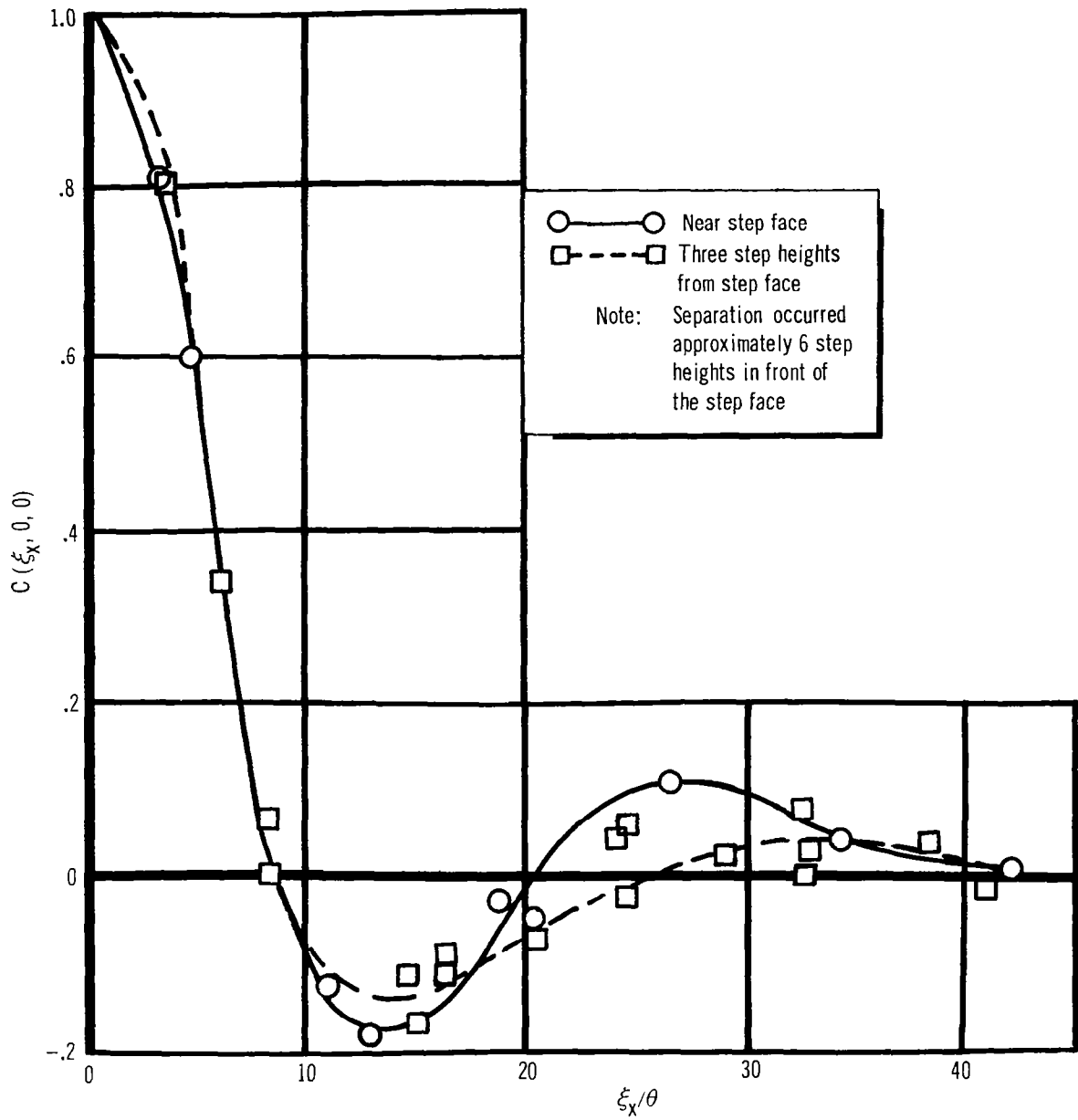
Figure 61. Comparison of Longitudinal Correlation Coefficients for Similar Flow Conditions, Forward Facing Step, M = 3.45, θ/h = .067

90
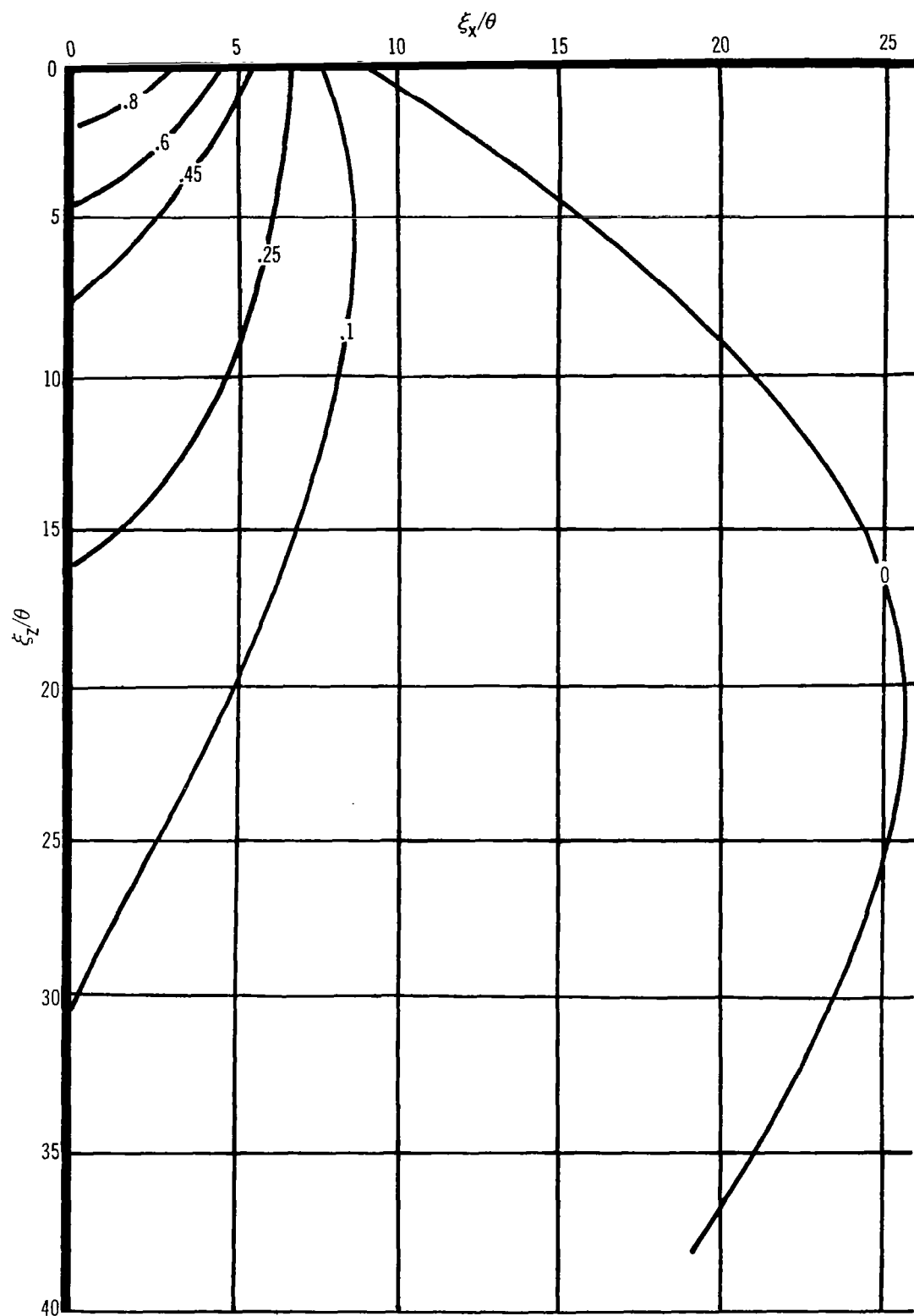
Figure 62. Approximate Contours of Equal Correlation Coefficient for a Forward Facing-Step, Near Step Face, M = 3.45, θ/h = .067

A convection velocity within the separated flow at M = 3.45 was calculated to be 1310 fps as an average (the extremes being 1282 fps and 1390 fps. No lateral convection velocity was observable for this forward-facing step configuration.

4.6 Shock-Perturbed Boundary Layer

One of the perturbed flow cases examined during this investigation was that of a two-dimensional shock wave impinging upon the turbulent boundary layer. A 7.5° shock wave was chosen because the static pressure ratio (3.15) across the shock ensured that the boundary layer would experience separation. It was also chosen because it had shown large increases in the FPL's in the previous investigation (ref. 1).

The overall levels of the fluctuating pressure are shown in fig. 63 as a function of the distance from the onset of the static pressure increase, x_s. Also shown is the static pressure distribution. As was the case for the forward-facing steps, a sharp peak in $\sqrt{\bar{p}^2}/q_\infty$ corresponds with the start of the steep static pressure increase. The power spectrum, shown in fig. 64, is similar to the forward-facing step with most of the energy concentrated at Strouhal numbers less than 0.02. In the first 0.2 in. (not shown), the slope of spectrum versus frequency was nearly equal to the slope for the 3/4-in. step-spoiler. As the static pressure approaches a constant value beyond separation, the rms pressures drop. An increase in spectral level at frequencies above $\omega\theta/U_\infty = 0.05$ and a decrease below 0.05 accompanies the region from $x_s = 0.3$ to 1.0 in. Beyond $x_s = 1.0$ in., the levels again begin to increase as more energy appears at the higher frequencies and the spectra are nearly flat out to $\omega\theta/U_\infty = 0.15$. At $x_s = 2.3$ in., the spectra show the humped spectra typical of reattached flow (fig. 48). This spectrum shape was unchanged for the remainder of the region investigated.

An attempt was made to cross-correlate the data, such that the pressure signature could be followed through and beyond the actual position of impingement. The results were difficult to analyze. The correlation was poor through the perturbed region. Cross-correlating the pressure signature found at the spatial position of maximum FPL with pressures further downstream in the x-direction indicated a reversal of phase, or a correlation coefficient of similar characteristics to the unperturbed case or to the region of separation ahead of a forward-facing step (but with a very significant negative lobe—see fig. 65). The correlation coefficient in all the other directions were down to 10% or less in only 8.0 ξ/θ distances, which is a much smaller spatial distribution than for any of the other perturbations examined. However, the convection velocity in the direction of the flow was poorly defined, suggesting very low velocities or conversely, simultaneity of events. It is inferred from this that the effects of an impinging shock wave should be examined in terms of instantaneous non-stationary data reduction techniques requiring special instrumentation for detailed analysis. A check

Legend (upper plot):
Tagged symbols – condenser microphone (AM)
Filled symbols – condenser microphone (FM)

Flow

Vertical axis (upper): $10^3 \sqrt{\overline{p^2}}/q_\infty$

Vertical axis (lower): P/P_∞

Horizontal axis: Distance from the shock impingement, x_s, in.
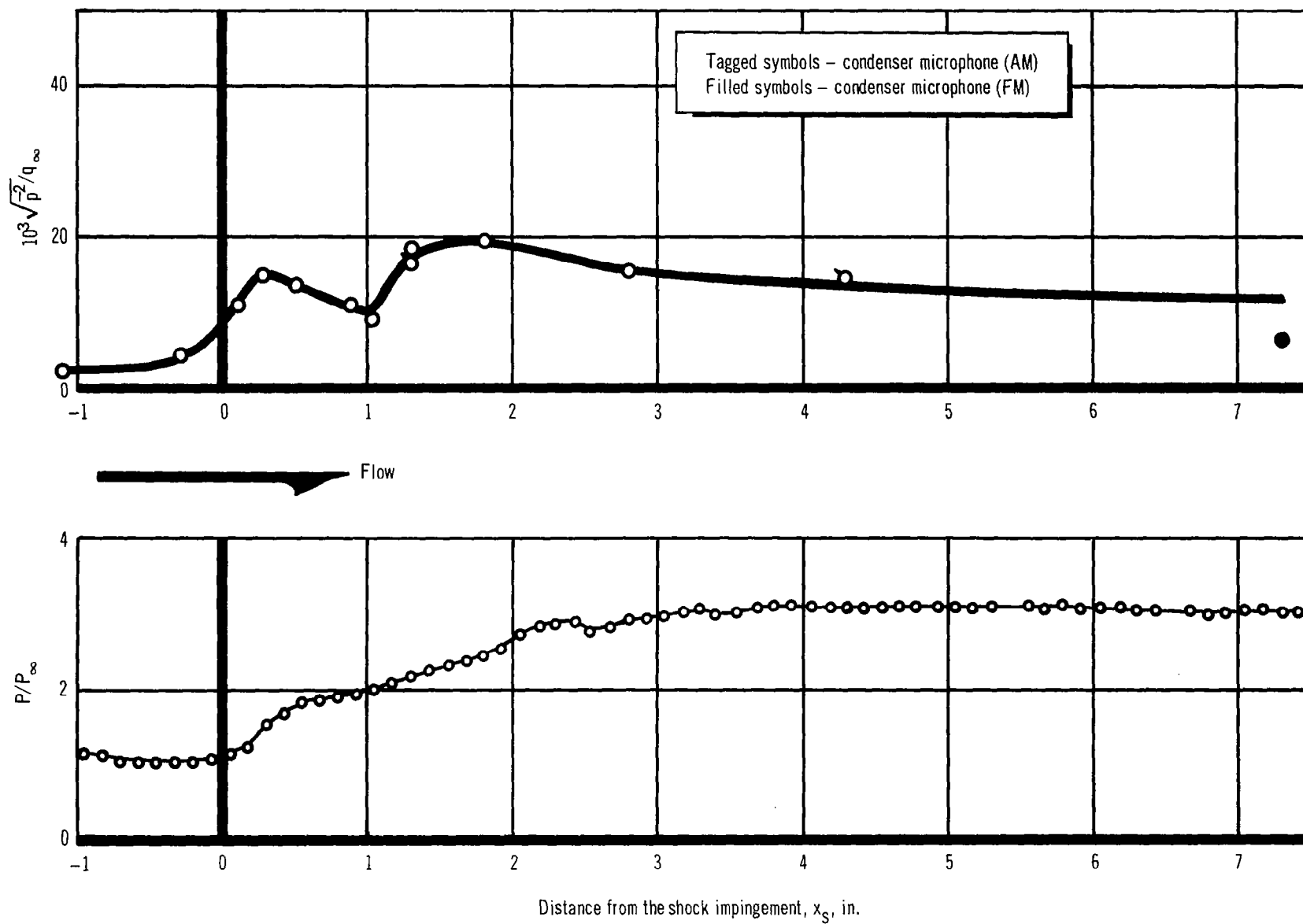
Figure 63. Static and Fluctuating Pressure Distributions for a 7.5° Shock Wave, $M_\infty = 3.45$
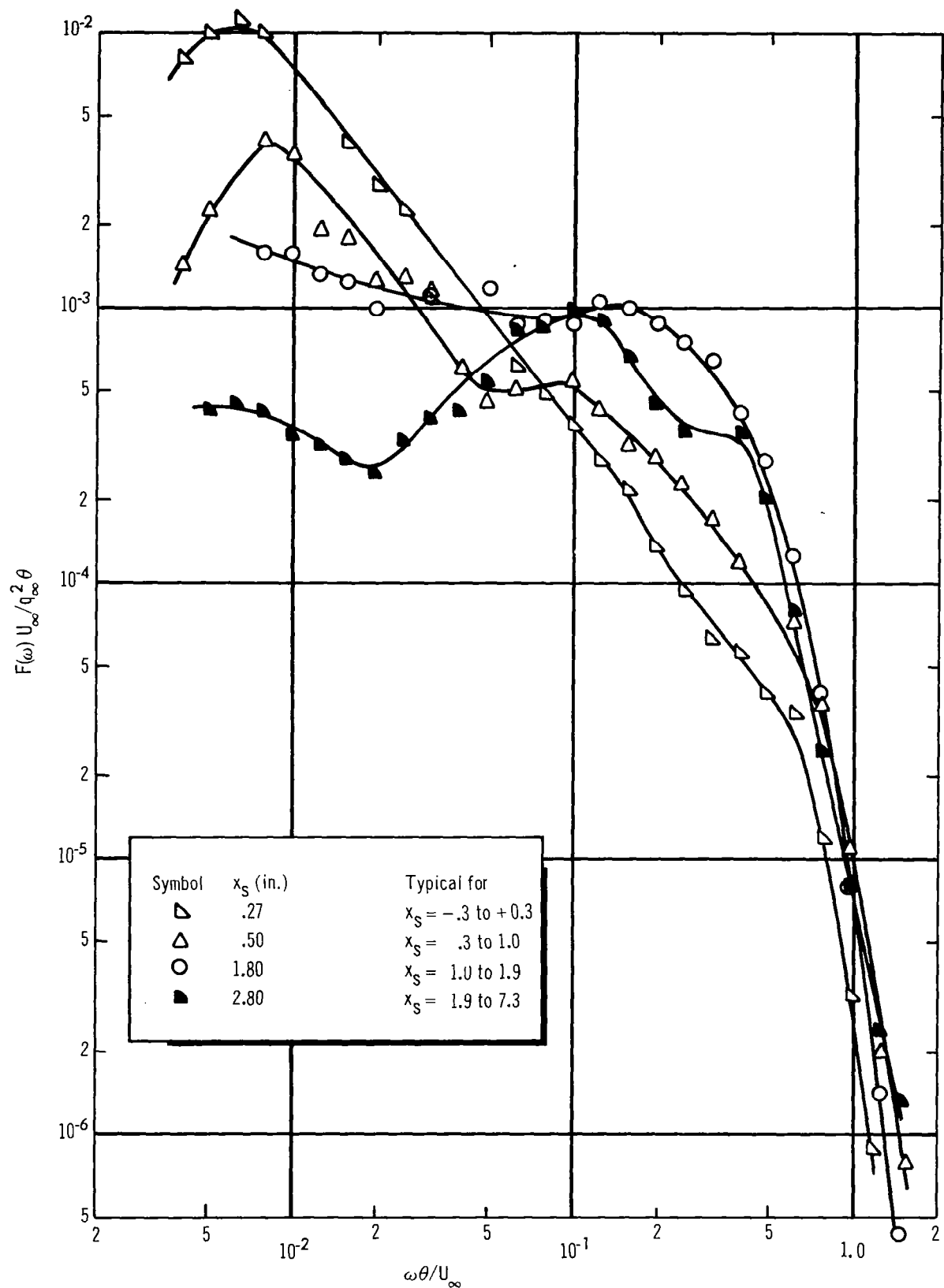
Figure 64. Power Spectra for a 7.5° Shock Wave, $M_\infty = 3.45$

The legend within the figure reads:

Symbol	x_S (in.)	Typical for
◁	.27	$x_S = -.3$ to $+0.3$
△	.50	$x_S = .3$ to 1.0
○	1.80	$x_S = 1.0$ to 1.9
◖	2.80	$x_S = 1.9$ to 7.3

The vertical axis is labeled $F(\omega) U_\infty / q_\infty^2 \theta$ and the horizontal axis is labeled $\omega\theta/U_\infty$.
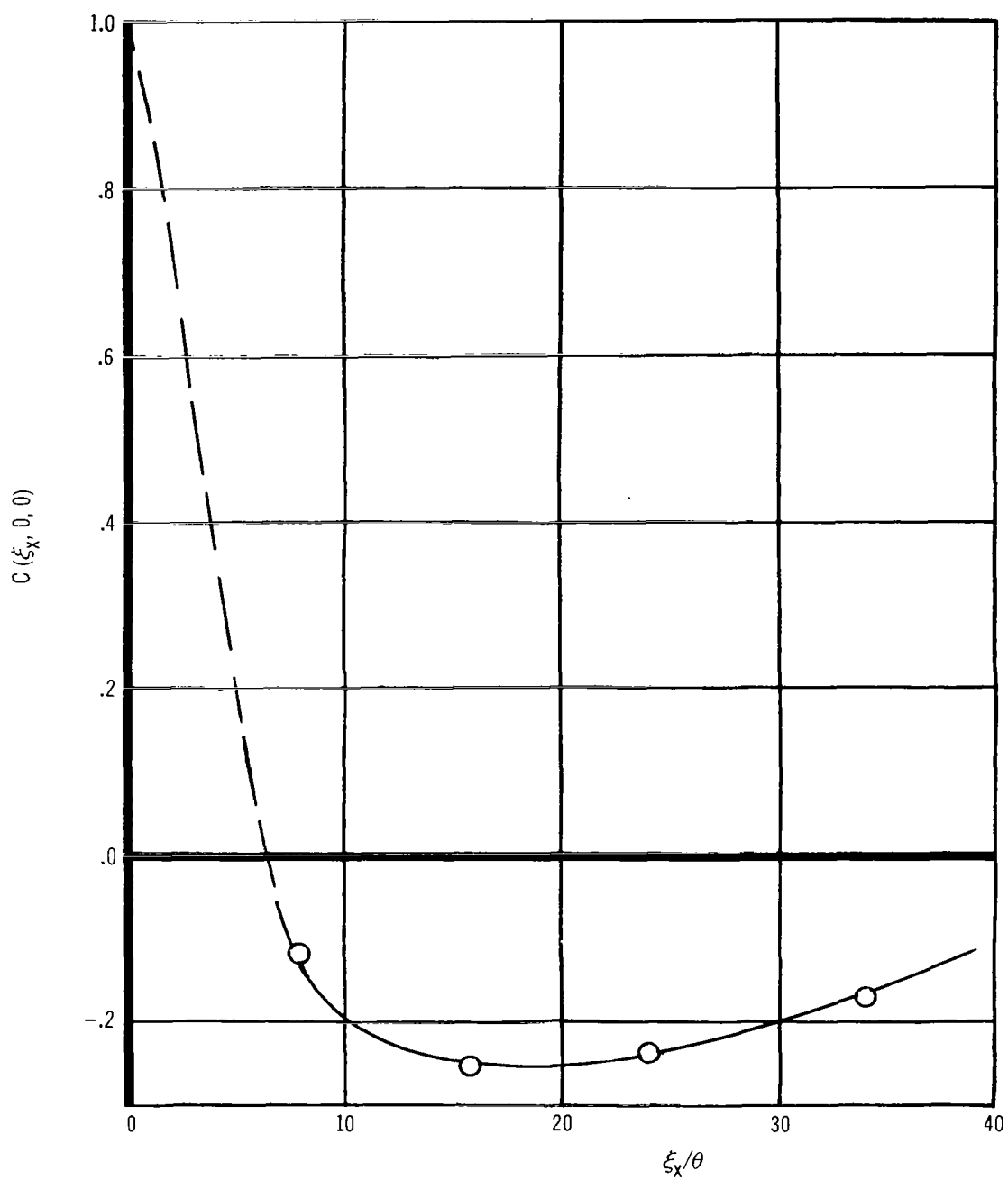
Figure 65. Longitudinal Correlation Coefficient for Supersonic (M = 3.45)
Flow Perturbed by a Shock Wave

was made of the turbulent boundary layer some 45 ξ_x/θ distances downstream to compare with the unperturbed case. The spatial correlation was comparable, but the time dependence differed, the pressure signature decaying more rapidly than in the unperturbed case. As noted before, the spectra were different and, in addition, the convection velocity was slightly less. (U_c behind the shock was 0.61 U_2, where U_2 is the stream velocity behind the impinging and reflecting shocks. The comparable value for the supersonic unperturbed boundary layer was 0.67 U_∞ at similar transducer separation distances.) More rigorous conclusions are not justified without considerably more effort being expended on the impinging shock phenomenon. This is beyond the scope of the present study.

DISCUSSIONS

It is of interest to compare the unperturbed flow data with data collected by other investigators and, in more limited fashion, with the perturbed flow data. Generalizations for the various flow conditions can provide the designers of high-performance vehicles with some insight into the fluctuating loads on various parts of the vehicle. In this section, data in unperturbed and perturbed flow will be compared, and convection velocity and temporal and spatial correlation functions will be discussed. The two final subsections contain comments on the separability of the cross-correlation functions and their mathematical description.

5.1 Comparison of Unperturbed Flow Data

In the previous investigation (ref. 1), spectra and overall levels of the fluctuating pressures were compared with data obtained by other investigators. However, because of the difficulties experienced in correcting the condenser microphone data for static pressure and finite size effects, the high-frequency data were questionable. One of the main purposes of the present investigation was to extend measurements to frequencies well into the roll-off region of the fluctuating pressure spectrum. In addition, although emphasis was on the supersonic boundary layer, it was necessary to obtain data at subsonic speeds. Favorable comparison of subsonic data from the present investigation with that reported in the literature would lend support to both the uniform supersonic data and the perturbed flow results. This substantiation is, in fact, borne out by the data presented below. In addition, the data provide a more complete description than now exists of the effects of Mach number from subsonic to middle supersonic speeds.

The early wind tunnel experimenters in the field, Harrison (ref. 10) and Willmarth (refs. 11 and 12) to mention but two, normalized the overall levels of the fluctuating pressures to dynamic pressure. Indeed, the flight experimenters, McLeod and Jordan (ref. 13), Mull and Algranti (ref. 14), and Von Gierke (ref. 15), also found that dynamic pressure was an easily measured parameter, convenient to use. (Von Gierke also normalized his data in a more complicated fashion, as discussed later in this section.) The use of dynamic pressure as a normalization factor is still popular, although other parameters have been more recently expounded, with good merit.

The question of which data from the present study should be compared with data from the literature posed a problem. The final decision was to present the data at a constant momentum thickness Reynolds number. For the curve of $\sqrt{\overline{p^2}}/q_\infty$ versus M on fig. 66, a value of $R_\theta = 20\,000$ was chosen. At M = 3.45, it was impossible to calculate a value of $\sqrt{\overline{p^2}}/q_\infty$ because $R_\theta = 20\,000$ was much too low. At the other Mach numbers, however, this R_θ was within or close to the range of measurements on the sidewall. (See figs. 18, 21, 23, 30, 32, and 35.)
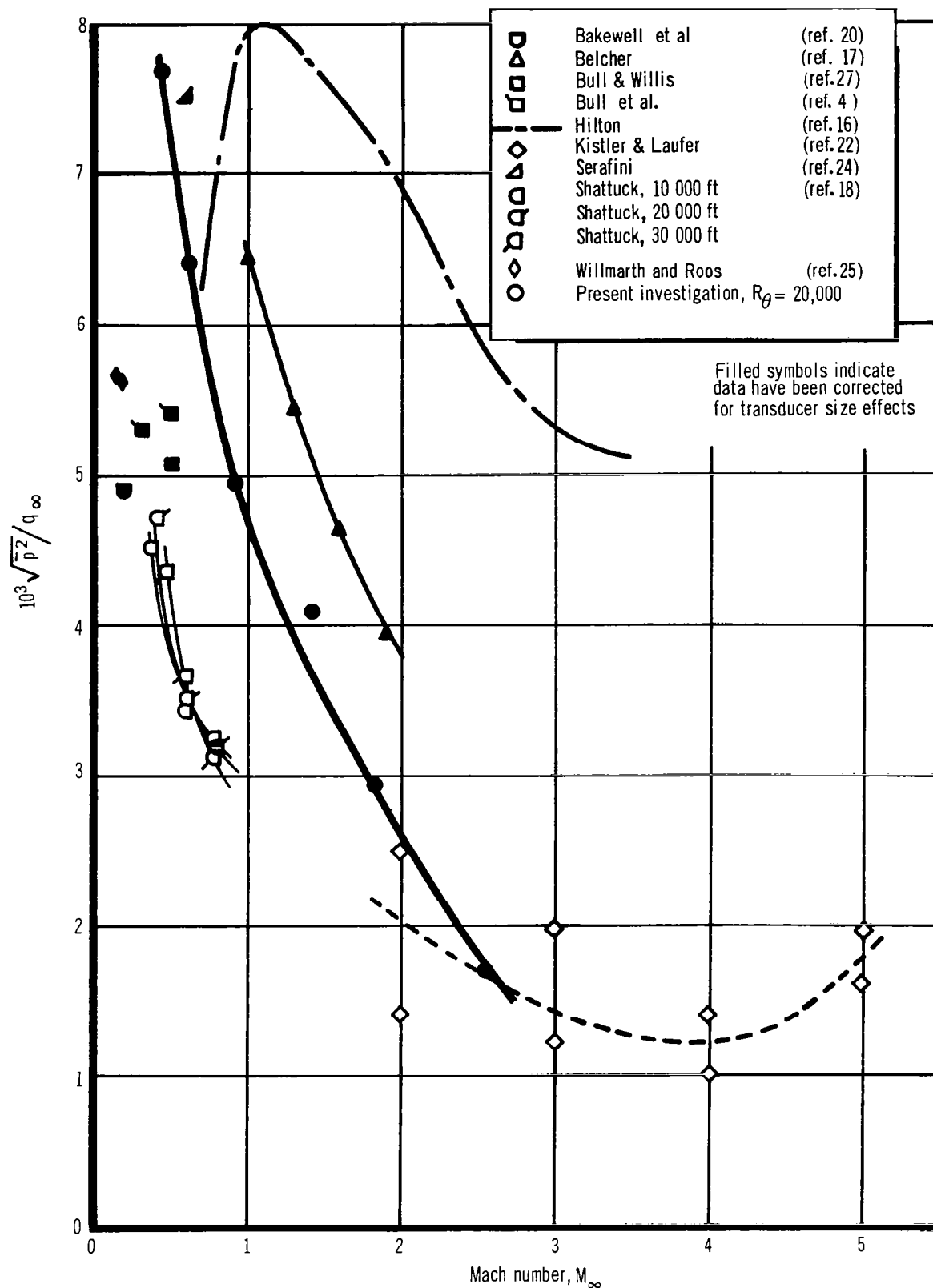
Figure 66. Variation with Mach Number of the Overall r m s Pressure Fluctuations Normalized to Free-Stream Dynamic Pressure

The data shown in fig. 66 combine a mixture of flight results (refs. 16 to 19), pipe studies (refs. 20 and 21), and wind tunnel tests (ref. 22 to 27). Unfortunately, R_θ is not known for most of the cases. It is known that Hilton's Scout rocket measurements (ref. 16) are in perturbed flow since they were taken at the extreme aft end of the vehicle between the fins. Belcher's values, taken far back on the fuselage of a large supersonic aircraft (ref. 17), are possibly slightly high in level, although the Reynolds number is very high also. Nevertheless, the trend is obvious: a sharp drop in the value of $\sqrt{\overline{p^2}}/q_\infty$ as Mach number increases. Kistler and Chen (ref. 6) did not report their data normalized with respect to q nor did they give values of c_f. Consequently, the data shown are earlier measurements of Kistler and Laufer as reported by Richards, Bull, and Willis (ref. 22). It is not known whether these data are included in ref. 6, in which wall shearing stress is the normalization parameter.

The data from the present investigation are shown again in fig. 67, this time normalized to the wall shearing stress. Except for Belcher's measurements (1965) and the present study, the data of the other investigators tend to increase with Mach number. Even Lilley (ref. 23) theoretically predicts a rise in level, although of lower magnitude than indicated by Kistler and Chen. The values at subsonic speeds are in good agreement with Maestrello (ref. 6) and Kistler and Chen but are higher than the values of Bull et al. (ref. 4) and Willmarth and Roos (ref. 25), which agree well with each other. Williams' values (ref. 26) are questionable because his transducers were quite large compared to the boundary-layer thickness. (Bull's corrections to Williams' data are also shown in fig. 67). An explanation of the differences between supersonic data of Kistler and Chen, Belcher, and the present investigation has not been found at this time.

Bull et al. (ref. 4) presented $\sqrt{\overline{p^2}}/\tau_w$ plotted as a function of R_θ, with data from several investigators. The present data were plotted on this curve (fig. 68) for Mach numbers from 0 to 0.6 and on another curve (fig. 69) for a Mach number range from 1.0 to 2.0. Although data from any given study are reasonably self-consistent, there appears to be no particular consistency between data obtained by the several investigators except that $\sqrt{\overline{p^2}}/\tau_w$ appears to increase with R_θ. A similar comparison of data as a function R_x was no better. Clearly, some anomalies still exist.

All the power spectra in sections 4.2 and 4.3 are normalized with respect to dynamic pressure and displacement thickness. These are relatively convenient parameters to obtain and are widely used throughout the field of pressure fluctuations research. It is, therefore, interesting to plot the power spectra at all the Mach numbers of this study. Fig. 70 shows typical power spectra from piezoelectric transducers located near the center of the sidewall insert. The data do not collapse into a single curve by any means, but good agreement exists for M = 0.42 and 0.59 up to $\omega\delta^*/U_\infty = 2.5$. The divergence of the data above $\omega\delta^*/U_\infty = 2.5$ for the unthickened boundary layer at M = 0.42 is perhaps the result of too large a correction for transducer size. The levels at higher Mach numbers decrease gradually, somewhat in proportion to the dynamic pressure increase. At M = 3.45, the data are much lower than the other data.
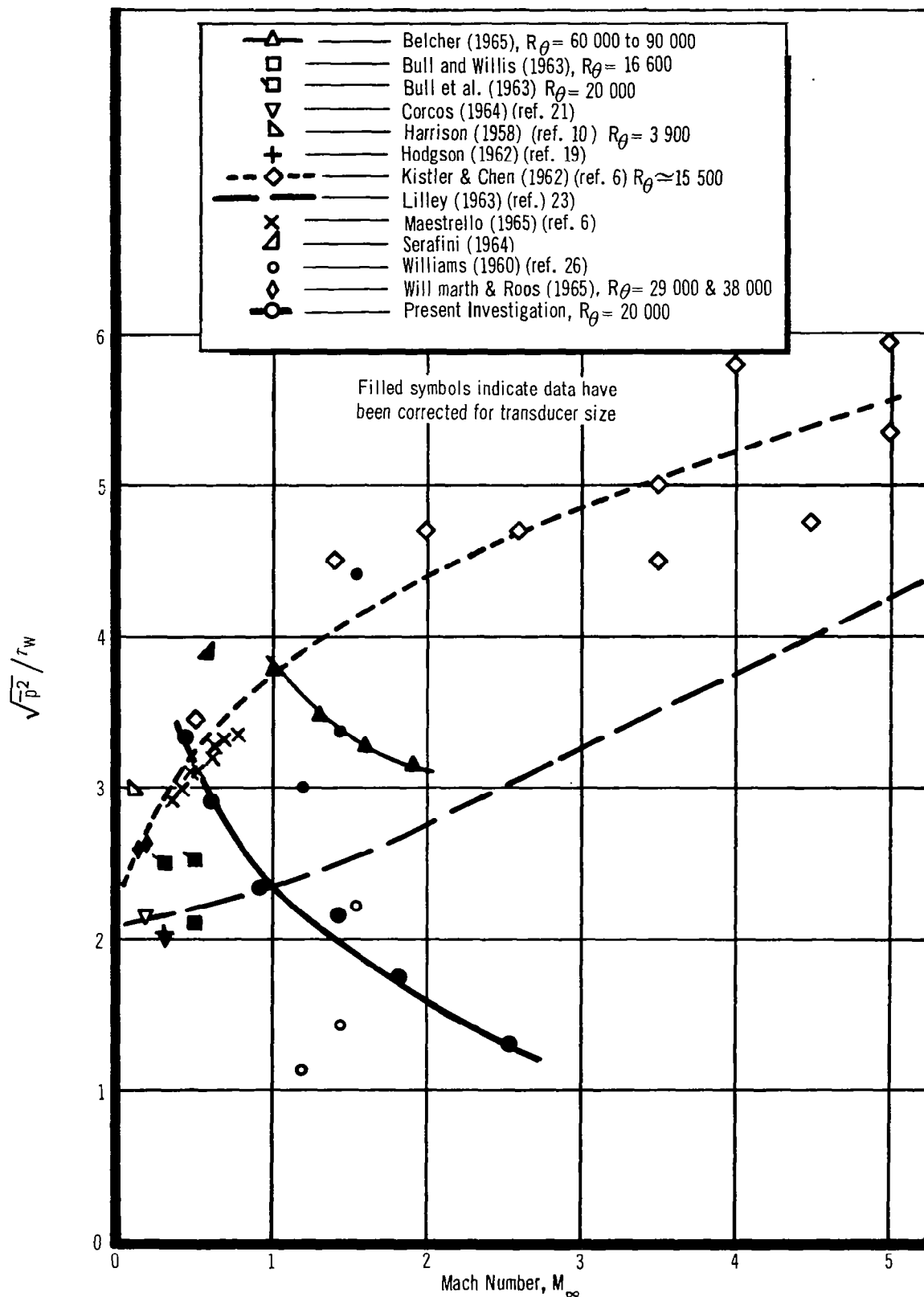
Figure 67. Variation with Mach Number of the Overall r m s Pressure Fluctuations Normalized to Wall Shearing Stress
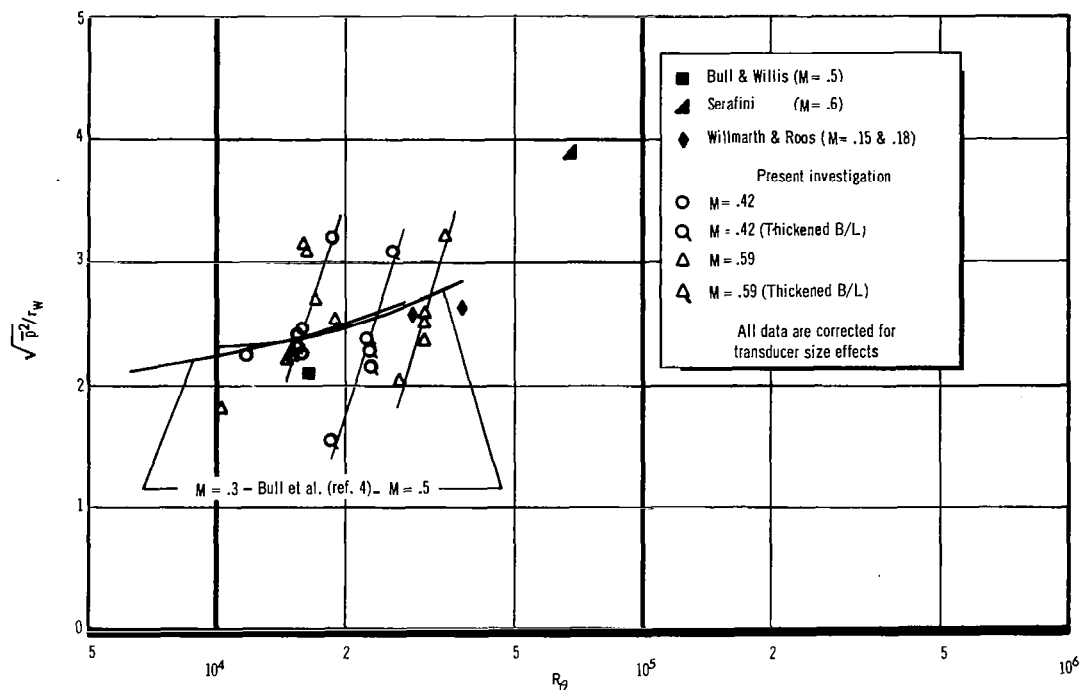
Figure 68. Variation of Overall rms Pressure Fluctuations as a Function of Momentum Thickness Reynolds Number, $M_\infty = 0$ to .6
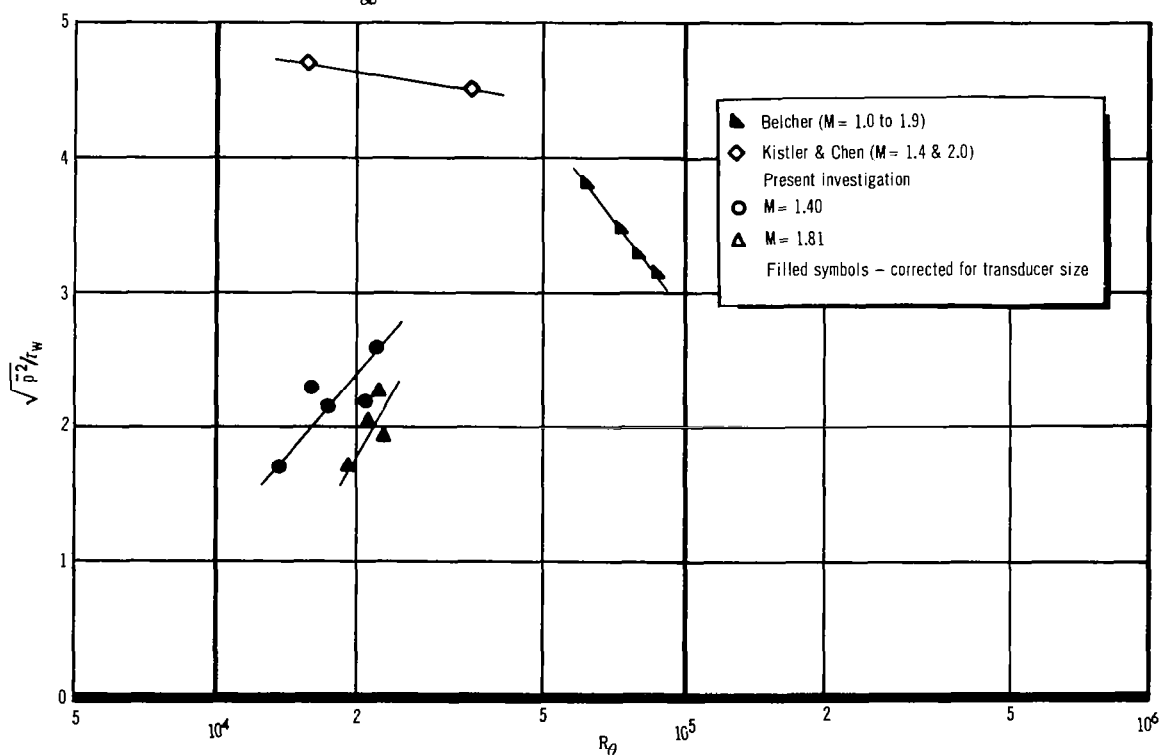
Figure 69. Variation of Overall r m s Pressure Fluctuations as a Function of Momemtum Thickness Reynolds Number, $M_\infty = 1.0$ to 2.0

101
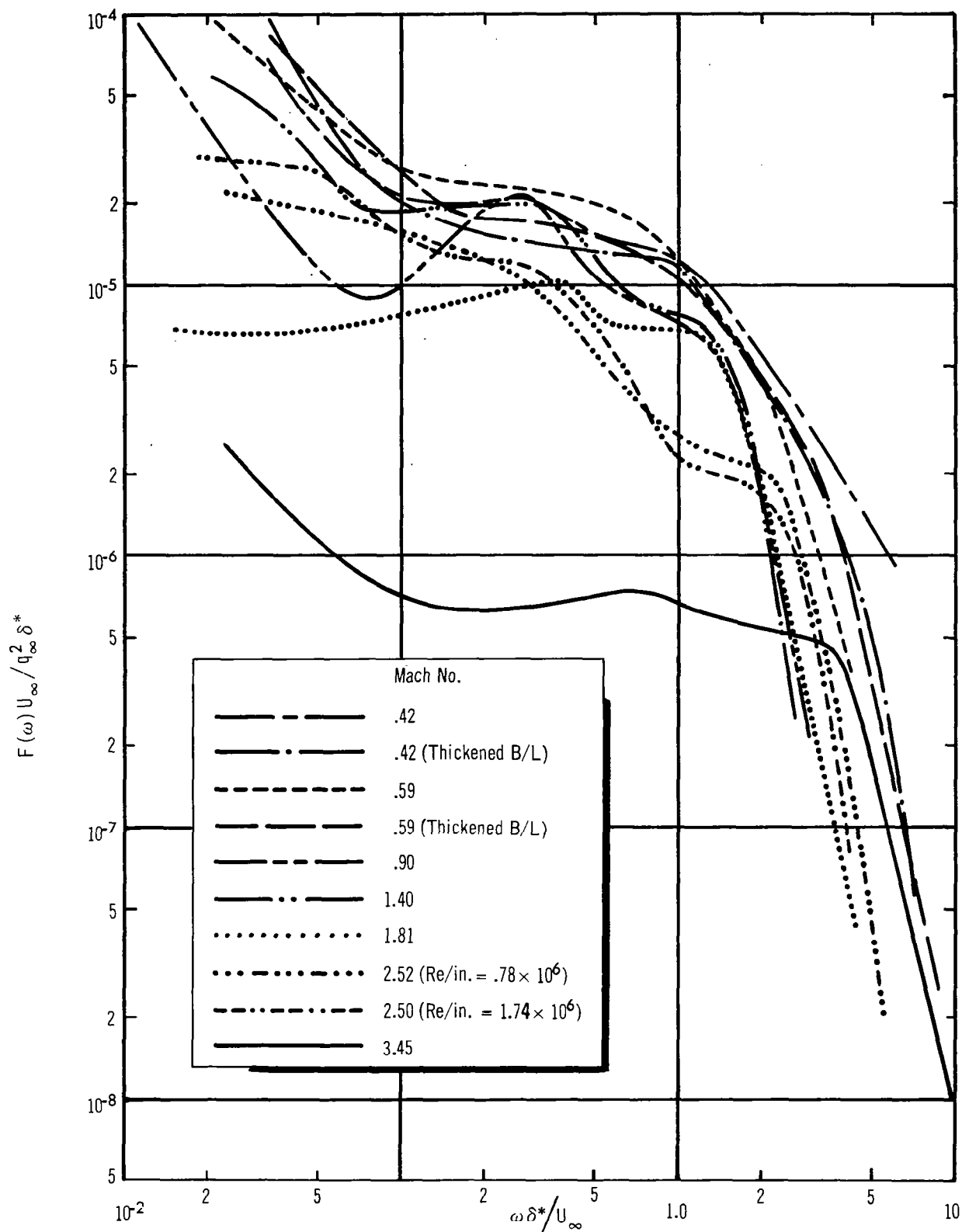
Figure 70. Nondimensional Power Spectra of the Wall Pressure Fluctuations at Several Mach Numbers as Function of q_∞ and δ^*

102

Most of the latest data which have been reported are normalized to wall shearing stress rather than to dynamic pressure. Fig. 71 presents the data of fig. 70 normalized in this manner. It can be seen that generally they are drawn closer together than in fig. 70. The data at M = 3.45 are still low and the M 2.5 data are now high at low Strouhal numbers. Although the data at high frequencies are essentially parallel, they shift to the right as δ^* increases. This phenomenon suggests that the use of some boundary-layer parameter other than δ^* would be more appropriate. Momentum thickness, which has little variation with Mach number (fig. 8) has been used in the perturbed flow results and seems to be an appropriate choice.

The data from fig. 71 have been normalized to θ in fig. 72 instead of δ^*. Except for data at M = 2.5, the data (including M 3.45 data) now show rather good agreement from $0.01 < \omega\theta/U_\infty < 0.6$. Beyond the roll-off, however, the data are in worse agreement than in fig. 71. Closer examination of the high-frequency data reveals an interesting trend. The data separate into essentially one curve for subsonic Mach numbers and another for transonic and supersonic Mach numbers. Eldred et al. (ref. 28) and Von Gierke (ref. 15) obtained rather good fits for a number of flight measurements (up to $U_\infty = 1,000$ fps) to a single curve by normalizing their spectral densities to $\bar{p}^2\delta$ rather than to $q_\infty^2\delta^*$ or $\tau_w^2\delta^*$ and also by introducing Mach number in the numerator. Thus the nondimensional power spectral density became $\dfrac{F(f)U_\infty M_\infty}{\bar{p}^2\delta}$ [**]. The frequency was similarly nondimensionalized to $f\delta/U_\infty M_\infty$ [†]. Data (not shown) from the present investigation were plotted to these scales, but the results presented a much greater separation of data in the high frequencies. Replacing θ with δ in fig. 72 would have had the result of compressing the data somewhat but would have eliminated the consistency with Mach number that is indicated in fig. 72. The authors have therefore concluded that use of wall shearing stress and boundary-layer momentum thickness provides the best normalization of the data. Further study may indicate a combination of parameters which provide a better fit to the data.

[**] In addition, Eldred et al. multiplied the expression by the ratio of the stagnation to free-stream kinematic viscosity.

[†] Eldred et al. also included the viscosity ratio in the denominator.
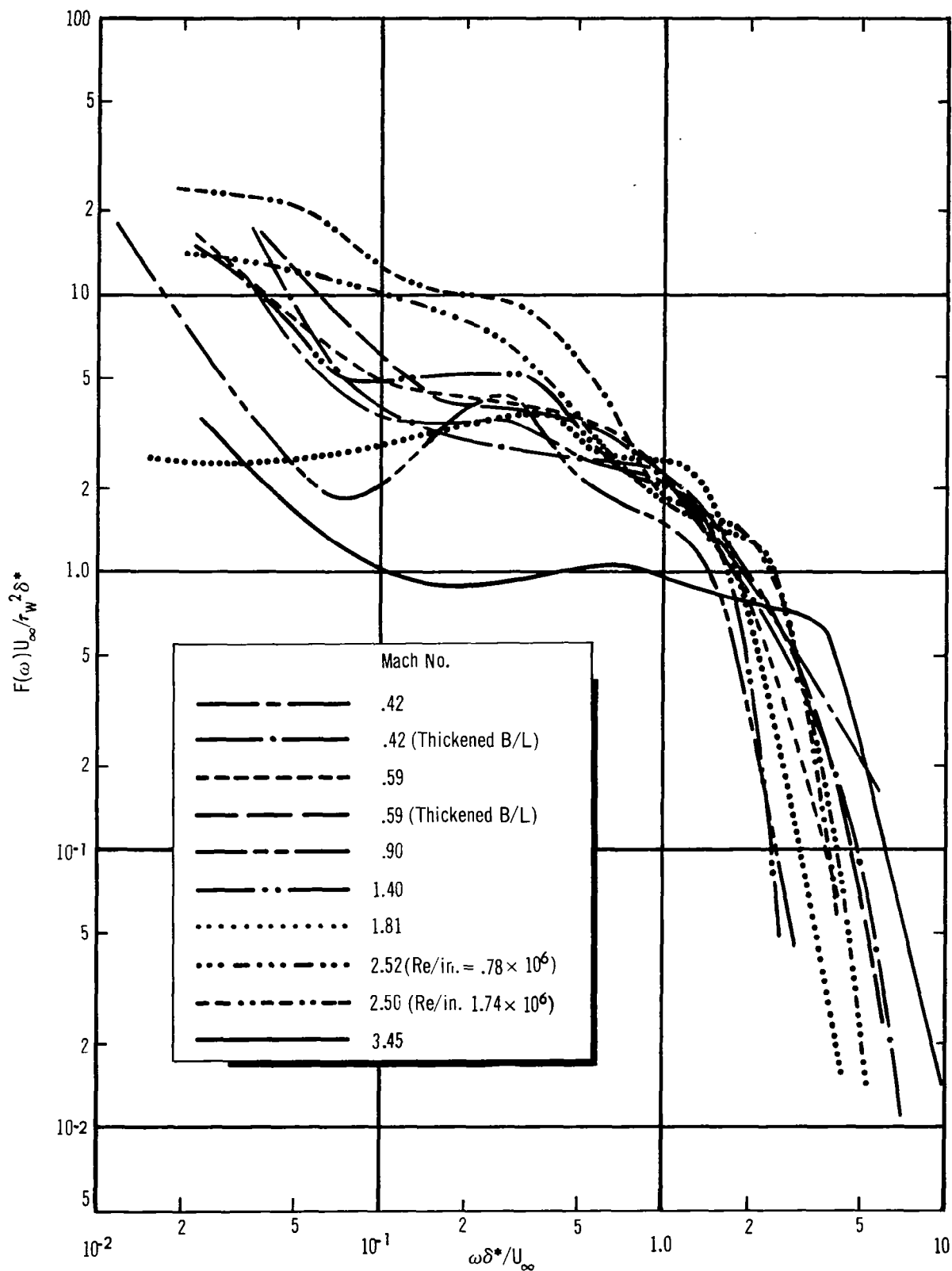
Figure 71. Nondimensional Power Spectra of the Wall Pressure Fluctuations
at Several Mach Numbers as Functions of τ_w and δ^*
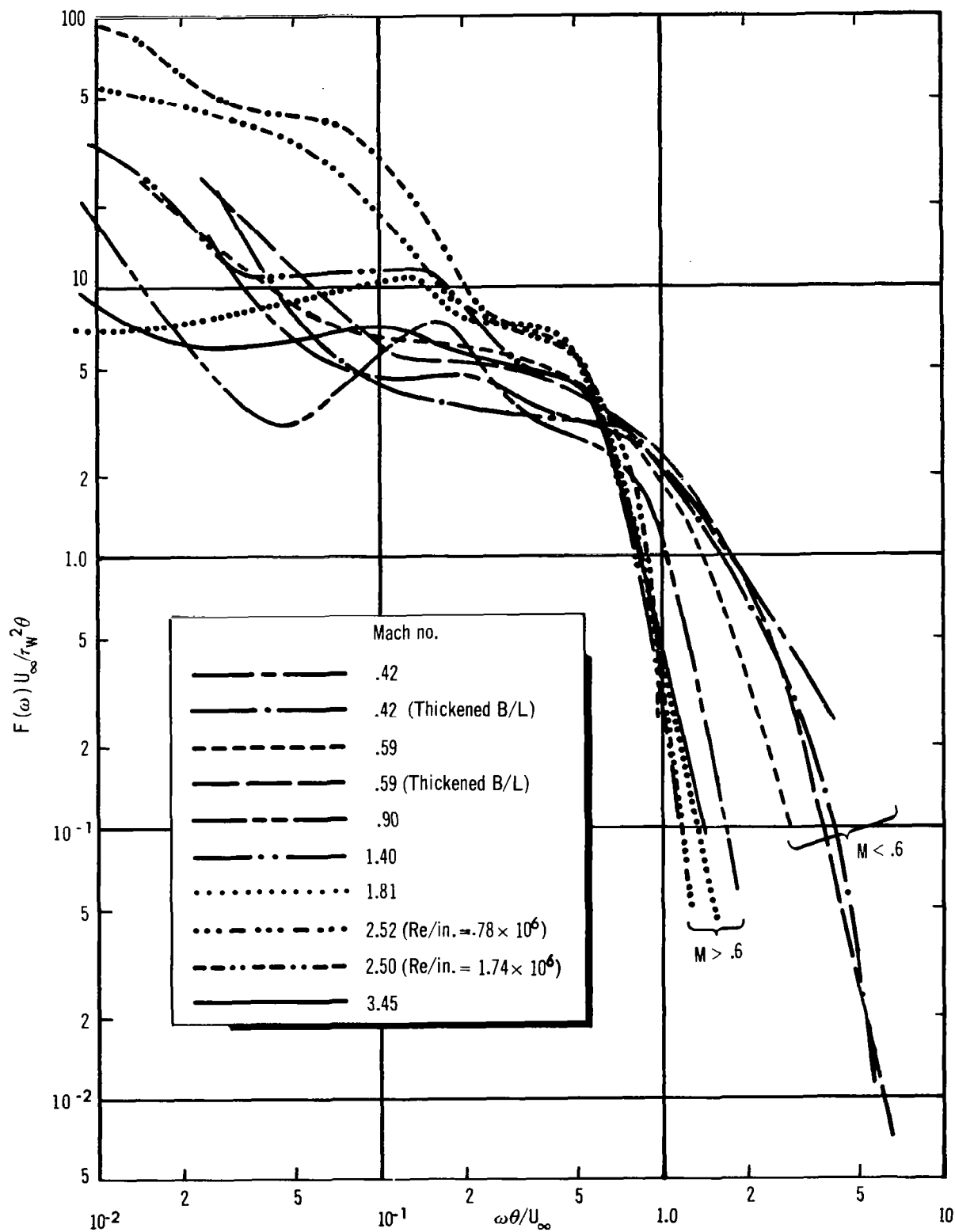
Figure 72. Nondimensional Power Spectra of the Wall Pressure Fluctuations at Several Mach Numbers as Functions of τ_w and θ

5.2 Perturbed Flow Trends

Certain trends become evident as spectra in the perturbed flow regions are examined. Similarities exist in the flow ahead of and behind steps and for impinging shocks. The following discussions are from study of the data presented herein. The generalizations are intended to apply to any supersonic flow although they were derived from the M 3.45 data. The limited amount of data taken at M = 1.40 appear to support the conclusions reached.

Fig. 73 presents a composite picture of the results of the investigations into the various regions in the flow around a step. A sketch of the flow field is shown at the top of the page. In the middle of the page, trends of the overall FPL's are shown in nine regions of flow. At the bottom of the page, spectral shapes are given for the nine regions.

Region ① is unperturbed. Region ② includes flow separation and is characterized by the concentration of energy at low frequencies. Region③ shows relatively high rms levels with more energy contained at the higher frequencies. Associated with Region ④ is a further increase in energy in the high-frequency bands. Apparently the spectra in region ⑤ reflect the oscillation or periodicity of the flow reattachment near the top of the step face. Maximum FPL's are predicted to occur at $\Delta x_{LE}/h = 0$. The result is the characteristic double-humped spectrum of very high level noted earlier by Kistler (ref. 8) and Ailman (ref. 9).

As the flow passes over the step into Region ⑥ , the pressure signature of the high velocity external flow is again in evidence. The levels in all frequency bands have diminished, but mostly at high frequencies. The length of the step now becomes important because the longer the step with respect to its height, the more chance the boundary layer has of becoming stabilized with a normal profile and energy content.

If the step is very long, the FPL's in Region ⑦ immediately downstream of the step may be slightly lower than unperturbed levels. The spectrum, however, consists predominately of low frequencies. Thus, in the base region, the effects of the external flow are felt through the low density "dead-air" region. If the step is very short, the levels in Region ⑦ will be much higher than in the unperturbed case. In fact, as the step length approaches zero, the downstream FPL's should be nearly equal to those in Region ⑤ .

As the flow approaches reattachment, Region ⑧ , the high-frequency content increases and FPL's maximize once again. Beyond reattachment in Region ⑨ , the low frequencies have diminished significantly and the fluctuating pressure spectra show considerable energy at high frequencies. Eventually, at some point in the field downstream of the 9.15 step heights investigated here, the spectrum will presumably return to normal level and shape. Additional testing is needed to define the extent of the perturbed region.
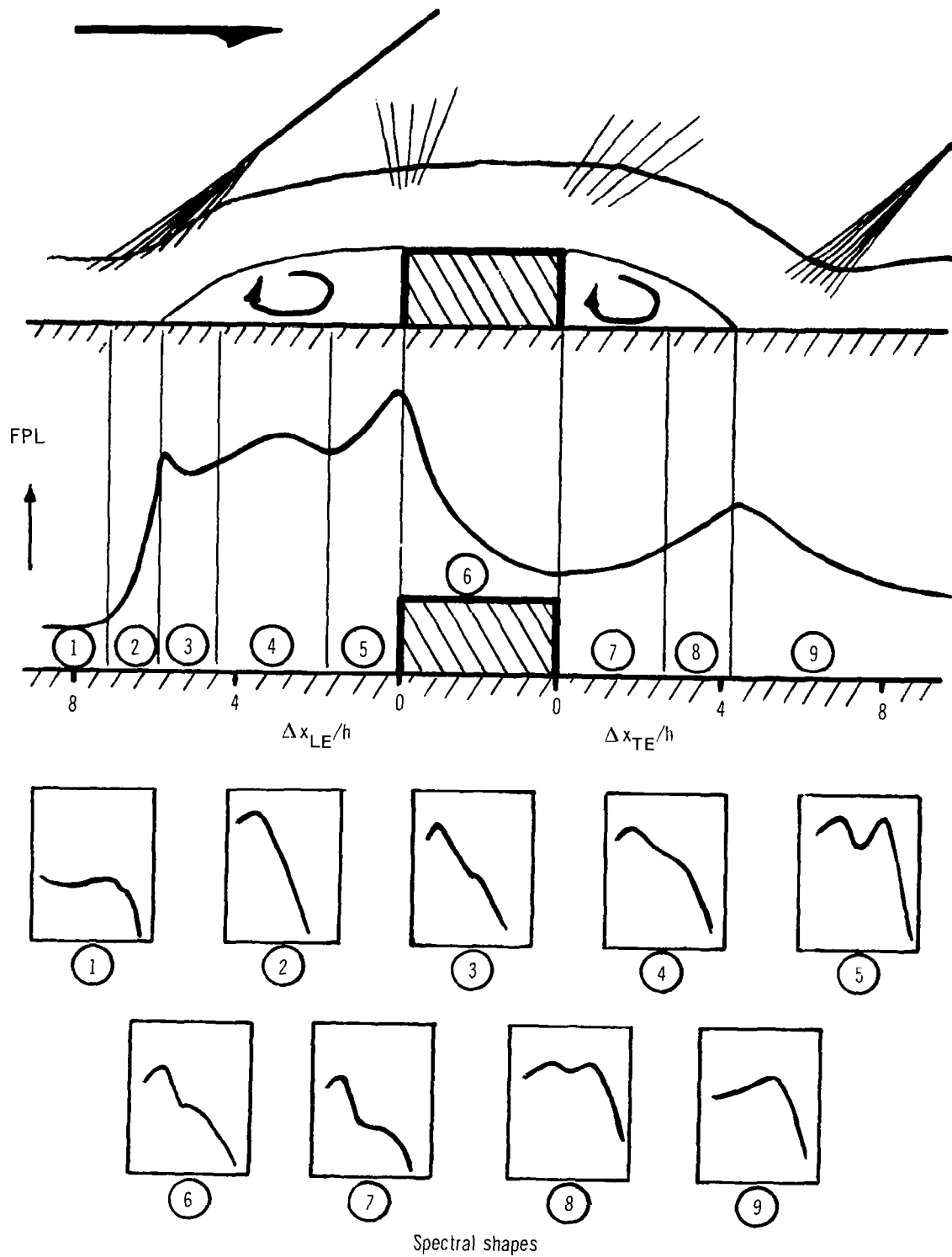
Figure 73. Sketch of the Flow Conditions in the Vicinity of a Step in Supersonic Flow

The preceding discussions have been concerned with the spectra in the vicinity of a step. An analogy can be drawn from the previous data discussions and the data for an impinging shock wave. To define the flow picture for the shock-perturbed boundary layer, Regions ④ through ⑦ should be ignored. Thus, Region ⑧ follows directly behind Region ③ and, if comparable levels are assumed, the foregoing step discussions are now relevant for the impinging shock case.

5.3 Convection Velocity

Convection velocities were computed in the direction of the flow for each type of flow examined. These have been quoted and/or illustrated in many instances under the appropriate data reporting section (e.g., see fig. 28 and 40). The following discussion compares convection velocities between the flows. Fig. 74 shows results calculated for each kind of flow examined. Differentiation has been made between configurations and between the regions of flow in question. At first glance, it would appear that a lack of uniformity exists. However, the following observations can be made:

1. A convection velocity for the pressure signature associated with an unperturbed flow falls on a line of constant slope (constant U_c/U_∞ ratio) on fig. 74. The ratio of convection velocity to free-stream velocity increases with Mach number and is approximately 0.83 at $M = 0.6$ and 0.94 at $M = 3.5$ (also see fig. 41).

2. If examined in terms of a U_c/U_∞ ratio versus distance, such as on fig. 40, the increase in the ratio might result from a flow mechanism as described in ref. 29. In that comprehensive work, the authors hypothesized that the large turbulent eddies near to the wall drift out into the higher velocity, constant stress layer while exchanging momentum. Thus, the smaller eddies (higher frequencies) either lose their identity or are carried to the extreme edge of the boundary layer and, consequently, are less influential. Meanwhile larger eddies travel faster and influence the pressure signature further downstream. The frequency coherence function, the integral length scales, and the convection velocities seem to substantiate portions of the hypothesis concerning the physical details of the unperturbed turbulent boundary layer flow.

3. Spectra from transducers in the region of flow that has reattached to the rigid boundary after being perturbed by separation generally indicate a slightly reduced convection velocity.

4. Within regions of separated flow resulting from aft-facing steps, the convection velocity of the pressure signature is calculated to be about comparable to the stream velocity ahead of the step. Since τ_c is ill-defined, U_c has a range of values. This could result from the fact that the stream velocity is increasing downstream of the

step. It also could be caused by the pressure signature having a multiple set of paths by which it can influence a particular location on the boundary from various positions on the path of motion.

5. In the case of a forward-facing step, the convection velocities within the separated region are calculated to be less than U_∞ ($U_c/U_\infty = 0.79$), but almost equal to the stream velocity behind the step-induced shock wave ($U_c/U_2 \simeq 0.9$). Here, too, a pressure signature can influence a surface location from various positions in its path of motion and make it difficult to calculate U_c accurately.

6. The high-level pressure signatures associated with the impingement of a shock-wave on the turbulent boundary layer are markedly changed in short distances. The velocity of convection is approximately 30% of the free-stream velocity in a region just prior to the location of the highest FPL's. In the region of separation, the convection velocity was not definable from the data. Downstream of the reattached flow, U_c/U_2 was approximately equal to 0.61. The peculiarities of the convection velocity data in the vicinity of a shock were not studied in sufficient detail to permit conclusive generalizations.
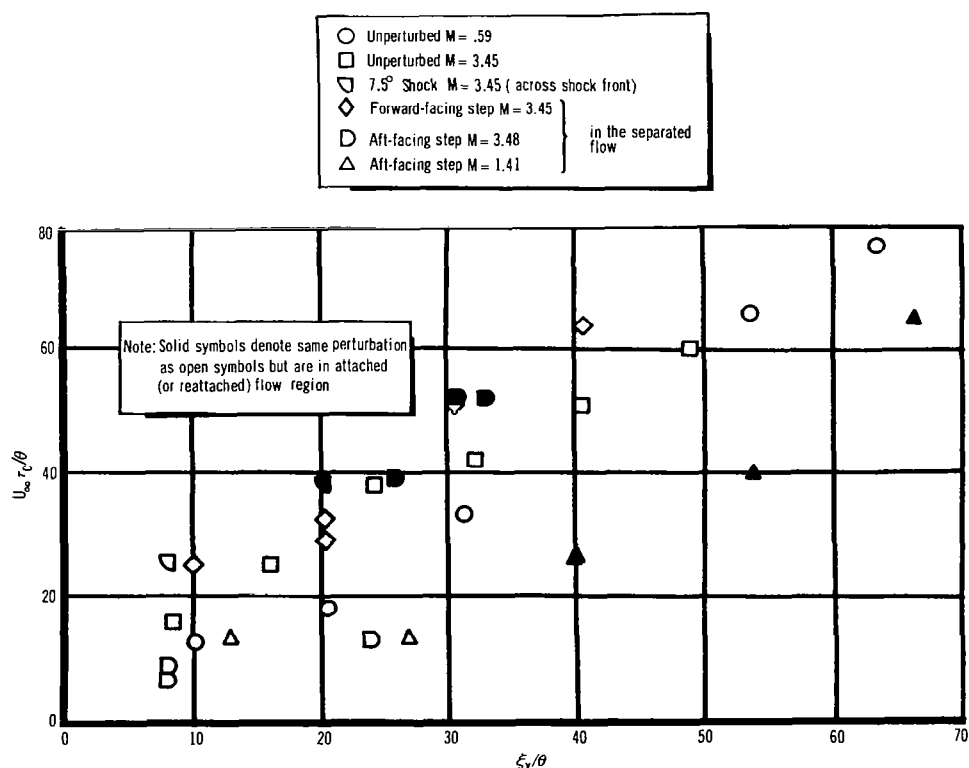
Figure 74. Nondimensionalized Convection Time Versus Nondimensionalized Spatial Separation for Various Types of Flow

5.4 Temporal Correlation Functions

Theory, verified by the data acquired in this study at supersonic speeds, uses the assumption that cross-correlation functions can be separated into a spatial and a temporal part. This discussion summarizes the results pertinent to the temporal portion.

In each of the supersonic flows examined, a typical functional relationship existed between the value of the maximum for the cross-correlation and the time delay. In the frame of reference moving with the boundary layer, this is the decay of the correlation coefficient maximum in time. The time decay took the form of $\frac{1}{1 + b\tau_c}$ where τ_c was the time difference and b was a constant. Other types of mathematical expressions were tried, but this typical function consistently fit the data best. The coefficient b must have the dimensions of $\sec^{-1}$ to make the function nondimensional. It is tempting to try to find a functional dependence which is independent of the type of flow. Several possibilities were tried unsuccessfully, but the perturbed flows do not appear to be related. Table V gives the values of b for each type of flow. The dimension of b suggests the inclusion of either a velocity or a frequency in a nondimensionalizing parameter. Both possibilities were pursued in the hope of finding a consistency between the different types of flow. For example, if $b = K\frac{U_c}{\theta}$ where K is a constant (hopefully, the same for all flow conditions), the time dependence becomes a function of separation only $(K\frac{U_c}{\theta} \cdot \tau_c = \frac{K\xi_x}{\theta})$. Values for such a constant K, shown in table V, indicated, as did the constant b, a lack of consistency between different flows.

The possibility of using frequency as a nondimensionalizing parameter was pursued, with the major frequency of coherency (ω_0) assumed to be the pertinent factor. If b could be written as such a frequency (in rad/sec), then $b\,\tau_c = L\omega_0\tau_c = L\omega_0\frac{\theta}{U_c}\frac{U_c\tau_c}{\theta} = L\frac{\omega_0\theta}{U_c}\frac{\xi_x}{\theta}$. The last product of three terms is a constant (L) times a Strouhal number times a nondimensionalized separation distance. It was hoped that as U_c varied with ξ_x, ω_0 would vary in a manner appropriate to maintaining L constant. Such a variation does seem to occur for any one particular type of flow (this trend is suggested by the coherency versus frequency of the cross-spectra for the broad-band calculations performed here). Narrow-band correlation calculations should provide detailed information on this concept. Based only on broad-band data, the different kinds of flow seem to produce dissimilar values of L (also given on table V). To date then, the desired general expression for time dependence of the fluctuating pressure correlation coefficient has not been obtained.

From table V, it is obvious that the decay of the correlation coefficient in time is slowest for the unperturbed case (for either subsonic or supersonic flow). Faster decays are found for the forward-facing step and the aft-facing step, respectively.

TABLE V

TYPICAL CONSTANTS ASSOCIATED WITH THE
TEMPORAL PART OF THE CROSS-CORRELATION[*]

	U_∞, in/sec	U_c, in/sec	U_c/θ, sec^{-1}	b, sec^{-1}	K	L
Aft-facing step M = 1.41 (near step face)	15.9×10^3	15.9×10^3	0.53×10^6	1.1×10^5	0.207	----
Aft-facing step M = 1.41 (in reattached flow)	15.9×10^3	11.0×10^3	0.367×10^6	9.0×10^4	0.24	3.6
Aft-facing step M = 3.48 (near step face)	25.7×10^3	25.7×10^3	0.523×10^6	6.3×10^4	0.12	30.0
Aft-facing step M = 3.48 (in reattached flow)	25.7×10^3	11.6×10^3	0.204×10^6	6.0×10^4	0.294	0.635
Unperturbed M = 3.45	25.3×10^3	23.0×10^3	0.465×10^6	1.27×10^4	0.0273	0.675
Forward - facing step M = 3.45 (near step face)	25.3×10^3	20.0×10^3	0.405×10^6	3.0×10^4	0.074	0.35
Forward - facing step M = 3.45 (near separation)	25.3×10^3	20.0×10^3	0.405×10^6	3.5×10^4	0.086	4.65

[*]where b comes from $R_{max} (\xi_x, 0, \tau_c) = R (0, 0, 0) \cdot \dfrac{1}{1 + b\tau_c}$

$$\frac{1}{1 + b\tau_c} = \frac{1}{1 + K\dfrac{\xi_x}{\theta}} = \frac{1}{1 + L\dfrac{\omega_o \theta}{U_c} \dfrac{\xi_x}{\theta}}$$

5.5 Comparisons of Spatial Correlation Coefficients

Correlation coefficients obtained for each kind of perturbed flow have been presented in previous sections. As noted, the forward- and aft-facing steps had two different correlation coefficients in the direction of flow, each being associated with a different region of the flow. These two distinctly different coefficients would suggest a completely different pressure signature for each region. Spectral comparisons do indeed show marked changes between different regions of the flow. The aft-facing step indicates a predominantly low-frequency power spectrum directly behind the step face, while the region of reattachment shows a broad spectrum of energy (with some modifications which are dependent on Mach number). The forward-facing step indicates a similar contrast—the predominantly low-frequency power spectrum is associated with the shock and region of separation, while the broad spectrum is found within the region of separated flow.

The lateral correlation coefficients are not so completely described because placement of the instrumentation did not permit examination of two pressure signatures for different regions of flow in a direction perpendicular to the flow. However, those which were examined seemed to possess more uniformity among themselves than did the longitudinal correlation coefficients.

It seems profitable to compare the correlation coefficients in the longitudinal and lateral directions for the regions of flow which generate the highest fluctuating pressure levels. Depending on the cause of the perturbation of the flow, this region may be found close to, or far from, the protuberance. Figs. 75 and 76 show the correlation coefficient for flow conditions which were well-defined from the data. In most instances, the longitudinal correlation coefficient for the unperturbed supersonic case, with its long tail, extends for a much greater distance than in perturbed cases. However, the lateral directions show the opposite effect. Part of the increase in the lateral correlation coefficient for perturbed flow might well be attributed to the observation of lateral convection velocities mentioned in section 4.4. The unperturbed flow in the longitudinal direction has a larger value of λ_x than the perturbed cases. The reverse situation exists when λ_z's are compared. Hence, the ratio of λ_z/λ_x is larger for the perturbed regions of flow.

The difference in results for the same aft-facing step at two supersonic Mach numbers is disconcerting. The pressure levels have changed (by as much as 8.5 dB), but it was not expected that the correlation coefficient would change so drastically (seemingly, a complete reversal of the type of function associated with each of the two regions of flow). Since the pressure signatures are different for each region of the flow (separated and reattached), it would appear that a careful study versus Mach number is warranted, especially since spectra associated with reattachment differ somewhat with Mach number. In such a study, careful placement of the transducers should permit detailed study of the plane under each flow region for each Mach number. Since the location of reattachment varies with Mach number, this kind of a study would require more versatility of, or a much larger quantity of, transducers than was available in the present study. Narrow-band analysis of the data taken in this study would be especially helpful in understanding differences in the correlation coefficients.
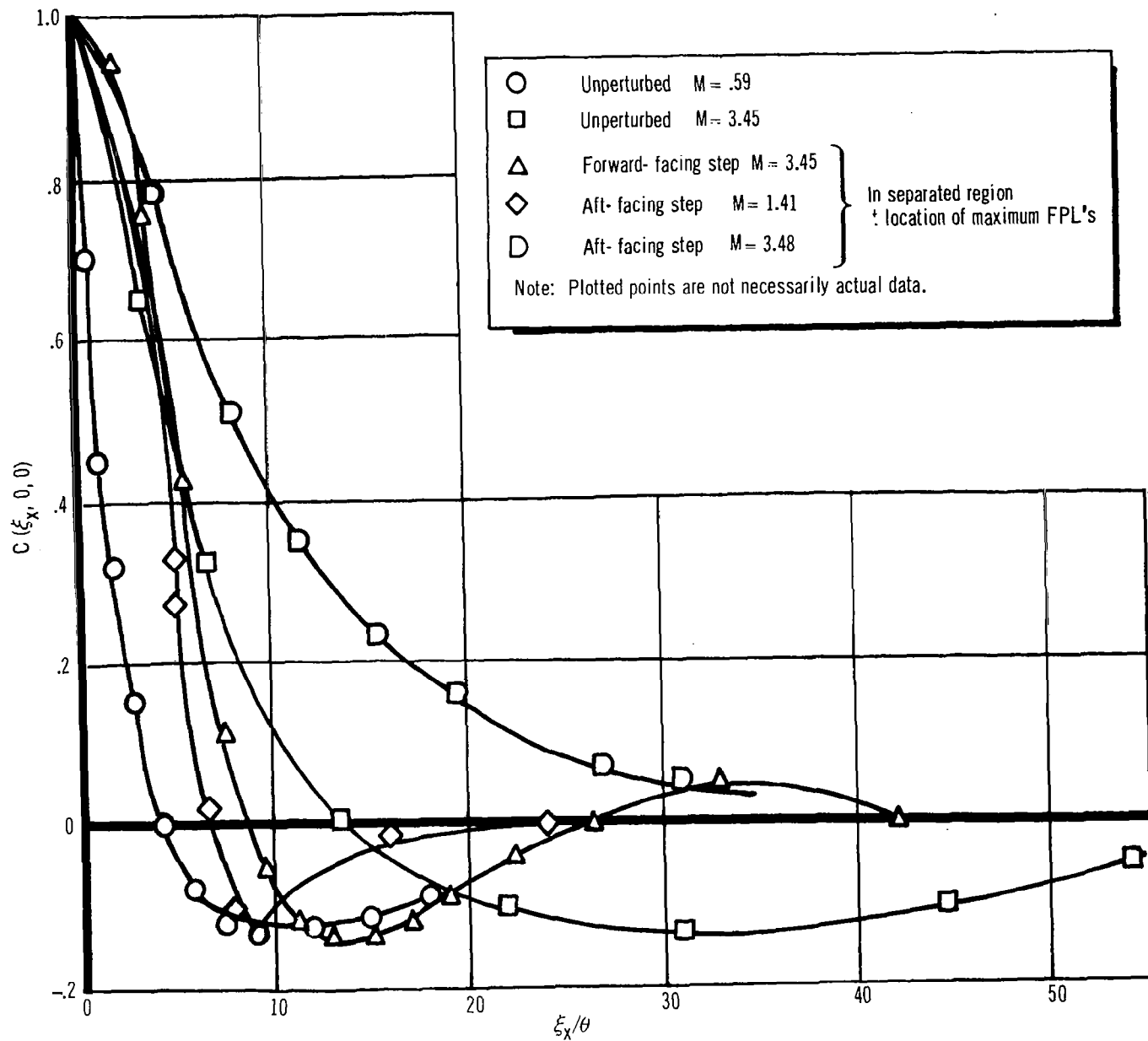
Figure 75. Comparison of Longitudinal Correlation Coefficients for Various Types of Flow
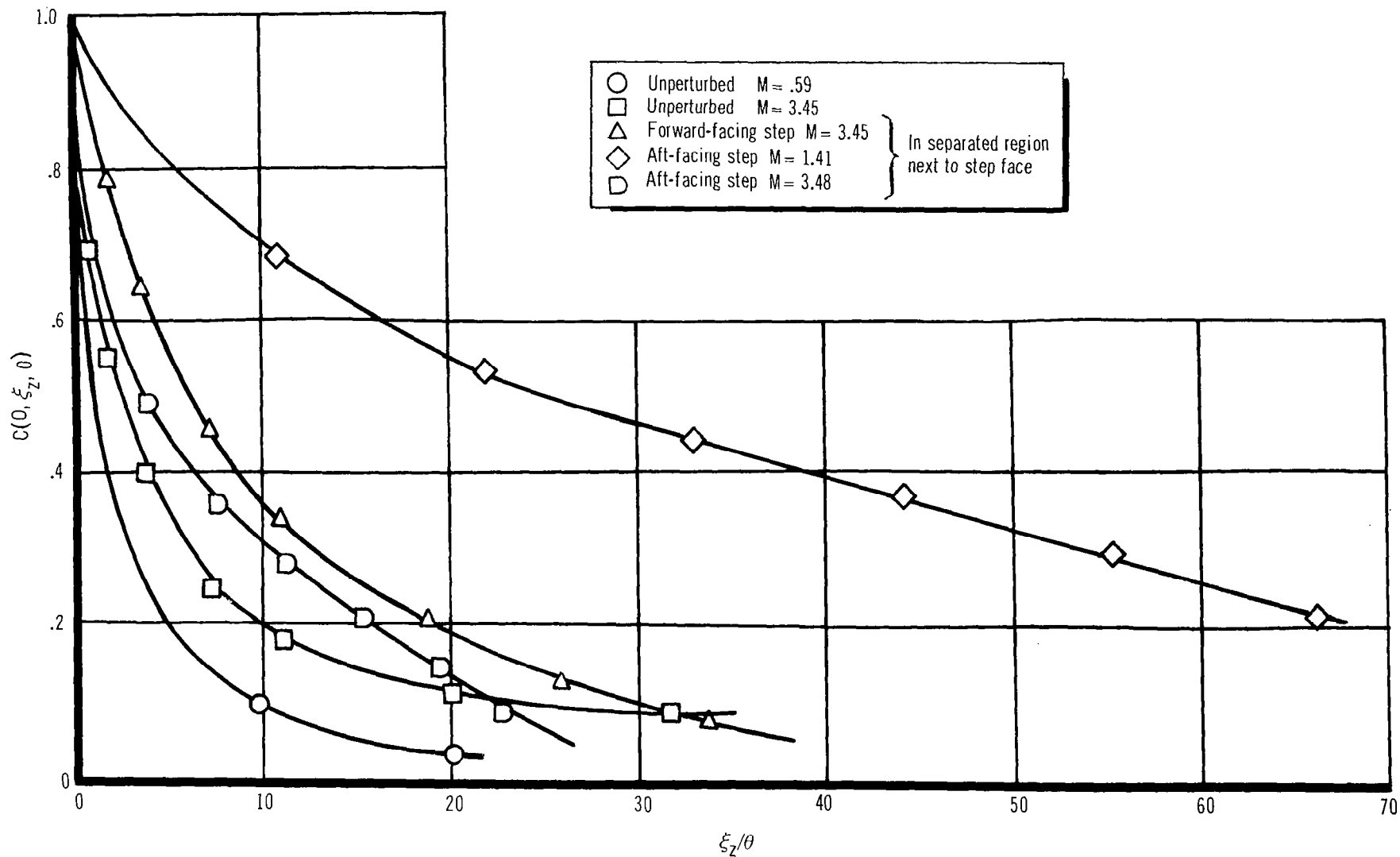
Figure 76. Comparison of Lateral Correlation Coefficients for Various Types of Flow

5.6 Separability of the Functional Representations of the Cross-Correlations

The question of separability of the cross-correlations into a product of functions, each of which depends on only one variable, is of major concern. The concept of separability is employed in calculations throughout the gamut of complex mathematical treatment of structural response, including calculation of the corrections to pressure-measuring devices caused by pressure cancellation effects. The term separability describes a particular feature of functions, i.e., $f(x, y, z) = f_1(x)f_2(y)f_3(z)$. It is a convenient tool mathematically and sometimes makes the difference between a simple solution and a lengthy computer-type calculation to reach an approximation. Part of the intent of this study has been to examine this feature in detail when applied to the fluctuating pressures at a wall under a turbulent boundary layer.

Separability is a property which can be proven in any frame of reference, since the transformation to a different reference frame quite probably will couple the variables, e.g., a distance x in a frame of reference moving with the boundary layer is a distance $(x \pm U_c \tau)$ in a frame of reference fixed with respect to the boundary layer—the plus or minus sign being chosen appropriately for the velocity direction. Hence, to prove separability, it may be convenient to choose one frame of reference in preference to another.

Within measurement accuracy, the spatial and temporal parts of the cross-correlations of the fluctuating pressures measured in this and similar studies are separable, i.e., the supersonic data indicate that the space-time correlation is changing uniformly with time. Some slight discrepancies to this conclusion do occur, but they are not of sufficient magnitude to dispute the fundamental precept. Therefore, the question restricts itself to one of separability of the correlation coefficient in the spatial variables. In the two-dimensional problem (the case at hand), this means that $f(x, z) = f_1(x)f_2(z)$. In terms of cross-correlations, this may be written as the following:

$$R(\xi \cos \beta, \ \xi \sin \beta, \ \tau) = C(\xi_x, 0, 0) \, C(0, \xi_z, 0) \, Z(\tau) \qquad (12)$$

where the R refers to the normalized space-time cross-correlation of an arbitrary point (in time and space) with a reference point, and each C depends on one spatial coordinate only. This expression implies that, for any instant of time in a frame of reference where time and space are uncoupled (a frame of reference moving with the boundary layer, or at the unique time $\tau = 0$ in the frame of reference of the fixed boundary), the local pressure signature has a correlation with nearby pressure signatures which is defined exactly in the entire plane by the product of the longitudinal and the lateral correlation coefficients. As time progresses, the pressure signature changes as it moves, and correlation with the original signature decreases. However, any new pressure signature, at a different time but in the identical region of flow, will have a similar spatial distribution of its correlation coefficient.

The maxima of the space-time correlations, at several locations on the axis parallel with the flow, trace out the time history of the maximum point of the correlation coefficient, as would be observed while moving with the

flow. If these maxima are measured at angles other than $0°$ to the direction
of the flow, they trace out the time history of a variable position in the moving
frame. These latter traces can be examined from the consideration of
separability if, and only if, it is recognized that they are comparable to a
single position in the direction of the flow times a linear distribution in a
direction perpendicular to the flow. In addition, this single x-position has
the unique feature of lying on the z-axis. Hence, the maxima of space-time
correlation functions measured in the fixed frame of reference do not pro-
vide sufficient evidence to prove separability of the two-dimensional correla-
tion coefficient for the frame of reference moving with the boundary layer.

Comparison of the correlation coefficients obtained from the measured
data in the plane with the product $C(\xi_x, 0, 0) \cdot C(0, \xi_z, 0)$ can readily be made.
Fig. 77 shows the contours resulting from the product of functions for super-
sonic unperturbed flow. This figure should be compared with fig. 44, which
presents the correlation coefficient obtained from measurements in the plane.
It is obvious that considerable difference exists. The difference between
the two figures can be described in several ways. For example, the plot of
C versus ξ_x, ξ_z describes a three-dimensional figure. For each case,
i.e., from planar measurements and with separability assumed, an approxi-
mate volume of the figure can be obtained graphically. This volume is
equivalent to the integral of the normalized function with integration limits
of 0.05 (or 0.1) to 1.0. Smaller values of C were not used because they
were within the noise floor of the calculations. (For this comparison,
only positive values are used.) This is somewhat analagous to the integral
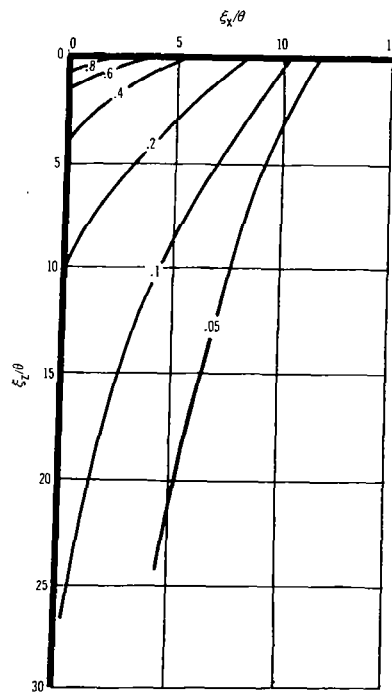
Figure 77. Contours of Equal Correlation Coefficient Assuming Separability,
Unperturbed Flow, M = 3.45

length scale described earlier and might be called a positive "integral area" scale. The ratio of the volume resulting from the separability assumption (V_s) to the actual coefficient volume resulting from measurements (V_m) was found to be 0.46. Assuming separability therefore can introduce an error of a factor of two in the "integral area" scale (the integrated correlation coefficient for the fluctuating pressures caused by, in this case, an unperturbed supersonic turbulent boundary layer).

The trend of nonseparability is sufficiently strong to suggest that, even for small areas within the flow field, there is error introduced by the assumption of separability. For such problems as the calculation of pressure cancellation corrections for the sensing element of a transducer, the discrepancy between the real case and the assumed separable case is probably much smaller than the factor of 2 quoted above for large correlated areas. Unfortunately, instrumentation was not previously available which could define the function for extremely small spacings—on the order of a sensing element diameter. Current development is providing such capability, at least for transducer sizes on the order of 0.25 in. in diameter.

Separability was argued for the forward-facing and aft-facing steps. Table VI gives the approximate ratio of V_s/V_m acquired by graphical integration. These ratios are based on figs. 78 to 81 which compare with figs. 49, 50, 52, and 62, respectively. Table VI indicates that in the case of the forward-facing step configuration, the assumption of separability seems to hold near the step face. The aft-facing steps are more like the unperturbed case, as significant discrepancies exist between V_s and V_m. If the lateral coefficient $C(0, \xi_z, 0)$ of the aft-facing step near the step face is assumed to be indicative of the lateral coefficient in the region of reattachment, then separability is nearly approximated. However, as mentioned previously, data were not acquired which would substantiate this use of the lateral coefficient from one region as applied to another region of flow.

It is interesting to note that, of the perturbed flows, the one without evidence of a lateral convection velocity is also the one in which the assumption of separability is a good approximation—i.e. the forward-facing step. Perhaps part of the nonseparable tendency in the aft-facing step case is caused by the pressure signature having a lateral convection velocity. If this latter phenomenon results solely from the confined volume of the separated flow (the two-dimensional boundary layer on the side wall being bounded by the floor and ceiling of the wind tunnel only 12 in. apart), then work in three-dimensional boundary layers may bring a closer agreement between V_s and V_m. However, the forward-facing step results remain to discourage such a thought, since the separated region in front of the step was also bounded in a distance of 12 in., and should therefore indicate a similar problem.

TABLE VI

COMPARISON OF THE GRAPHICALLY INTEGRATED CORRELATION
COEFFICIENT BASED ON THE MEASURED DATA IN
THE TWO-DIMENSIONAL PLANE WITH THAT BASED ON THE
MEASURED DATA PLUS THE SEPARABILITY ASSUMPTION *

	V_m	V_s	V_s/V_m (= 1.0 if the spatial variables are separable)
Unperturbed supersonic, M = 3.45	27.9	14.0	0.46
Aft-facing step, M = 1.41 near step face	599.1	443.2	0.74
Aft-facing step, M = 3.48 near step face	41.4	22.0	0.53
Aft-facing step, M = 3.48 near reattachment (assumed lateral coefficient)	56.1	49.6	0.88
Forward-facing step, M = 3.45	35.7	37.1	1.04

$$* \text{ where } V_m = \sum_{C = 0.05 \text{ or } 0.1}^{1.0} \left[\frac{C(\xi \cos \beta, \xi \sin \beta, 0) \Delta (\xi \cos \beta) \Delta (\xi \sin \beta)}{\theta^2} \right]$$

$$V_s = \sum_{C = 0.05 \text{ or } 0.1}^{1.0} \left[\frac{C(\xi_x, 0, 0) \cdot C(0, \xi_z, 0) \Delta \xi_x \Delta \xi_z}{\theta^2} \right]$$
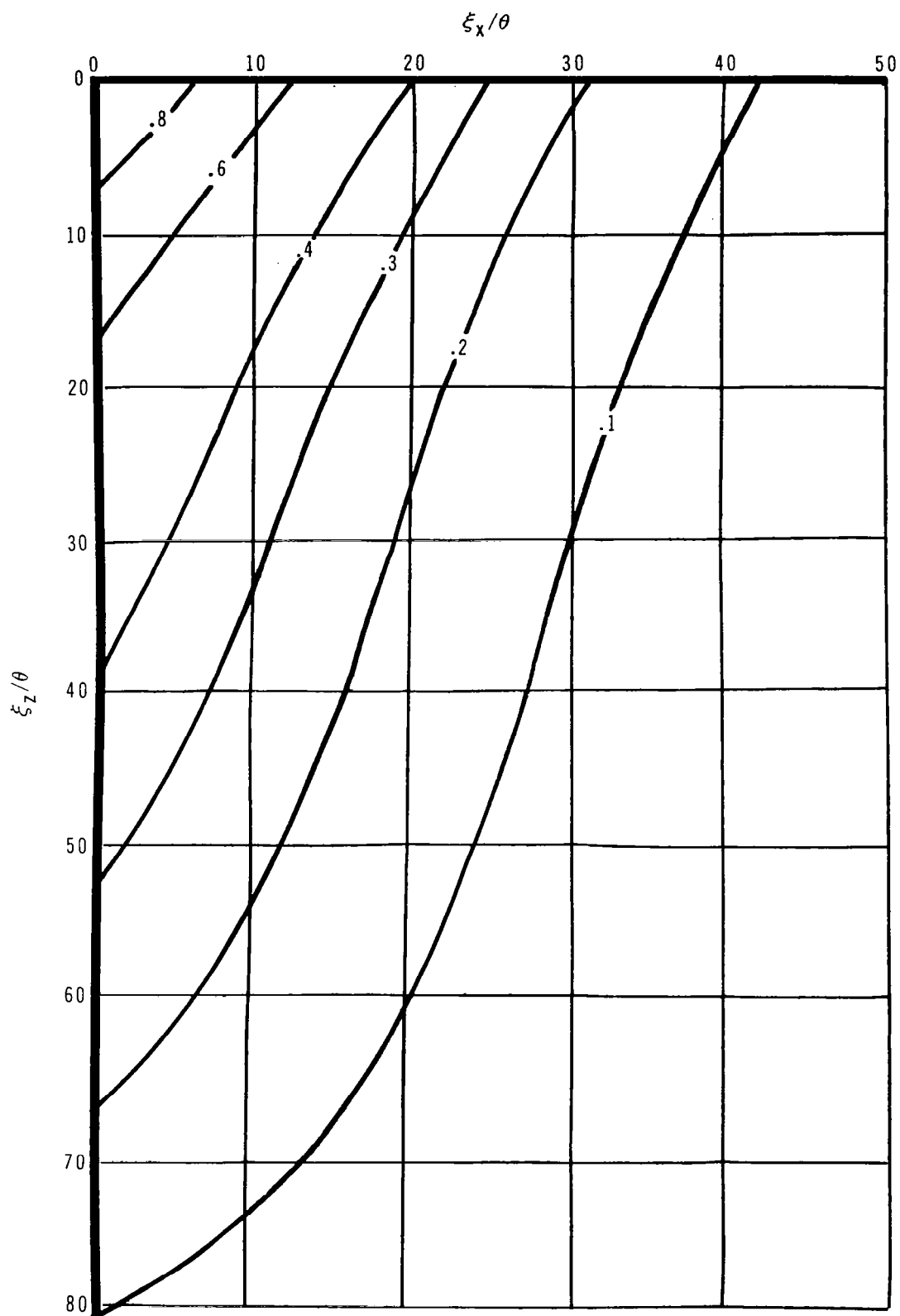
Figure 78. Contours of Equal Correlation Coefficient, Assuming Separability, for an Aft-Facing Step, Near Step Face, M = 1.41
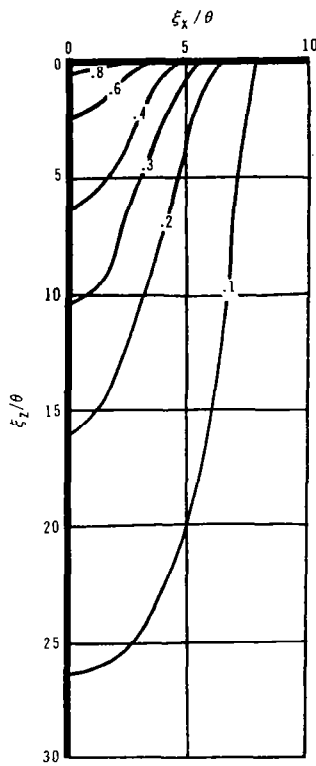
Figure 79. Contours of Equal Correlation Coefficient, Assuming Separability,for an Aft-Facing Step, Near Step Face, M = 3.48
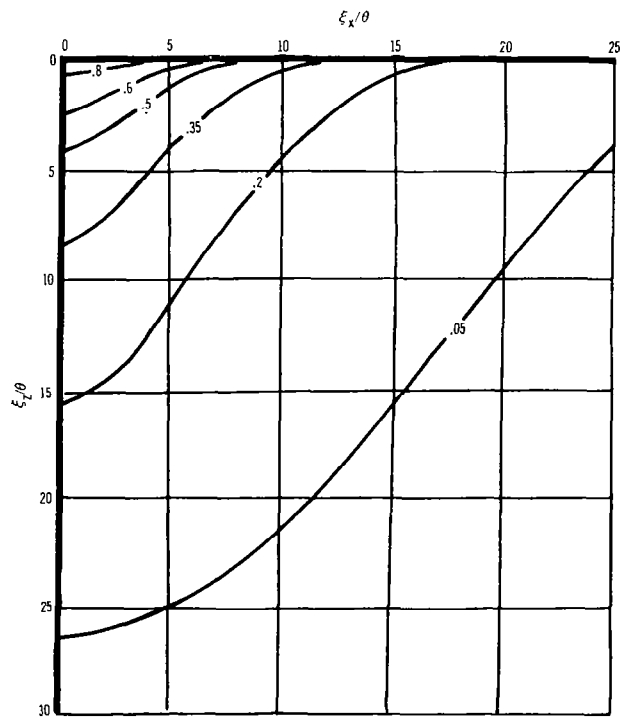
Figure 80. Contours of Equal Correlation Coefficient, Assuming Separability,for an Aft-Facing Step, Near Reattachment, M = 3.48
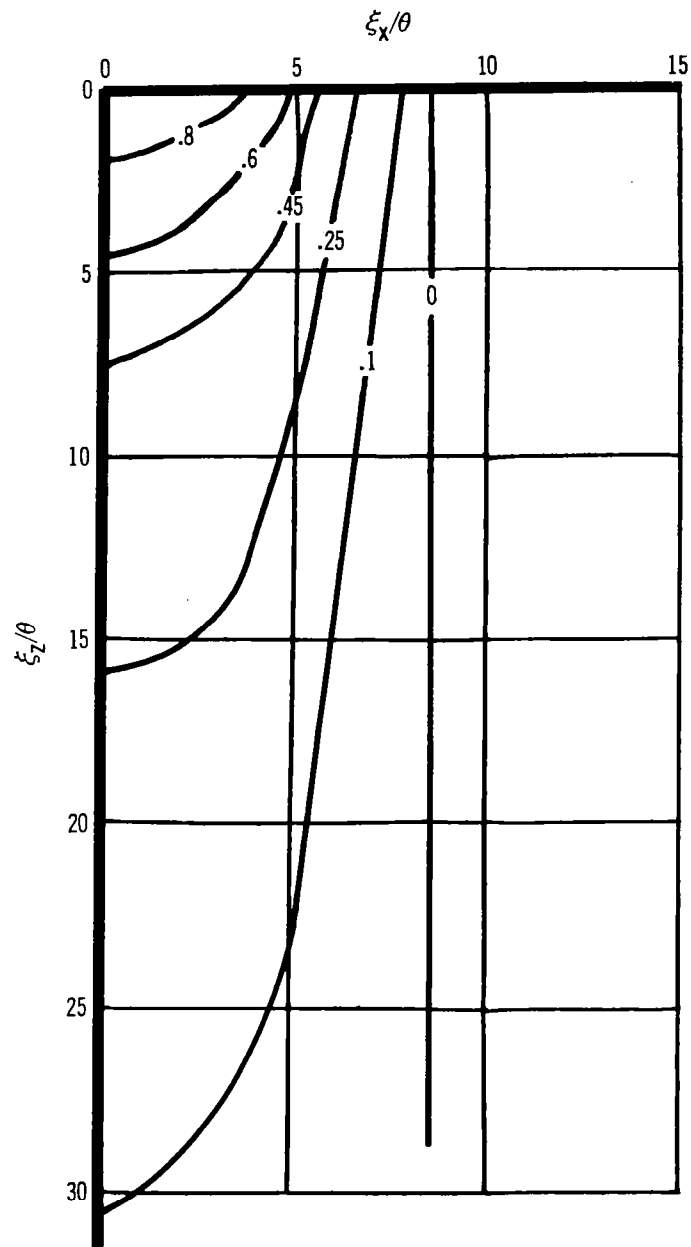
Figure 81. Contours of Equal Correlation Coefficient, Assuming Separability, for a Forward-Facing Step, Near Step Face, M = 3.45

5.7 Mathematical Description of the Cross-Correlation Functions

One of the main goals of this study was to describe the correlation functions of the fluctuating pressure field in terms of mathematical relationships. The broad-band functions determined from the data could then be inserted in mathematical formulation of structural response studies to permit numerical evaluation. Obviously, some of the assumptions inherent in such an approach are that (1) capability exists to describe the structural response by an equation, (2) the use of a broad-band correlation function to approximate the various narrow-band correlation functions for each mode of response is acceptable for preliminary design calculations, and (3) the correlation functions are known and are usable in the formal approach. In essence, such a procedure is normally employed to predict gross response characteristics and to aid in preliminary design efforts. Of the three items assumed, the third most often presents difficulties.

It had been hoped that description of the longitudinal and lateral spatial correlation coefficients and the temporal dependence would be sufficiently accurate to describe the total function mathematically. The previous section on separability concluded that such a formulation is inadequate. Unfortunately, the contours of equal correlation coefficients in the plane did not lend themselves to mathematical description in simple format. For example, assuming

$$C(\xi \cos \beta, \xi \sin \beta, 0) = C(\xi_x, 0, 0) \cdot C(0, \xi_z, 0) \cdot E(\xi \cos \beta, \xi \sin \beta, 0) \tag{13}$$

for the unperturbed supersonic boundary layer resulted in the following complex expression for E

$$E(\xi_x, \xi_z, 0) = 10^{-2} \left[5.3 \sin 2\beta + 1.9 \sin 4\beta + 0.3 \sin 6\beta \right]$$

$$\cdot e^{-0.6 \sin 2\beta} \, r \left[1.55 + 1.45 \tan \beta - r \right] \tag{14}$$

where

$$r = \sqrt{\xi_x^2 + \xi_z^2} \quad \text{and} \quad \theta = \tan^{-1} (\xi_z / \xi_x) \quad .$$

122

Table VII lists the various "best fit" mathematical functions obtained during this study. These equations assume separability and thus are incorrect by at least the amount indicated in the previous section. In that sense, the table is presented for the academician rather than as a systematic valuation of the cross-correlation in the plane. A better, but far more time-consuming, presentation would be a numerical analysis of the functions resulting from the measured data. Such a presentation would dictate the use of complicated computer programs to predict simple structural response. It is concluded that, for purposes of gross prediction by analytical procedures, the separated functions in table VII could be used if properly weighted by correction factors similar to the factors listed in table VI.

TABLE VII

MATHEMATICAL DESCRIPTION OF CORRELATION FUNCTIONS*

Type of Flow	Region	$C(\xi_x/\theta,\ 0,\ 0)$	$C(0,\ \xi_z/\theta,\ 0)$	$Z(\tau)$
Unperturbed M = 3.45	Anywhere	$e^{-0.043\,\xi_x/\theta}\left[\dfrac{2.175}{(1+0.015\,\xi_x/\theta)^3}-1.175\right]$	$\dfrac{1}{1+0.412\,\xi_z/\theta}$	$\dfrac{1}{1+1.27\times10^4\tau}$
Forward-Facing Step M = 3.45	In separated region	$\dfrac{1}{1+9.5\times10^{-4}(\xi_x/\theta)^3}\cos(0.059\pi\xi_x/\theta)$	$\dfrac{1}{1+0.055(\xi_z/\theta)^{1.5}}$ **	$\dfrac{1}{1+3.5\times10^4\tau}$
Aft-Facing Step M = 3.48	Reattachment max FPL's	$e^{-0.09\,\xi_x/\theta}\left[\cos\left(\dfrac{\pi}{40}\dfrac{\xi_x}{\theta}\right)+\sin\left(\dfrac{\pi}{80}\dfrac{\xi_x}{\theta}\right)\right]$	—	$\dfrac{1}{1+6.0\times10^4\tau}$
Aft-Facing Step M = 3.48	Near step face	$e^{-0.115\,\xi_x/\theta}\left[\cos(0.057\pi\xi_x/\theta)\right]$	$\left(0.55e^{-0.425\,\xi_z/\theta}\right)-0.015\,\xi_z/\theta+0.45$	$\dfrac{1}{1+6.3\times10^4\tau}$
Aft-Facing Step M = 1.41	Reattachment max FPL's	$e^{-0.02(\xi_x/\theta)^2}\left[\cos\left(\dfrac{\xi_x}{\theta}\dfrac{\pi}{11.5}\right)+0.32\sin\left(\dfrac{\xi_x}{\theta}\dfrac{\pi}{20}\right)\right]$	—	$\dfrac{1}{1+9.0\times10^4\tau}$
Aft-Facing Step M = 1.41	Near step face	$e^{-0.05\,\xi_x/\theta}\left[\cos\left(\dfrac{\pi}{80}\dfrac{\xi_x}{\theta}\right)+\sin\left(\dfrac{\pi}{160}\dfrac{\xi_x}{\theta}\right)\right]$	$\left(0.33e^{-0.12\,\xi_z/\theta}\right)-0.007\,\xi_z/\theta+0.67$	$\dfrac{1}{1+1.1\times10^5\tau}$
Shock M = 3.45	Through shock ($U_c/U_\infty = 0.3$ Data)	$e^{-0.05\,\xi_x/\theta}\left[\dfrac{2.05}{(1+0.035\,\xi_x/\theta)^3}-1.05\right]$	—	$\dfrac{1}{1+5.5\times10^4\tau}$

* The correlation functions given above are even functions of their respective arguments.

** Only the positive square root is to be taken.

Section 6

CONCLUSIONS

This report has presented data obtained during small-scale wind tunnel tests. The turbulent boundary-layer-induced pressure fluctuations at a rigid wall have been discussed for uniform and perturbed flows, and this empirical description of the fluctuating pressure field has pointed out specific details of each type of flow. From the total study, the following general conclusions have been made:

(1) The spectra for unperturbed flow compare best for the different Mach numbers when normalized to θ and τ_w.

(2) The overall rms levels showed consistency with Mach number and with data of other investigators when normalized with dynamic pressure. When normalized to wall shearing stress, the levels were consistent with Mach number but deviated considerably from data of other investigators.

(3) Certain characteristic spectral shapes may be associated with the different flow phenomena, particularly in the regions of separation and reattachment.

(4) The approximate location of separation and reattachment in perturbed flow may be predicted from fluctuating pressure spectra.

(5) FPL's normalized with respect to free-stream dynamic pressure produced the following maximum values in various perturbed flow regions:

(A) Aft-facing step at M = 1.41, $\sqrt{\overline{p^2}}/q_\infty = 28.0 \times 10^{-3}$, near reattachment, compared to 4.2×10^{-3} in unperturbed flow

(B) Aft-facing step at M = 3.48, $\sqrt{\overline{p^2}}/q_\infty = 8.8 \times 10^{-3}$, near reattachment, compared to 1.7×10^{-3} in unperturbed flow

(C) Forward-facing step (h ≈ 1.2δ) at M = 1.40, $\sqrt{\overline{p^2}}/q_\infty \geq 27.5 \times 10^{-3}$, at the step face and $\sqrt{\overline{p^2}}/q_\infty = 28.5 \times 10^{-3}$, near reattachment behind the step

(D) Forward-facing step (h ≈ 0.9δ) at M = 3.45, $\sqrt{\overline{p^2}}/q_\infty = 31.5 \times 10^{-3}$, at the step face

(E) Forward-facing step (h ≈ 1.9δ) at M = 3.45, $\sqrt{\overline{p^2}}/q_\infty = 46.0 \times 10^{-3}$, at the step face

(F) Incident shock wave (7.5°) at M = 3.45, $\sqrt{\overline{p^2}}/q_\infty = 15.0 \times 10^{-3}$, near separation and $\sqrt{\overline{p^2}}/q_\infty = 19.5 \times 10^{-3}$, near reattachment.

(6) The flow behind an aft-facing step contains two distinct regions with different typical spectra and correlation coefficients. One is associated with the phenomenon of separation of the flow, and one with the region of reattachment.

(7) The flow in front of a forward-facing step exhibits a similar sub-division as described in (6) for the aft-facing step—one set of results for the separation phenomenon, and one for the region of separation.

(8) The flow in the region of an impinging shock wave exhibits combined characteristics for the separation and reattachment regions as discussed in (6) and (7) for the aft- and forward-facing steps.

(9) Correlation across a region of boundary layer perturbed by an incident shock indicates a very localized, but severe phenomenon in which the pressure signature is rapidly dissipated (bearing resemblance to the characteristics of separation in front of a step). The pressure signature reverses in polarity as it passes through the incident and reflected shocks.

(10) The time dependence of the cross-correlations behaves similarly for all the flows encountered in this study, but a completely generalized mathematical description of the broad-band results was not obtained. Frequency dependence might be the reason for the difficulty in finding a generalized expression, but narrow-band calculations would be necessary to substantiate such a conjecture (to accurately determine the major frequency).

(11) Assuming separability of the spatial part of the cross-correlation into functions dependent on only one variable introduces an error of as much as 100% in a "correlation area" scale.

APPENDIX A

DETERMINATION OF BOUNDARY-LAYER PARAMETERS
AND THEIR VARIATION WITH DISTANCE

The characteristics of the turbulent boundary layer on the tunnel sidewall were determined from measurements of boundary-layer total pressure profiles and local wall static pressures. The variation of these parameters with distance along the sidewall was determined from measurements of the parameters at different tunnel stations and from turbulent boundary-layer growth theory.

The velocity ratio, u/U_e, was calculated from the total pressure ratio, and local static pressure, using the Rayleigh pitot formula. The Crocco relationship between velocity and temperature was used to calculate the static temperature in the boundary layer. Previously (ref. 1), measurements of the wall temperatures during 10- to 15-sec. runs had shown that the mean wall temperature was approximately equal to the stagnation temperature. Stagnation temperature was thus assumed to be constant throughout the boundary layer and the Crocco equation reduced to

$$T = T_{t_e} - \left(T_{t_e} - T_e\right)\left(u/U_e\right)^2 \quad . \tag{A-1}$$

From eq. (A-1) and the perfect gas equation of state, the density ratio becomes

$$\rho/\rho_e = \frac{T_e}{T_{t_e} - \left(T_{t_e} - T_e\right)\left(u/U_e\right)^2} \quad . \tag{A-2}$$

The boundary-layer thickness was defined as the intersection on log-log paper of a $1/n$ power law fit to the measured distances from the wall with the velocity at the edge of the boundary layer. (See section 3.3 and fig. 5.) The boundary-layer displacement and momentum thicknesses were then obtained from the following equations:

$$\delta^* = \int_0^\infty \left(1 - \rho u/\rho_e U_e\right) dy \tag{A-3}$$

$$\theta = \int_0^\infty \left(\rho u/\rho_e U_e\right)\left(1 - u/U_e\right) dy \tag{A-4}$$

and

$$H \equiv \delta^*/\theta \quad . \tag{A-5}$$

APPENDIX A

In the previous investigation (ref. 1), the value of the local skin-friction coefficient was obtained using Eckert's reference enthalpy method (ref. 30). However, the values obtained using this method were considered to be slightly high and a procedure described by Roshko and Thomke**, based on theory and experiments of Coles (ref. 31), was used to determine skin-friction coefficient:

$$c_f = (\rho_w/\rho_\infty)(\mu_w/\mu_\infty)(\bar{R}_{\bar{\theta}}/R_\theta)\bar{c}_f. \tag{A-6}$$

where $\bar{c}_f$ and $\bar{R}_{\bar{\theta}}$ are the transformed skin-friction coefficient and the transformed momentum thickness Reynolds numbers, respectively.

In eq. (A-6),

$$\rho_w/\rho_\infty = T_\infty/T_w = T_\infty/T_{t_e} \tag{A-7}$$

and

$$\mu_w/\mu_\infty = \mu_{t_e}/\mu_\infty = (T_{t_e}/T_\infty)^{3/2}\left(\frac{T_\infty + 200}{T_{t_e} + 200}\right) \tag{A-8}$$

Values obtained from the above equations for δ, δ^*, θ, H, c_f, and τ_w were tabulated for the various test Mach numbers in table I for tunnel station $x_w = 0$.

Fluctuating pressure measurements were taken at a number of stations on the 14.5-in. sidewall insert. These measurements were normalized to various boundary-layer parameters. It was therefore necessary to determine the boundary-layer parameters over the entire sidewall insert. Data from ref. 1, taken at $x_w = -4$ in., were available and were used together with the present values (at $x_w = 0$) to determine spatial variation of the parameters. The data were used as experimental points in eq. (7) of Tucker (ref. 32) to calculate the apparent growth distance of the boundary layer and the slope of the curve where the subscripts A and B refer to the two stations at which data were measured.

$$\frac{\theta_B}{12} = \frac{\theta_A}{12} + \frac{7K}{6}\left[\frac{32}{M_\infty}\frac{(1 + 0.2M_\infty^2)^2}{(2 + 0.2M_\infty^2)^5}\right]^{1/7}\left[\frac{x_B}{12}^{6/7} - \frac{x_A}{12}^{6/7}\right] \tag{A-9}$$

**The procedure was outlined by Professor Roshko and published at Douglas Aircraft Company as an internal memorandum by Thomke. The method used a rapidly converging iteration to obtain so-called "transformed skin-friction coefficient and transformed momentum thickness Reynolds number."

128

APPENDIX A

The next step was to normalize the boundary-layer thickness values at each Mach number to a constant unit Reynolds number (Re/in. = 10^6) as follows:

$$\delta = \frac{0.41\, x^{4/5}}{(\text{Re/in.})^{1/5}} \qquad\qquad (A\text{-}10)$$

where the constant 0.41 was the best average from all the measured data. These values were plotted versus Mach number (not shown) and found to give a smooth variation.

The next step was to calculate the variation of δ and Θ with distance along the wall. Where necessary, the calculated data were adjusted vertically (i.e., retaining constant slope) to best fit the measured points. Figs. A-1 and A-2 show the variation of δ and Θ, respectively, at all Mach numbers for the test. Displacement thicknesses were calculated from the known form parameters**, $H \equiv \delta^*/\Theta$, and also plotted as a function of distance (fig. A-3).

The remaining final calculation was the variation of skin-friction coefficient with distance. The data of fig. A-2 were used to calculate values of R_Θ. The values of R_Θ were then used in eq. (A-6) to compute c_f variation along the sidewall at each Mach number. This variation is given in fig. A-4.

The data presented in figs. A-1 through A-4 were used exclusively in this report to normalize the fluctuating pressure data even in perturbed flow regions. No attempts were made to determine boundary-layer parameters ahead of, or behind, the steps or shock waves. In all cases, uniform flow boundary-layer parameters were used at equivalent sidewall stations for the perturbed flow.

** The form parameters calculated from the measured data were compared for consistency with the data of Reshotko and Tucker (ref. 35). The comparison is shown on fig. 8.

Figure A-1. Calculated Variation of Boundary Layer Thickness with Distance Along the Tunnel Sidewall

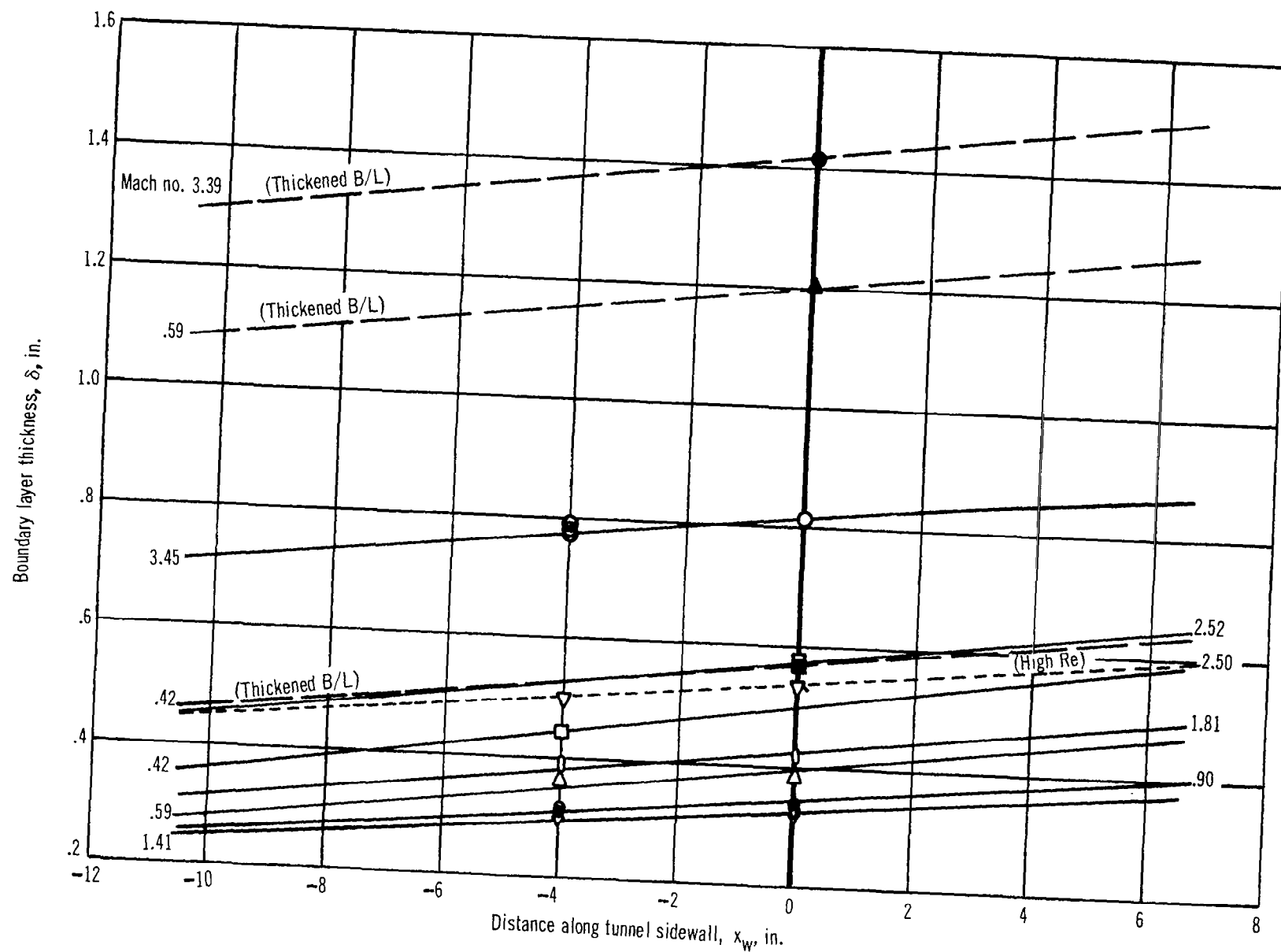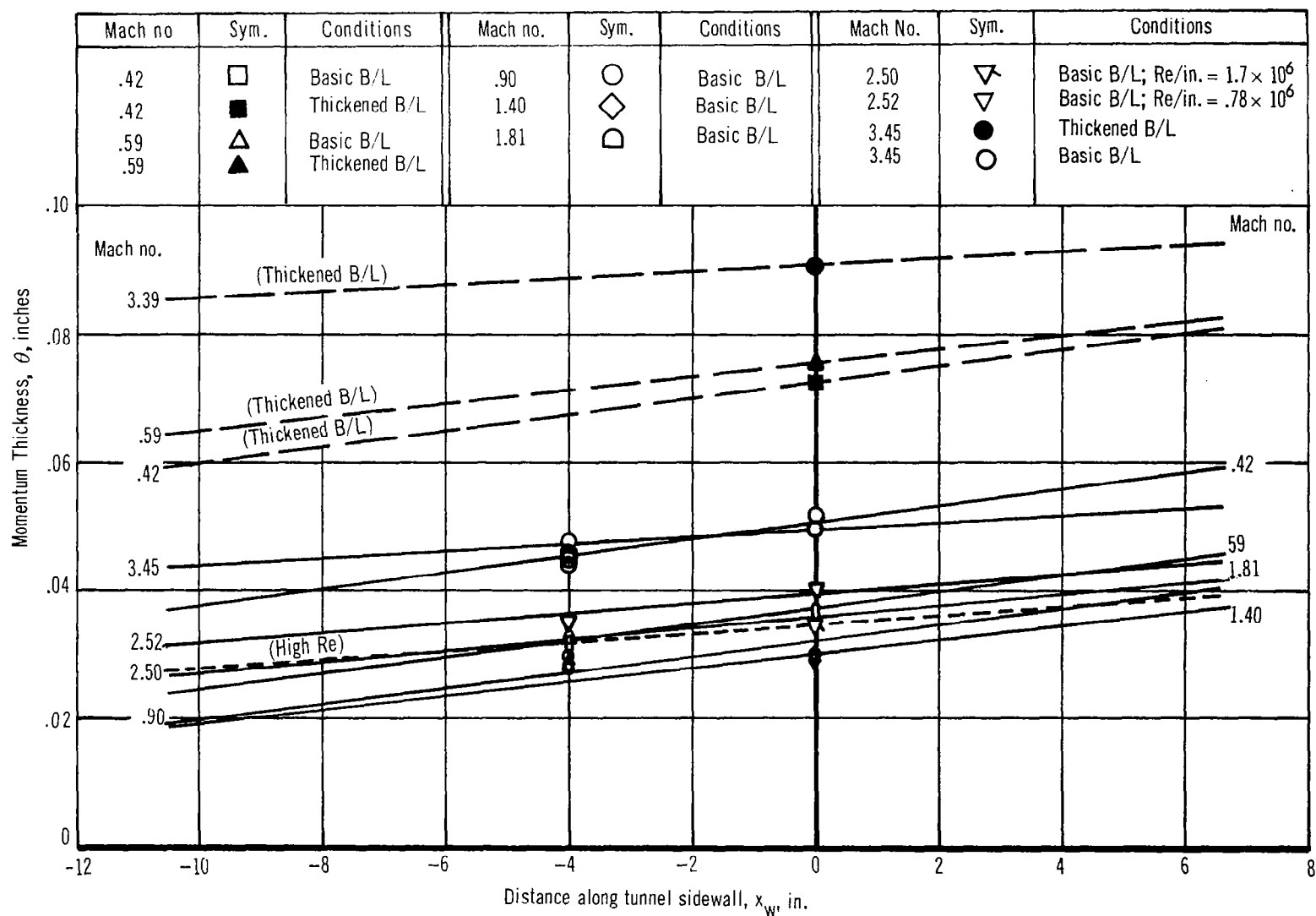| Mach no	Sym.	Conditions	Mach no.	Sym.	Conditions	Mach No.	Sym.	Conditions
.42	□	Basic B/L	.90	○	Basic B/L	2.50	▽	Basic B/L; Re/in. = 1.7×10^6
.42	■	Thickened B/L	1.40	◇	Basic B/L	2.52	▽	Basic B/L; Re/in. = $.78 \times 10^6$
.59	△	Basic B/L	1.81	⬠	Basic B/L	3.45	●	Thickened B/L
.59	▲	Thickened B/L				3.45	○	Basic B/L

Figure A-2. Calculated Variation of Boundary Layer Momentum Thickness with Distance Along the Tunnel Sidewall
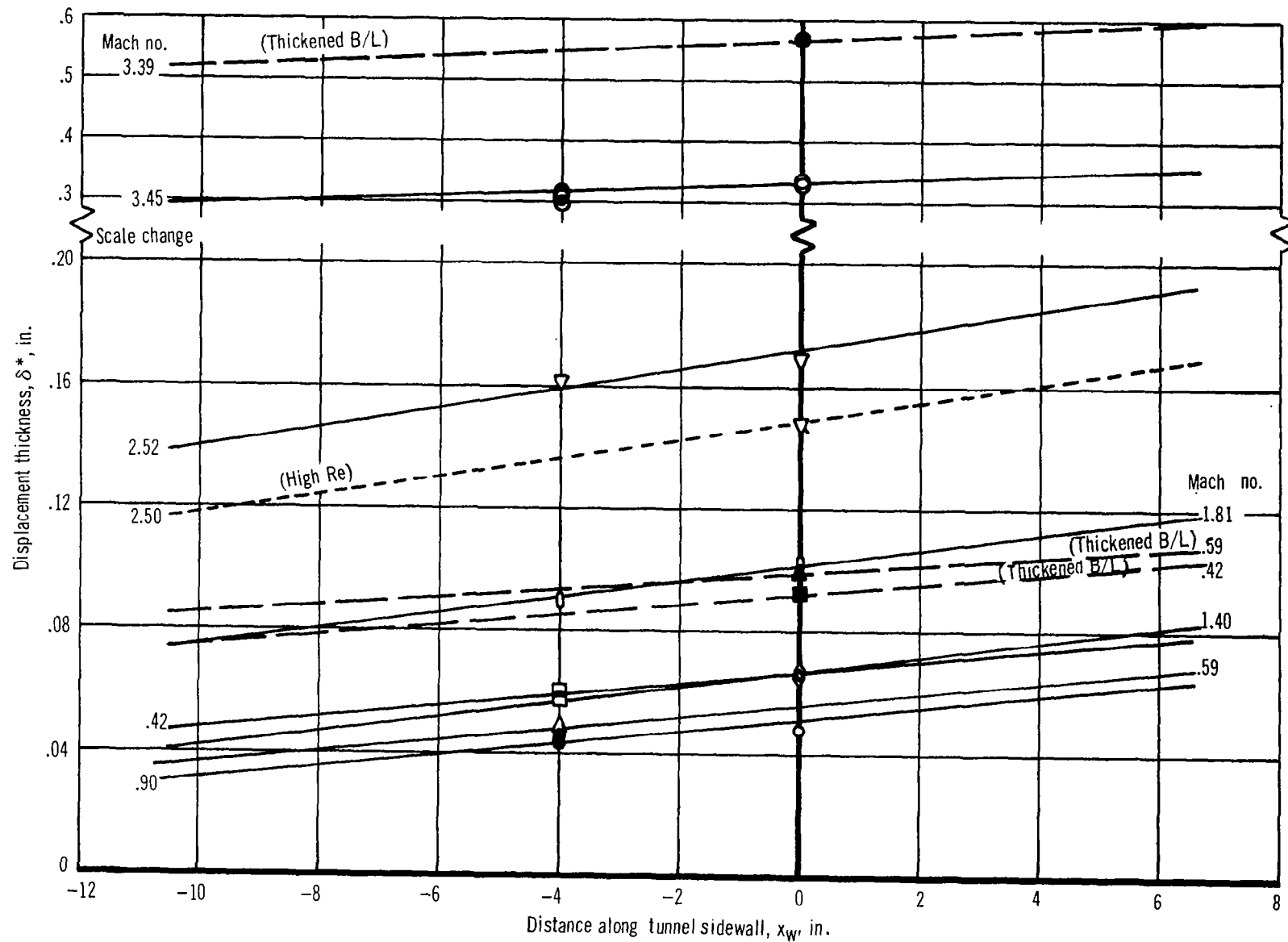
Figure A-3. Calculated Variation of Boundary Layer Displacement Thickness with Distance Along the Tunnel Sidewall
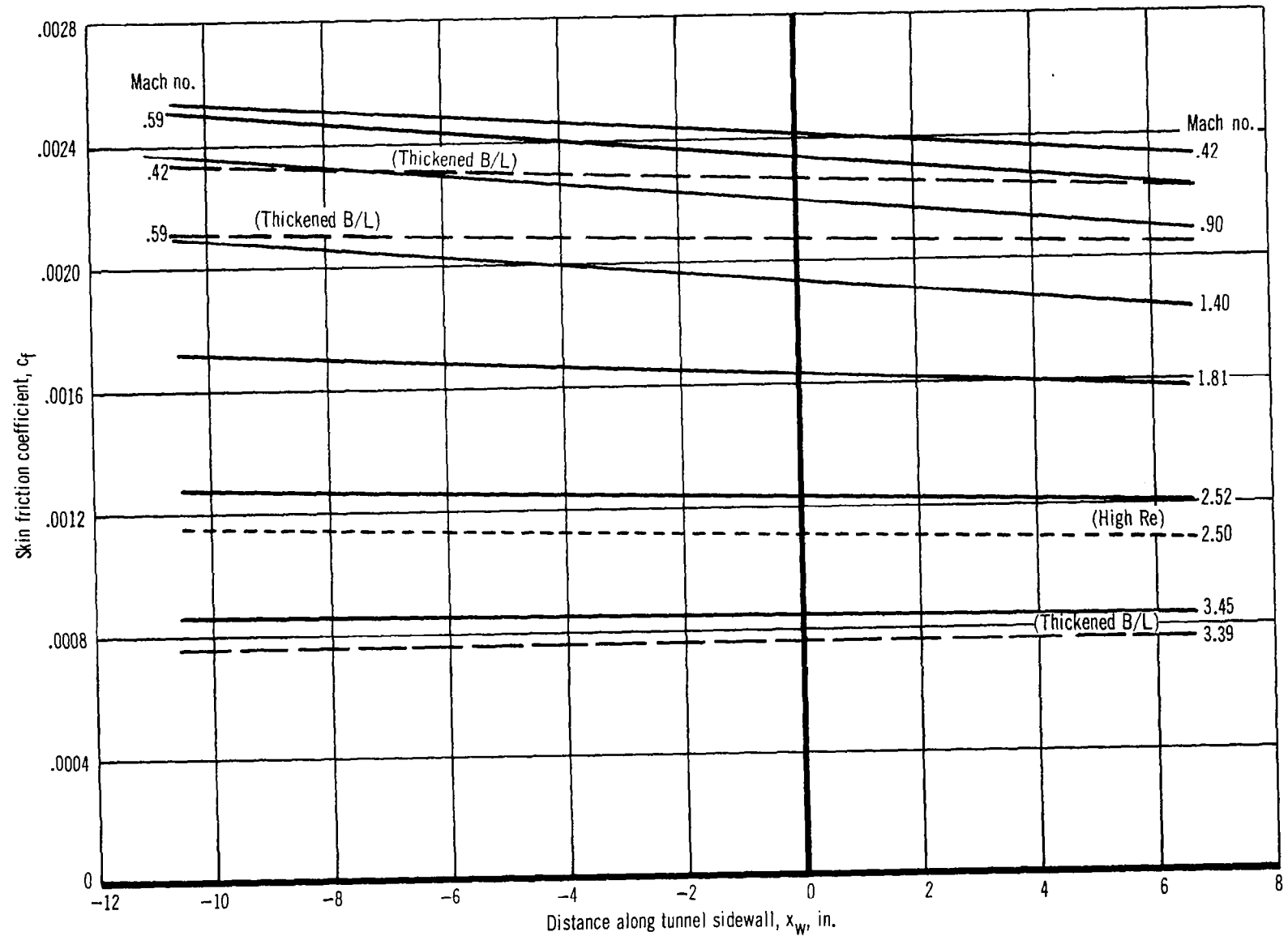
Figure A-4. Calculated Variation of Skin Friction Coefficient with Distance Along the Tunnel Sidewall

Appendix B

CALIBRATIONS OF INSTRUMENTATION USED FOR
MEASURING FLUCTUATING PRESSURES

Many subassemblies and total systems were calibrated in preparation for the test series discussed in this report. The more important calibrations are briefly summarized in this appendix.

Prior to specialized calibrations, all the electronic support equipment was checked to ensure that its performance was within manufacturer's specifications for noise, frequency response, phase shift, sensitivity, and linearity. These checks included characteristics of the low noise cables, the tape recorder and its frequency compensation, magnetic tape noise, reproduce amplifiers and filter compensation characteristics, switching networks, and all checkout equipment such as voltage meters, the phase meter, oscilloscopes, etc. The only equipment permitted to deviate from the manufacturer's specifications were the Columbia Research Corporation's amplifiers in the data acquisition system. The noise floor in these borrowed Columbia amplifiers exceeded the specifications by a factor of 2 to 3 in some cases (rather than the specified maximum of 40 μV of noise). Several factors were involved in the decision to make this one exception. The only observable detrimental effect of this compromise on the quality of the test equipment was in the cross-correlation of the low signal voltages corresponding to low-level subsonic turbulent boundary-layer-induced pressure fluctuations.

B.1 Microphone Calibration

The sensitivity and frequency response of the Brüel and Kjaer (B&K) 1/4-in. Model 4136 condenser microphones were established at both atmospheric and reduced (1.0 psia) pressure. These were the same microphones used previously, and the results of the calibrations agreed with the typical curves presented on fig. 41 of ref. 1. The test setup, as given in fig. B-1, represents a standard B&K calibration procedure except for the addition of the vacuum chamber. The dc voltage to the actuator was reduced at the lower static pressure to avoid arcing, so that the low pressure data were restricted to frequencies less than or equal to 60 000 cps. This was sufficient, however, to measure the expected resonance between 40 000 and 50 000 cps.

The Atlantic Research Corporation's (ARC) LD107-M1 piezoelectric transducer was calibrated in several ways. The sensitivity was checked against the manufacturer's data by comparison with a calibrated B&K 1/4 in. microphone. A progressive wave tube was used to maintain 140 dB* at

---

*All decibel levels are re 0.0002 dyn/cm^2 whether describing acoustic pressure levels or pressure fluctuation levels.
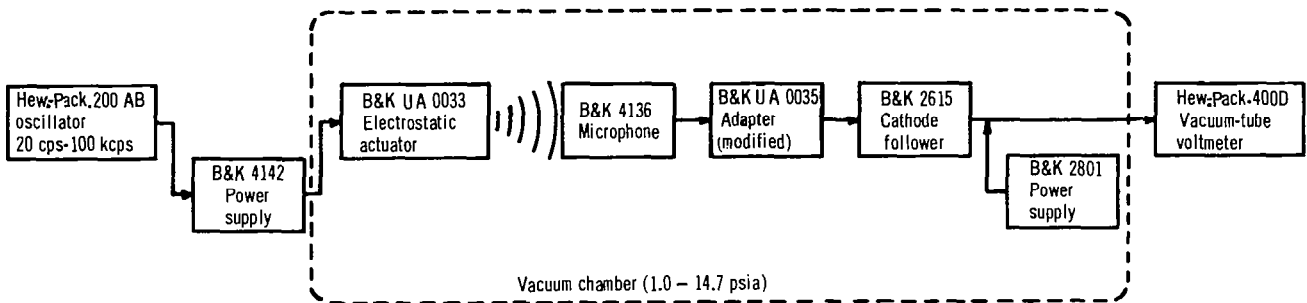
Figure B-1. Schematic Diagram for Calibration of the B & K 4136 Microphones

400 cps (see fig. B-2A). Next, the 500 to 20 000 cps frequency range was investigated for the ARC's by a comparative free field calibration. A loudspeaker, with a swept harmonic input and a constant acoustical output, was the acoustical source (fig. B-2B). Diffraction effects were calculated to be negligible for this grazing incidence test. Finally, the frequency response of the LD107-M1 transducer was measured between 20 000 and 90 000 cps. A special electrostatic loudspeaker was built to provide a pressure level of 138 dB over the frequency range of interest. Both the LD107-M1 and a reference microphone were mounted in a baffle with their sensing elements flush with the surface. Grazing incidence of the nearly plane waves kept diffraction and/or reflection effects to a minimum (acoustic pressure cancellation on the sensing element of the LD107-M1 was negligible in this frequency range). A booster amplifier with a fixed gain kept the output level of the LD107-M1 at a suitable voltage. Fig. B-2C is a block diagram of the system. The resultant responses of the transducers used in this study were flat within ±3 dB to 100 000 cps. Minor variations were noted within the range, and added as a correction to the wide frequency power spectral density plots. No correction was made to the data prior to the space-time correlation calculations, since frequency averaging is involved and the minor fluctuations about a mean in the frequency range of interest would be cancelled.

A – Sensitivity Calibration

B&K 1014 oscillator 400 cps → McIntosh 60W Audio amplifier → Altec Lansing 594B Speakers (2))))))

2-in Progressive wave tube

Atlantic Res. LD 107-M1 Transducer → B&K 2613 Cathode follower

B&K 4136 Microphone → B&K UA 0030 adapter → B&K 2615 Cathode follower

Reference system

B&K 2801 Power supply

B&K 2801 Power supply

B&K 2112 Spectrometer

B – Frequency Calibration 500 – 20 000 cps

B&K 1014 Oscillator 500 cps – 20 Kcps → J.B. Lansing L.E. 85 Speaker)))))

Atlantic Res. LD 107-M1 Transducer → B&K 2613 Cathode follower

B&K 4136 Microphone → B&K UA 0030 Adapter → B&K 2615 Cathode follower

B&K 2801 Power supply

B&K 2801 Power supply

Anechoic chamber

Output control

B&K 2112 Spectrometer → B&K 2305 Level recorder

C – Frequency Calibration 20 000 – 90 000 cps

Hew.-Pack. 400 CD Oscillator → McIntosh 200 W Amplifier → Electrostatic speaker)))))

Atlantic Res. LD 107-M1 Transducer → Ad-Yu Mod 102B Amplifier → Ballantine true rms voltmeter

Reference system

B&K 4136 Microphone → B & K·UA 0030 Adapter → B&K 2615 Cathode follower

B & K 2801 Power supply
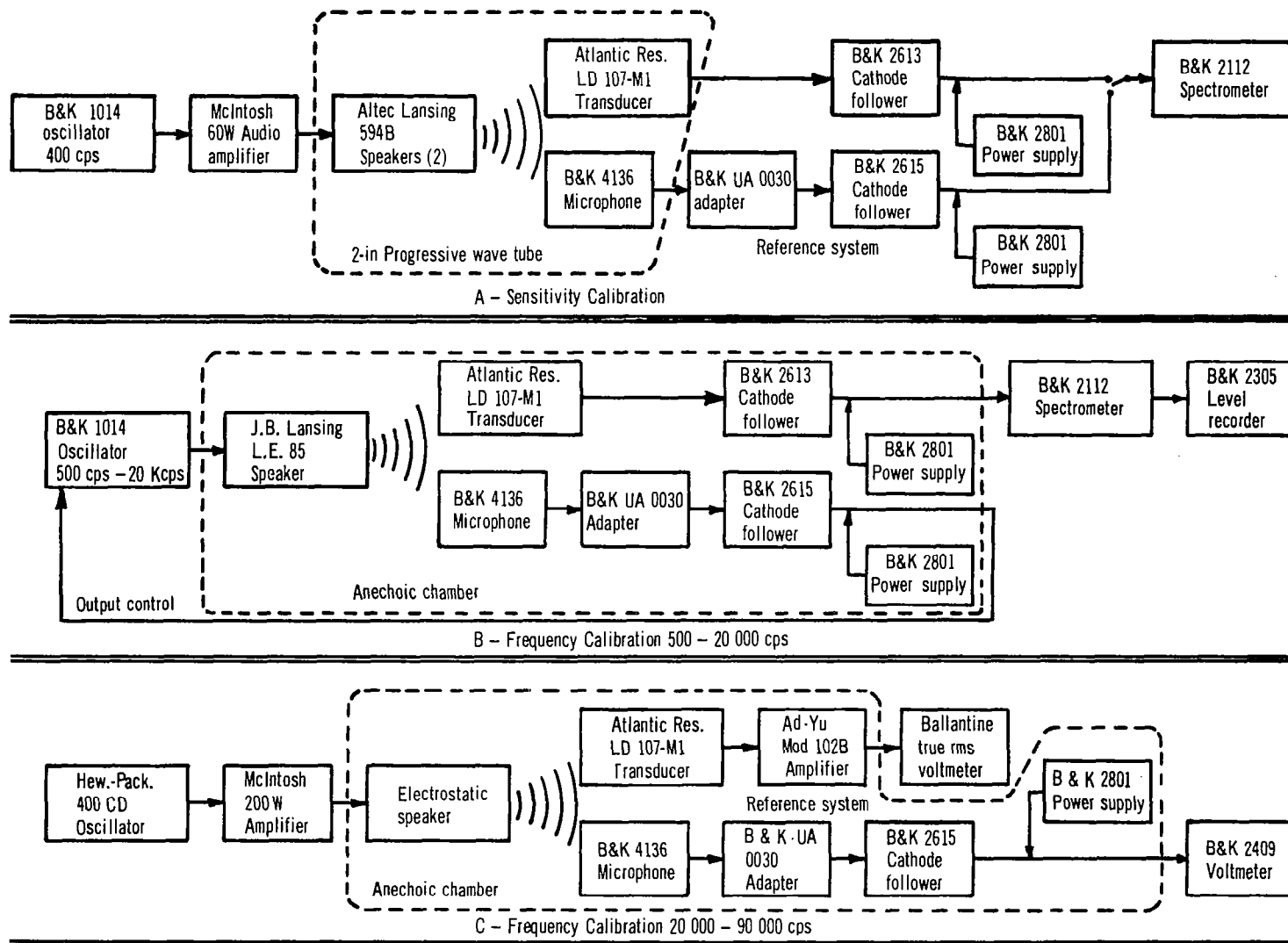
Anechoic chamber

B&K 2409 Voltmeter

Figure B-2. Schematic Diagrams for Calibrations of the A.R.C. LD 107-M1 Transducers

APPENDIX B

The LD107-M1 was calibrated for vibration sensitivity in the two major directions (parallel and perpendicular to the case). The sensitivity proved to be very frequency dependent reaching a maximum of 10 mV/g at about 8000 cps and falling off steeply on both sides. One LD107-M1 was buried during preliminary testing of the unperturbed boundary layer and the output was found to be below the signal from an exposed transducer. The difference was 6 dB in the octave band that included 8000 cps, and was always 20 dB or more in the other octave bands. An accelerometer mounted on the side wall insert holding the transducers indicated levels of vibratory response sufficiently low as to make the induced signal from vibration a negligible quantity. The minimum difference of 6 dB between vibration-induced and aerodynamically-induced signals could introduce, at most, an error of 1 dB in the data in a very narrow band of frequencies. Hence, no corrections for vibration sensitivity were included at any time.

B. 2   Phase Calibrations

Sets of channels were calibrated simultaneously with sinusoids at 63, 125, 250, 500, 1000, 2000, 4000, 8000, 16 000, 31 500, 63 000, and 126 000 cps. This calibration was performed electrically by inserting the voltage directly behind the transducer. When played back on the data acquisition system, it gave a measure of the frequency response for the complete system of data acquisition and data reduction minus only the transducer. In addition, this calibration permitted a check on the frequency dependence of the relative phase between channels, which were to be compared for cross-correlation studies. For purposes of data handling, the data tapes were transcribed from AM to the FM mode prior to digitizing. This relative phase calibration included the entire system from just behind the transducer, through the original data acquisition and recording system, the tape duplication system, and the tape playback and foldback preventive filtering system to just prior to the digitizing equipment. In most instances, the relative phase between two channels intended for cross-correlation (as measured by an Ad-Yu 405H phase meter) was less than 15° from 160 to 16 000 cps, the frequency range of the data used. The larger angles always occurred in the last octave band, the values being less than 10° at 8000 cps. Such phase deviation magnitudes would not introduce an error in the absolute value of the cross spectra, but would make the ratio of the erroneous cospectra to the true cospectra equal to approximately 0.966 of the true value, a negligible error.

For comparisons with one channel (13), however, the relative phase became considerable (error ratios were on the order of 0.6-0.7 at 16 000 cps). The data resulting from these cross-correlations have been used very sparingly, and where possible, deleted altogether. When used, the spectral content of energy concentrated in the low frequencies justified ignoring the higher frequency error.

138

APPENDIX B

B.3 Acoustical Sensitivity Calibration

At the beginning of each new series of tests, acoustical sinusoids at 250 or 500 cps were applied to the transducer, giving a sensitivity calibration for the entire data acquisition and reduction system. These calibrations used standard calibration equipment, as designated in fig. 11 of this report and provided the basic acoustical to electrical conversion information.

Appendix C

DETERMINATION OF CORRECTIONS TO ACCOUNT
FOR FINITE SIZE OF THE TRANSDUCERS

The attenuation of the electrical signal from a transducer that is sub-jected to very high frequencies has been a major annoyance to investigators since the problem was first recognized. Most reports published since 1962 have either noted the use of small ratios of $d/\delta*$ (≤ 0.2) or have attempted to correct for the attenuation.

Corcos (ref. 34) expressed his analytically determined correction, assuming spatial separability of the cross-correlation function, as

$$\phi_m/\phi = f(\omega d/2U_c) \tag{C-1}$$

where ϕ_m/ϕ is the ratio of the measured to actual spectral densities.

Assuming a known variation of U_c/U_∞ as a function of Mach number and $\omega\delta*/U_\infty$, an explicit derivation of ϕ_m/ϕ for each Mach number and frequency was obtained in ref. 1 and applied to the data. A more recent similarity model by Corcos (ref. 21) was originally used to calculate corrections for the data of the present investigation. This was done in spite of the present knowledge that some of Corcos' assumptions are questionable, particularly at supersonic speeds. (Specifically, correlations at small spatial separations of the transducers are not known.) It had been hoped that sufficient data would be available at an early time from the present study to allow better calculation of the finite size correction. Unfortunately, this was not the case and such a study must be undertaken at a later time.

In the meantime, however, Willmarth and Roos (ref. 25) published an article (in July 1965) in which they concluded that Corcos' corrections were generally too large (fig. 8 of ref. 25) at values of $d/2\delta^*$ less than 0.221. When $d/2\delta^*$ is much larger than 0.221, Corcos' corrections probably are nearly correct. The curves of fig. 8 (ref. 25) were cross-plotted as a function of $d/2\delta^*$ and appropriate corrections were then calculated for the spectral density data of the present investigation. It should be noted that only at $M = 3.45$ were the new corrections radically different from those calculated using Corcos' procedure. This is because the ratio of $d/2\delta^*$ varied from 0.17 to 0.6 at the other Mach numbers using the 0.060-in. piezoelectric transducer. These ratios were almost doubled for the condenser microphone. A sample of the results of the correction calculations may be seen in Table II.

An even more recent treatment of the subject was published (in August 1965) by Gilchrist and Strawderman (ref. 35) shortly before completion of the present contract. Of particular interest was their calculation of an

141

effective diameter for the same transducer used in the present study (the Atlantic Research Corporation LD-107). The value obtained was 0.068 in. as compared to the crystal diameter of 0.060 in. This amounted to a 14% error in the calculation of $d/2\delta^*$, but this error factor was considered to have a negligible effect on the finite size corrections.

Gilchrist and Strawderman (ref. 35) also determined the ratio of measured to actual spectral densities by careful tests at several velocities in a 3.5-in. diam. pipe. A comparison was made with Corcos' theoretical treatment (ref. 34), and the agreement was good except that their corrections were even larger than those found by Corcos.

In summary, several methods are available to calculate the effect of finite transducer size (refs. 25, 34, and 35), but widely divergent results may be shown at very high frequencies. In the present investigation, the method of Willmarth and Roos (ref. 25) was used although some evidence exists that their corrections may be insufficient. The obvious, though not always practical, solution is to conduct tests in thick boundary layers with the smallest transducers obtainable.

REFERENCES

1. Murphy, J. S.; Bies, D. A.; Speaker, W. V.; and Franken, P. A.: Wind Tunnel Investigation of Turbulent Boundary Layer Noise as Related to Design Criteria for High Performance Vehicles. NASA TN D-2247, Apr. 1964.

2. Bies, D. A.: A Wind Tunnel Investigation of Panel Response to Boundary Layer Pressure Fluctuations at Mach 1.4 and Mach 3.5. (To be published as a NASA Contractor Report).

3. Staff of Douglas Aerophysics Laboratory: Trisonic One-Foot Wind Tunnel; Description of the Facility and Provisions for Testing. Douglas Report ES 29278, Jan. 1959.

4. Bull, M. K.; Wilby, J. F.; and Blackman, D. R.: Wall Pressure Fluctuations in Boundary Layer Flow and Response of Simple Structures to Random Pressure Fields. University of Southampton, AASU Report 243, July 1963.

5. Maestrello, L.: Measurement and Analysis of the Response Field of Turbulent Boundary Layer Excited Panels. J. Sound and Vibration, vol. 2, no. 3, July 1965, pp. 270-292.

6. Kistler, A. L.; and Chen, W. S.: The Fluctuating Pressure Field in a Supersonic Turbulent Boundary Layer. JPL Technical Report No. 32-277, Aug. 1962.

7. Roshko, A.; and Thomke, G. T.: Observations of Turbulent Reattachment Behind an Axisymmetric Downstream-Facing Step in Supersonic Flow. Douglas Report SM-43069, Apr. 1965, (also submitted for publication to the AIAA Journal).

8. Kistler, A. L.: Fluctuating Wall Pressure Under a Separated Supersonic Flow. J. Acoust. Soc. Am., vol. 36, no. 3, Mar. 1964, pp. 543-550.

9. Ailman, C. M.: Wind Tunnel Investigation of the Fluctuating Pressures on the Surface of a Saturn I Vehicle, 2.75% Model. Douglas Report SM-44148, Aug. 1963.

10. Harrison, M.: Pressure Fluctuations on the Wall Adjacent to a Turbulent Boundary Layer. David Taylor Model Basin Report 1260, Dec. 1958.

11. Willmarth, W. W.: Wall Pressure Fluctuations in a Turbulent Boundary Layer. NACA TN 4139, Mar. 1958.

12. Willmarth, W. W.: Space-Time Correlations and Spectra of Wall Pressure in a Turbulent Boundary Layer. NASA Memo 3-17-59W, Mar. 1959.

13. McLeod, N. J.; and Jordan, G. H.: Preliminary Flight Survey of Fuselage and Boundary Layer Sound Pressure Levels. NACA RM H48B11, May 1958.

14. Mull, H. R.; and Algranti, J. S.: Flight Measurements of Wall Pressure Fluctuations and Boundary Layer Turbulence. NASA TN D-280, Oct. 1960.

15. Von Gierke, H. E.: Types of Pressure Fields of Interest in Acoustical Fatigue Problems. WADC- University of Minnesota Conference on Acoustical Fatigue, W. J. Trapp and D. H. Forney, eds. WADC ASD Technical Report 59-576, Mar. 1961.

16. Hilton, D. A.: In-Flight Aerodynamic Noise Measurements on a Scout Launch Vehicle. NASA TN D-1818, July 1963.

17. Belcher, P. M.: Predictions of Boundary-Layer Turbulence Spectra and Correlations for Supersonic Flight. Presented at the 5th International Acoustical Congress, Liege, Belgium, Sept. 1965.

18. Shattuck, R. D.: Sound Pressures and Correlations of Noise on the Fuselage of a Jet Aircraft in Flight. NASA TN D-1086, Aug. 1961.

19. Hodgson, T. H.: Pressure Fluctuations in Shear Flow Turbulence. Cranfield College of Aeronautics Note 129, 1962.

20. Bakewell, H. P., Jr.; Carey, G. F.; Libuha, J. J.; Schlormer, H. H.; and Von Winkle, W. A.: Wall Pressure Correlations in Turbulent Pipe Flows. USN USL Report 559, Aug. 1962.

21. Corcos, G. M.: The Structure of the Turbulent Pressure Field in Boundary-Layer Flows. J. of Fluid Mech., vol. 18, part 3, Mar. 1964, pp. 353-384.

22. Richards, E. J.; Bull, M. K.; and Willis, J. L.: Boundary Layer Noise Research in the U.S.A. and Canada - A Critical Review. Aeronautical Research Council ARC 21,766, Feb. 1960.

23. Lilley, G. M.: Wall Pressure Fluctuations under Turbulent Boundary Layers at Subsonic and Supersonic Speeds. Cranfield College of Aeronautics Note 140, Mar. 1963.

24. Serafini, J. S.: Wall-Pressure Fluctuations and Pressure-Velocity Correlations in a Turbulent Boundary Layer. NASA TR R-165, Dec. 1963.

25. Willmarth, W. W.; and Roos, F. W.: Resolution and Structure of the Wall Pressure Field Beneath a Turbulent Boundary Layer. J. of Fluid Mech., vol. 22, part 1, May 1965, pp. 81-94.

26. Williams, D. J. M.: Measurements of the Surface Pressure Fluctuations in a Turbulent Boundary Layer in Air at Supersonic Speeds. University of Southampton, AASU Report 162, Dec. 1960.

27. Bull, M. K.; and Willis, J. L.: Some Results of Experimental Investigations of the Surface Pressure Field Due to a Turbulent Boundary Layer. ASD Technical Documentary Report 62-425, Aug. 1962.

28. Eldred, K.; Roberts, W.; and White, R.: Structural Vibrations in Space Vehicles. WADD Technical Report 61-62, Mar. 1961.

29. Runstadler, P. W.; Kline, S. J.; and Reynolds, W. C.: An Experimental Investigation of the Flow Structure of the Turbulent Boundary Layer. Air Force Office of Scientific Research Technical Note - TN-5241, June 1963.

30. Eckert, E. R. C.: Engineering Relations for Friction and Heat Transfer to Surfaces in High Velocity Flow, J. Aeron. Sci., vol. 22, no. 8, Aug. 1955, pp. 585-587.

31. Coles, D. E.: The Turbulent Boundary Layer in a Compressible Fluid, RAND Corporation Report R-403-PR, Sept. 1962.

32. Tucker, M.: Approximate Calculation of Turbulent Boundary Layer Development in Compressible Flow. NACA TN 2337, Apr. 1951.

33. Reshotko, E.; and Tucker, M.: Approximate Calculation of the Compressible Turbulent Boundary Layer with Heat Transfer and Arbitrary Pressure Gradient. NACA TN 4154, Dec. 1957.

34. Corcos, G. M.: Resolution of Pressure in Turbulence. J. Acoust. Soc. Am., vol. 35, no. 2, Feb. 1963, pp. 192-199.

35. Gilchrist, R. B.; and Strawderman, W. A.: Experimental Hydrophone - Size Correction Factor for Boundary-Layer Pressure Fluctuations. J. Acoust. Soc. Am., vol. 38, no. 2, Aug. 1965, pp. 298-302.

36. Korst, H. H.: Theory for Base Pressures in Transonic and Supersonic Flow. J. Appl. Mech., vol. 23, Dec. 1956, pp. 593-600.